LHCb上底介子产生截面测量

（申请清华大学理学博士学位论文）

培 养 单 位 ： 工程物理系

学　　　科 ： 物理学

研　究　生 ： 刘　　勃

指 导 教 师 ： 高 原 宁 教 授

副指导教师 ： Patrick Robbe 研 究 员

联 合 导 师 ： 何 吉 波 博 士

二〇一二年十月

Measurements of the B meson production cross-sections at LHCb

Dissertation Submitted to

Tsinghua University

in partial fulfillment of the requirement

for the degree of

Doctor of Philosophy

in

Physics

by

LIU Bo

Dissertation Supervisor :	Professor GAO Yuanning
Associate Supervisor :	Researcher Patrick ROBBE
Cooperate Supervisor :	Doctor HE Jibo

October, 2012

关于学位论文使用授权的说明

本人完全了解清华大学有关保留、使用学位论文的规定，即：

清华大学拥有在著作权法规定范围内学位论文的使用权，其中包括：（1）已获学位的研究生必须按学校规定提交学位论文，学校可以采用影印、缩印或其他复制手段保存研究生上交的学位论文；（2）为教学和科研目的，学校可以将公开的学位论文作为资料在图书馆、资料室等场所供校内师生阅读，或在校园网上供校内师生浏览部分内容；（3）根据《中华人民共和国学位条例暂行实施办法》，向国家图书馆报送可以公开的学位论文。

本人保证遵守上述规定。

（保密的论文在解密后应遵守此规定）

作者签名：______________ 导师签名：______________

日　　期：______________ 日　　期：______________

摘 要

量子色动力学 (QCD) 是粒子物理学的标准模型理论的一个最基础的组成部分，描述夸克和胶子这两种基本粒子之间的强相互作用。对于强子对撞过程中底介子的产生截面，微扰QCD (pQCD) 能够在次领头阶下通过确定阶加次领头阶对数近似方法给出理论计算结果。在大型强子对撞机 (LHC) 上测量底介子产生截面是对这些 pQCD 计算的很好检验。

LHCb 探测器是一个单臂向前探测器，用于收集 LHC 上质子-质子对撞产物的物理信息。利用探测器在2010和2011年收集的35 pb^{-1}和370 pb^{-1}数据，通过重建和筛选底介子， LHCb 对质心能量为7 TeV的质子-质子对撞中底介子(包括B^+，B^0 和 B_s^0) 的微分产生截面与总截面的进行了测量。总截面的测量结果是

$$
\begin{aligned}
\sigma(B^+, 0 < p_{\rm T} < 40\,{\rm GeV}/c, 2.0 < y < 4.5) &= 41.4 \pm 1.4\,({\rm stat.}) \pm 3.2\,({\rm syst.})\ \mu{\rm b}\,(2010),\\
\sigma(B^+, 0 < p_{\rm T} < 40\,{\rm GeV}/c, 2.0 < y < 4.5) &= 41.6 \pm 0.3\,({\rm stat.}) \pm 2.7\,({\rm syst.})\ \mu{\rm b}\,(2011),\\
\sigma(B^0, 2 < p_{\rm T} < 40\,{\rm GeV}/c, 2.0 < y < 4.5) &= 32.3 \pm 0.4\,({\rm stat.}) \pm 2.4\,({\rm syst.})\ \mu{\rm b}\,(2011),\\
\sigma(B_s^0, 0 < p_{\rm T} < 40\,{\rm GeV}/c, 2.0 < y < 4.5) &= 7.9 \pm 0.2\,({\rm stat.}) \pm 2.5\,({\rm syst.})\ \mu{\rm b}\,(2011).
\end{aligned}
$$

括号中的数字表示数据的年份。这些结果与FONLL理论的预言符合得很好。

B_c^+ 介子由两种不同的重味夸克$\overline{b}$ 和 c组成，目前关于其性质的实验结果还不多。利用探测器在2011年收集的数据重建B_c^+ 介子， LHCb 测得的产生比率为

$$
\frac{\sigma(B_c^+) \times \mathcal{B}(B_c^+ \to J/\psi\,\pi^+)}{\sigma(B^+) \times \mathcal{B}(B^+ \to J/\psi\,K^+)} = 0.72 \pm 0.10\,({\rm stat.}) \pm 0.08\,({\rm syst.})\%,
$$

其中σ是横动量在$4-100\,{\rm GeV}/c$，赝快度在$2.5-4.5$范围内的产生截面， $\mathcal{B}$是分支比。这个结果可以为理解高能质子对撞中双重味强子的产生机制提供重要的实验信息。

关键词：味物理； 重夸克产生； 底介子产生

Abstract

Quantum Chromodynamics (QCD), one of the most fundamental components of the S-tandard Model theory of Particle Physics, is dedicated to describe the strong interactions among quarks and gluons. For the B meson production cross-sections in hadron-hadron collisions, perturbative QCD (pQCD) calculations are available at next-to-leading order (NLO) and with the fixed-order plus next-to-leading logarithms (FONLL) approximations. Measuring B meson production cross-sections at the Large Hadron Collider (LHC) is of great importance to test the pQCD calculations.

The LHCb detector is a single-arm forward spectrometer. It collects the physical information of the products in proton-proton collisions at the LHC. The differential and total production cross-sections of B mesons (including B^+, B^0 and B_s^0) in proton-proton collisions at $\sqrt{s} = 7$ TeV are studied using $35\,\mathrm{pb}^{-1}$ of data in 2010 and $370\,\mathrm{pb}^{-1}$ of data in 2011 collected by the LHCb detector, and reported in this dissertation. The total cross-sections are measured to be

$$\begin{aligned}
\sigma(B^+, 0 < p_\mathrm{T} < 40\,\mathrm{GeV}/c, 2.0 < y < 4.5) &= 41.4 \pm 1.4\,(\mathrm{stat.}) \pm 3.2\,(\mathrm{syst.})\ \mu\mathrm{b}\,(2010), \\
\sigma(B^+, 0 < p_\mathrm{T} < 40\,\mathrm{GeV}/c, 2.0 < y < 4.5) &= 41.6 \pm 0.3\,(\mathrm{stat.}) \pm 2.7\,(\mathrm{syst.})\ \mu\mathrm{b}\,(2011), \\
\sigma(B^0, 2 < p_\mathrm{T} < 40\,\mathrm{GeV}/c, 2.0 < y < 4.5) &= 32.3 \pm 0.4\,(\mathrm{stat.}) \pm 2.4\,(\mathrm{syst.})\ \mu\mathrm{b}\,(2011), \\
\sigma(B_s^0, 0 < p_\mathrm{T} < 40\,\mathrm{GeV}/c, 2.0 < y < 4.5) &= 7.9 \pm 0.2\,(\mathrm{stat.}) \pm 2.5\,(\mathrm{syst.})\ \mu\mathrm{b}\,(2011).
\end{aligned}$$

The numbers in the brackets indicate the year during which the data sample was collected. These results are in good agreement with FONLL theoretical predictions.

The B_c^+ meson, composed of two different heavy flavor quarks $\overline{b}$ and c, has not been well studied experimentally up to now. Using data collected by the LHCb detector in 2011, the production ratio is measured to be

$$\frac{\sigma\,(B_c^+) \times \mathcal{B}\,(B_c^+ \to J/\psi\,\pi^+)}{\sigma\,(B^+) \times \mathcal{B}\,(B^+ \to J/\psi\,K^+)} = 0.72 \pm 0.10\,(\mathrm{stat.}) \pm 0.08\,(\mathrm{syst.})\%,$$

where σ is the production cross-section in the range $4 < p_\mathrm{T} < 100\,\mathrm{GeV}/c$ and $2.5 < \eta < 4.5$ and $\mathcal{B}$ is the branching ratio. This result may shed light on the production mechanism of doubly flavored hadrons.

Key words: flavor physics; heavy quark production; B meson production

Contents

List of main acronyms

c	Speed of light, = $3 \times 10^8 \mathrm{ms}^{-1}$
E	Energy
M	Mass
p	Momentum
p_{T}	Transverse momentum
y	Rapidity
η	Pseudo rapidity
σ	Cross-section
SM	Standard Model
QCD	Quantum Chromodynamics
U(n)	Unitary (group) of degree n
SU(n)	Special unitary (group) of degree n
LO	Leading order
NLO	Next to leading order
FONLL	Fixed order plus next leading logs
MC	Monte Carlo
LHC	Large Hadron Collider
LHCb	LHC Bottom
$\mathcal{L}_{\mathrm{int}}$	Integrated luminosity
$\mathcal{B}$	Branching ratio
ϵ	Efficiency
ϵ_{acc}	Acceptance efficiency
ϵ_{rec}	Reconstruction efficiency
ϵ_{tri}	Trigger efficiency
IP	Impact parameter
PV	Primary vertex
TCK	Trigger configuration key
GEC	Global event cut
$\Delta \mathrm{LL}_{AB}$	Difference of the logarithmic likelihood between A&B hypothesizes

Chapter 1 Introduction

In the Standard Model, physical matter is composed of tiny elementary particles, *e.g.* quarks, leptons and mediators propagating the interactions between them. The B meson is a particle made up of a bottom quark/anti-quark $b/\bar{b}$ together with another anti-quark/quark $\bar{q}/q$ ($q = u, d, c, s$). The B mesons in the ground state and their quark contents are summarized in Table 1.1. In this dissertation, we use B^0, B^+, B_s^0 and B_c^+ to present both these B mesons and their anti-particles $\bar{B}^0$, B^-, $\bar{B}_s^0$ and B_c^- for simplicity.

Table 1.1 The B mesons in the ground state and their quark contents.

B meson	Quark content	anti-B meson	Quark content
B^0	$d\bar{b}$	$\bar{B}^0$	$\bar{d}b$
B^+	$u\bar{b}$	B^-	$\bar{u}b$
B_s^0	$s\bar{b}$	$\bar{B}_s^0$	$\bar{s}b$
B_c^+	$c\bar{b}$	B_c^-	$\bar{c}b$

B mesons are heavy and unstable. They do not exist in the daily low energy condition. Their properties are studied at the particle physics experiment where the B mesons can be produced from the collisions of particles accelerated to a very high speed by the accelerator. The Large Hadron Collider (LHC)[1] is the largest hadron collider with the highest colliding energy all over the world. Its research, development and construction started from 1994 and it succeeded to get the first proton-proton (pp) collision event on November 28, 2009. And then, in 2010 and 2011, it ran in stable pp beam conditions at the center-of-mass energy $\sqrt{s} = 7\,\text{TeV}$. The LHCb detector[2], located in the LHC[1] is a forward single arm spectrometer dedicated to search for possible New Physics evidence in heavy flavor physics. At $\sqrt{s} = 7\,\text{TeV}$, the $b\bar{b}$ cross-section is estimated approximately to be 260 μb. With the nominal luminosity of about $2 \times 10^{32}\text{cm}^{-2}\text{s}^{-1}$, 2×10^{11} $b\bar{b}$ events would be expected in one year of the LHCb data taking, about 90% of which containing B mesons.

The production cross-sections of the B mesons at pp collisions can be predicted by the perturbative quantum chromodynamics (pQCD). The calculations are available at next-to-leading order (NLO)[3] and with the fixed-order plus next-to-leading logarithms

(FONLL)[4,5] approximations. In the NLO and FONLL calculations, the theoretical predictions have large uncertainties due to the choice of the renormalization and factorization scales and the b-quark mass[6]. Accurate measurements will shed light on the validity of the different production models.

Several recent measurements of the B meson and $b\bar{b}$ production cross-sections in hadron collisions are summarized in Table 1.2. These results are consistent with pQCD

Table 1.2 Recent measurements of the B meson and $b\bar{b}$ production cross-sections in hadron collisions.

Variable	Decay mode	Region	Result
$\sigma(B^+)$ at CDF[7]	$B^+ \to J/\psi K^+$	$p_T > 6\,\text{GeV}/c$ and $\lvert y\rvert < 1$	$2.78 \pm 0.24\,\mu\text{b}$
$\sigma(B^+)$ at CMS[8]	$B^+ \to J/\psi K^+$	$p_T > 5\,\text{GeV}/c$ and $\lvert y\rvert < 2.4$	$28.1 \pm 2.4 \pm 2.0 \pm 3.1^{\dagger}\,\mu\text{b}$
$\sigma(B^0)$ at CMS[9]	$B^0 \to J/\psi K_s^0$	$p_T > 5\,\text{GeV}/c$ and $\lvert y\rvert < 2.2$	$33.2 \pm 2.5 \pm 3.5\,\mu\text{b}$
$\sigma(B_s^0)$ at CMS[10]*	$B_s^0 \to J/\psi\phi$	$8 < p_T < 50\,\text{GeV}/c$ and $\lvert y\rvert < 2.4$	$6.9 \pm 0.6 \pm 0.6\text{nb}$
$\sigma(b\bar{b})$ at LHCb[11]	$b \to D^0 X \mu^- \bar{\nu}$		$284 \pm 20 \pm 49\,\mu\text{b}$
$\sigma(b\bar{b})$ at LHCb[12]	J/ψ from B decays		$288 \pm 4 \pm 48\,\mu\text{b}$

* In fact $Br(B_s^0 \to J/\psi\phi)\sigma(B_s^0)$.

† Uncertainty from the luminosity measurement.

predictions within experimental and theoretical uncertainties.

This dissertation presents measurements of the B meson production cross-sections in pp collisions at a center-of-mass energy of $\sqrt{s} = 7\,\text{TeV}$ using data collected by the LHCb detector in 2010 and the first half of 2011, for a total luminosity of $34.6 \pm 1.2\,\text{pb}^{-1}$ for 2010 and $369.8 \pm 12.9\,\text{pb}^{-1}$ for 2011. In this dissertation, we use 2011 to present the first half of 2011 for simplicity. In Chapter 2, the theoretical background of B meson production cross-section calculation is given. The LHC machine, the LHCb detector and computing strategy are described in Chapter 3.

Measurements of the total production cross-section and the differential cross-sections as a function of p_T, $\frac{d\sigma}{dp_T}$, in the rapidity range $2.0 < y < 4.5$ using $34.6\pm1.2\,\text{pb}^{-1}$of data collected in 2010, are given in Chapter 4. p_T is the transverse momentum of the B meson and y is the rapidity, defined as $y = \frac{1}{2}\ln[(E + p_L)/(E - p_L)]$, where E is the particle energy and p_L is the particle momentum along the beam direction.

Due to the different analysis strategies, the B mesons are grouped into two categories in the analysis with 2011 data:

- The B mesons including B^+, B^0 and B_s^0 with a production rate at $\sigma(B)/\sigma(b\bar{b}) \sim \mathcal{O}(10^{-1})$;
- The B_c^+ meson with a production rate at $\sigma(B_c^+)/\sigma(b\bar{b}) \sim \mathcal{O}(10^{-3})$.

Measurements of both the total production cross-sections and the differential cross-sections as a function of $p_{\rm T}$ and y, $\frac{{\rm d}^2\sigma}{{\rm d}p_{\rm T}{\rm d}y}$, for $B^+$and B^0 and as a function of $p_{\rm T}$, $\frac{{\rm d}\sigma}{{\rm d}p_{\rm T}}$, for B_s^0 in the rapidity range $2.0 < y < 4.5$ using $370 \pm 13\,{\rm pb}^{-1}$ of data collected in 2011 at LHCb with $\sqrt{s} = 7\,{\rm TeV}$, are given in Chapter 5.

Measurement of the ratio

$$R_{c/u} = \frac{\sigma\,(B_c^+) \times \mathcal{B}\,(B_c^+ \to J/\psi\,\pi^+)}{\sigma\,(B^+) \times \mathcal{B}\,(B^+ \to J/\psi\,K^+)},$$

for $p_{\rm T}\,(B_c^+, B^+) > 4\,{\rm GeV}/c$ and $2.5 < \eta\,(B_c^+, B^+) < 4.5$, where η is the pseudo-rapidity ($\eta = \frac{1}{2}\ln\left[(|p| + p_{\rm L})/(|p| - p_{\rm L})\right]$, with p the particle momentum), is given in Chapter 6.

Finally, Chapter 7 presents a summary of this dissertation.

Chapter 2 Theoretical overview

This chapter describes the theoretical background for B meson production in Particle Physics. Particle Physics is one of the most fundamental and frontier branches of modern Physics. It touches the deepest structure of matter and handles the highest energy phenomena. The ideas and technologies of Particle Physics can help the society and improve the way we live, *e.g.* the particle accelerator technology, developed for Particle Physics experiment, is widely used in the diagnosis and treatment of lots of diseases. The World Wide Web was firstly invented in order to provide help for Particle Physicists to communicate in an international collaboration, and then spread all over the world. Further and more precise explorations in Particle Physics will deepen our understanding of the universe and benefit human beings even more.

Up to now, the Standard Model (SM) of Particle Physics is the most successful and effective theory to model almost everything in the physical university in modern elementary particle physics. We start with the elementary principles of this model[13] in Section 2.1. And then, the Quantum Chromodynamics (QCD), a component of Standard Model, is introduced in Section 2.2 to describe the properties and activities of quarks and gluons, of which the B meson is made. In the following Section 2.3, an approach of perturbative QCD (pQCD) to calculate the B meson production cross-section is given. In Section 2.4, the specific approach for B_c^+ production cross-section calculation is provided. The simulation of B meson productions at the LHC is described in Section 2.5.

2.1 Standard Model

The Standard Model is a relativistic quantum field theory (QFT)[14] of the elementary particles and their electromagnetic, weak and strong interactions. It is based on the local gauge symmetry group $SU(3) \otimes SU(2) \otimes U(1)$ with spontaneous symmetry breaking (SSB)[13,15,16].

In the Standard Model, physical matter is composed of spin-$\frac{1}{2}$ fermions and the interactions between the fermions, which are propagated by spin-1 gauge bosons① . There are twenty-four species of fermions, including quarks/anti-quarks and leptons/anti-leptons,

① Fermions and bosons are particles which obey the Fermi-Dirac[17] and Bose-Einstein statistics, respectively.

arranged in three generations:

$$\underbrace{\begin{pmatrix} u & d \\ c & s \\ t & b \end{pmatrix}}_{\substack{\text{Quarks}\\ \text{Anti-quarks}}} \quad \underbrace{\begin{pmatrix} e^- & \nu_e \\ \mu^- & \nu_\mu \\ \tau^- & \nu_\tau \end{pmatrix}}_{\substack{\text{Leptons}\\ \text{Anti-leptons}}}$$

$$\overbrace{\begin{pmatrix} \bar{u} & \bar{d} \\ \bar{c} & \bar{s} \\ \bar{t} & \bar{b} \end{pmatrix}} \quad \overbrace{\begin{pmatrix} e^+ & \bar{\nu}_e \\ \mu^+ & \bar{\nu}_\mu \\ \tau^+ & \bar{\nu}_\tau \end{pmatrix}}$$

Quarks have an electrical charge of $\frac{2}{3}e$ ($-e$ is the electron charge) for u, c, t and $-\frac{1}{3}e$ for d, s, b. Leptons have an electrical charge of $-e$ for e^-, μ^-, τ^- and 0 for neutrinos ν_e, ν_μ, ν_τ. Each quark and lepton has an anti-particle, which has the same nature but opposite electrical charge. Free quarks can not exist in the nature. Instead, a quark and an anti-quark form a meson and three quarks form a baryon.

In the SM, the interactions between fermions are carried by spin-1 bosons. These bosons can be divided into three categories: the eight gluons g of the strong interaction, the three vector bosons, $W^\pm$ and Z^0, of weak interaction and the photon γ of the electromagnetic interaction.

The Quantum Chromodynamics (QCD) describes the strong interactions among quarks and gluons. Theoretical calculation of B meson production cross-section could be established by several different approaches as detailed in the QCD section, Section 2.2.

The electromagnetic and weak interactions are uniformed by the electroweak (EW) model based on the $\mathrm{SU(2)} \otimes \mathrm{U(1)}$ gauge symmetry group[18]. The group theory[15] indicates the three gauge bosons W^i_μ, $i = 1, 2, 3$, and B_μ corresponding to the SU(2) and U(1) factors. The combinations of $W^{1,2}_\mu$ correspond to the weak bosons $W^\pm$, while the combinations of W^3_μ and B_μ correspond to the weak boson Z^0 and the electromagnetic boson γ.

In the weak interaction, the Parity, Charge and the Charge-Parity (CP) symmetries are broken[19–21]. Thus the weak force interacts differently between left and right handed particles, *i.e.* the left handed fermion fields transform as doublets and the right handed as singlets. The left handed doublets can be described as

$$\Psi_i = \begin{pmatrix} \nu_i \\ l_i^- \end{pmatrix}_L \text{ and } \begin{pmatrix} u_i \\ d_i' \end{pmatrix}_L ,$$

where i run from 1 to 3 indexing the generations of fermions. The d_i' indicate the quark flavor mixing, with $d_i' = \sum_j V_{ij} d_j$ where V_{ij} are the Cabibbo-Kobayashi-Maskawa (CKM)[22] mixing matrix elements. The right-handed neutrino does not exist in the Standard Model.

The electroweak force can interact between all kinds of fermions, thus fermions and bosons except for gluons can be classified under their SU(2) ⊗ U(1) transformation properties. The transformation properties of particles under SU(2) gauge transformation are described by the weak isospin I, while those under U(1) gauge transformation by the weak hyper-charge Y. The (I, Y) species of different particles, including a Higgs boson which is described below, under SU(2) ⊗ U(1) transformation are listed in Table 2.1.

Table 2.1 The (I, Y) of different particles under SU(2) ⊗ U(1) transformation[13]. The fermion symbols stand for three generations of fermions.

Types	Leptons		Quarks			Gauge bosons		Higgs
Particles	$\nu_L\ e_L$	e_R	$u_L\ d_L$	u_R	d_R	W/Z	γ	ϕ
(I, Y)	$(\frac{1}{2}, -1)$	$(0, -2)$	$(\frac{1}{2}, \frac{1}{3})$	$(0, \frac{4}{3})$	$(0, -\frac{2}{3})$	$(1, 0)$	$(0, 0)$	$(\frac{1}{2}, 1)$

There are several differences between the electromagnetic and weak forces, as summarized in Table 2.2. The different natures of the electromagnetic and weak forces indicate that the SU(2) ⊗ U(1) symmetry is broken. Besides, the gauge symmetry group SU(3) ⊗ SU(2) ⊗ U(1) theory is a massless theory, which can not tell why fermions and

Table 2.2 Differences between the weak and electromagnetic forces

Electromagnetic force	Weak force
Long distance	Short distance
Strong	Weak
Charge conservation	Charge non conservation
CP conservation	CP non-conservation

W/Z bosons have masses. To explain the symmetry breaking and origin of mass, the Higgs mechanism[23] is introduced.

The $\mathcal{L}$agrangian of the Higgs field is described as

$$\mathcal{L} = (D_\mu \Phi)^\dagger (D_\mu \Phi) - V(\Phi) \tag{2-2}$$

where the first term is the kinematic component with the covariant derivative D_μ and the second term is the Higgs potential with Φ as the Higgs field doublet.

The $SU(2) \otimes U(1)$ symmetry requires that, in the perturbative expansion of $V(\Phi)$, Φ and $\Phi^\dagger$ should appear together, while the theoretical renormalizability requires that the power of the Higgs field can not exceed 4 orders. Thus, the Higgs potential $V(\Phi)$ can be described as

$$V(\Phi) = -\mu^2 \Phi^\dagger \Phi + \lambda (\Phi^\dagger \Phi)^2 \tag{2-3}$$

with two free parameters λ and μ. If $\mu^2 > 0$ and $\lambda > 0$ is required, the minimum of the potential $V(\Phi)$ is negative at $\Phi^\dagger \Phi = \frac{\mu^2}{2\lambda}$. This means that the physical vacuum corresponds to non-zero Higgs field, or in other words, the Higgs field has non-zero vacuum expectation. If the potential $V(\Phi)$ is described as

$$V(\Phi) = \frac{1}{\sqrt{2}} \begin{pmatrix} \phi_1 + i\phi_2 \\ \phi_3 + i\phi_4 \end{pmatrix} \tag{2-4}$$

with ϕ_1, ϕ_2, ϕ_3 and ϕ_4 real, all the field quantities Φs satisfying

$$\Phi^\dagger \Phi = \frac{1}{2}(\phi_1^2 + \phi_2^2 + \phi_3^2 + \phi_4^2) = \frac{\mu^2}{2\lambda}, \tag{2-5}$$

which follow the $SU(2) \otimes U(1)$ symmetry, lead to the lowest potential but only one of the Φs corresponds to the physical vacuum. This is called the spontaneous symmetry breaking.

The Higgs field could be written in the unitary gauge as

$$\Phi = \frac{1}{\sqrt{2}} \begin{pmatrix} 0 \\ H + v \end{pmatrix} \tag{2-6}$$

where H is the real Higgs field and $v = \frac{\mu}{\sqrt{\lambda}}$ is the vacuum expectation value. Using this field to calculate the covariant derivative component of the Higgs $\mathcal{L}$agrangian in Equation 2-2, one can extract the non-zero Higgs mass and the weak boson W/Z masses proportional to the vacuum expectation from the quadratic term coefficients. After symmetry breaking, there is still an $U(1)$ symmetry left, corresponding to the electromagnetic interaction, and the propagator of the remaining symmetry is the massless photon. The Higgs boson hasn't been discovered experimentally up to now, which is one of the most important problems in the Standard Model as discussed in the following.

Exactly as the name "Standard Model", physicists want this model to cover everything in the physical universe. However, there are still several problems left, experimentally or philosophically. These problems draw extensive concern from the physics community and are listed below:

1. The Higgs boson hasn't been found experimentally. By now, some evidences have been reported by two experiments ATLAS[24] and CMS[25] at LHC. However, physicists from both experiments need more time and data to confirm the existence of Higgs boson or discard it.
2. Gravity is not included in the SM, although it exists everywhere and has been studied for a long time. Great efforts on the grand unification of the SM forces (strong and electroweak) and gravity have been made but nobody succeed.
3. Hierarchy or "unnaturalness" problems, which addresses the problem of the desert between the EW scale and the Plank scale.
4. Neutrino mass: Non-zero neutrino masses are not accommodated within the Standard Model but found experimentally[26]. This also corresponds to the existence of right-handed neutrinos.
5. Dark matter and dark energy[27], not included in the SM, are necessary to explain the discrepancies between the mass of astronomical objects determined from their gravitational effects, and the mass calculated from their luminous components.
6. Matter and anti-matter asymmetry is much large in the observable universe than what can be allocated by the CP violation in the SM.
7. The large quantity of free parameters, 18 in addition to the physical constants c and $\hbar$, make the SM unnatural to be a fundamental theory. Many theorists believe that the SM is a low energy effective theory, part of a more fundamental one, which will connect all the parameters together.

2.2 Quantum Chromodynamics

Quantum Chromodynamics (QCD), the gauge field theory that describes the strong interactions of colored quarks and gluons, is the SU(3) component of the $SU(3) \otimes SU(2) \otimes U(1)$ Standard Model of Particle Physics[28]. The color of quark and gluon is the charge of strong interaction indexed by three nominal labels, called ”red”, ”green” and ”blue”, which have no relations to optical colors.

The Lagrangian of QCD is given by

$$\mathcal{L} = \sum_{q} \bar{\psi}_q^a (i\gamma^\mu \partial_\mu \delta_{ab} - g_s \gamma^\mu t_{ab}^C A_\mu^{\mathrm{C}} - m_q \delta_{ab}) \psi_q^b - \frac{1}{4} F_{\mu\nu}^{\mathrm{A}} F^{\mathrm{A}\mu\nu}. \tag{2-7}$$

In the first sum, the first term corresponds to the interactions between quarks, the second to the interactions between a gluon and a quark and the third to the mass component. The last component of the Lagrangian describes the gluon field interactions.

The γ^μ are the Dirac γ matrices which satisfy the anti-commutation relations. The $\bar{\psi}_q^a$ and ψ_q^b are quark-field spinors for a quark with flavor q (flavor is the index of different quarks, *i.e.* $q = d, u, s, c, b, t$.) and mass m_q, and a, b are the color indices.

The g_s (or $\alpha_s = \frac{g_s^2}{4\pi}$) is the QCD coupling constant, which is one of the fundamental parameters of QCD. It has special ”running” properties: the value of g_s depends on the square of exchanged momentum between particles of a specific process, Q^2. If one neglects all but the lowest order, the relation is

$$g_s = \sqrt{\frac{48\pi^2}{(33 - 2N_f) \ln Q^2/\Lambda^2}}, \tag{2-8}$$

where Λ is a integration constant, which corresponds to the scale where the perturbatively-defined coupling would diverge. $N_f = 6$ is the number of quark flavors. More details are discussed below.

The A_μ^{C} represent the gluon fields, with C running from 1 to $N_{\mathrm{C}}^2 - 1 = 8$. As mentioned in Section 2.1, these eight gluon fields correspond to the adjoint representation of the SU(3) color group[15]. The t_{ab}^{C}, eight 3×3 matrices, are the generators of SU(3) color group defined by the commutation relations:

$$[t^{\mathrm{A}}, t^{\mathrm{B}}] = i f_{\mathrm{C}}^{\mathrm{AB}} t^{\mathrm{C}} = i \sum_{\mathrm{A} \neq \mathrm{B} \neq \mathrm{C}}^{1-8} \epsilon_{\mathrm{C}}^{\mathrm{AB}} t^{\mathrm{C}} \tag{2-9}$$

where the $f_{\mathrm{C}}^{\mathrm{AB}}$ are the structure constants of the SU(3) group.

Finally, the field tensor $F_{\mu\nu}^{A}$ is constructed from the gluon field A_μ^{C},

$$F_{\mu\nu}^{\mathrm{A}} = \partial_\mu A_\nu^{\mathrm{A}} - \partial_\nu A_\mu^{\mathrm{A}} - g_s f_{\mathrm{BC}}^{\mathrm{A}} A_\mu^{\mathrm{B}} A_\nu^{\mathrm{C}}. \tag{2-10}$$

The complex QCD Lagrangian leads to several problems in the perturbative calculation of physical observable, as discussed below. From the Lagrangian, Feynman rules of QCD

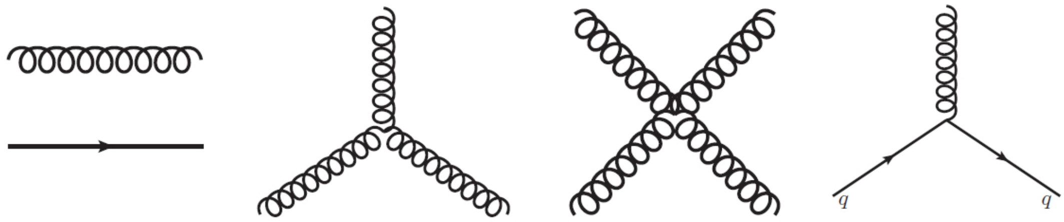

Figure 2.1 QCD Feynman rules for gluons (curly lines) and fermions (solid lines)[29].

can be calculated, shown in Figure 2.1. QCD has seven fundamental parameters: the coupling constant g_s and the quark masses m_q, as discussed below.

In Quantum Field Theory, when calculating the Green function using the perturbative Feynman rules, the divergence problem arises from loop diagram momentum integral. The renormalization approach[30–32] is introduced to the QFT to subtract the ultraviolet divergence in high energy. The physical constants, such as electron charge, mass or coupling constants, would be redefined in terms of quantities measured at a specific kinematic renormalization point, which has a characteristic energy, to absorb the divergence[32]. The characteristic energy is called the renormalization scale μ_{R}. The renormalization approach must be developed in a specific subtraction scheme. The most commonly used one is the modified minimal subtraction ($\overline{\mathrm{MS}}$) scheme[33]. In this scheme, the dimensional regularization approach is introduced to reduce the time-space dimension and calculate the momentum integral in the reduced dimension. The integral under the reduced $4-\epsilon$ dimensions instead of 4 has a pole when $\epsilon \to 1$, corresponding to the divergence component, and can be absorbed in the renormalization procedure. The infrared (low energy) divergence mainly from gluon emission is subtracted by a factorization approach as discussed in Section 2.3.1.

In the framework of perturbative QCD (pQCD), the strong interaction coupling constant α_s is ”running” as a function of the renormalization scale μ_{R}, and satisfies the following renormalization group equation (RGE)[28]

$$\mu_R^2 \frac{\mathrm{d}\alpha_s}{\mathrm{d}\mu_R^2} = \beta(\alpha_s) = -(b_0\alpha_s^2 + b_1\alpha_s^3 + b_2\alpha_s^4 + \cdots) \tag{2-11}$$

where b_0, b_1 and b_2 are the 1-loop, 2-loop and 3-loop beta-function coefficients respectively. When neglecting all but the $b_0 = (33-2n_f)/(12\pi)$ term and taking μ_R close to the scale of the momentum transfer Q, one can get the Equation 2-8. The minus sign of the coefficients in Equation 2-11 is the origin of asymptotic freedom. The strong coupling α_s decreases as the μ_{R} increases, which means that quarks can be considered as ”free” particles in high energy collisions with large momentum transfer.

Quark masses are fundamental parameters of QCD both theoretically and experimentally; however, the definition of the quark mass is a complex question. Free quarks have never been observed, which leads to a property called color confinement. A single quark with color does not exist on its own but has to hadronize with other quarks into a color singlet state (meson or baryon) except for the top quark. The top quark lifetime is so short that it decays before it has time to form a resonance state. A perturbatively defined prescription of the quark mass is the pole mass m_q[34], which corresponds to the value for which the propagator diverges. However, when relating it to observable quantities, it suffers from substantial non-perturbative ambiguities[35]. An alternative could be the $\overline{\mathrm{MS}}$ mass, $m_q(\mu_{\mathrm{R}}^2)$, which depends on the renormalization scale μ_{R}. In general, heavy quarks (c, b, t) masses are described either as the pole mass or as the $\overline{\mathrm{MS}}$ mass with the scale equal to its mass; light quark masses are described in the $\overline{\mathrm{MS}}$ scheme at the scale $\mu_R \sim 2\,\mathrm{GeV}$[28].

2.3 B meson production cross-section calculation in perturbative QCD

B meson is the particle made of one bottom quark $b/\bar{b}$ and another quark $\bar{q}/q$. $b\bar{b}$ quarks were predicted theoretically in 1973-1975[20,36] and found with the Υ ($b\bar{b}$) resonance state at the Fermilab E288 experiment in 1977[37]. The b quark has an electric charge of $-\frac{1}{3}e$, $I(J^P) = 0(\frac{1}{2}^+)$[①] and a bottom number equal to -1. Its mass in the $\overline{\mathrm{MS}}$ scheme is $4.19^{+0.18}_{-0.06}$ GeV/c^2[28]. The $\bar{b}$ quark has the same nature except for the opposite electric charge and bottom number.

In the Quantum Field Theory calculation, perturbation theory is a powerful tool to get the approximate solutions of complex equations which are hard to solve analytically. In Section 2.2, perturbative expansions have already been introduced to deal with the running property of the coupling constant α_s. In this section, the perturbative QCD (pQCD) approach to calculate the B meson production cross-section is given. We start with the parton model, which describes the hadron structure in a framework consistent with the perturbation theory. In the following Section 2.3.2, general perturbative formulae for $b\bar{b}$ production cross-section calculation are introduced in the picture of the parton model

① I is the isospin, J the angular momentum and P the parity.

and the calculation at the lowest order is described. In Section 2.3.3 and 2.3.4, higher order corrections are discussed. The Section 2.3.5 gives a description of fragmentation and hadronization which are processes describing how the $b\overline{b}$ quarks evolve to form B mesons. Section 2.3.6 summarizes the theoretical uncertainty of these calculations and provides the results of cross-section calculations.

2.3.1 Parton model and deep inelastic scattering

Parton model was developed to explain the deep inelastic scattering (DIS): $e + p \to e + X$ process at first[38]. In the parton model, when the momentum transfer is extremely high ($Q \gg m_{\text{proton}}$) (so-called "deep" scattering), the partons (including quarks and gluons) of the proton can be treated as point-like free particles, in other words, the interactions between electron and different partons are uncorrelated elastic scatterings. The differential cross-section of DIS processes is determined by the proton structure function, which is independent of the momentum transfer, and of the kinematic variables.

The structure functions are given by the non-perturbative parton distribution functions (PDFs), which are the momentum distributions of partons in proton. Including higher orders, the structure functions can be expanded into a serie in powers $\alpha_s(\mu_{\text{R}}^2)$[28],

$$F(x, Q^2) = x \sum_{n=1}^{\infty} \frac{\alpha_s^n(\mu_{\text{R}}^2)}{(2\pi)^n} \sum_{i=q,g} \int_x^1 \frac{\mathrm{d}z}{z} C_i^{(n)}(z, Q^2, \mu_{\text{R}}^2, \mu_{\text{F}}^2) f_i\left(\frac{x}{z}, \mu_{\text{F}}^2\right) + O\left(\frac{\Lambda^2}{Q^2}\right). \tag{2-12}$$

where μ_{F} is the factorization scale which is described below. The expansion coefficients $C_i^{(n)}$ can be calculated according to Feynman diagrams. The functions $f_i(\frac{x}{z}, \mu_{\text{F}}^2)$ are the PDFs of the i^{th} parton in the proton. The momentum of the quark when interacting can be different from that when "departing" from the proton as a free parton, because of the soft gluon emission. The integration variable z is defined as the ratio of these two momenta. Both the coefficients $C_i^{(n)}$ and the PDFs depend on the ratio z.

Considering the soft gluon emission process, which may lead to infrared divergence in perturbative expansion coefficients of the structure function, one can treat the process as a modification of the PDF instead of the perturbative interaction between electron and parton, so that the divergence can be absorbed into PDFs. This procedure, called factorization, is most commonly developed in the modified minimal subtraction ($\overline{\text{MS}}$) scheme. It introduces an arbitrary factorization scale μ_{F} to separate the two categories: processes with momentum transfer $Q > \mu_{\text{F}}$ are included in the expansion coefficients; processes with $Q < \mu_{\text{F}}$ are absorbed into the PDFs. The coupling constant α_s, the short distance cross-section $\hat{\sigma}$ and the PDFs all depend on the choice of subtraction scheme. The change of scheme only varies the weights of the divergence corrections among these three variables and has no impact upon the observable quantities.

Parton distribution functions are non-perturbative and not easy to calculate, but have to be mainly determined from experiments. If the same factorization scheme, $\overline{\text{MS}}$ scheme, is used in both DIS and pp collision, the PDFs from DIS can be used in the prediction of pp collision[39]. The relation between PDFs and the factorization scale μ_{F} is described by the Dokshitzer-Gribov-Lipatov-Altarelli-Parisi (DGLAP) equation[40–42]. Using this equation, one can extract PDFs for the perturbative calculation of $b\overline{b}$ production cross-section.

2.3.2 Perturbative expansion of $b\bar{b}$ production cross-section

The $b\overline{b}$ production in hadronic collisions can be described in the parton model, which is described in Section 2.3.1, as shown in Figure 2.2

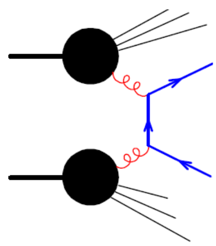

Figure 2.2 Typical diagram for $b\overline{b}$ production[43].

The standard perturbative QCD formula for the inclusive production of a heavy quark q with momentum p and energy E of a colliding process

$$H_A(P_1) + H_B(P_2) \to q(p) + X$$

where P_1 and P_2 are the momenta of the colliding hadrons H_A and H_B, describes the cross-section as

$$\frac{E\mathrm{d}^3\sigma}{\mathrm{d}p^3} = \sum_{i,j} \int \mathrm{d}x_1 \mathrm{d}x_2 [\frac{E\mathrm{d}^3\hat{\sigma}_{ij}(x_1P_1, x_2P_2, p, \mu_{\text{R}}, \mu_{\text{F}})}{\mathrm{d}p^3}] f_i^A(x_1, \mu_{\text{F}}) f_j^B(x_2, \mu_{\text{F}}) \tag{2-14}$$

where i and j run for the partons in the colliding hadrons. $\hat{\sigma}_{ij}$ corresponds to the short distance cross-section for the production of $b\overline{b}$ pair from the interacting partons, and can be calculated as a perturbation serie in $\alpha_s(\mu^2)$. x_1 and x_2 are the momentum fractions of the partons, *i.e.* $p_1 = x_1 P_1$ and $p_2 = x_2 P_2$. $f_i^A(x_1, \mu_F^2)$ and $f_j^B(x_2, \mu_F^2)$ are the i^{th} and j^{th} parton distribution functions[3].

By integrating the Equation 2-14 over the momentum p, the total production cross-section σ of a $b\bar{b}$ pair is written as

$$\sigma(S) = \sum_{i,j} \int \mathrm{d}x_1 \mathrm{d}x_2 F_i(x_1, \mu_F^2) F_j(x_2, \mu_F^2) \hat{\sigma}_{ij}(x_1 x_2 S, \mu_R^2, \mu_F^2) \tag{2-15}$$

where S is the square of the center-of-mass energy of the colliding hadrons H_A and H_B. The short distance cross-sections $\hat{\sigma}_{ij}$ can be written as

$$\hat{\sigma}_{ij}(s, \mu_R^2, \mu_F^2) = \frac{\alpha_s^2(\mu_R^2)}{m^2} f_{ij}(\rho, \mu_R^2, \mu_F^2) \tag{2-16}$$

where s is the square of the partonic center of mass energy and m the mass of the parton. The variable $\rho = 4m^2/s$ represents the energy dependance of the cross-section. pQCD gives an approach for calculating $\hat{\sigma}_{ij}$ as a power serie expansion in $\alpha_s(\mu^2)$. The expansion of the $f_{ij}(\rho)$ function[43] is written as

$$f_{ij}(\rho, \mu_R^2, \mu_F^2) = f_{ij}^{(0)}(\rho) + 4\pi\alpha_s(\mu_R^2)[f_{ij}^{(1)}(\rho) + \bar{f}_{ij}^{(1)}(\rho) \log(\frac{\mu^2}{m^2})] + O(\alpha_s^2). \tag{2-17}$$

The n^{th} order short distance cross-section coefficients $f_{ij}^{(n)}(\rho)$ and $\bar{f}_{ij}^{(n)}(\rho)$ should be calculated for different contributing parton subprocess diagrams.

At the leading order (LO), $b\bar{b}$ pairs will be produced by the flavor creation (FC) mechanism. In this mechanism, two incoming gluons or quarks annihilate to produce outgoing heavy quarks. Examples of Feynman diagrams of FC are shown in Figure 2.3. The lowest order $f_{ij}^{(0)}(\rho)$ corresponding to these diagrams can be calculated analytically[3]

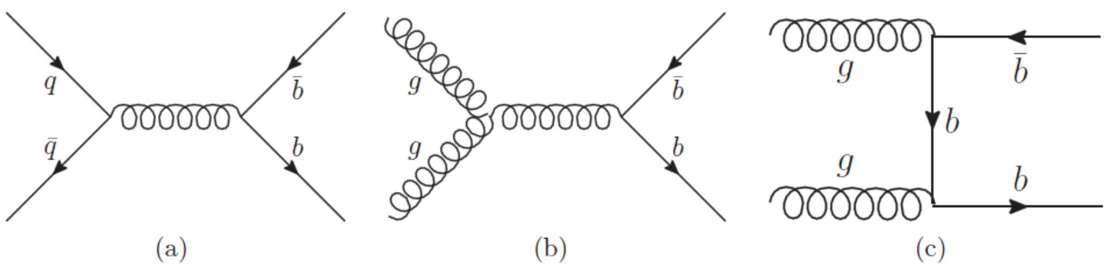

Figure 2.3 Feynman diagrams for LO $b\bar{b}$ production.

as shown in Figure 2.5 in Section 2.3.3.

In the high energy limit, called Balitsky-Fadin-Kuraev-Lipatov (BFKL) limit[44,45], where the center-of-mass energy is much larger than the scale of the specific process, which is just the $b\bar{b}$ production case at LHC, each power of α_s higher than the leading order can be accompanied with a power of $\log(\frac{\mu^2}{m^2})$. The leading logarithmic (LL) terms and next-to-leading logarithmic (NLL) terms, which invalidate the convergence, are calculated by a resummation approach.

Next leading order (NLO) corrections of short distance cross-sections are described in the Section 2.3.3, and the resummation approaches are introduced as the fixed order plus next to leading order logarithms (FONLL) method in the Section 2.3.4 .

2.3.3 Next to leading order calculation

The parton processes which contribute in the next to leading order α_s^3 are:

$$
\begin{aligned}
q + \bar{q} &\to b + \overline{b} \quad \text{at } \alpha_s^2,\ \alpha_s^3 \\
g + g &\to b + \overline{b} \quad \text{at } \alpha_s^2,\ \alpha_s^3 \\
q + \bar{q} &\to b + \overline{b} + g \quad \text{at } \alpha_s^3 \\
g + g &\to b + \overline{b} + g \quad \text{at } \alpha_s^3 \\
q + g &\to b + \overline{b} + q \quad \text{at } \alpha_s^3 \\
\bar{q} + g &\to b + \overline{b} + \bar{q} \quad \text{at } \alpha_s^3.
\end{aligned}
$$

Besides the diagrams in Section 2.3 with the addition of a self coupling loop or gluon emission, two production mechanisms of gluon splitting (GS) and flavor excitation (FEX) have to be taken into account. In GS an outgoing off-shell gluon from a $gg \to gg$ process splits into a $b\bar{b}$ pair. In case of FEX at least one of the b-quarks is scattered by e.g. a gluon. Examples of Feynman diagrams of GS and FEX are shown in Figure 2.4.

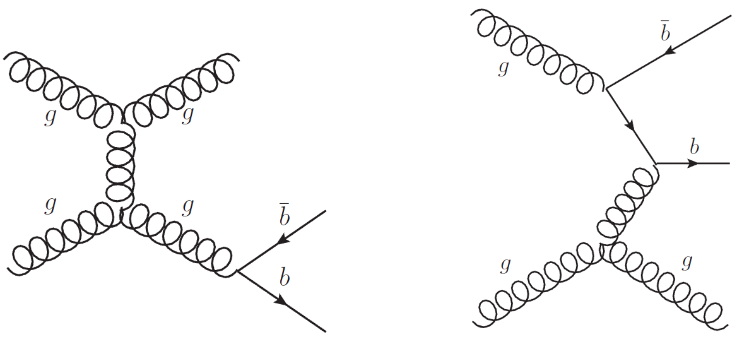

Figure 2.4 Feynman diagrams for NLO $b\bar{b}$ production by *left*: gluon splitting and *right*: flavor excitation.

In the calculations of these diagrams, ultraviolet and infrared divergences can be subtracted using the renormalization and factorization approaches, respectively, as discussed in the above sections. Since the scheme change effects on the observable quantities are corrections at high order and thus negligible, a decoupling scheme[46] similar to the $\overline{\text{MS}}$ scheme is used to deal with the divergences from heavy-flavor loops. In this decoupling scheme, differently from the $\overline{\text{MS}}$ scheme, the flavors are not treated equally. When the energies of the loops are much lower than the heavy quark mass, the heavy quark is neglected and the flavor number N_{f} becomes $N_{\text{lf}} = N_{\text{f}} - 1$ instead. An approach in order to translate the result from the N_{lf} scheme to the N_{f} scheme is discussed in Ref.[4].

The short distance cross-section coefficients $f_{ij}^{(1)}$ as mentioned in Equation 2-17 for the $g-g$ and $q-\bar{q}$ subprocesses have been calculated[43] and are illustrated in Figure 2.5. The Figure 2.5 (right) shows that the gg diagram leads to a logarithm divergence in the

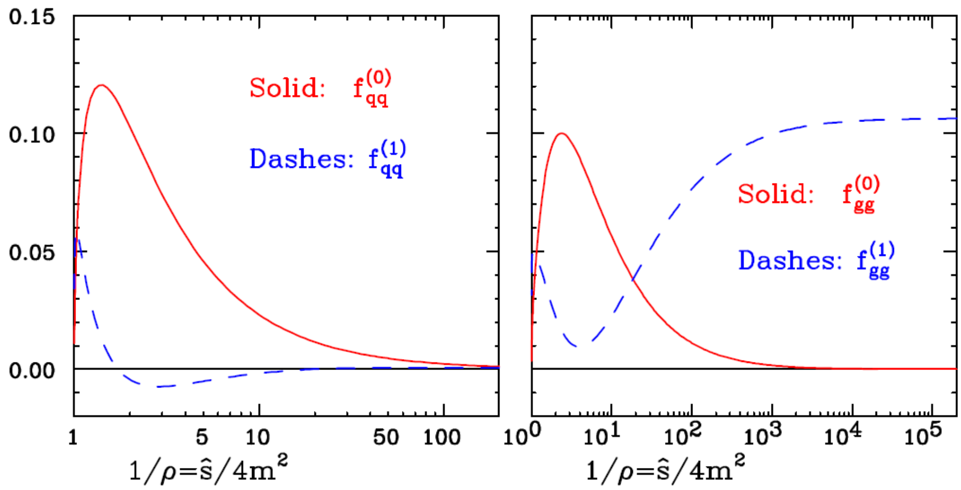

Figure 2.5 The short distance cross-section coefficients $f_{ij}^{(0)}$(solid red) and $f_{ij}^{(1)}$(dashed blue) for the *left*: $q-\bar{q}$ and *right*: $g-g$ subprocesses from Ref.[43].

high energy region at the NLO. As discussed in Section 2.3.2, the divergences are originated from the logarithmic terms in the high energy limit. An approach is introduced to estimate the first LL terms ($\alpha_s^2(\alpha_s \log \frac{\mu}{m})^2$) by choosing the μ_{R} and μ_{F} scale at the order of p_{T}. This approach gives a reasonable estimate in the low p_{T} range and fails at very large p_{T}. The FONLL process with a resummation approach to cover the large p_{T} range are described in the next section.

2.3.4 Fixed order plus next to leading order logs

The NLO calculation in Section 2.3.3 is reasonable when the heavy-quark mass is the only relevant mass scale of the specific process, and it fails when the transverse momentum of the heavy quark is much larger than its mass. In that case, the order of neither the heavy quark mass nor the transverse momentum can be chosen as the renormalization and factorization scales, since the large logarithms in terms of $\alpha_s^2(\alpha_s \log \frac{p_\mathrm{T}}{m})^n$ (LL) and $\alpha_s^3(\alpha_s \log \frac{p_\mathrm{T}}{m})^n$ (NLL) break the convergence.

Since the scale is fixed to the heavy quark mass in the LO and NLO calculations, these two components are called fixed order (FO) calculations. A resummation approach is introduced in Ref.[47] which transforms the fragmentation functions to fold and resum the LL and NLL terms in the short distance cross-section. This approach considers mediate processes like $ij \to k \to b$, where the $k \to b$ processes are described by the fragmentation functions. i, j, k indicate quarks with all the flavors by neglecting the heavy quark mass. It is not reasonable in the low p_T range because all the contributions suppressed by $\frac{m}{p_\mathrm{T}}$ are neglected. In other words, it is a "massless" approach.

The combination of the fixed order together with the LL and NLL resummed calculations of the hadron production cross-section is written[4] as

$$\begin{aligned} \frac{\mathrm{d}\sigma}{\mathrm{d}p_\mathrm{T}^2} &= A(m)\alpha_s^2 + B(m)\alpha_s^3 \\ &+\left(\alpha_s^2 \sum_{i=2}^{\infty} a_i(\alpha_s \log \frac{\mu}{m})^i + \alpha_s^3 \sum_{i=1}^{\infty} b_i(\alpha_s \log \frac{\mu}{m})^i\right) \times G(m, p_\mathrm{T}) \\ &+O(\alpha_s^4), \end{aligned}$$

where coefficients $A(m)$ and $B(m)$ are extracted from the LO and NLO calculations discussed in previous section. The coefficients a_i and b_i depend on the colliding center-of-mass energy S, p_T and scales μ. The function $G(m, p_\mathrm{T})$ has to approach unity when $\frac{m}{p_\mathrm{T}} \to 0$ and to suppress the logarithm terms in the low p_T range. It can be determined from the order of $\frac{m}{p_\mathrm{T}}$ at which the massless resummation approach is a good approximation of the massive calculation.

The FONLL approach makes use of the existing calculations from the FO approach and the resummation (RS) approach. The final result[4] is described as

$$\mathrm{FONLL} = \mathrm{FO} + (\mathrm{RS} - \mathrm{FOM0}) \times G(m, p_\mathrm{T}) \tag{2-19}$$

where FOM0, the "massless limit" component, corresponds to the FO terms in the RS calculation which should be subtracted to avoid double counting. A matching procedure is introduced to match the RS and the FOM0 calculations [4].

2.3.5 Fragmentation

b and $\bar{b}$ quarks can not exist as free particles due to the quark confinement. The process where a $b/\bar{b}$ quark forms a bound state ($\overline{B}/B$ hadron) with another quark $\bar{q}/q$ is called hadronization. The hadronization process happens much later than the $b\bar{b}$ quark pair creation and doesn't affect the inclusive $b\bar{b}$ production cross-section. The creation of quark pairs and their hadronizations are called fragmentation, which can be described by the following formula in the parton model,

$$\frac{\mathrm{d}\sigma_{\mathrm{had}}}{\mathrm{d}P_{\mathrm{T}}} = \int_{\frac{P_{\mathrm{T}}}{E_{\mathrm{beam}}}}^{1} \frac{\mathrm{d}z}{z} f(z, \mu^2_{\mathrm{frag}}) \frac{\mathrm{d}\sigma}{\mathrm{d}p_{\mathrm{T}}}(\mu^2_{\mathrm{frag}}) \tag{2-20}$$

where P_{T} is the transverse momentum of the produced hadron, $\frac{\mathrm{d}\sigma}{\mathrm{d}p_{\mathrm{T}}}$ is the differential production cross-section and p_{T} is equal to $\frac{P_{\mathrm{T}}}{z}$. The fragmentation scale μ_{frag}, like the factorization scale, is introduced to absorb the final state soft gluon radiations into the fragmentation function. The fragmentation functions $f(z, \mu^2_{\mathrm{frag}})$ can be described in several different forms. The Peterson fragmentation function,

$$f(z) = \frac{1}{z(1 - \frac{1}{z} - \frac{\epsilon_Q}{1-z})^2} \tag{2-21}$$

where ϵ_Q corresponds to the ratio of the light quark mass with respect to the heavy quark mass, is commonly used [48] for heavy flavor production.

Experimental inputs are required to improve the accuracy of fragmentation functions. And then the functions can be used to give theoretical predictions for more experiments. The hadronization fractions for B hadrons [28], which are the branching fractions of $\bar{b} \to B$, are listed in Table 2.3. These fractions need feedback from the LHC experiments. The B meson production cross-section measurements in this dissertation can be extended to extract hadronization fraction results.

2.3.6 Theoretical uncertainties and differential cross-section distributions

From Equation 2-14 and the discussions above, the theoretical uncertainties on the B meson production cross-section calculation arise from the renormalization and factorization scales, the b quark mass and the parton distribution functions, theoretically. In the FONLL calculation, the largest uncertainty comes from the renormalization and factorization

Table 2.3 Summary of hadronization fractions for B hadrons[28].

B hadron	Hadronization fraction
B^0	$40.1 \pm 1.3\%$
B^+	$40.1 \pm 1.3\%$
B_s^0	$11.3 \pm 1.3\%$
b baryon	$8.5 \pm 2.2\%$
Others	Negligible

treatments of the high order effects, as shown in Figure 2.6. It is estimated by varying the renormalization and factorization scales by a factor of two both above and below the central values. As discussed in Section 2.2, the quark masses are not yet determined accurately theoretically and are not easy to measure experimentally. The mass uncertainty is estimated by varying the mass by 0.25 GeV/c^2. The uncertainty on PDFs are determined together with the PDFs experimentally.

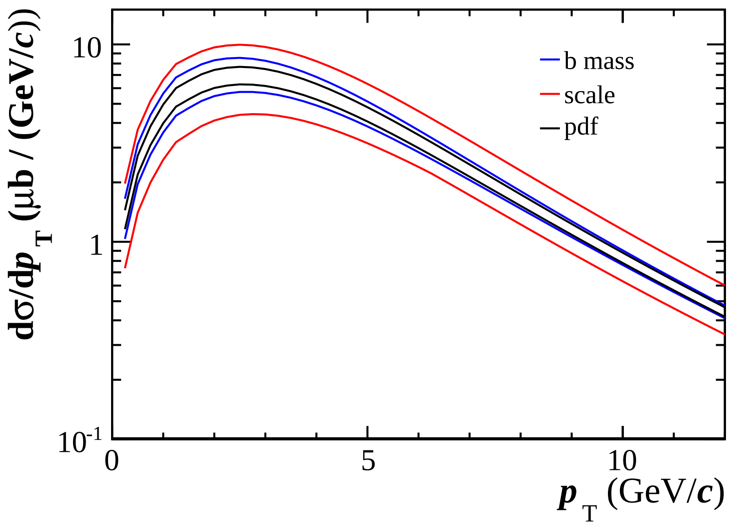

Figure 2.6 Theoretical uncertainties on FONLL calculation from three sources[49]. The red line corresponds to the upper and lower limits by varying the renormalization and factorization scales, the blue to the b quark mass and the black to the PDF uncertainties.

A comparison of NLO and FONLL calculations from Ref.[43] is shown in Figure 2.7. The uncertainty bands of FONLL are much narrower than those of the NLO calculations. The overall distribution of FONLL calculation is steeper than the NLO ones, because the resummation approach takes multiple radiation into account.

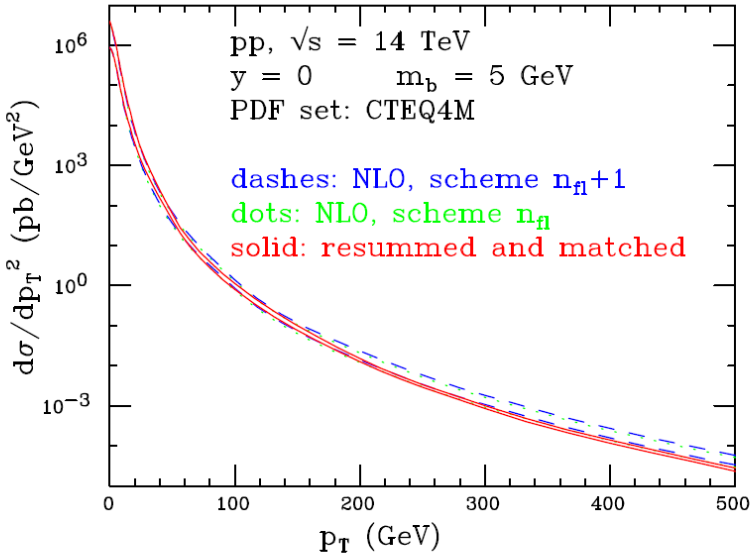

Figure 2.7 The comparison of NLO and FONLL calculations of differential cross-sections for b production at $\sqrt{s} = 14\text{TeV}$[43]. The dashed and dotted lines correspond to the NLO calculation in $\overline{\text{MS}}$ and extended $\overline{\text{MS}}$ schemes, respectively. The solid line corresponds to the FONLL calculation as a combination of FO and resummed and matched terms. The bands are uncertainties from the renormalization and factorization scales described in the text.

2.4 B_c^+ production cross-section

The extra heavy c quark makes the B_c^+ production different from the other B mesons. Theoretical approaches have also been developed in the picture of parton model. Similar as the FONLL approach discussed in Section 2.3.4, the B_c^+ production is also predicted at LO using a fixed-order approach and an resummation approach by resumming the mediate fragmentation function[50,51]. The effect of the later one has been studied and found to be not dominant at the energy level of LHC[52].

In the calculation of fixed order component, due to the heavy quark c, the leading order of B_c^+ production is $O(\alpha_s^4)$[53]. It is assumed that only the light flavors (u, d, s) are active and their PDFs contribute to the cross-section. The contributions of the heavy flavors are studied by resumming the collinear logarithms in the initial state and found to be very small[54,55]. The contributions from the resummation approached of the initial and final states are negeligeble, and the LO calculation can be found in Ref.[56,57].

2.5 Simulation of B meson production

The production of B meson is simulated by Pythia[58], a general Particle Physics particle generator software package. The b-hadron production in Pythia emerges from leading order $2 \to 2$ QCD processes: $q\bar{q} \to gg$, $qg \to qg$, $gg \to q\bar{q}$ and $gg \to gg$. Signal B meson samples are generated using the following procedure: once a b quark is found in a primary event, the same primary event is repeatedly hadronized until the B meson is obtained.

With the QCD processes listed above, the only possibility to obtain a B_c^+ meson in Pythia is that a $c\bar{c}$ pair is created from vacuum or from the proton structure function. This process has a very small probability ($O(10^{-4})$) and the generation of B_c^+ events with Pythia is extremely inefficient and does not describe fully the dynamics of B_c^+ production. A dedicated generator is used to generate B_c^+ events: BCVEGPY[59–61], which is implemented as a Pythia external user process. This generator provides explicit matrix elements for the production of B_c^+ and of the excited states $B_c^{*(*)+}$ through the dominant hard process $gg \to B_c^+ b\bar{c}$. The computations are realized at the leading order in the perturbative QCD framework. The fragmentation of the events is done by Pythia using the same configuration as other B mesons.

Chapter 3 The LHCb Experiment

The LHCb experiment is dedicated to heavy flavor physics at the LHC. Its primary goal is to look for indirect evidence of New Physics in CP violation and rare decays of bottom and charm hadrons. In this chapter, we introduce some general aspects of the LHC and the LHCb most relevant to the studies in this dissertation. We start with a brief introduction of the LHC, where the LHCb detector is located, and its performance in Section 3.1. The instrumentations and operations of LHCb, as well as its performance during the data taking in 2010 and 2011, are described in Section 3.2. The LHCb computing strategy and corresponding software packages are outlined in Section 3.3.

3.1 The Large Hadron Collider

The revolution on physics in 20$^{\text{th}}$-century, represented by Relativity and Quantum Theory, originated from the study of physical phenomena in high velocity (energy) and tiny spatial scale, respectively. Particle Physics, based on these two theories, is dedicated to probe the deep structure of matter by studying heavy particles and high energy phenomena. The well-known Einstein mass-energy equation[62]

$$E = mc^2 \tag{3-1}$$

asks physicists to produce energy as high as possible in order to create heavy particles, which cannot exist in the daily low energy world. Meanwhile, the de Broglie relations[63,64]

$$\lambda = \frac{h}{p} \tag{3-2}$$

where $\hbar$ is the reduced Planck's constant, tells physicists that higher momentum p leads to smaller wave length λ, which means better spatial accuracy. These motivations encourage physicists' consistent pursuance of high energy so that Particle Physics is also called High Energy Physics. Great efforts have been made to produce high energy, and several methods, *i.e.* cosmic rays and accelerators, have been used to study the heavy particles and high energy interactions. Up to now, the most effective instruments are the particle accelerators and colliders.

The LHC is a two-ring-superconducting-hadron accelerator and collider built in the 26.7 km LEP underground tunnel[1], which makes it the largest machine ever built in the human history. The LHC tunnel has two beam pipes, in which the proton or ion beams are accelerated close to the speed of light. There are eight arcs and eight straight sections, tagged as Point 1 to 8, in the tunnel. At four of the straight sections, the two beams collide and four large detectors are installed. ATLAS and CMS, newly built, are located at point 1 and point 5, respectively. ALICE and LHCb, located at point 2 and 8, respectively, inherit the LEP engineering structure. Two transfer tunnels near Points 2 and 8 link the LHC to the CERN accelerator complex which injects beams with an energy of 450 GeV. The schematic layout of the LHC is illustrated in Figure 3.1.

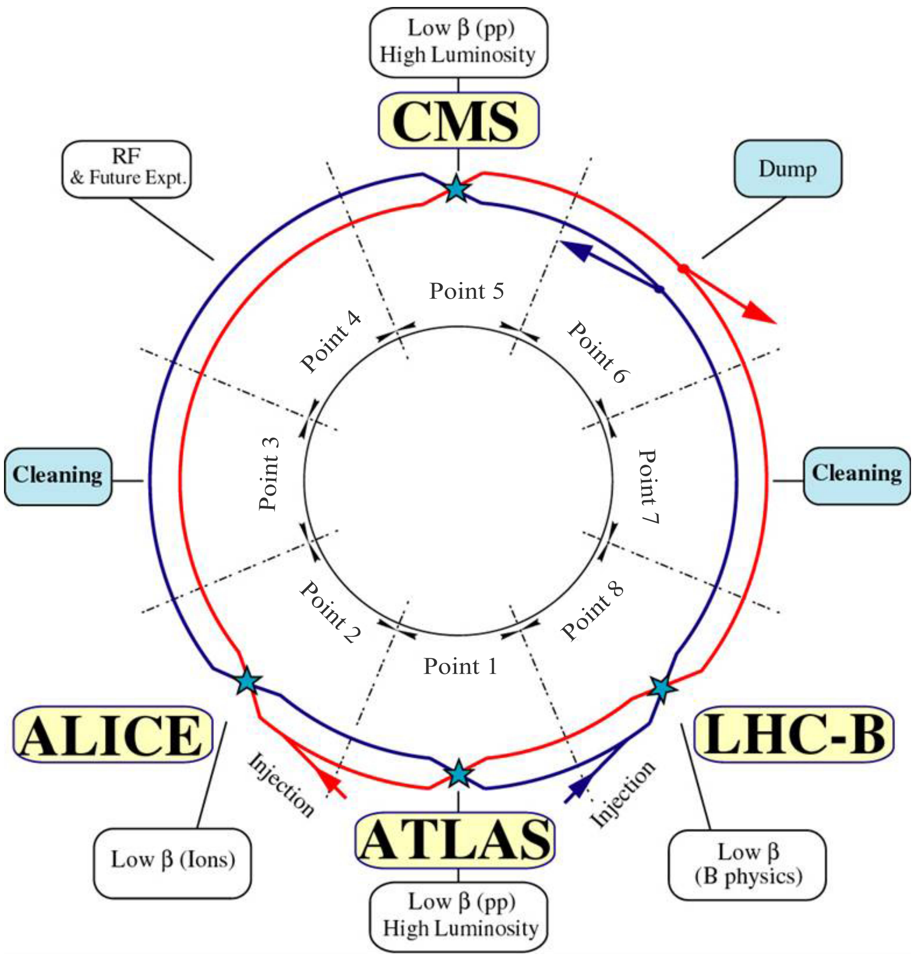

Figure 3.1 The schematic layout of the LHC[1].

One of the most important feature of the LHC, the center-of-mass energy ($\sqrt{s}$) of the pp collisions, is designed to be 14 TeV. In 2010 and 2011, the LHC was operated at $\sqrt{s} = 7$ TeV, which already made the LHC the highest energy particle accelerator in the world. In 2012, the $\sqrt{s}$ is 8 TeV.

Another important feature of the LHC performance is the luminosity. The visible number of interactions per second generated in the pp collisions is given by

$$N_{\text{visible}} = \mathcal{L}\sigma_{\text{visible}} \tag{3-3}$$

where σ_{visible} is the visible cross-section and $\mathcal{L}$ is the machine instantaneous luminosity. The latter depends only on the beam parameters and can be written as

$$\mathcal{L} = \frac{N_b^2 n_b f_{\text{rev}} \gamma_r}{4\pi\epsilon_n \beta*} F \tag{3-4}$$

where N_b is the number of particle per bunch, n_b the number of bunch per beam, f_{rev} the revolution frequency, γ_r the relativistic gamma factor, ϵ_n the normalized transverse beam emittance, $\beta*$ the beta function at the collision point and F the geometry luminosity reduction factor due to the beam crossing angle[1]. The LHC is built to reach a peak pp instantaneous luminosity of $10^{34}\text{cm}^{-2}\text{s}^{-1}$ at ATLAS and CMS, and a peak luminosity of $10^{32}\text{cm}^{-2}\text{s}^{-1}$ at LHCb. The peak luminosities at the LHC in 2010 and 2011 are measured and shown in Figure 3.2. In 2010, the peak luminosity, $10^{32}\text{cm}^{-2}\text{s}^{-1}$, nearly reached the

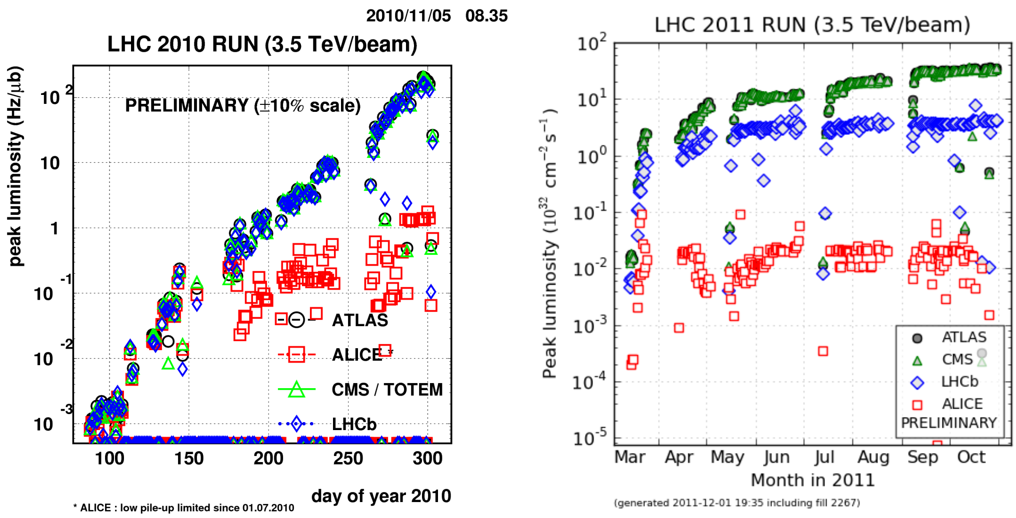

Figure 3.2 Peak luminosity in *left*: 2010 and *right*: 2011[65] for the four LHC experiments. The gaps in the running period correspond to the technical stop of the LHC.

design value at LHCb, $2 \times 10^{32}\text{cm}^{-2}\text{s}^{-1}$. However, this peak was achieved with beam conditions with a higher average number of visible pp interactions per bunch crossing (μ) and much lower number of bunches per beam n_b than the LHCb design. μ as well as another parameter called "pileup", which is the average number of pp interactions in visible events and is equal to $\frac{\mu}{1-e^{-\mu}}$, are generally used as indicators for the luminosity. In 2011, the instantaneous luminosity for LHCb was lower than that for ATLAS and CMS. This was done by displacing one beam with respect to the other. The number of bunches per beam achieved half of the design and the peak luminosity for LHCb was $3.5 \times 10^{32} \mathrm{cm}^{-2}\mathrm{s}^{-1}$, 1.75 times the design.

During the LHC running period, the machine instantaneous luminosity is not constant but has a decay lifetime mainly due to the beam loss from collisions. The luminosity lifetime depends on the initial beam intensity, initial luminosity, total cross-section and number of interacting points. Considering some other machine effects, a typical net luminosity lifetime τ_{L} is equal to 14.9 hours[1]. The whole LHC running time is therefore divided into short periods labeled as “Fill”.

The integrated luminosities, the integral of the instantaneous luminosity over time, at the LHC in 2010 and 2011 running are measured and are shown in Figure 3.3. LHCb

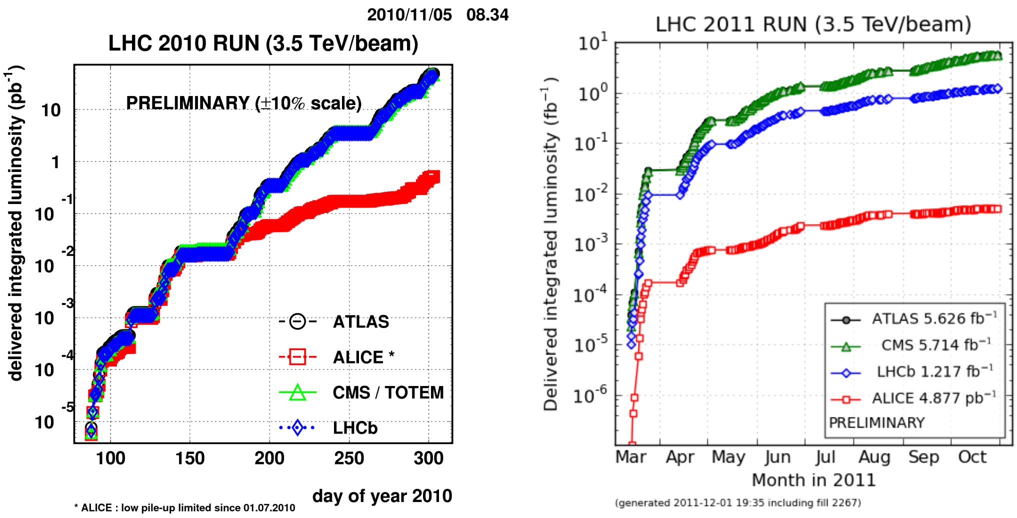

Figure 3.3 Integrated luminosity in the *left*: 2010 and *right*: 2011 running periods[65].

collected 37 pb^{-1} of data in 2010 and 1.1 fb^{-1} in 2011, respectively. In this dissertation, the luminosity collected up to August 2011 is used, corresponding to 0.37 fb^{-1}.

3.2 The LHCb detector

The LHCb detector is a single-arm forward spectrometer dedicated to *b* physics as described in Ref.[2,66,67]. In this section, we introduce some general aspects of the LHCb detector most relevant to the studies in this dissertation.

With a $b\bar{b}$ production cross-section of about 500 μb at the designed center-of-mass energy of 14 TeV, the LHC will be the largest B meson source all over the world. The pp collide in the LHCb detector at a luminosity of $2 \times 10^{32}\mathrm{cm}^{-2}\mathrm{s}^{-1}$, lower than ATLAS and CMS. At this luminosity and energy of 14 TeV, 10^{12} of $b\bar{b}$ pairs are expected to be produced in one year of data taking. The lower luminosity has several advantages:

- The number of interactions per bunch crossing is limited, *i.e.* the number for LHCb is always less than 5 while for ATLAS/CMS it may be up to 20. Events with higher number of pp interactions are much harder to analyse due to the complexity due to the high multiplicity of the products in the pp collision.
- The occupancy in the detector remains low, hence trigger requirements can be loosen to cover larger phase space.
- The radiation damage on the detector can be reduced.

In 2010 and 2011, the $b\bar{b}$ cross-section at the energy of 7 TeV was measured to be $284 \pm 20 \pm 49$ μb[11] and $288 \pm 4 \pm 48$ μb[12]. Measurements of $b\bar{b}$ cross sections are also given as an extrapolation of the B meson cross-sections in Chapter 4 and Chapter 5.

The detector layout and overview are outlined in Section 3.2.1. In the following sections, the sub detectors are described and their performances are shown and discussed. Principles and concepts for several experimental methods, *e.g.* track reconstruction and particle identification are introduced together with the relative sub detectors. The trigger system using the information from these sub detectors are described in Section 3.2.5.

3.2.1 Detector layout and overview

The LHCb detector layout is demonstrated in Figure 3.4. The z axis goes along the beam and its positive direction corresponds to the anti-clockwise direction of the beam. The y axis goes up and the coordinate system is right-handed.

The LHCb detector has a unique geometrical acceptance with a forward angular coverage from approximately 10 to 300 (horizontally) and 250 (vertically) mrad. This detector geometry is set up to account for the fact that the b and $\bar{b}$ hadrons are produced dominantly in the same forward or backward region so that a large fraction of B hadrons are distributed in the LHCb geometrical acceptance, as shown in Figure 3.5.

The descriptions of the sub detectors together with their performances are organized in the following sequence:

- The dipole magnet is described in Section 3.2.2.

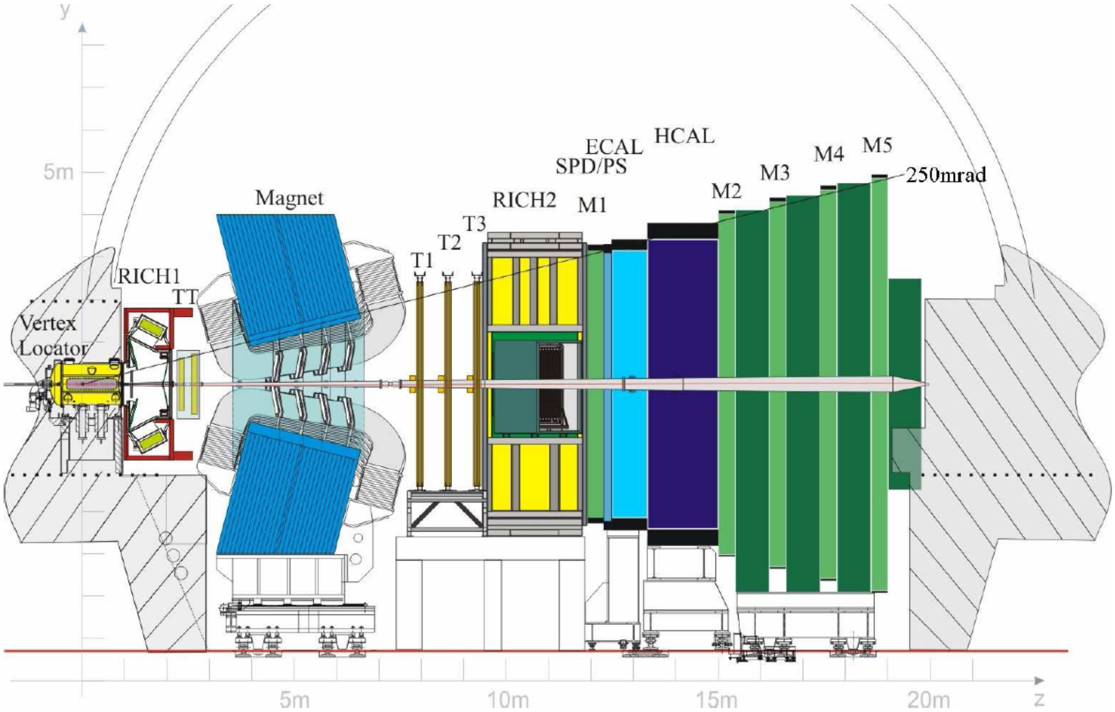

Figure 3.4 The LHCb detector layout[2].

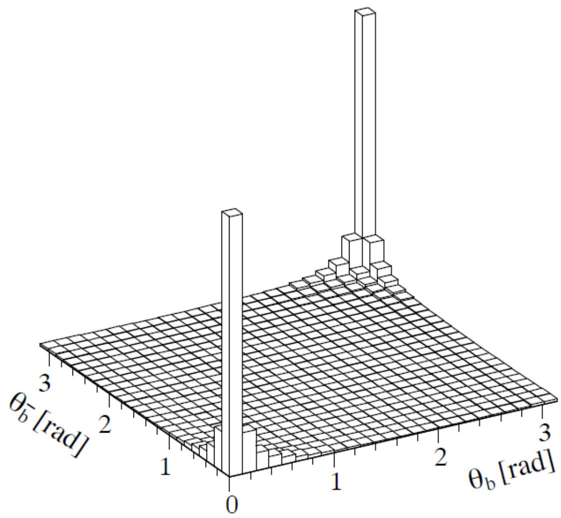

Figure 3.5 The angular distribution of the b and $\bar{b}$ hadrons calculated by the PYTHIA 6 generator[2].

- The tracking system composed of the vertex locator (VELO) around the collision point, a trigger tracker (TT) and three tracking stations (T1-T3), located in front of the magnet and behind, respectively, is described in Section 3.2.3. The track category at LHCb is also discussed in that section.
- The particle identification system consists of three sub-systems: RICH, calorimeter and MUON as described in Section 3.2.4. The two ring imaging Cherenkov (RICH) detectors are dedicated to hadron identification. The calorimeter system, composed of a scintillator pad detector and preshower (SPD/PS), an electromagnetic calorimeter (ECAL) and a hadronic calorimeter (HCAL), contributes to the trigger and measurements for electrons and photons. The MUON system and the muon identification method by this system are described in the last part of Section 3.2.4.

After the sections of detector apparatuses, an introduction of the LHCb trigger system is given in Section 3.2.5.

3.2.2 Magnet

A warm dipole magnet, detailed in Ref.[68], is used in the LHCb detector to measure the momentum of charged particles. The magnet is designed with an integrated magnetic field ($\int B\mathrm{d}l$) of 4 Tm. The polarity of the magnet can be inverted to study the left-right asymmetry of the detector. A magnetic shielding technique[69] is used to restrict the field level inside the RICH detectors. The magnetic field is therefore measured in three regions separately: the tracking volume inside the magnet, the region of VELO and TT, and the magnetic shielding region in RICH1 and RICH2. The relative precision of the field measurement in the tracking volume is about 4×10^{-4}. The comparisons of the measured field component, B_y, and approximative calculation by finite element method for both polarities (up and down) are shown in Figure 3.6. Good agreement between the measurement and calculation is observed.

3.2.3 Tracking system

The tracking detectors together with the magnet compose the LHCb tracking system, responsible for the track reconstruction of charged particles and the measurement of their momentum. Excellent momentum resolution is very important for example to measure the mass of B mesons, *e.g.* a mass resolution of 10 MeV/c^2 for $B_s^0 \to D_s^- \pi^+$ requires a

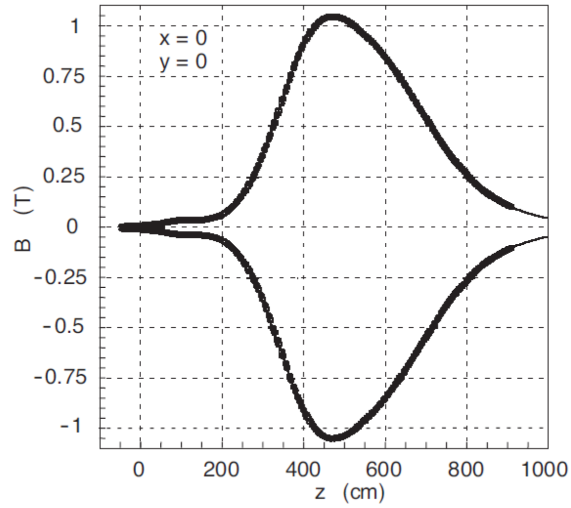

Figure 3.6 Comparisons of the measured (dots) and calculated (line) field component, B_y, for both polarities [2].

momentum resolution of $\frac{\delta p}{p} \approx 0.4\%$ [2]. The LHCb tracking detectors consist of the VELO around the interaction point and four tracking stations (T stations including TT and T1-T3) installed close to the magnet. The VELO and TT are made of silicon microstrip detectors. The detector structure of T1-T3 consists of two components: the inner tracker (IT) close to the beam pipe is made of silicon microstrip detectors and the outer tracker (OT) in the outside region is made of straw-tube detectors.

The VELO provides precise tracking measurements close to the pp collision point to reconstruct and identify the primary vertex (PV), corresponding to the collision point, and secondary vertex, usually corresponding to the decays of hadrons with b or c quarks. The VELO is made of a serie of silicon microstrip modules arranged along the beam pipe as shown in Figure 3.7. One VELO module is composed of two sensors for R and ϕ coordinates, by which the full spacial coordinate of hits can be determined. Two modules form a module pair, which can move alone the x axis to avoid radiation damage during the LHC injection. The four R sensors located upstream of the VELO form the pile-up veto system to distinguish bunch crossings with single and multiple visible pp interactions.

Relying on the tracking measurements by the VELO, the primary and secondary vertices are determined at a better accuracy, which provides more precise measurements of physical quantities used in the studies of this dissertation, *e.g.* the lifetime and impact parameter χ^2 of B meson. The performance of the VELO in 2011 data taking is demonstrated in Figure 3.8 and 3.9.

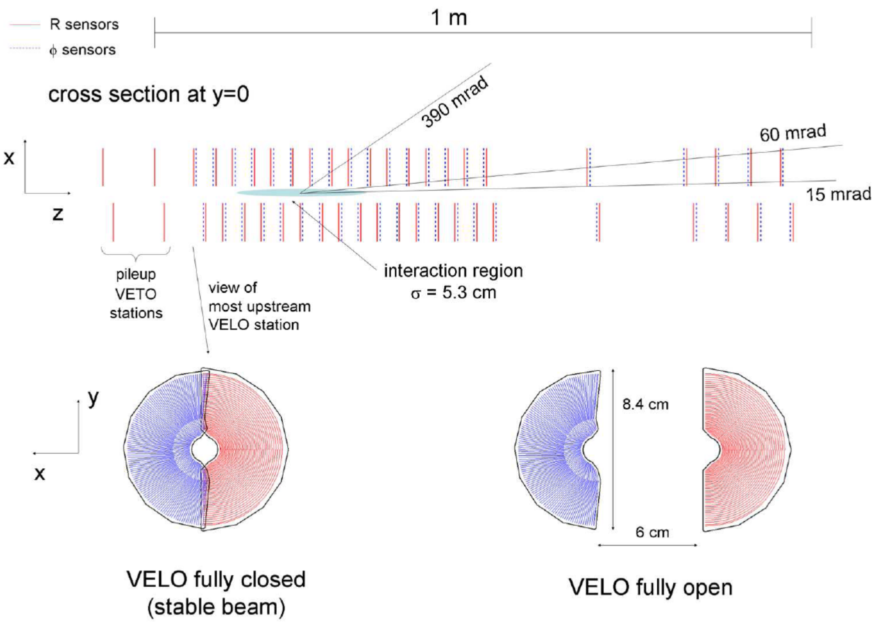

Figure 3.7 *Top*: Cross section of the VELO silicon sensors in the (x, z) plane. *Bottom*: The front face of the module pair in *left*: closed and *right*: open positions[2].

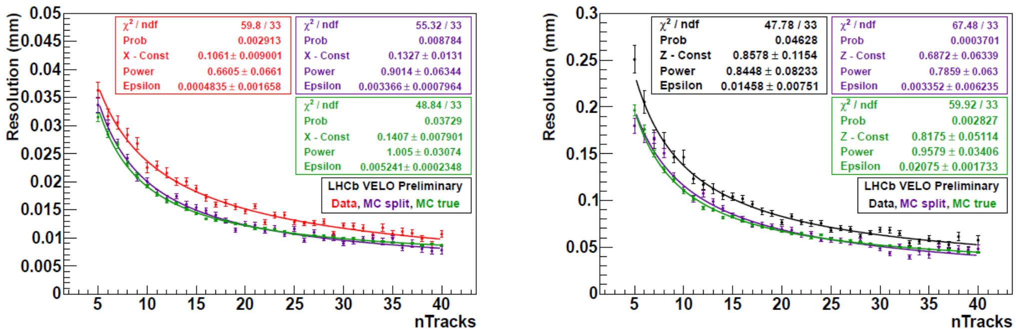

Figure 3.8 PV spacial resolution of events with exactly 1PV as a function of track multiplicity[70]. The red line and points in the left plot correspond to x resolution and the black in the righ plots correspond to z resolution. Comparisons with MC simulation using the reconstruction method (purple) and truth (green) are superimposed.

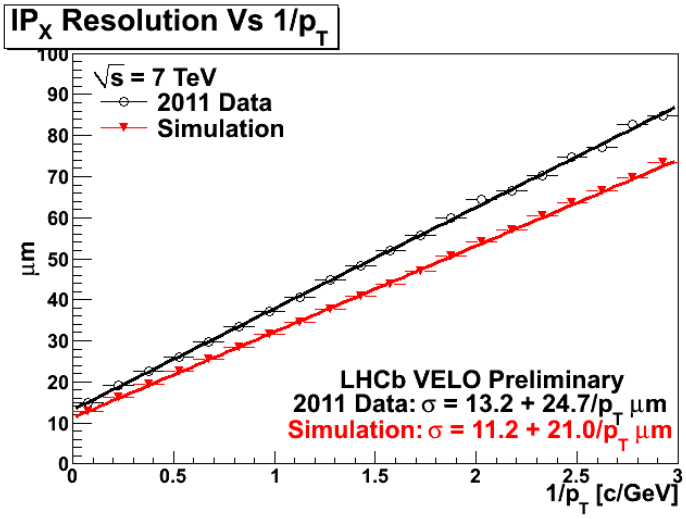

Figure 3.9 Comparison of impact parameter in the x direction (IPx) resolutions as a function of $1/p_{\mathrm{T}}$ between measured and simulated[71].

Two types of detectors: silicon microstrip for TT and IT and straw tube for OT are used in the tracking stations. The design of IT and TT are organized together in a project named "Silicon tracker".

The research and development of the silicon tracker mainly take these considerations into account: spatial resolution, hit occupancy, signal shaping time, single-hit efficiency, radiation damage, material budget and readout channel number. Silicon microstrip sensors with a strip pitch of $\sim$ 200µm, satisfying the momentum resolution requirements dominated by multiple scattering, are piled up to construct the TT and IT stations. Each of these stations has four layers with an $x-u-v-x$ arrangement: the first and last layers x are vertical, while the second u and third v are rotated by a angle of $-5°$ and $5°$, respectively. The third TT detection layer is shown in Figure 3.10. Two half modules are joined together to cover the full LHCb acceptance and to arrange the front-end electronics and other detector units outside of the acceptance.

Each IT station consists of four individual detector boxes and each box contains four layers. The detection layer, composed of seven modules, surrounds the beam pipe as illustrated in Figure 3.11. Neighboring modules are staggered to avoid possible acceptance gaps and improve the alignment.

The LHCb outer tracker is a drift-time detector composed of arrays of straw tube modules as shown in Figure 3.12. The design of the straw-tube module is driven by the requirements of rigidity, material budget, electrical shielding and radiation hardness. The module is composed of two staggered layers of 64 drift tubes with inner diameters of 4.9

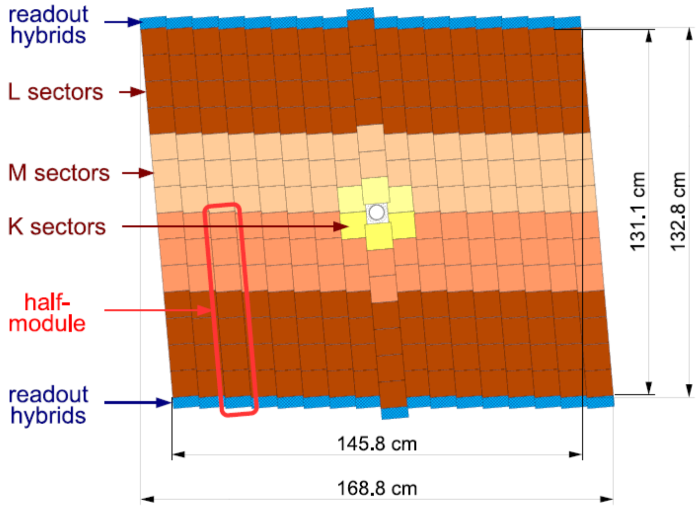

Figure 3.10 Layout of the third TT detection layer. Different readout sectors are indicated by different shadings[2].

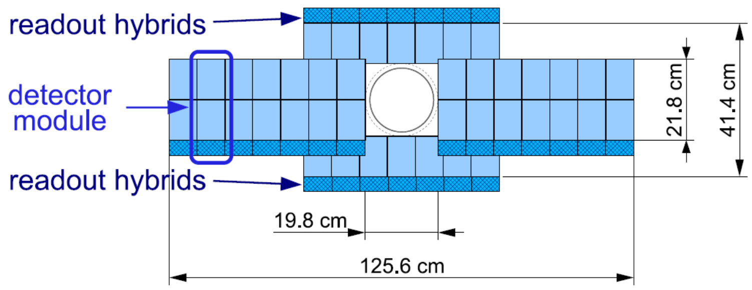

Figure 3.11 Cross section in x-y plane of the detection layer in the second IT station[2].

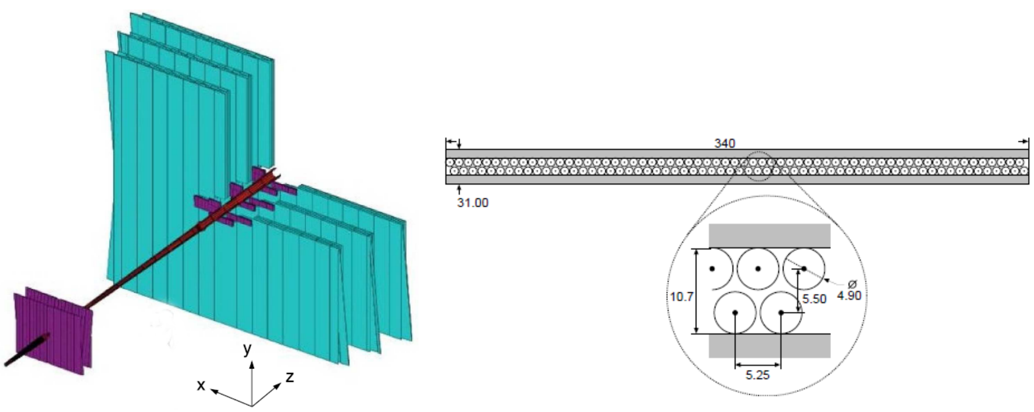

Figure 3.12 *Left*: Arrangement of straw tube modules in layers and stations. *Right*: Cross section of a straw tube module[2].

mm. 168 long and 96 short modules, with about 55 000 tube channels, compose the three OT stations. Each station has four layers arranged in the $x-u-v-x$ geometry in the same way as the IT. The detector boundary corresponds to the acceptance of 300 mrad horizontally and 250 mrad vertically. The performances of the OT in 2011 data taking[72] are shown in Figure 3.13. The spatial resolution basically achieves the design objective

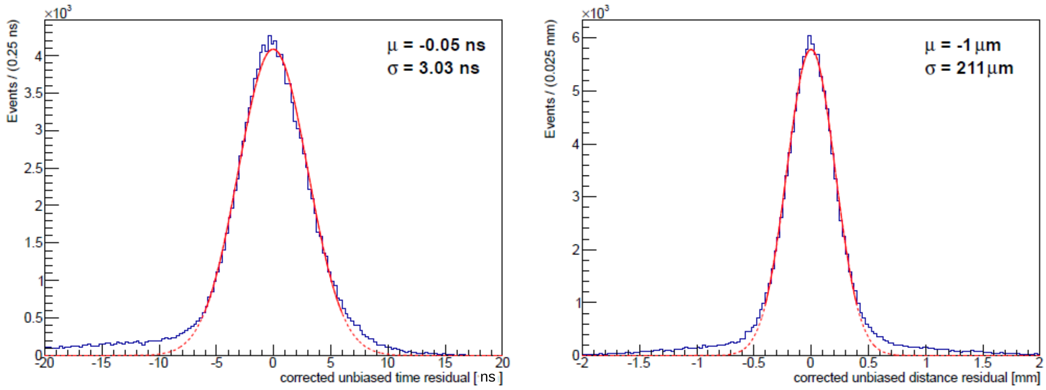

Figure 3.13 Comparisons of single hit resolution between data (blue) and MC simulation(red). *Left*: hit time resolution and *Right*: hit distance resolution[72].

and good agreements are observed between data and MC simulation.

The hits from the VELO, TT, IT and OT detectors are combined to reconstruct charged particle tracks. From the tracking detectors (trackers) used in the reconstruction algorithm, the tracks are classified into the following types:

- *Long* tracks pass through and have hits in all the trackers from VELO to the T stations. They have the best precision thus are used as the most important track type in most analysis;
- *Upstream* tracks go through VELO and TT. They are usually softer tracks that are swept out by the magnet;
- *Downstream* tracks travel only through TT and T stations. The most possible sources of this type are the decay products of K_S^0 and Λ decaying outside the VELO;
- *VELO* tracks transverse only the VELO due to the large polar angle or backward flight direction;
- *T* tracks are reconstructed by hits only in the T stations. They are always produced by secondary interaction.

These track types are demonstrated in Figure 3.14.

The performance of the LHCb tracking system can be described by the bias of the scale α for momentum calibration in the mass measurement[73], as shown in Figure 3.15.

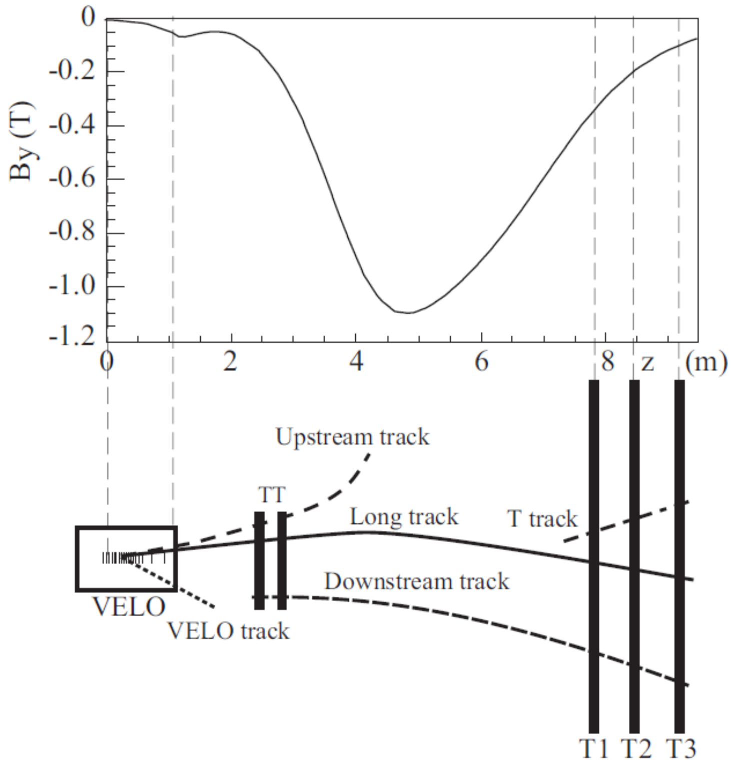

Figure 3.14 A schematic diagram of the track types: Long, Upstream, Downstream, VELO and T tracks. For reference the main B-field component (B_y) is plotted above as a function of the z coordinate[2].

The momentum scale α is defined in such a way that: when multiplying all the daughter particle momenta by $1 - \alpha$, the measured mass is equal to the world average one. The $J/\psi \to \mu^+\mu^-$ decay is considered as the reference so that $\alpha = 0$ is expected. Great mass measurement precision is achieved, as detailed in Ref.[73].

3.2.4 Particle identification

The LHCb particle identification (PID) system consists of RICH, calorimeter and MUON systems. Optimal identification of charged particles, including e, μ, π, K and p, is achieved by the combination of PID information from the RICH, calorimeters and MUON system. ECAL provides the identification for the neutral particles: γ and π^0.

Charged $\pi - K$ separation is a fundamental requirement for B physics analysis. All kinds of B meson hadronic decays highly depend on the $\pi - K$ separation, *e.g.* $B^0 \to J/\psi K^{*0}(K^{*0} \to \pi K)$ and $B_s^0 \to J/\psi \phi(\phi \to KK)$. The RICH is a Cherenkov detector developed for $\pi - K$ separation based on Cherenkov radiation[74], which is the light emitted by a charged particle passing through dielectric medium at a speed higher

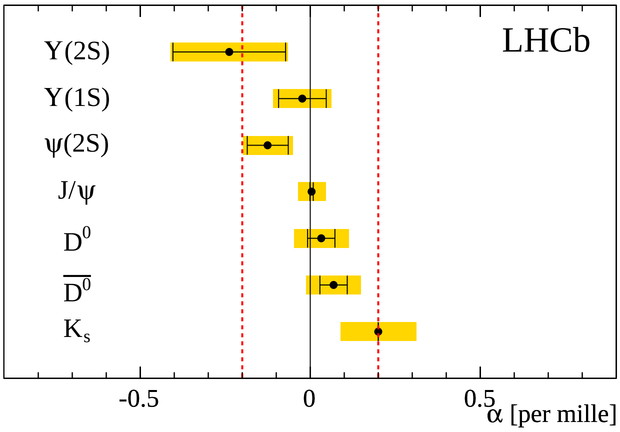

Figure 3.15 Momentum scale bias α extracted from the reconstructed mass of various two-body decays[73]. The black error bars and the yellow shaded areas represent the statistical and systematic uncertainty. The red lines correspond to the assigned systematic uncertainty in the mass measurement.

than the light speed in the medium as shown in Figure 3.16. The emission angle depends on the velocity of the charged particle as well as the refractive index of different radiators as demonstrated in Figure 3.17.

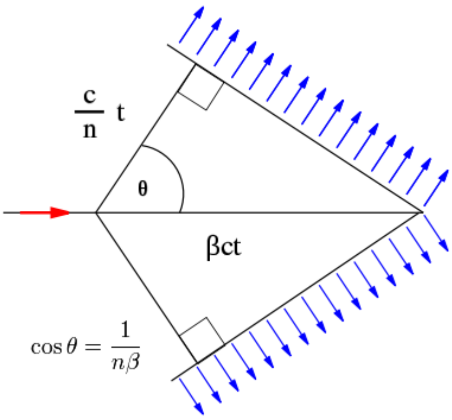

Figure 3.16 Schematic diagram of Cherenkov radiation.

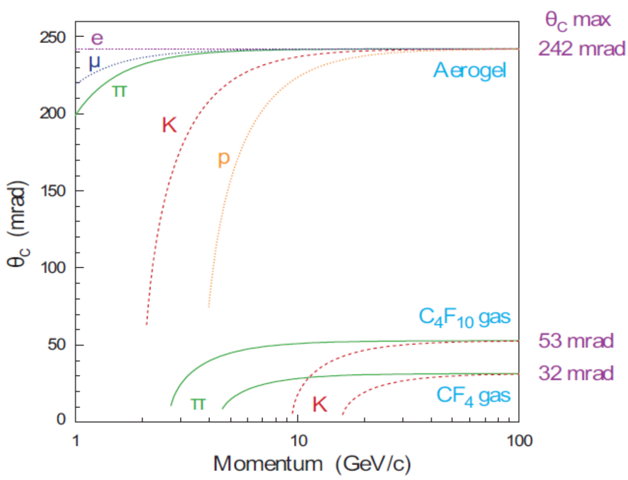

Figure 3.17 Cherenkov angle versus particle momentum for different radiators[2].

Since each kind of radiator covers a specific particle momentum range, and the momentum spectrum is harder at large polar angles and softer at small polar angles, two detectors, RICH1 and RICH2, are installed upstream and downstream the magnet, respectively, to cover different momentum regions. RICH1 cover the 1 to 60 GeV/c region with C_4F_{10} radiators, while RICH2 the 15 to beyond 100 GeV/c region with CF_4 radiators.

In both RICH detectors, combinations of spherical and flat mirrors are used to focus and reflect the Cherenkov light to Hybrid Photon Detectors (HPDs) for the photon reception. The layouts of both RICH detectors are illustrated in Figure 3.18. From Figure 3.16 and

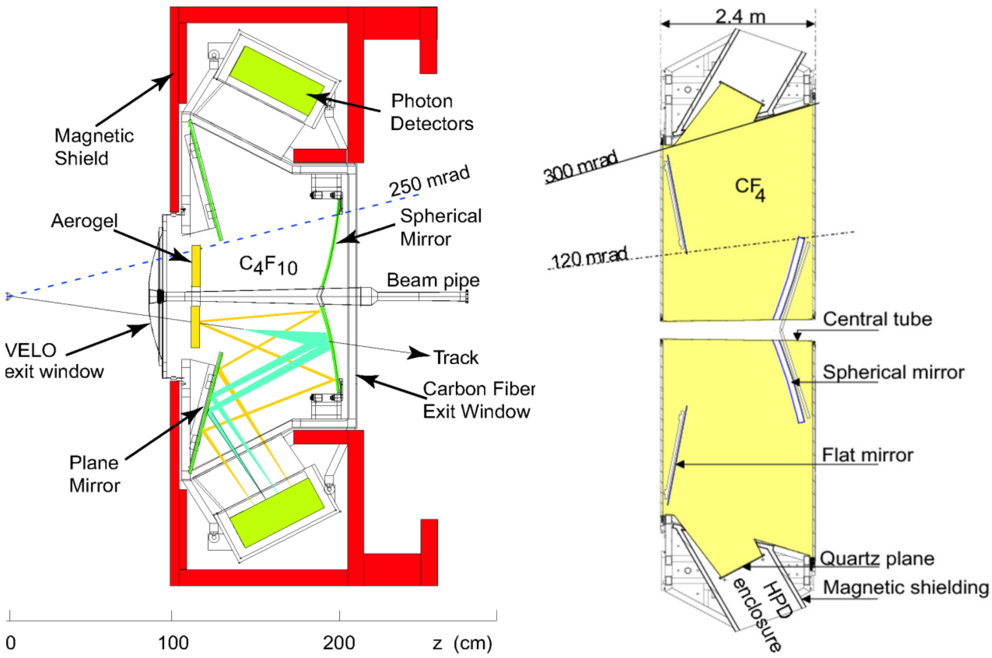

Figure 3.18 Cross sections for *left*: RICH1 in *y*-*z* plane and *right*: RICH2 in *x*-*z* plane [2].

Figure 3.18 (left), one can see that the emitted photons form a cone, which leads to a ring image on the HPD output. A typical LHCb event in RICH1 is displayed in Figure 3.19.

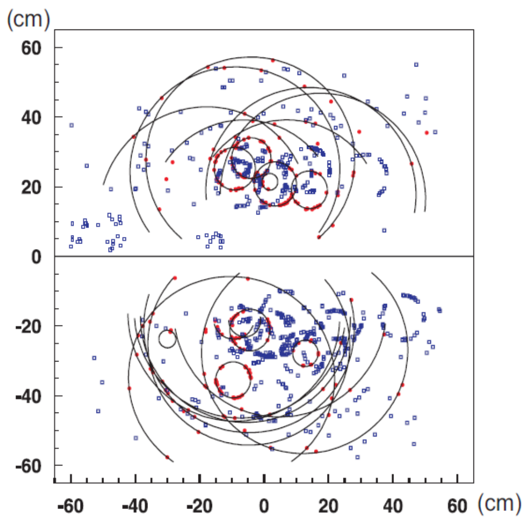

Figure 3.19 Event display of a typical LHCb simulated event in RICH1 [2].

The hadron identification is mainly based on a log-likelihood approach which matches the pattern of the hit rings in RICH HPD to the one under a given particle type hypothesis[75], *e.g.* pion, kaon or proton. The output of this approach is a logarithmic likelihood value for each type of charged particle hypotheses LL_π, LL_K or LL_p. The difference of two likelihoods, *e.g.* $\Delta\mathrm{LL}_{K\pi} = \mathrm{LL}_K - \mathrm{LL}_\pi$ gives the separation between the kaon and pion hypotheses. The charged $\pi - K$ separation performances in LHCb 2011 data taking are shown in Figure 3.23. A kaon identification efficiency ($\epsilon(K \to K)$) of more than 90% and

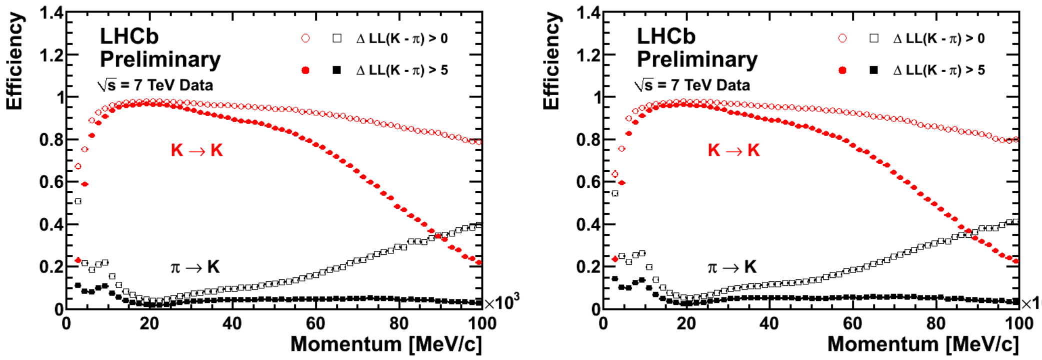

Figure 3.20 Charged $\pi - K$ separation performances in LHCb 2011 data taking for *left*: magnet down and *right*: magnet up[76]. The red points correspond to the kaon-id efficiency while the black to the pion-kaon mis-id rate. The solid points correspond to the efficiencies for $\mathrm{DLL}_{K\pi} > 5$ cut while the hollow points for $\mathrm{DLL}_{K\pi} > 0$.

a pion misidentification efficiency ($\epsilon(\pi \to K)$) of less than 10% are achieved in a large momentum range.

Several functions are carried out by the LHCb calorimeter system:

- Transverse energy of candidates, measured very fast by calorimeter 4 μs after the pp collision, is employed by the hardware trigger discussed in Section 3.2.5.
- Identification of electrons, photons and hadrons. The most demanding identification is that of electrons.
- Measurements of energies and positions of electrons, photons and hadrons. Good energy resolution can be achieved by the high detector cell density and detector z thickness.

The silicon pad detector (SPD) is installed as the first component of the calorimeter system to reduce the yield of neutral pion background in the trigger stage. After SPD, the preshower (PS) detector provides a rejection of background with high charged pion multiplicity. The shashlik calorimeter technology[77] is used in the design and construction of ECAL on account of modest energy resolution, fast time response and acceptable radiation resistance. A ECAL module, from one of the 66 layers in total, is made of 4 mm thick scintillator and 2 mm thick lead for shower excitation. The HCAL is a sampling detector composed of iron absorbers and scintillating tiles for detection. Several cell segmentation patterns are employed in the ECAL and HCAL as illustrated in Figure 3.21, since the hit density varies over different region on the calorimeter surface. In

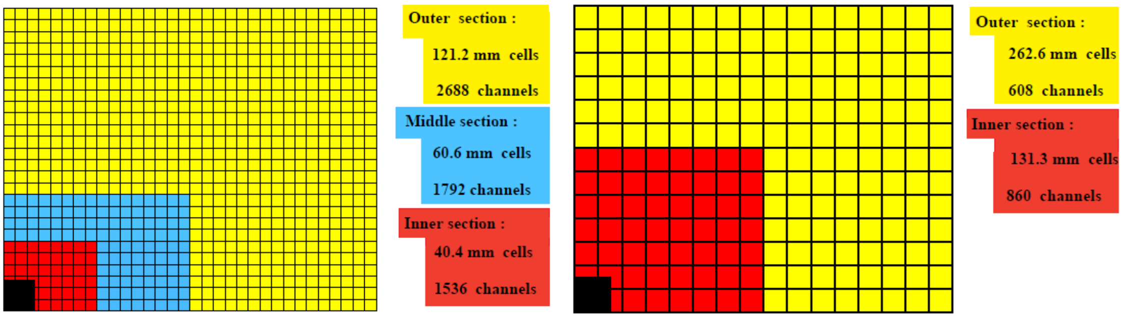

Figure 3.21 Lateral segmentation of the SPD/PS and ECAL (left) and the HCAL (right). One quarter of the detector in the $x-y$ plane is shown. The black blocks correspond to the beam pipe.

each calorimeter the scintillation light is transmitted by wavelength-shifting fibres to a Photo-Multiplier.

The muon system provides realtime information for the hardware muon trigger and muon identification for the software trigger and offline analysis. The muon system consists of five stations M1-M5 along the beam direction. These stations are mostly composed of multi-wire proportional chambers (MWPCs). M1 is located in front of the calorimeters to give a p_{T} measurement in the L0 trigger, as discussed in Section 3.2.5. In the most inner region of M1, the particle flux rate is extremely high. The triple gas electron multiplier (GEM) chambers are used in order to keep a good gain without significant ageing in 10 years of LHCb running. M2-M5 are placed after the HCAL with 80 cm thick iron absorbers interleaved to reduce soft muons. The schematic diagram of the muon system is illustrated in Figure 3.22.

The muons are identified by extrapolating tracks with momentum larger than 3 GeV/c into the muon system. In each muon station, an algorithm is applied to search hits in fields of interests (FOI) around the extrapolated point of the track. A track is identified as a muon candidate, which is labeled as "isMuon", only if enough stations have hits found in their FOIs. The requirements of station with hits are listed in Table 3.1. Another variable, the difference of log-likelihood between the muon and pion hypotheses $\mathrm{DLL}_{\mu\pi}$, can improve the muon identification. It is constructed from the comparison of track slopes in the tracking and muon system, and from the average hit-track distance of

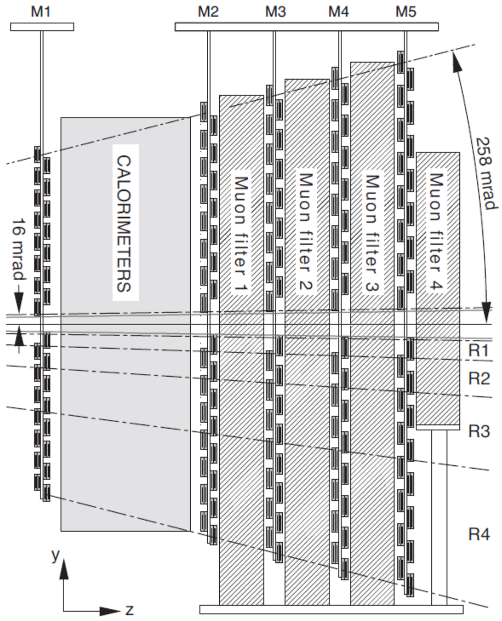

Figure 3.22 Cross section of the muon system in $y-z$ plane.

Table 3.1 The station requirements for “isMuon” identification.

Momentum range	Muon station requirements
$3\,\mathrm{GeV}/c < p < 6\,\mathrm{GeV}/c$	M2+M3
$6\,\mathrm{GeV}/c < p < 10\,\mathrm{GeV}/c$	M2+M3+(M4 or M5)
$p > 10\,\mathrm{GeV}/c$	M2+M3+M4+M5

hits related to the track in the FOI. The muon system performances in LHCb 2011 data taking are illustrated in Figure 3.23.

3.2.5 Trigger

During the LHC running, pp beams keep colliding and the collision events are recorded and sampled by the detector at a high frequency of 40 MHz. This lead to a high data production rate. Nevertheless, the speed of data acquisition is limited by the detector electronics and data bandwidth of the storage farms. Trigger system is introduced to reduce the data rate by selecting events of physical interests and removing background events.

The LHCb trigger system[79] consists of two levels: Level-0 (L0) and High Level Trigger (HLT) as shown in Figure 3.24. The first level (L0), implemented in hardware, is designed to reduce the LHC bunch crossing frequency of 40 MHz to a maximum of

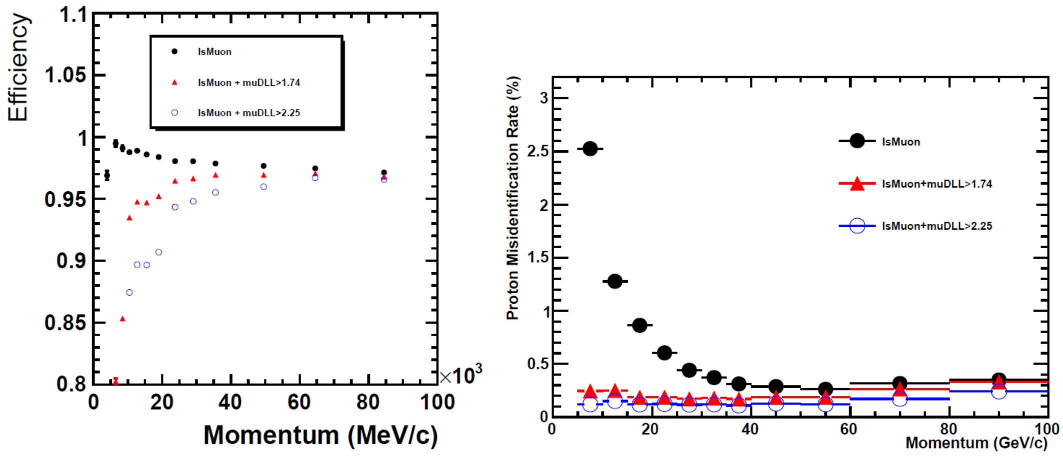

Figure 3.23 Muon system performances in LHCb 2011 data taking for *left*: muon identification efficiency and *right*: proton-muon mis-identification rate[78]. The black points correspond to efficiency of "isMuon" cut, and the red points to efficiency of "isMuon" plus a looser $DLL_{\mu\pi}$ cut. The blue circles correspond to efficiency of "isMuon" plus a tighter $DLL_{\mu\pi}$ cut.

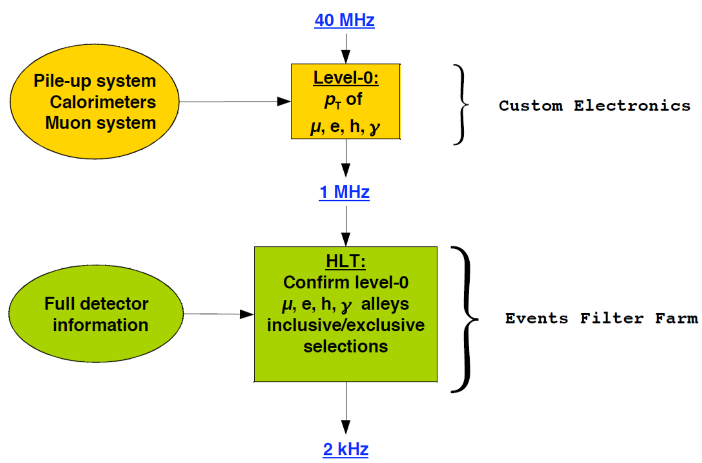

Figure 3.24 Scheme of the LHCb trigger[2].

1 MHz, at which rate the complete detector response is read out. Since the particles produced by B hadron decays often have large transverse momentum and energy due to the large mass of B hadrons, the L0 trigger reconstructs the highest E_{T} hadron, electron and photon clusters in the calorimeters and two highest p_{T} muons in the muon chambers. An additional requirement is the number of pp interactions in the bunch crossing estimated by the pile-up system as described in Section 3.2.3. Events passing the L0 requirements are read out and sent to an event filter farm (EFF) for further selection in HLT.

The High Level Trigger (HLT) consists of a C++ application with two components: HLT1 and HLT2. The HLT application can use the entire information of a event. However, considering the high L0 rate and computing limitation, only part of the information is used. Since HLT is implemented in software level, it is more adapt than L0 to be adjusted according to the development of event reconstruction and selection.

The first stage of the software trigger (HLT1), performs a partial event reconstruction to confirm or discard the L0 trigger decision. This event reconstruction mainly uses information from the VELO and T-stations. And then, HLT1 applies cuts on simple signatures of the candidates, *e.g.* p_{T} or impact parameter. The event rate is reduced to about 30 kHz by HLT1, which is a reasonable level for the full pattern recognition at HLT2 stage.

The second stage of the software trigger (HLT2) performs a full event reconstruction to further discriminate signal events from the background. Selection cuts on momentum, invariant mass and impact parameter are applied to form composite particles, *e.g.* J/ψ, K^0_{S} or ϕ, which are used in the selections to avoid duplication of final state particles. Both inclusive and exclusive selections are used in this stage. The inclusive selections are less dependent on the on-line tracking ability than the exclusive ones which suffer from the partial B decay reconstruction. Meanwhile, the exclusive selections can produce a smaller event rate thus can be relaxed. Combining the inclusive and exclusive triggers by logical OR, the event rate is further reduced to about 2 kHz, at which the data is recorded in the storage farms.

Global event cuts (GEC) were introduced in the trigger stage to cope with the high pile-up running conditions encountered during the running period of the LHC while only a part of the Event Filter Farm was installed. To limit the rate at which the detector is read out, a cut on the Scintillating Pad Detector (SPD) hit multiplicity at L0 is applied. To avoid that a few events with a high occupancy in the Vertex Locator (VELO), Outer

Tracker (OT), and Inner tracker (IT) dominate the HLT CPU time, a set of global event cuts is applied on the hits/tracks multiplicities as listed in Table 3.2. These requirements

Table 3.2 Global event cuts in the trigger stage.

Trigger level	GEC
L0	SPD hit multiplicity
HLT1	VELO cluster multiplicity IT cluster multiplicity OT cluster multiplicity
HLT2	VELO track multiplicity

are set for each sub-detector that is used by the pattern recognition algorithms.

The events passing both the L0 and HLT triggers are stored in the storage farms for online monitoring, *e.g.* the mass distribution of J/ψ candidates passing the muon trigger in the online monitoring is shown in Figure 3.25. To trace the trigger conditions during

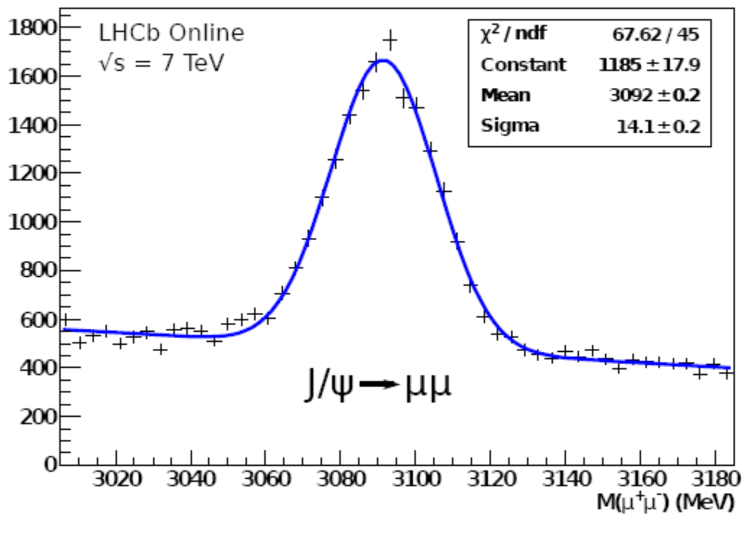

Figure 3.25 Mass distribution of J/ψ candidates passing the trigger requirements in the online monitoring system[71].

the off-line analysis, a trigger configuration key (TCK) is assigned to each combination of trigger algorithms.

3.3 The LHCb computing

This section describes the computing processes for both real and simulated event data. The software packages used in this analysis are introduced together with the corresponding sub-processes.

The schematic of LHCb dataflow is shown in Figure 3.26. The RAW data are pro-

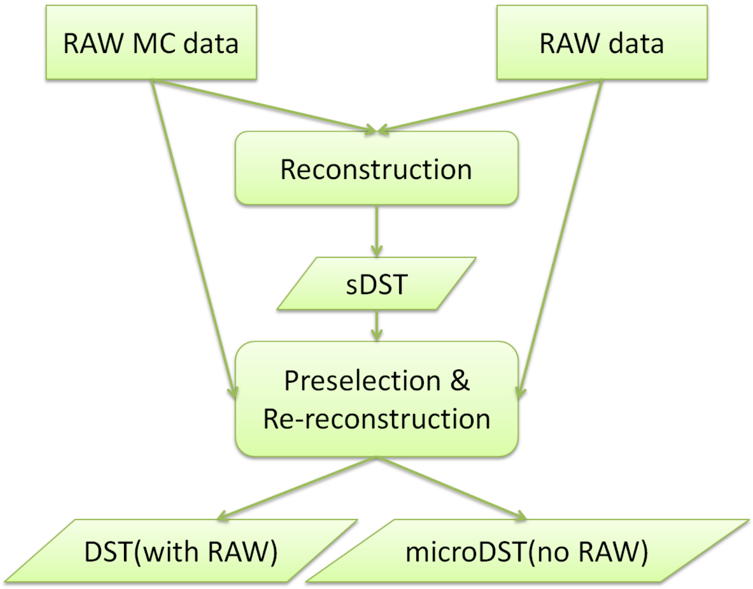

Figure 3.26 Schematic of LHCb dataflow.

duced by the Event Filter Farm using the electric signals recorded by the detector. The RAW MC data are produced by Monte Carlo (MC) simulation as described below. Triggered event informations are stored in the RAW data in the form of detector electronic output. The collider and detector are not running all the time and the running conditions may change, therefore, the RAW data are divided by the running periods and labeled by "run number".

The RAW data are reconstructed using the BRUNEL package[80] to form physical quantities including hits, clusters and tracks. Positions, momentum, energy and particle identification informations are stored in the output data file, named as Data Summary Tape (DST). The DST of this reconstruction stage only store necessary information for the next preselection step and is named as "sDST".

A preselection algorithm is carried out on the sDST to select events of physical interests. These selected events are re-reconstructed using information from both sDST and RAW data. This re-reconstruction approach mainly focuses on trigger information. Then these events are written on disk within several DST (with RAW information) or microDST (without RAW information for saving storage spaces) files, each per type of analysis, *e.g.* one for muons, one for hadrons *etc.*. An indicator line will be assigned to the candidates selected by each specific preselection algorithm, *e.g.* $B^+ \to J/\psi K^+$ or $B^0 \to J/\psi K^{*0}$ candidates, as a shortcut to the actual DST record. This approach is called "Stripping" and these indicator lines are called "Stripping Lines". The stripping is done through the DaVinci package detailed in the end of this section. After the reconstruction and stripping approaches, long-lived final state particles, *e.g.* $\pi^\pm$, $K^\pm$, $\mu^\pm$ and γ *etc.*, and the candidates for b or c hadrons are reconstructed and stored in the DST file. The reconstruction and stripping approaches can be tuned according to the alignment and analysis requirements. The DST files are labeled by the reconstruction version and stripping version, *e.g.* "Reco08Stripping12b" for 2010 data and "Reco10Stripping13b" for 2011 data. Using the reconstructed and stripped data files, the individual user analysis can be performed.

Three LHCb software packages, Gauss[81], Boole[82] and Moore[83], contribute to the LHCb Monte Carlo simulation. The Gauss simulation software is used to simulate the pp collision, generate particles and describe the behaviors of particles in the detector. Its particle generator is based on Pythia 6.4 generator[58] with parameters configured for LHCb[84]. The EvtGen package[85] is used in Gauss to describe the decays of the particles generated by Pythia. QED radiative corrections are modeled using Photos[86]. The Geant4[87] package is introduced to trace the decay products through the detector.

The digitization simulation package Boole applies the detector response to hits previously generated in the sensitive detectors by the Geant4 based simulation. The output of Boole is digitized electronic signal similar to the real data from the detector. The Moore simulation package is used to simulate the trigger effect in pass-through mode. As described above, the simulated sample is also reconstructed and stripped by Brunel.

The real and simulated data samples after the reconstruction and stripping are stored on the computer grid, which is a distributed computer system that involve a large number of data files, and is based at CERN and distributed at several European countries. Individual user analysis can be made by applying further selection algorithms on the reconstructed and/or stripped events to build specific candidates, and then combining the information of the candidates to find out the physical quantities of interests, *e.g.* production cross-section or lifetime. Several software packages are involved in the analysis approaches:

- Dirac[88] and Ganga[89] are distributed processing system packages making use of the distributed computer grid to arrange the data file input & output and organize the distributed program execution.
- DaVinci[90] is the core physics analysis software based on C++. Besides stripping, one can use DaVinci to combine the final state particles, reconstructed and/or stripped by Brunel, to construct candidates of physical interests, *e.g.* B mesons. All kinds of analysis algorithms are embed in DaVinci to meet different analysis needs, *e.g.* trigger information extraction and primary vertex refitting.
- Root[91] is an object-oriented program and library based on C++ and developed by CERN. Histogramming, graphing, data fitting and statistics tools are provided by the Root package.

Chapter 4 Measurement of B^+ production cross-section with 2010 data

Measurements of the total production cross-section and the differential cross-section for B^+ as a function of p_T are given in this chapter. The total production cross-section is calculated by integrating the differential cross-section over p_T. The differential cross-section is equal to

$$\frac{d\sigma}{dp_T} = \frac{N_{B^+}(p_T)}{\mathcal{L}_{int} \times \epsilon_{tot}(p_T) \times \mathcal{B}(B^+ \to J/\psi K^+) \times \mathcal{B}(J/\psi \to \mu^+\mu^-) \times \Delta p_T}, \tag{4-1}$$

where $N_{B^+}(p_T)$ is the number of selected signal $B^+ \to J/\psi K^+$ candidates in a given p_T bin, $\mathcal{L}_{int}$ is the integrated luminosity, $\epsilon_{tot}(p_T)$ is the total efficiency of $B^+ \to J/\psi K^+$ including acceptance, reconstruction, selection and trigger effects, $\mathcal{B}(B^+ \to J/\psi K^+)$ is the branching fraction for the $B^+ \to J/\psi K^+$ decay, $\mathcal{B}(J/\psi \to \mu^+\mu^-)$ is the branching fraction for the $J/\psi \to \mu^+\mu^-$ decay and Δp_T is the p_T bin width. The determinations of all these parameters are described in this chapter.

We start with the data samples and corresponding triggers in Section 4.1. The event selection requirements are outlined in Section 4.2. The determinations of the parameters quoted in Equation 4-1 are presented in Section 4.2 and the systematic uncertainties on these parameters are discussed in Section 4.4. At last, Section 4.5 presents the results and some discussions.

4.1 Samples and trigger

This section introduces the data samples for the signal yield extraction and MC simulation samples for efficiency estimation. As discussed in Section 3.2.5, the triggers used to collect the data samples are discussed afterwards.

This analysis uses $34.6 \pm 1.2\,\text{pb}^{-1}$ of pp collision data taken at the LHC at a center-of-mass energy of 7 TeV between October and November 2010. The range of run numbers, which is described in Section 3.3, is from 79571 to 81685 in this data sample. For the data included in this analysis, all detector components were fully operational and in a stable condition. The reconstruction and stripping version is “Reco08Stripping12b”. The data were collected using 12 different trigger configuration keys (TCKs) detailed in Table 4.3.

The MC simulation samples were generated at a center-of-mass energy of $\sqrt{s}$ = 7 TeV, with a mean number of interactions per non-empty bunch crossing $\nu = 2.5$ (including diffractive and elastic processes), a horizontal crossing angle between the two beams of 0.170 mrad and $\beta^* = 3.5$ m. The samples were generated, simulated and reconstructed with the following software versions:

- Gauss v39r1
- Boole v21r9
- Moore v10r1 and v10r2
- Brunel v37r8p5

These samples are labeled as ”MC10” in the LHCb computing strategy. The trigger with TCK 0x002e002a, which covered most of the data yield, was simulated with the Moore package.

The total B^+ production cross-section in the MC simulation is equal to 406 μb with these settings, in the full polar angle range. The cross-section in the analysis range, defined as $2 < y < 4.5$, is equal to 79.4 μb. Figure 4.1 shows the simulated B^+ differential cross-section as a function of p_T in the $2 < y < 4.5$ range.

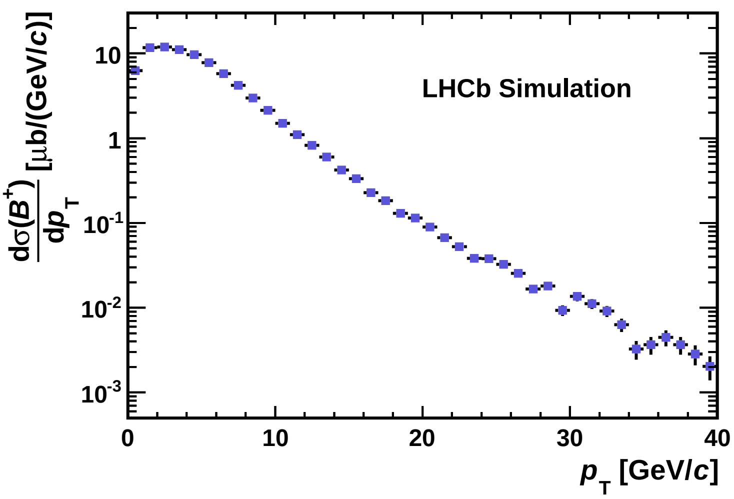

Figure 4.1 Differential production cross-section for B^+ as a function of the transverse momentum in the LHCb simulation.

The basic concepts of trigger system are described in Section 3.2.5. This analysis is based on two L0 lines: the single muon line, which requires one muon candidate with a p_T larger than 1.4 GeV/c, and the di-muon line, which requires two muons with p_T larger than 0.56 GeV/c and 0.48 GeV/c, respectively. For the data used for this analysis, the maximum visible interaction rate is 3 MHz and the L0 output rate 200 kHz. The L0 trigger outputs provide the input candidates for the HLT1 lines: the first one (*Hlt1SingleMuonNoIP*) confirms the muon candidate found by the L0 single muon, and applies a harder cut on the muon p_{T} at 1.8 GeV/c; the second line (*Hlt1DiMuonNoIPL0Di*) confirms the di-muon candidates found by the L0 di-muon line and requires their combined mass to be greater than 2.5 GeV/c^2; the third line (*Hlt1DiMuonNoIP2L0*) confirms two independent L0 candidates found by the L0 muon system and requires their combined mass to be greater than 2.5 GeV/c^2. At the HLT2 stage, events which have two muon candidates with an invariant mass in a ±120 MeV/c^2 mass window around the nominal J/ψ mass[28] are selected. The trigger lines used in the analysis are summarized in Table 4.1.

Table 4.1 Summary of the trigger lines used for this analysis.

Trigger line	Main requirements
L0SingleMuon	$p_{\mathrm{T}} > 1.4\,\mathrm{GeV}/c$
L0DiMuon	$p_{\mathrm{T},1} > 0.56\,\mathrm{GeV}/c$, $p_{\mathrm{T},2} > 0.48\,\mathrm{GeV}/c$
Hlt1SingleMuonNoIP	*L0SingleMuon* and $p_{\mathrm{T}} > 1.8\,\mathrm{GeV}/c$
Hlt1DiMuonNoIPL0Di	*L0DiMuon* and $M_{\mu\mu} > 2.5\,\mathrm{GeV}/c^2$
Hlt1DiMuonNoIP2L0	*L0SingleMuon* and $M_{\mu\mu} > 2.5\,\mathrm{GeV}/c^2$
Hlt2DiMuonUnbiasedJPsi	$M_{\mu\mu} \in [M_{J/\psi} - 120\,\mathrm{MeV}/c^2; M_{J/\psi} + 120\,\mathrm{MeV}/c^2]$

It should be noted that only trigger lines with no impact parameter information ("*NoIP*") are used in this analysis. The impact parameter (IP) is defined as the perpendicular distance between the primary vertex and the particle track. The primary vertex (PV) is the vertex reconstructed by the reconstruction algorithm as the pp collision point. Since the IP requirements bias the lifetime distributions of the candidates and there is a lifetime cut applied in Section 4.2, no IP cuts are used in the trigger, as well as in the analysis selection.

Since the event filter farm was not fully installed in 2010, in order to reduce the event rate to an acceptable level, trigger line *Hlt1SingleMuonNoIP* was pre-scaled by a factor of five during the 2010 data taking with some of the TCKs used (indicated as Group 2 in Table 4.3).

As discussed in Section 3.2.5, GEC requirements are set for each sub-detector that is used by the pattern recognition algorithms in the 2010 data, as illustrated in Table 4.2. Generally, the cut values are chosen to loose a minimal amount of luminosity while effec-

Table 4.2 Summary of global event cuts in 2010 data-taking.

Trigger level	GEC	Maximum number of hits/clusters
L0	SPD hit multiplicity	< 900
HLT1	VELO cluster multiplicity	< 3000
HLT1	IT cluster multiplicity	< 3000
HLT1	OT cluster multiplicity	< 10000
HLT2	VELO track multiplicity	< 350

tively rejecting busy events. The only global event cut that rejects a significant fraction of the luminosity is the requirement on the VELO cluster multiplicity, detailed in Section 4.3.2. A more detailed discussion of the trigger configuration and performance for the 2010 run can be found in Ref.[92].

4.2 Event selection

As described in Section 3.3, particle candidates, B^+, are formed by the final state particles reconstructed by the recognition algorithm. The set of reconstructed B^+ candidates is a combination of both signal and background candidates. Event selection cuts are applied on the candidates to reduce background candidates and keep as many as possible signal candidates at the same time. To reduce the trivial background candidates and save the data processing time, a set of stripping cuts is applied to the reconstructed candidates. Consequently the event selection cuts are applied on the "stripped" candidates to further reduce background.

A set of stripping selection cuts, labeled as a "B2JpsiHDetached" line in the LHCb stripping version "Stripping12b", is used in this analysis. This stripping line selects events based on the B^+ lifetime to distinguish the long-lived B^+ candidates ($\tau > 0.15$ps) from a lot of combinatorial background candidates formed by particles satisfying all the other cut requirements by coincidence, due to the large particle production rate near the collision point. The selection cuts used in the stripping process are listed in Table 4.4.

$B^+ \to J/\psi K^+$ candidates are further selected using the selection requirements described below. J/ψ candidates are formed from pairs of opposite sign long tracks that must have p_T larger than 700 MeV/c, have a good quality of the track fit ($\chi^2/\text{ndf} < 4$) and be identified as muons, requiring that the track has enough hits in the muon detector

Table 4.3 List of TCKs in 2010 data.

TCK	$\mathcal{L}$	SPD	*L0SingleMuon*	*L0DiMuon*		*HLT1SingleMuon*	
	(pb^{-1})	Mult.	p_T	$p_{T,1}$	$p_{T,2}$	Prescale	p_T
				Group 1			
0x001D0030	0.16	900	> 1.4 GeV/c	> 0.56 GeV/c	> 0.48 GeV/c	1	> 1.8 GeV/c
0x001E0030	2.04						
0x0024002A	1.21						
0x0024002C	1.06						
0x002A002A	4.12						
0x002A002C	0.43						
0x002E002A	8.65						
0x002E002C	9.30						
Total	26.97						
				Group 2			
0x001F0029	3.02	900	> 1.4 GeV/c	> 0.56 GeV/c	> 0.48 GeV/c	0.2	> 1.8 GeV/c
0x001F0031	0.10						
0x0025002C	1.82						
0x002B002A	1.69						
Total	7.63						
Total all TCKs	34.60						

and that the difference in the logarithms of combined likelihoods computed for the muon and pion hypotheses ($\Delta\mathrm{LL}_{\mu\pi}$) of the two muon tracks is larger than 0. The two muons are required to originate from a common vertex and only candidates with a χ^2/ndf of the vertex fit smaller than 9 are kept. The mass of the reconstructed J/ψ is required to be in the range $3.04 - 3.14\ \mathrm{GeV}/c^2$.

J/ψ candidates are combined with a charged track in the rest of the event, with p_T above $0.5\,\mathrm{GeV}/c$ and a χ^2/ndf of the track fit smaller than 4. Since the yield of $B^+ \to J/\psi K^+$ is large, the contamination from $B^+ \to J/\psi\pi^+$ is relatively small, to simplify the analysis, no particle identification requirement is imposed on the bachelor kaon. A vertex fit is performed that constrains the three daughter particles to originate from a common point and the mass of the muon pair to match the nominal J/ψ mass. It is required that $\chi^2/\mathrm{ndf} < 9$ for this fit. A single charged track can be reconstructed as two different tracks, named "clone" tracks, by the reconstruction software. Clone tracks are eliminated using the clone identification algorithm based on the Kullback-Liebler distance described in Ref.[93–95].

Only B candidates of which the J/ψ candidates satisfy that the L0, HLT1 and HLT2 triggers are triggered on signal (TOS), as described in Section 4.3.2, are kept. The proper time distributions of signal and background candidates are shown in Figure 4.2. As one can see, there are many more background candidates in the short lifetime region. The B candidates are selected with a proper time larger than 0.3 ps. Finally, the fiducial selection cut $y \in [2.0, 4.5]$ is applied.

Figure 4.3 shows the distribution of μ, as defined in Section 3.1, for the selected signal events (background subtracted). The μ of the pp interactions is at a reasonably low level and the PV reconstruction is not affected much by μ. No selection cut except nPV>0 required by the lifetime determination is assigned for the PV reconstruction. The final selection criteria are listed in Table 4.4. Figure 4.4 shows the invariant mass distribution of the $B^+ \to J/\psi K^+$ candidates obtained with the selections described above.

After the event selection, a background subtraction procedure on the distributions of selection variables can be done using ${}_s\mathit{Weights}$ by the ${}_s\mathit{Plot}$ technique detailed in Section 4.3. The background subtracted distributions correspond to the distributions of signal candidates. The comparisons of distributions of selection variables between background subtracted data and MC simulation are illustrated in Appendix A.1. Good agreements are observed in these comparisons, however, there are some discrepancies which are dis-

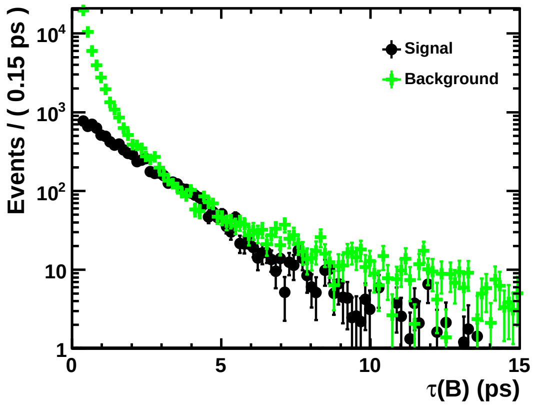

Figure 4.2 Proper time distributions of signal B^+ candidates (*black dots with error bars*) and of background candidates (*green crosses with error bars*) in real data, in logarithmic scale.

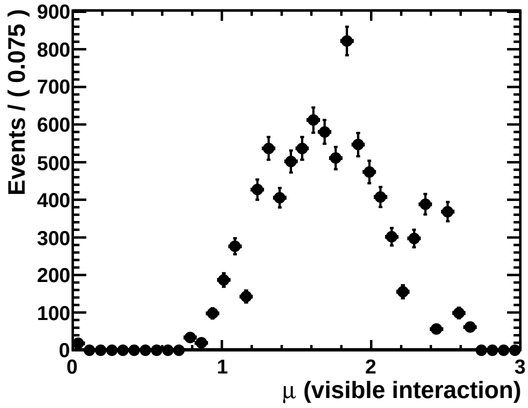

Figure 4.3 Distribution of the average number of visible interactions, μ for the selected signal (background subtracted) events.

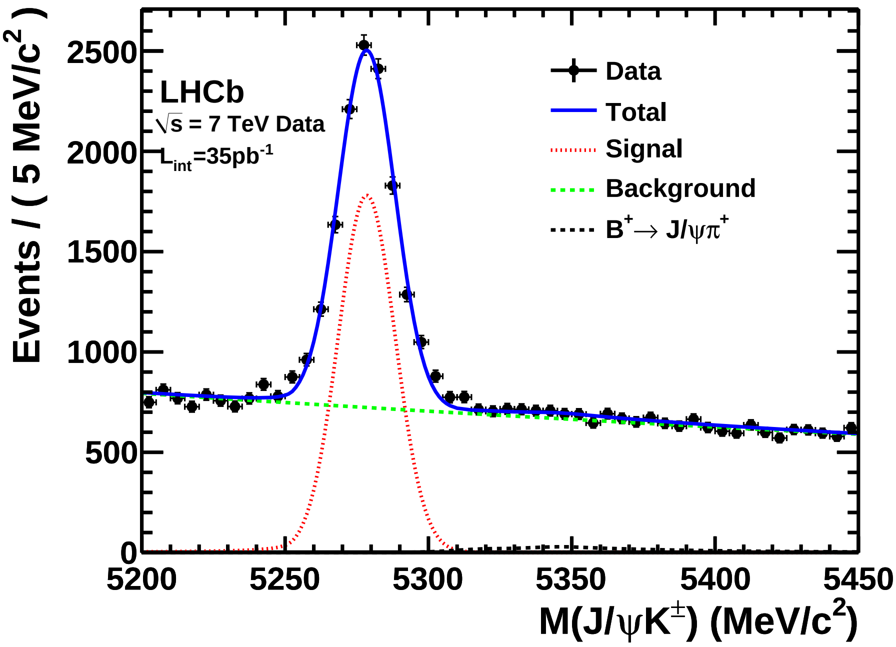

Figure 4.4 Invariant mass distribution of $B^+ \to J/\psi K^+$ candidates obtained with the analysis selection. The fit results with the function described in Section 4.3.1 are superimposed. The solid blue line is the total fit function, the dashed red line shows the signal contribution, the dashed green line is the combinatorial background and the black dashed line is the feed-down from Cabibbo suppressed decays.

Table 4.4 $B^+ \to J/\psi\, K^+$ stripping and final selection criteria.

Quantity	Stripping	Final selection
μ		
track	Long track with muon detector hits (IsMuon)	-
$\Delta\mathrm{LL}_{\mu\pi}$	> 0	-
p_T	-	$> 700\,\mathrm{MeV}/c$
track fit quality χ^2/ndf	< 5	< 4
J/ψ		
Mass window	$3017 < M_{\mu\mu} < 3177\,\mathrm{GeV}/c^2$	$3040 < M_{\mu\mu} < 3140\,\mathrm{GeV}/c^2$
vertex fit χ^2/ndf	< 16	< 9
L0 Trigger On Signal	-	L0SingleMuon or L0DiMuon
HLT1 Trigger On Signal	-	Hlt1SingleMuonNoIPL0 or Hlt1DiMuonNoIPL0Di or Hlt1DiMuonNoIP2L0
HLT2 Trigger On Signal	-	Hlt2DiMuonUnbiasedJPsi
K^+		
track	Long track	-
p_T	$> 500\,\mathrm{MeV}/c$	-
track fit quality χ^2/ndf	< 5	< 4
B^+		
vertex fit χ^2/ndf	< 10	< 9
τ	$> 0.15\,\mathrm{ps}$	$> 0.3\,\mathrm{ps}$

cussed as systematic uncertainties in Section 4.4.

4.3 Cross-section determination

The production cross-section is determined by Equation 4-1. The number of reconstructed signal B^+ candidates is obtained from a fit to the candidates invariant mass distribution, in bins of p_T. The total efficiency ϵ_{tot} is the product of the geometrical acceptance ϵ_{acc}, the detection, reconstruction and selection efficiencies combined in the efficiency term ϵ_{rec} and the trigger efficiency ϵ_{tri},

$$\epsilon_{tot} = \epsilon_{acc} \times \epsilon_{rec} \times \epsilon_{tri}. \tag{4-2}$$

Monte Carlo (MC) samples of generator level and fully simulated signal $B^+ \to J/\psi K^+$ events are used to estimate the ϵ_{acc} and ϵ_{rec} in bins of p_T and y. A trigger unbiased data sample of inclusive J/ψ is used to determine the trigger efficiencies from data directly.

The rapidity distributions of background subtracted data and MC are shown in Figure 4.5. In order to reduce the dependance of the results on the exact y spectrum inside

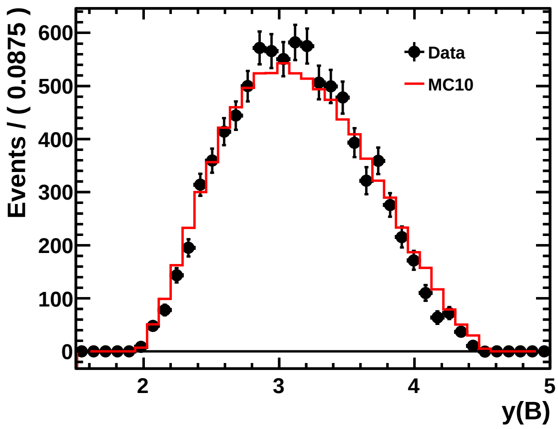

Figure 4.5 The rapidity distributions of background subtracted data (black points with error bars) and MC (blue line).

the p_T bins in the MC simulation, the following method is applied. Mass distributions are fitted with a maximum likelihood fit in bins of p_T. Then the rapidity distribution of signal candidates in these p_T bins is obtained using a $_s\mathcal{P}lot$ technique[96]. The number of signal events in bins of p_T and y, $N_{B^+}(p_T, y)$, is then divided by the efficiencies to obtain the efficiency-corrected number of B^+ signal in the p_T bin,

$$\frac{N_{B^+}(p_T)}{\epsilon_{tot}(p_T)} = \sum_{y_{bin}} \left[\frac{N_{B^+}(p_T, y)}{\epsilon_{tot}(p_T, y_{bin})} \right], \tag{4-3}$$

where y_{bin} is one rapidity bin, $\epsilon_{\text{tot}}(p_{\text{T}}, y_{\text{bin}})$ the total efficiency for this rapidity bin. The underlying assumption of this method is that the mass distribution shape does not depend on the B^+ rapidity inside each p_{T} bin.

4.3.1 Signal yield determination

The number of signal candidates is obtained from an extended unbinned maximum likelihood fit to the invariant mass distributions of the selected B^+ candidates, in the interval $M_{J/\psi K^+} \in [5.15; 5.55]\,\text{GeV}/c^2$. The candidates entering the mass distributions can be divided into three components that are reflected in the choice of the fit function.

The first component is the signal, which is described by a Crystal Ball function[97,98] to take the final state radiation (FSR) of the $\mu^\pm$ and K^+ into account. The Crystal Ball function is defined as

$$F_{\text{CB}}(x; M, \sigma, \alpha, n) = \begin{cases} \dfrac{\left(\frac{n}{|\alpha|}\right)^n e^{-\frac{1}{2}\alpha^2}}{\left(\frac{n}{|\alpha|} - |\alpha| - \frac{x-M}{\sigma}\right)^n} & \text{if} \quad \dfrac{x-M}{\sigma} < -|\alpha| \\ \exp\left(-\dfrac{1}{2}\left(\dfrac{x-M}{\sigma}\right)^2\right) & \text{otherwise.} \end{cases} \tag{4-4}$$

where M is the fitted mass and σ the mass resolution. The α and n parameters define the tail shape of the function. These two parameters are correlated with the signal mass resolution σ. The relations between these parameters and the resolution are obtained from fits to the mass distributions of a Gaussian smeared generator level MC simulation event sample. n is fixed to 1, and the α is parameterized as a second order polynomial function of the signal resolution σ, as demonstrated in Figure 4.6.

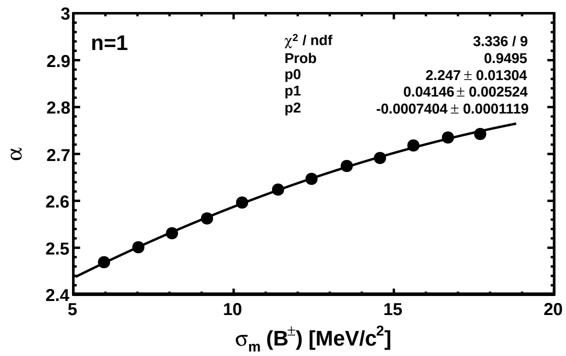

Figure 4.6 Parameterization of the Crystal Ball function parameter α as a function of mass resolution of B^+.

The second component is the combinatorial background which is described by an exponential function

$$F_{\text{background}}(x;p) = e^{-px}. \tag{4-5}$$

The last component is the feed-down background from other b-hadron decay modes. Decay modes with similar topology as the reconstructed one may be reconstructed in the signal mass window. The decay channel considered in this analysis as potential feed-down background is the Cabibbo suppressed decay $B^+ \to J/\psi\pi^+$, while the feed-down from other decay channels, like $B^0 \to J/\psi K^{*0}$ and $B^0_s \to J/\psi\phi$ are mostly outside the fit region, as discussed in Appendix A.4.

The invariant mass distribution of fully simulated $B^+ \to J/\psi\pi^+$, reconstructed by taking the pion as a kaon with the same selection cuts as described in Section 6.2, is shown in Figure 4.7. It has a peak at a value approximatively 50 MeV/c^2 higher than the nominal B^+ mass, and presents a long tail extending to higher mass values. The shape of this feed-down background is then parameterized with a function which is the sum of two Crystal Ball functions as

$$\begin{aligned} &F_{\text{Cabibbo}}(x;M,\Delta M_1,\sigma_1,\alpha_1,n_1,\Delta M_2,\sigma_2,\alpha_2,n_2) = \\ &\qquad \beta F_{\text{CB}}(x;M+\Delta M_1,\sigma_1,\alpha_1,n_1) + (1-\beta)F_{\text{CB}}(x;M+\Delta M_2,\sigma_2,\alpha_2,n_2), \end{aligned} \tag{4-6}$$

where β and $(1-\beta)$ are the fractions of Crystal Ball functions ΔM_1 and ΔM_2 are the offsets of the central values of the Crystal Ball functions with respect to the mass values M extracted from the fit to the mass distribution of $B^+ \to J/\psi K^+$ signal in MC simulation. These parameters are obtained from a fit to the mass distribution in Figure 4.7 using all candidates instead of dividing them into p_{T} bins. The result of the fit is superimposed in Figure 4.7 and the fit parameters are detailed in Table 4.5. These parameters are fixed in the final fits of the mass distributions in p_{T} bins. The ratio of the number of $B^+ \to J/\psi\pi^\pm$ candidates to that of the signal is fixed to $\mathcal{B}(B^+ \to J/\psi\pi^+)/\mathcal{B}(B^+ \to J/\psi K^+)$ from Ref.[28].

The total fit function is therefore

$$\begin{aligned} F_{\text{mass}}\left(x;M,\sigma,p,N_{\text{signal}},N_{\text{background}}\right) = &N_{\text{signal}}\,F_{\text{signal}}(x;M,\sigma) + \\ &N_{\text{background}}\,F_{\text{background}}(x;p) + \\ &\frac{\mathcal{B}(B^+ \to J/\psi\pi^+)}{\mathcal{B}(B^+ \to J/\psi K^+)} N_{\text{Signal}} F_{\text{Cabibbo}}(x;M), \end{aligned} \tag{4-7}$$

and has in total five free parameters:

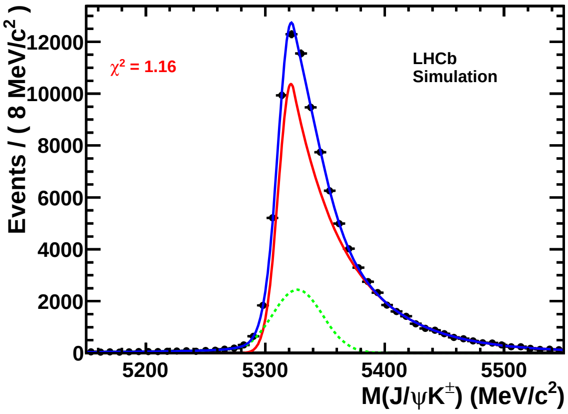

Figure 4.7 Invariant mass distribution of $B^+ \to J/\psi\, K^+$ candidates obtained on simulated $B^+ \to J/\psi\,\pi^+$ sample. The fit results as described in the text are superimposed. The solid blue line represents the total fit function F_{Cabibbo}, while the dashed green and red lines are the individual contributions of two Crystal Ball functions.

Table 4.5 $B^+ \to J/\psi\, K^+$ Parameters used to fit the shape of the Cabibbo suppressed background.

Parameter	$B^+ \to J/\psi\, K^+$
β	0.178 ± 0.016
ΔM_1	47.9 ± 0.7 MeV/c^2
σ_1	20.9 ± 0.7 MeV/c^2
a_1	1.90 ± 0.07
n_1	0.84 ± 0.08
ΔM_2	42.2 ± 0.3 MeV/c^2
σ_2	10.6 ± 0.3 MeV/c^2
a_2	-0.238 ± 0.015
n_2	16.7 ± 4.9

- M and σ are the central value and the resolution of the signal;
- p is the background constant parameter;
- N_{signal} and $N_{\text{background}}$ are the numbers of signal and combinatorial background components.

The result of the fit on the total mass distribution is shown in Figure 4.4. The total number of signal events is equal to $9\,007 \pm 141$ and the resolution of the Gaussian signal function is $\sigma = 10.0 \pm 0.2\,\text{MeV}/c^2$. The two uncertainties are statistical only.

The reconstructed candidates are divided into p_{T} bins of variable sizes. To obtain enough entries in these p_{T} bins, the variable bin size is determined in this way:

- The B^+ candidates in the data sample are binned by every $500\,\text{MeV}/c$ at first.
- Some of these bins with small statistics are combined to obtain enough entries, *i.e.* larger than 250.

Figure 4.8 shows the invariant mass distribution together with the fit result in one of the p_{T} bins ($5 < p_{\text{T}} < 5.5$) used for the cross-section determination in the range $2 < y < 4.5$[99]. Individual plot in each p_{T} bin is demonstrated in Appendix A.2.

For the first p_{T} bin ($0 < p_{\text{T}} < 500\,\text{MeV}/c$), the background level is too high to determine the signal resolution by mass fit directly. Figure 4.9 shows the variation of the mass resolution as a function of p_{T}. The resolution of the Crystal Ball function is thus fixed to a value extrapolated from the fit results of the other p_{T} bins, $\sigma = 8.2\,\text{MeV}/c^2$.

A $_s\mathcal{P}lot$ approach is applied in each p_{T} bin to separate signal and background using

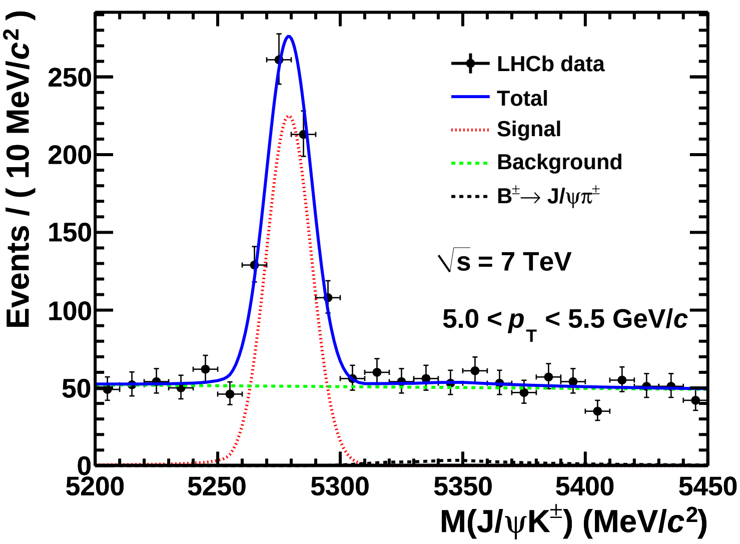

Figure 4.8 Invariant mass distribution of the selected $B^+ \to J/\psi\,K^+$ candidates for one bin ($5.0 < p_{\text{T}} < 5.5$ GeV/c)[99]. The result of the fit to the model described in the text is superimposed.

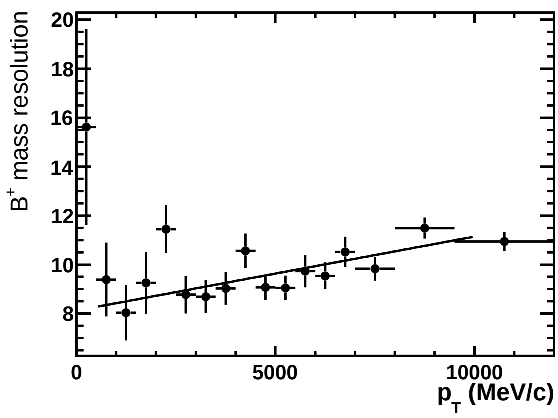

Figure 4.9 Fitted resolution of the B^+ mass distribution as a function of the B^+ transverse momentum. The first point is not used in the fit.

the mass fit result, and a ${}_s\mathit{Weight}$, ${}_sP_\mathrm{n}(M_i)$ is assigned to every candidate, both signal and background. M_i is the invariant mass of the i^{th} candidate indicating that the weight is determined from mass. In each bin, the signal event yield is equal to the sum of the ${}_s\mathit{Weights}$

$$N_{B^+}(p_\mathrm{T}, y) = \sum_{i \in (p_\mathrm{T}, y_\mathrm{bin})} {}_sP_\mathrm{n}(M_i, p_\mathrm{T}). \tag{4-8}$$

and the statistical uncertainty is equal to the sum of the square ${}_s\mathit{Weights}$

$$\sigma_{B^+}(p_\mathrm{T}, y) = \sqrt{\sum_{i \in (p_\mathrm{T}, y_\mathrm{bin})} {}_sP^2_\mathrm{n}(M_i, p_\mathrm{T})}. \tag{4-9}$$

Tables 4.6 and 4.7 give the number of estimated signal event yields and the statistical uncertainties in different (p_T, y) bins for the samples with both TCK groups, respectively.

4.3.2 Efficiency calculation

The first efficiency term is the generator-level acceptance, defined as

$$\epsilon_\mathrm{acc} = \frac{B^+ \text{ with } 2 < y < 4.5 \text{ and all tracks in LHCb}}{B^+ \text{ with } 2 < y < 4.5}. \tag{4-10}$$

It is estimated with Monte Carlo samples generated without any cut at the generator level. In Equation (4-10), "all tracks in LHCb" means that the polar angles θ of the momentum direction of the two μ and of the K^+ are all required to be $\theta \in [10; 400]$ mrad before the magnet. The acceptance efficiency as a function of p_T in different y bins is given in Table 4.8 and shown in Figure 4.10.

Table 4.6 Number of signal candidates for the non-prescaled group of TCK (group 1).

p_{T} (GeV/c)	$2.0 < y < 2.5$	$2.5 < y < 3.0$	$3.0 < y < 3.5$	$3.5 < y < 4.0$	$4.0 < y < 4.5$	Total
(0.0, 0.5]	-0.8 ± 1.3	7.1 ± 6.8	15.6 ± 11.0	19.2 ± 10.1	3.5 ± 5.0	44.7 ± 17.2
(0.5, 1.0]	4.6 ± 3.6	50.0 ± 13.7	72.5 ± 19.4	53.3 ± 15.8	-0.1 ± 6.8	180.4 ± 29.5
(1.0, 1.5]	9.9 ± 4.8	81.7 ± 16.2	75.5 ± 20.5	69.8 ± 17.1	3.7 ± 7.8	240.5 ± 32.5
(1.5, 2.0]	16.6 ± 6.4	90.9 ± 19.4	86.4 ± 24.8	78.0 ± 18.9	23.0 ± 9.7	294.9 ± 38.5
(2.0, 2.5]	22.9 ± 7.5	125.5 ± 22.2	158.2 ± 27.0	132.2 ± 21.2	45.2 ± 11.0	483.9 ± 43.0
(2.5, 3.0]	17.7 ± 6.5	139.6 ± 20.5	190.2 ± 24.2	70.2 ± 16.6	27.0 ± 8.7	444.7 ± 37.4
(3.0, 3.5]	27.3 ± 7.6	135.6 ± 19.5	177.0 ± 22.4	87.6 ± 15.8	13.8 ± 7.1	441.4 ± 35.2
(3.5, 4.0]	35.2 ± 8.7	147.5 ± 20.0	202.9 ± 23.3	101.3 ± 16.0	28.1 ± 8.3	515.1 ± 36.6
(4.0, 4.5]	29.6 ± 8.8	158.5 ± 19.8	195.1 ± 22.0	138.2 ± 16.7	30.5 ± 7.9	551.8 ± 36.0
(4.5, 5.0]	59.5 ± 9.9	132.6 ± 16.3	193.3 ± 18.8	124.5 ± 14.6	24.8 ± 6.3	534.7 ± 31.2
(5.0, 5.5]	29.9 ± 7.3	172.5 ± 16.9	160.0 ± 16.5	84.0 ± 11.7	20.7 ± 5.6	467.0 ± 27.9
(5.5, 6.0]	40.4 ± 8.5	141.6 ± 15.7	153.1 ± 16.2	91.4 ± 12.0	17.0 ± 5.3	443.5 ± 27.4
(6.0, 6.5]	40.4 ± 8.1	126.0 ± 14.0	129.9 ± 14.0	89.6 ± 11.3	19.3 ± 5.4	405.2 ± 24.8
(6.5, 7.0]	42.0 ± 7.7	117.0 ± 13.0	118.4 ± 12.9	61.8 ± 9.3	9.3 ± 3.6	348.5 ± 22.2
(7.0, 7.5]	43.2 ± 7.6	112.8 ± 12.3	82.7 ± 10.4	37.0 ± 7.3	5.3 ± 2.9	280.9 ± 19.5
(7.5, 8.0]	40.8 ± 7.3	100.6 ± 11.4	101.7 ± 11.5	37.7 ± 7.1	9.8 ± 3.6	290.8 ± 19.5
(8.0, 8.5]	17.9 ± 5.0	86.2 ± 10.2	91.5 ± 10.6	46.9 ± 7.5	4.2 ± 2.3	246.7 ± 17.4
(8.5, 9.0]	36.7 ± 6.6	67.4 ± 9.1	60.1 ± 8.7	34.0 ± 6.2	2.2 ± 2.0	200.4 ± 15.7
(9.0, 9.5]	24.0 ± 5.2	84.2 ± 9.8	68.6 ± 8.8	29.8 ± 5.9	9.4 ± 3.4	216.1 ± 15.7
(9.5, 10.0]	25.8 ± 5.3	35.9 ± 6.8	36.0 ± 6.8	24.9 ± 5.4	7.6 ± 2.9	130.2 ± 12.6
(10.0, 10.5]	14.2 ± 4.2	60.2 ± 8.2	48.6 ± 7.4	18.1 ± 4.6	5.7 ± 2.5	146.8 ± 13.0
(10.5, 11.0]	25.8 ± 5.4	36.9 ± 6.5	38.8 ± 6.6	14.6 ± 4.2	3.9 ± 2.1	119.9 ± 11.7
(11.0, 12.0]	42.7 ± 6.8	67.7 ± 8.6	50.7 ± 7.7	36.3 ± 6.1	4.6 ± 2.6	202.0 ± 15.0
(12.0, 13.0]	25.4 ± 5.4	55.2 ± 7.7	36.4 ± 6.4	21.7 ± 4.9	9.0 ± 3.2	147.7 ± 12.8
(13.0, 14.5]	30.6 ± 5.9	71.8 ± 9.0	46.0 ± 6.8	18.8 ± 4.6	3.0 ± 1.7	170.1 ± 13.6
(14.5, 16.5]	47.4 ± 7.1	47.1 ± 7.3	33.2 ± 6.0	20.2 ± 4.7	3.1 ± 1.7	151.0 ± 12.8
(16.5, 21.5]	49.8 ± 7.4	42.2 ± 6.7	36.7 ± 6.4	10.1 ± 3.6	2.5 ± 1.5	141.2 ± 12.5
(21.5, 40.0]	41.6 ± 6.5	34.0 ± 5.9	16.6 ± 4.1	4.5 ± 2.3	1.0 ± 1.0	97.8 ± 10.0

Table 4.7 Number of signal candidates for the prescaled group of TCK (group 2).

p_T (GeV/c)	$2.0 < y < 2.5$	$2.5 < y < 3.0$	$3.0 < y < 3.5$	$3.5 < y < 4.0$	$4.0 < y < 4.5$	Total
(0.0, 0.5]	1.4 ± 1.5	5.8 ± 3.0	7.9 ± 4.7	1.5 ± 3.6	-0.5 ± 1.0	16.1 ± 6.9
(0.5, 1.0]	0.0 ± 0.0	6.5 ± 4.1	5.9 ± 6.6	4.7 ± 5.7	-1.1 ± 2.7	15.9 ± 10.0
(1.0, 1.5]	0.0 ± 0.0	12.1 ± 5.4	17.5 ± 8.1	12.7 ± 6.9	1.0 ± 2.9	43.3 ± 12.2
(1.5, 2.0]	1.9 ± 2.3	11.5 ± 5.6	11.6 ± 8.0	17.3 ± 7.8	4.8 ± 3.8	47.2 ± 13.3
(2.0, 2.5]	3.5 ± 2.6	17.6 ± 6.9	18.9 ± 8.6	22.1 ± 8.4	1.4 ± 3.1	63.6 ± 14.5
(2.5, 3.0]	0.6 ± 1.1	12.8 ± 6.1	32.4 ± 9.4	21.4 ± 7.0	8.0 ± 4.0	75.2 ± 13.9
(3.0, 3.5]	0.3 ± 1.5	7.9 ± 5.4	32.1 ± 8.5	13.2 ± 5.9	1.7 ± 2.2	55.2 ± 11.9
(3.5, 4.0]	2.7 ± 2.5	24.8 ± 7.3	22.4 ± 7.6	21.8 ± 6.9	4.5 ± 3.2	76.1 ± 13.3
(4.0, 4.5]	1.0 ± 2.1	20.5 ± 6.9	26.9 ± 7.6	10.1 ± 5.3	2.0 ± 2.3	60.6 ± 12.0
(4.5, 5.0]	6.4 ± 3.3	11.7 ± 5.2	27.9 ± 7.1	10.7 ± 4.6	1.0 ± 1.8	57.6 ± 10.6
(5.0, 5.5]	1.9 ± 2.2	23.2 ± 6.2	19.8 ± 6.0	11.1 ± 4.4	0.3 ± 1.3	56.3 ± 10.0
(5.5, 6.0]	8.5 ± 3.6	6.0 ± 4.2	23.0 ± 6.1	3.7 ± 2.8	2.1 ± 1.9	43.3 ± 8.9
(6.0, 6.5]	6.0 ± 2.8	13.3 ± 4.9	20.4 ± 5.8	11.2 ± 3.9	2.5 ± 1.9	53.3 ± 9.2
(6.5, 7.0]	2.4 ± 2.0	14.2 ± 4.7	16.7 ± 4.9	9.3 ± 3.9	1.8 ± 1.6	44.4 ± 8.2
(7.0, 7.5]	6.2 ± 2.8	11.2 ± 4.0	13.5 ± 4.3	6.5 ± 2.7	3.1 ± 2.0	40.5 ± 7.3
(7.5, 8.0]	2.3 ± 2.0	15.1 ± 4.6	17.8 ± 4.7	5.4 ± 2.7	0.8 ± 1.2	41.5 ± 7.5
(8.0, 8.5]	3.6 ± 2.0	9.0 ± 3.3	9.0 ± 3.4	9.2 ± 3.3	-0.0 ± 0.2	30.8 ± 6.1
(8.5, 9.0]	2.1 ± 1.6	13.3 ± 3.9	13.7 ± 4.0	3.7 ± 2.1	2.1 ± 1.4	34.9 ± 6.3
(9.0, 9.5]	3.3 ± 2.0	5.1 ± 2.8	11.5 ± 3.8	1.6 ± 1.5	1.4 ± 1.3	23.0 ± 5.5
(9.5, 10.0]	4.2 ± 2.1	9.0 ± 3.3	7.9 ± 2.9	2.7 ± 1.8	0.0 ± 0.0	23.7 ± 5.2
(10.0, 10.5]	5.2 ± 2.3	1.9 ± 1.6	10.4 ± 3.3	2.1 ± 1.5	2.1 ± 1.5	21.6 ± 4.8
(10.5, 11.0]	3.1 ± 1.9	8.9 ± 3.2	4.8 ± 2.7	2.2 ± 2.0	0.0 ± 0.0	19.0 ± 5.0
(11.0, 12.0]	4.9 ± 2.2	9.6 ± 3.2	10.7 ± 3.5	3.7 ± 2.1	1.4 ± 1.1	30.4 ± 5.7
(12.0, 13.0]	3.0 ± 1.7	12.0 ± 3.5	6.0 ± 2.6	4.7 ± 2.4	3.8 ± 1.9	29.6 ± 5.6
(13.0, 14.5]	10.8 ± 3.5	9.9 ± 3.4	8.5 ± 3.1	3.4 ± 2.0	1.0 ± 1.1	33.6 ± 6.2
(14.5, 16.5]	7.9 ± 2.9	5.5 ± 2.5	4.8 ± 2.2	2.4 ± 2.4	0.0 ± 0.0	20.6 ± 5.0
(16.5, 21.5]	10.3 ± 3.3	14.1 ± 3.8	7.0 ± 2.7	3.3 ± 1.8	0.0 ± 0.0	34.6 ± 6.0
(21.5, 40.0]	5.4 ± 2.4	6.4 ± 2.9	5.8 ± 2.4	0.0 ± 0.0	0.0 ± 0.0	17.6 ± 4.5

Table 4.8 Acceptance efficiency (ϵ_{acc}, in %) in bins of B^+ p_T and y.

p_T (GeV/c)	$2.0 < y < 2.5$	$2.5 < y < 3.0$	$3.0 < y < 3.5$	$3.5 < y < 4.0$	$4.0 < y < 4.5$
(0.0, 0.5]	42.1 ± 1.1	75.9 ± 1.0	88.3 ± 0.8	84.8 ± 1.0	67.8 ± 1.3
(0.5, 1.0]	39.8 ± 0.7	76.3 ± 0.6	88.5 ± 0.5	84.7 ± 0.6	67.0 ± 0.9
(1.0, 1.5]	41.9 ± 0.6	76.7 ± 0.5	89.1 ± 0.4	84.9 ± 0.6	67.7 ± 0.8
(1.5, 2.0]	41.5 ± 0.6	77.6 ± 0.5	89.6 ± 0.4	86.0 ± 0.5	67.7 ± 0.8
(2.0, 2.5]	44.6 ± 0.5	79.7 ± 0.5	90.0 ± 0.4	86.8 ± 0.5	70.4 ± 0.8
(2.5, 3.0]	45.2 ± 0.6	80.7 ± 0.5	90.6 ± 0.4	87.7 ± 0.5	73.3 ± 0.8
(3.0, 3.5]	48.1 ± 0.6	82.3 ± 0.5	91.5 ± 0.4	88.2 ± 0.5	74.0 ± 0.9
(3.5, 4.0]	50.0 ± 0.6	82.6 ± 0.5	92.2 ± 0.4	89.0 ± 0.5	75.0 ± 0.9
(4.0, 4.5]	52.9 ± 0.6	85.2 ± 0.5	92.3 ± 0.4	90.1 ± 0.5	77.5 ± 0.9
(4.5, 5.0]	54.9 ± 0.6	86.3 ± 0.5	93.0 ± 0.4	91.3 ± 0.5	77.2 ± 0.9
(5.0, 5.5]	58.5 ± 0.6	87.2 ± 0.5	94.0 ± 0.4	92.1 ± 0.5	79.7 ± 1.0
(5.5, 6.0]	60.5 ± 0.7	88.3 ± 0.5	93.8 ± 0.4	92.8 ± 0.5	81.5 ± 1.0
(6.0, 6.5]	62.5 ± 0.7	89.4 ± 0.5	95.4 ± 0.4	92.6 ± 0.6	82.3 ± 1.1
(6.5, 7.0]	64.8 ± 0.7	90.6 ± 0.5	95.2 ± 0.4	93.3 ± 0.6	83.7 ± 1.2
(7.0, 7.5]	66.4 ± 0.8	91.1 ± 0.5	96.3 ± 0.4	94.8 ± 0.6	84.1 ± 1.3
(7.5, 8.0]	71.3 ± 0.8	92.3 ± 0.5	96.1 ± 0.4	95.1 ± 0.6	84.9 ± 1.4
(8.0, 8.5]	70.2 ± 0.9	93.3 ± 0.5	96.0 ± 0.5	96.7 ± 0.6	86.6 ± 1.4
(8.5, 9.0]	72.5 ± 1.0	92.9 ± 0.6	96.1 ± 0.5	95.4 ± 0.7	88.5 ± 1.5
(9.0, 9.5]	75.2 ± 1.0	93.4 ± 0.6	97.4 ± 0.5	96.3 ± 0.7	86.2 ± 1.8
(9.5, 10.0]	75.6 ± 1.1	94.5 ± 0.6	97.3 ± 0.5	96.9 ± 0.7	90.3 ± 1.8
(10.0, 10.5]	76.6 ± 1.1	95.2 ± 0.6	97.1 ± 0.6	95.5 ± 1.0	91.0 ± 1.9
(10.5, 11.0]	80.2 ± 1.2	94.0 ± 0.8	97.7 ± 0.6	95.7 ± 1.0	95.2 ± 1.7
(11.0, 12.0]	78.6 ± 0.9	95.3 ± 0.6	97.9 ± 0.4	97.6 ± 0.6	94.0 ± 1.4
(12.0, 13.0]	85.5 ± 0.9	96.1 ± 0.6	97.9 ± 0.5	98.1 ± 0.7	94.8 ± 1.6
(13.0, 14.5]	85.0 ± 0.9	96.2 ± 0.6	98.5 ± 0.4	98.0 ± 0.6	96.7 ± 1.3
(14.5, 16.5]	86.4 ± 1.0	97.2 ± 0.6	99.0 ± 0.4	99.1 ± 0.5	94.5 ± 2.0
(16.5, 21.5]	91.4 ± 0.8	98.7 ± 0.4	99.0 ± 0.4	99.0 ± 0.6	96.7 ± 1.9
(21.5, 40.0]	95.5 ± 0.8	99.6 ± 0.3	100.0 ± 0.0	100.0 ± 0.0	100.0 ± 0.0

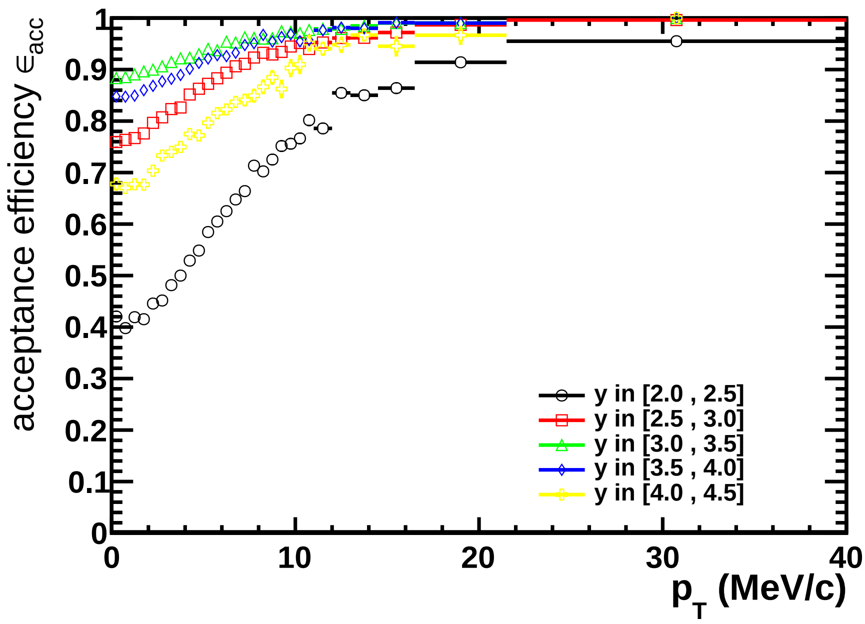

Figure 4.10 Acceptance efficiency as a function of p_{T} in bins of y.

The second term of the efficiency ϵ_{rec} combines the B^+ meson detection, reconstruction and selection efficiencies. It is defined as

$$\epsilon_{\mathrm{rec}} = \frac{B^+ \text{ detected, reconstructed and selected}}{B^+ \text{ with } 2 < y < 4.5, \text{ and all tracks in LHCb}}. \tag{4-11}$$

The reconstruction efficiency as a function of p_{T} in the different y bins is given in Table 4.9 and shown in Figure 4.11. The effect of tracking efficiency correction as discussed below is included in this efficiency. The reconstruction efficiencies computed from the Monte Carlo simulation also include the efficiency to match a reconstructed B^+ to a true generated $B^+ \to J/\psi K^+$. This term should not be included when correcting the data for the reconstruction efficiency. However, given that the matching efficiency is measured to be very large ($\sim 99.9\%$), this effect is negligible.

The decomposition of the selection cut efficiency is shown in Table 4.10. Each cut efficiency is defined with respect to all the selections imposed before it.

Using a tag-and-probe method[100,101], the tracking efficiencies are extracted from $J/\psi \to \mu^+\mu^-$ decay from inclusive J/ψ data samples. The schematic diagram of the tag-and-probe method is shown in Figure 4.12 and includes the following steps:

- Use a muon track of type “Long track” and a muon track reconstructed using information from the VELO and calorimeter but not from the tracking stations (TT and T1-T3), called “VELO-CALO” track, to form a J/ψ candidate. Fit the mass

Table 4.9 Reconstruction efficiency ($\epsilon_{\rm rec}$, in %) in bins of B^{+} $p_{\rm T}$ and y. The effect of tracking efficiency correction is included.

$p_{\rm T}$ (GeV/c)	$2.0 < y < 2.5$	$2.5 < y < 3.0$	$3.0 < y < 3.5$	$3.5 < y < 4.0$	$4.0 < y < 4.5$
(0.0, 0.5]	11.0 ± 0.4	26.4 ± 0.5	33.0 ± 0.5	28.4 ± 0.5	14.1 ± 0.5
(0.5, 1.0]	12.3 ± 0.3	26.1 ± 0.3	33.0 ± 0.3	29.3 ± 0.3	14.5 ± 0.3
(1.0, 1.5]	11.8 ± 0.2	26.5 ± 0.3	33.7 ± 0.3	29.5 ± 0.3	15.1 ± 0.3
(1.5, 2.0]	12.5 ± 0.2	26.0 ± 0.2	34.5 ± 0.3	30.9 ± 0.3	15.8 ± 0.3
(2.0, 2.5]	11.9 ± 0.2	26.6 ± 0.2	35.6 ± 0.3	30.9 ± 0.3	15.6 ± 0.3
(2.5, 3.0]	12.8 ± 0.2	26.9 ± 0.2	35.7 ± 0.3	31.4 ± 0.3	16.2 ± 0.3
(3.0, 3.5]	12.7 ± 0.2	27.8 ± 0.2	35.1 ± 0.3	33.2 ± 0.3	15.9 ± 0.3
(3.5, 4.0]	13.1 ± 0.2	28.6 ± 0.2	37.0 ± 0.3	33.2 ± 0.3	16.6 ± 0.3
(4.0, 4.5]	12.8 ± 0.2	28.3 ± 0.2	37.2 ± 0.3	32.3 ± 0.3	16.6 ± 0.4
(4.5, 5.0]	13.8 ± 0.2	28.8 ± 0.3	38.6 ± 0.3	33.8 ± 0.3	17.0 ± 0.4
(5.0, 5.5]	13.2 ± 0.2	30.0 ± 0.3	36.7 ± 0.3	33.0 ± 0.4	16.8 ± 0.4
(5.5, 6.0]	13.9 ± 0.2	30.4 ± 0.3	38.0 ± 0.3	33.8 ± 0.4	15.9 ± 0.4
(6.0, 6.5]	14.4 ± 0.3	31.3 ± 0.3	38.7 ± 0.4	34.4 ± 0.4	17.7 ± 0.5
(6.5, 7.0]	14.8 ± 0.3	32.2 ± 0.3	39.3 ± 0.4	36.2 ± 0.5	18.7 ± 0.5
(7.0, 7.5]	15.3 ± 0.3	32.0 ± 0.4	39.4 ± 0.4	37.8 ± 0.5	19.3 ± 0.6
(7.5, 8.0]	15.2 ± 0.3	34.2 ± 0.4	38.8 ± 0.4	34.9 ± 0.5	21.1 ± 0.7
(8.0, 8.5]	16.5 ± 0.3	35.5 ± 0.4	40.9 ± 0.5	39.8 ± 0.6	20.9 ± 0.7
(8.5, 9.0]	17.9 ± 0.4	35.1 ± 0.5	43.9 ± 0.6	40.1 ± 0.7	18.9 ± 0.7
(9.0, 9.5]	17.4 ± 0.4	37.6 ± 0.5	43.2 ± 0.6	41.2 ± 0.8	21.3 ± 0.9
(9.5, 10.0]	20.2 ± 0.5	38.4 ± 0.5	46.0 ± 0.7	40.2 ± 0.8	24.5 ± 1.1
(10.0, 10.5]	20.6 ± 0.5	38.0 ± 0.6	46.0 ± 0.7	43.8 ± 0.9	24.9 ± 1.2
(10.5, 11.0]	21.5 ± 0.5	43.1 ± 0.7	50.9 ± 0.8	36.8 ± 0.9	28.0 ± 1.4
(11.0, 12.0]	21.7 ± 0.4	42.0 ± 0.5	46.4 ± 0.6	44.3 ± 0.8	27.7 ± 1.1
(12.0, 13.0]	22.6 ± 0.5	43.4 ± 0.6	44.2 ± 0.7	42.6 ± 0.9	26.9 ± 1.3
(13.0, 14.5]	26.2 ± 0.5	47.7 ± 0.6	48.7 ± 0.7	41.3 ± 0.9	29.3 ± 1.3
(14.5, 16.5]	29.0 ± 0.5	51.7 ± 0.7	48.1 ± 0.8	43.2 ± 1.1	33.0 ± 1.7
(16.5, 21.5]	33.0 ± 0.5	52.9 ± 0.6	51.2 ± 0.8	48.8 ± 1.1	42.9 ± 2.1
(21.5, 40.0]	36.5 ± 0.7	46.0 ± 0.9	59.0 ± 1.3	54.4 ± 1.9	37.6 ± 3.7

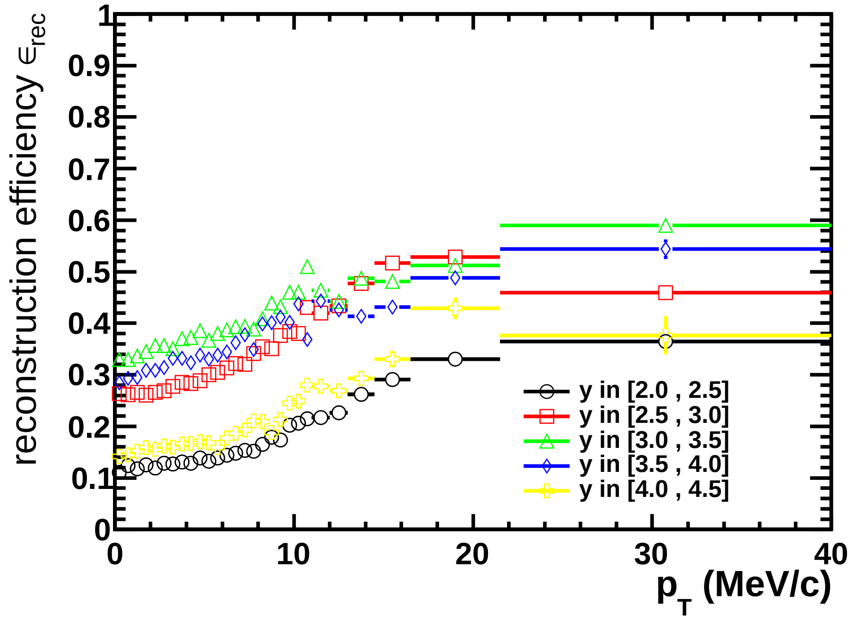

Figure 4.11 Reconstruction efficiency as a function of p_{T} in bins of y. The effect of tracking efficiency correction in Section 4.3.2 is included.

Table 4.10 Efficiency of each selection cut

Selection	Efficiency
All charged tracks reconstructed	$(53.28 \pm 0.04)\%$
χ^2/ndf of muons < 4	$(99.04 \pm 0.01)\%$
χ^2/ndf of kaon < 4	$(98.71 \pm 0.01)\%$
$p_{\mathrm{T}}(\mu) > 700\ \mathrm{MeV}/c$	$(89.07 \pm 0.03)\%$
IsMuon	$(81.56 \pm 0.04)\%$
$\Delta LL_{\mu\pi}(\mu) > 0$	$(96.20 \pm 0.02)\%$
J/ψ vertex $\chi^2/\mathrm{ndf} < 9$	$(97.70 \pm 0.02)\%$
$M_{\mu\mu} \in [3040, 3140]\ \mathrm{MeV}/c^2$	$(93.75 \pm 0.03)\%$
$p_{\mathrm{T}}(K) > 0.5\ \mathrm{GeV}/c$	$(97.83 \pm 0.02)\%$
B vertex $\chi^2/\mathrm{ndf} < 9$	$(98.89 \pm 0.01)\%$
$\tau(B) > 0.3$ ps	$(81.78 \pm 0.05)\%$
B Mass window	$(99.28 \pm 0.01)\%$
Clone rejection	$(98.33 \pm 0.02)\%$
Total	$(25.75 \pm 0.03)\%$

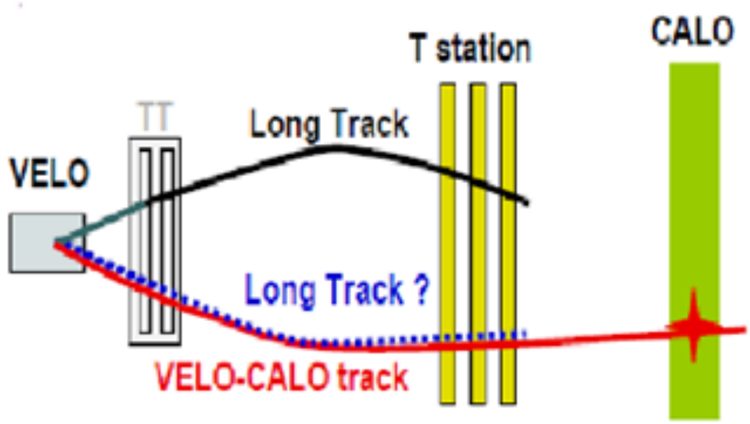

Figure 4.12 The schematic of tag-and-probe method[100].

distribution of these candidates and get the event yield of J/ψ "Tag" signal, N_{Tag}.

- Use a muon track of type "Long track" and a muon track with both Long and "VELO-CALO" track types, to form a J/ψ candidate. Fit the mass distribution of these candidates and get the event yield of J/ψ "Probe" signal, N_{Probe}.
- The tracking efficiency is therefore equal to $\frac{N_{\text{Probe}}}{N_{\text{Tag}}}$.

Differences of the tracking efficiency between data and MC simulation are found to be not negligible. The discrepancy is highly correlated with the momentum and pseudo rapidity of the track and has to be treated separately in bins. The ratio of tracking efficiency from data with respect to that from MC, as a function of momentum p and pseudo rapidity η of the track[102], are shown in Figure 4.13.

Using the efficiency ratio between data and MC, the following steps are taken to correct the tracking efficiency from the MC simulation sample[103]. The first thing is to weight the MC sample according to the best track multiplicity, since there are significant variations in the measured efficiency with respect to this parameter, as shown in Figure 4.14, and since the distributions of best track multiplicity are typically different in the data and MC simulation, which can be observed in Figure 4.15. The best track contains all the track types described in Section 3.2.3 and is selected by two clone elimination algorithms in the reconstruction software[104]. The best track multiplicity distribution in MC simulation sample is weighted to the background subtracted data distribution. The best track multiplicity distributions before and after the weight procedure are shown in Figure 4.15.

After the best track multiplicity weighting procedure, the efficiency ratios in Fig-

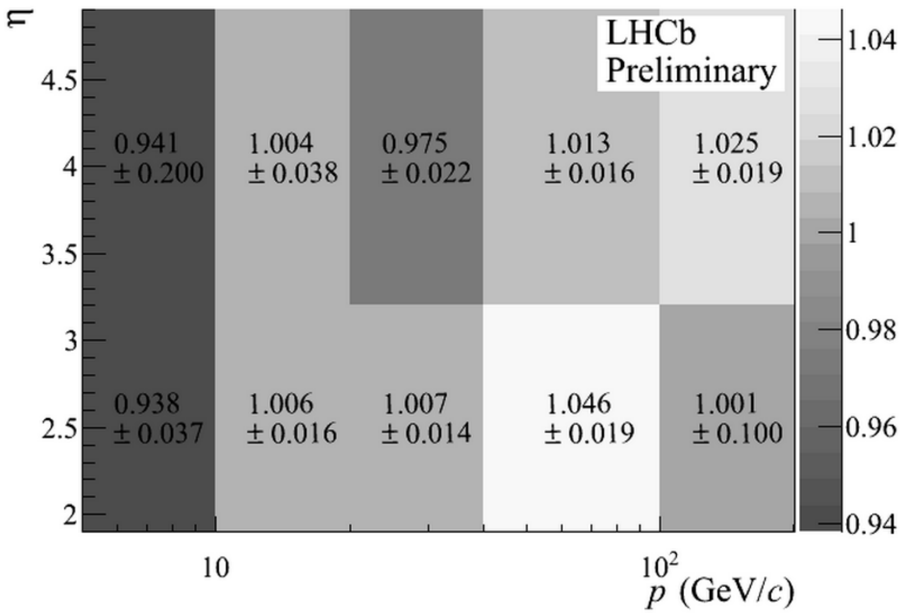

Figure 4.13 The ratio of tracking efficiency from 2010 data with respect to MC10[102] in bins of track momentum p and pseudo rapidity η. The uncertainties are statistical.

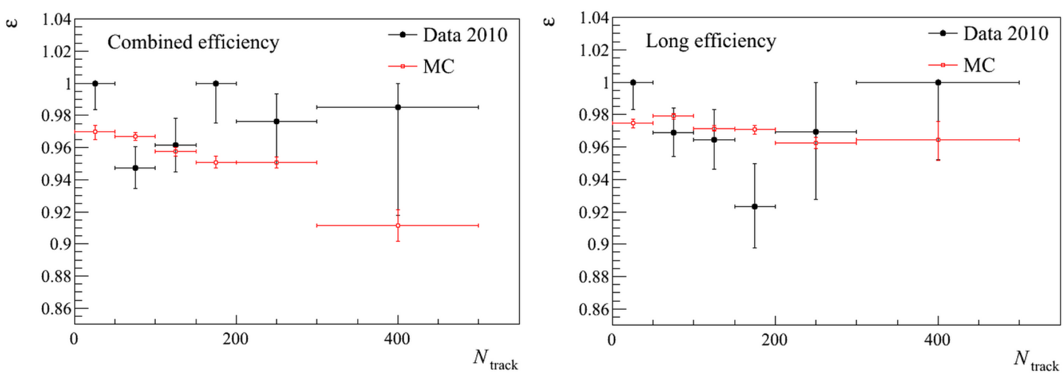

Figure 4.14 The tracking efficiency for *left*: all track average and *right*: long track as a function of the best track multiplicity[102]. The red points correspond to the real data and the black to the MC simulation.

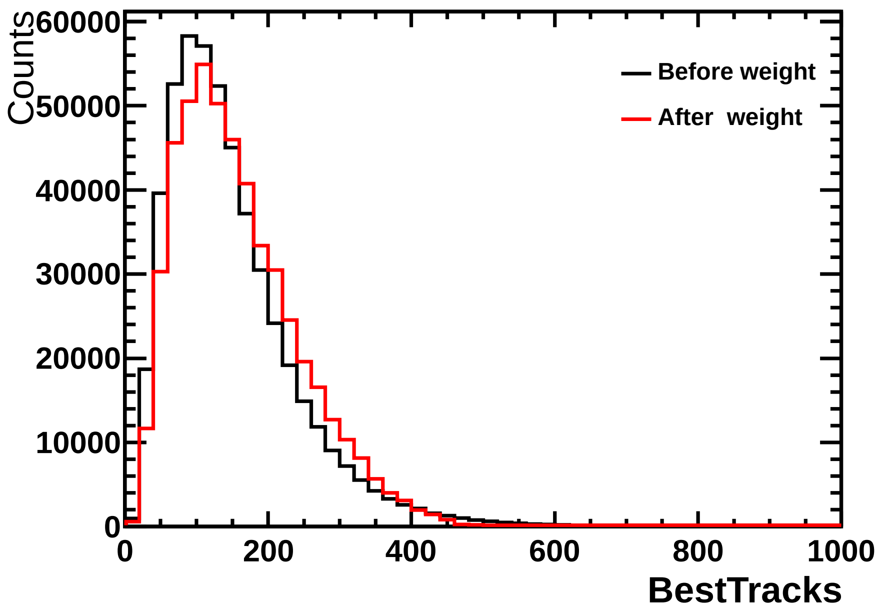

Figure 4.15 The best track multiplicity distributions before (black) and after (red) the weight procedure.

ure 4.13 are used to weight the MC simulation sample to correct the reconstruction efficiency. The variations of reconstruction efficiency from the correction in two rapidity bins are shown in Figure 4.16. The tracking efficiency ratios are extracted with limited

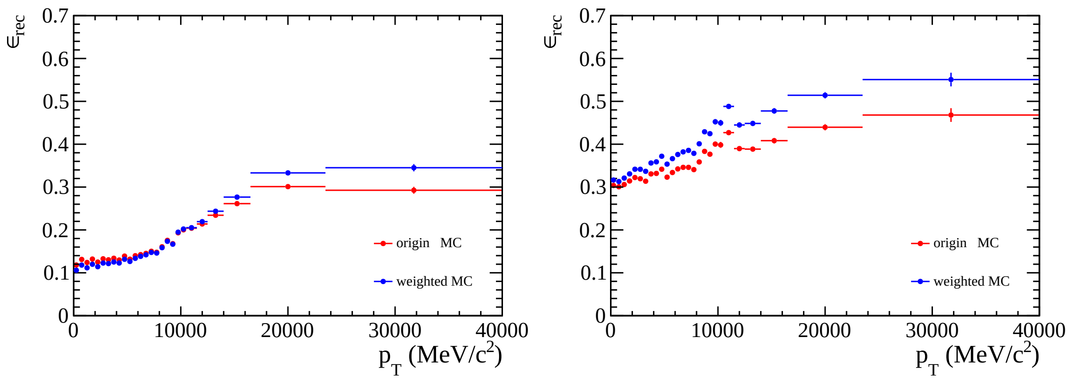

Figure 4.16 The variation of reconstruction efficiency from the tracking efficiency correction with *left:* $2.0 < y < 2.5$ and *right:* $3.0 < y < 3.5$. The red and blue lines correspond to the efficiencies before and after correction, respectively.

real and simulated data samples thus their statistical fluctuations have to be taken into account. The uncertainties from the tracking efficiency correction approach are propagated by a MC procedure with these steps:

- For each track p and η bin, a efficiency ratio is generated by a Gaussian function with the central value and uncertainty from Figure 4.13. A different ratio table is then extracted.

- The MC simulation B^+ candidates are weighted according to p and η of their decay products, μ and K, by the ratios in the new table.
- The weighted candidates are binned by their p_{T} and the yield of candidates in B^+ p_{T} bins are accumulated.

By repeating these 1 000 times, a distribution of weighted yield of MC candidates is extracted in each B^+ p_{T} bin. A Gaussian fit to this distribution gives a central value N_{weighted} and a sigma $\sigma_{\mathrm{weighted}}$. The relative uncertainty can be calculated by $\frac{\sigma_{\mathrm{weighted}}}{N_{\mathrm{weighted}}}$. Since the tracking efficiency ratios in different B^+ p_{T} bins could be the same, the uncertainties in different B^+ p_{T} bins are correlated. The total uncertainty in the entire p_{T} range is determined independently of that in each bin by summing up the yields of all the bins in the step 3. The uncertainties propagated from the statistical uncertainties of tracking efficiency ratios in bins of B^+ p_{T} are shown in Table 4.11. And in total, the uncertainty

Table 4.11 Relative tracking efficiency uncertainties from the statistical uncertainty of tracking efficiency ratio in bins of B^+ p_{T}.

p_{T} (GeV/c)	Relative uncertainty (%)	p_{T} (GeV/c)	Relative uncertainty (%)
0.0 – 0.5	3.3	7.0 – 7.5	3.0
0.5 – 1.0	3.3	7.5 – 8.0	2.9
1.0 – 1.5	3.2	8.0 – 8.5	2.9
1.5 – 2.0	3.3	8.5 – 9.0	2.8
2.0 – 2.5	3.2	9.0 – 9.5	2.8
2.5 – 3.0	3.3	9.5 – 10.0	2.8
3.0 – 3.5	3.2	10.0 – 10.5	2.8
3.5 – 4.0	3.1	10.5 – 11.0	2.8
4.0 – 4.5	3.2	11.0 – 12.0	2.7
4.5 – 5.0	3.2	12.0 – 13.0	2.7
5.0 – 5.5	3.3	13.0 – 14.5	2.7
5.5 – 6.0	3.2	14.5 – 16.5	2.7
6.0 – 6.5	3.2	16.5 – 21.5	2.7
6.5 – 7.0	3.0	21.5 – 40.0	3.0

from the statistical uncertainty of tracking efficiency ratio is determined to be 2.9%.

The L0 × HLT1 × HLT2 trigger efficiency ϵ_{tri} is defined as

$$\epsilon_{\mathrm{tri}} = \frac{B^+ \text{ selected and with } J/\psi \text{ TOS of L0} \times \text{HLT1} \times \text{HLT2}}{B^+ \text{ selected}}. \tag{4-12}$$

Trigger efficiencies are determined directly from data, using an inclusive J/ψ sample selected with the same requirement on J/ψ candidates as listed in Table 4.4.

At first, the trigger efficiencies are computed as a function of the J/ψ transverse momentum ($p_T < 15\,\mathrm{GeV}/c$) and rapidity ($2 < y < 4.5$) using events triggered independently of the J/ψ signal (or TIS, Trigger Independent of Signal). The trigger efficiency is then the fraction of events with a J/ψ passing the L0, HLT1 and HLT2 requirements (*i.e.* that are Triggered On Signal (TOS) of L0 × HLT1 × HLT2) in the sample of events triggered independently,

$$\epsilon_{\mathrm{tri}} = \frac{N_{\mathrm{TOS\ \&\ TIS}}}{N_{\mathrm{TIS}}} = \frac{N_{\mathrm{TOS\ \&\ TIS}}}{N_{\overline{\mathrm{TOS}}\mathrm{\&TIS}} + N_{\mathrm{TOS\&TIS}}} \tag{4-13}$$

where $\overline{\mathrm{TOS}}$ means not TOS. The numbers N are extracted from a fit to the distribution of J/ψ invariant mass in the corresponding (TOS&TIS or $\overline{\mathrm{TOS}}$&TIS) sample. The signal component of the fit function is a Crystal Ball function with tail shape parameterized as a function of signal mass resolution. The background component is described by an exponential function. Since the triggers used in this analysis are very efficient, the TOS efficiencies for these triggers are high. Thus, there are so few candidates in some p_T bins for $\overline{\mathrm{TOS}}$&TIS samples that the mass fit performs badly. To solve this problem, the mass and its resolution of the fit function for TOS&TIS and $\overline{\mathrm{TOS}}$&TIS distributions are fixed to those from the fit to the mass distributions in the entire TIS samples.

The TOS trigger uses the same requirements as the one listed in Table 4.4. If the TIS trigger uses the same requirements as the TOS, the TIS yield will be very small and not enough to make a mass fit to extract the signal yield. A different TIS trigger requirements are used as listed in Table. 4.12.

Table 4.12 Trigger lines for J/ψ TIS trigger in TISTOS method.

Trigger level	Trigger Lines
L0 TIS	L0Muon or L0DiMuon or L0Hadron
HLT1 TIS	Hlt1SingleMuonNoIPL0 or Hlt1DiMuonNoIPL0 or Hlt1DiMuonNoIP2L0 or Hlt1TrackAllL0 or Hlt1TrackMuon or Hlt1SingleHadron
HLT2 TIS	Hlt2Global

The TIS candidates with "Hadron" and "Track" trigger lines are independent of the J/ψ signal and are used together with muon and di-muon TIS candidates to extract enough events for the mass fit. The "Hlt2Global" line combines all the HLT2 selections to give a joint determination.

The trigger efficiencies are computed separately for the two TCK groups used in the analysis. The trigger efficiencies as a function of the J/ψ transverse momentum, in bins of J/ψ rapidity are shown in Tables 4.13 and 4.14.

Table 4.13 Trigger efficiency (ϵ_{tri}, in %) in bins of J/ψ p_T and y, for the TCKs of Group 1 (not prescaled).

p_T (GeV/c)	$2.0 < y < 2.5$	$2.5 < y < 3.0$	$3.0 < y < 3.5$	$3.5 < y < 4.0$	$4.0 < y < 4.5$
(0, 1.0]	3.5 ± 0.9	15.6 ± 1.2	25.9 ± 1.5	31.8 ± 1.6	29.3 ± 1.6
(1.0, 2.0]	15.0 ± 1.5	41.8 ± 1.3	48.8 ± 1.3	47.6 ± 1.4	44.3 ± 1.6
(2.0, 3.0]	38.0 ± 2.1	58.7 ± 1.5	59.8 ± 1.3	56.0 ± 1.5	53.5 ± 1.9
(3.0, 4.0]	48.5 ± 2.6	65.4 ± 1.4	71.4 ± 1.3	63.2 ± 1.4	52.2 ± 2.3
(4.0, 5.0]	65.5 ± 2.2	74.9 ± 1.4	77.0 ± 1.4	69.8 ± 1.7	59.3 ± 3.8
(5.0, 6.0]	70.9 ± 2.4	83.4 ± 1.5	81.3 ± 1.6	76.7 ± 1.4	66.6 ± 2.8
(6.0, 7.0]	84.1 ± 1.6	84.0 ± 1.5	83.6 ± 1.8	77.0 ± 2.3	62.9 ± 3.9
(7.0, 8.0]	86.3 ± 3.1	86.7 ± 2.0	85.3 ± 1.8	77.4 ± 2.6	69.9 ± 18.5
(8.0, 9.0]	85.6 ± 2.5	84.7 ± 2.8	86.2 ± 1.9	79.7 ± 3.6	64.0 ± 8.2
(9.0, 11.0]	88.7 ± 1.9	86.8 ± 2.4	87.8 ± 2.3	82.5 ± 2.5	64.1 ± 6.5
(11.0, 15.0]	86.1 ± 3.6	87.2 ± 2.9	84.0 ± 3.1	83.4 ± 5.2	53.5 ± 7.8

Table 4.14 Trigger efficiency (ϵ_{tri}, in %) in bins of J/ψ p_T and y, for the TCKs of Group 2 (prescaled).

p_T (GeV/c)	$2.0 < y < 2.5$	$2.5 < y < 3.0$	$3.0 < y < 3.5$	$3.5 < y < 4.0$	$4.0 < y < 4.5$
(0, 1.0]	2.0 ± 0.5	9.2 ± 1.8	23.1 ± 2.5	24.5 ± 2.7	26.3 ± 3.7
(1.0, 2.0]	7.4 ± 1.5	19.0 ± 1.7	30.2 ± 1.9	30.3 ± 2.1	28.6 ± 2.6
(2.0, 3.0]	7.6 ± 1.7	24.2 ± 1.6	32.2 ± 1.7	29.8 ± 2.0	32.5 ± 3.0
(3.0, 4.0]	17.5 ± 2.3	30.8 ± 1.9	37.1 ± 1.9	35.9 ± 2.4	34.6 ± 3.9
(4.0, 5.0]	24.4 ± 2.8	39.6 ± 2.2	43.3 ± 2.1	36.7 ± 2.5	31.0 ± 4.8
(5.0, 6.0]	32.3 ± 3.2	47.3 ± 2.7	49.3 ± 2.7	38.8 ± 3.0	32.6 ± 4.5
(6.0, 7.0]	41.3 ± 3.9	47.0 ± 3.2	52.8 ± 3.5	41.6 ± 3.8	28.0 ± 6.2
(7.0, 8.0]	52.0 ± 4.4	53.6 ± 3.6	45.0 ± 4.1	43.9 ± 4.3	21.9 ± 5.9
(8.0, 9.0]	47.6 ± 5.8	58.1 ± 4.6	58.3 ± 5.6	48.4 ± 7.0	29.4 ± 11.4
(9.0, 11.0]	55.0 ± 4.9	46.9 ± 4.0	50.0 ± 4.3	42.9 ± 5.4	19.8 ± 12.1
(11.0, 15.0]	53.6 ± 5.5	60.6 ± 5.3	50.9 ± 4.5	58.1 ± 7.1	46.2 ± 20.0

The B^+ candidates are then weighted by the inverse of the trigger efficiency, according to the TCK applied when recording it and to the p_{T} and y of the J/ψ candidate. For the very few candidates with a J/ψ outside the range used to determine the trigger efficiency ($p_{\mathrm{T}} > 15\,\mathrm{GeV}/c$, $y < 2$ or $y > 4.5$), the efficiency of the nearest bin is used. The number of these candidates is small and the bias is negligible.

Since candidates in different B^+ bins may have J/ψ candidates in the same bin, the J/ψ trigger efficiencies in different B^+ bins are correlated. The statistical uncertainty of trigger efficiency is estimated by the MC method similar to the one for tracking as described in Section 4.3.2. The results in p_{T} bins are shown in Table 4.15. And in total,

Table 4.15 The relative statistical uncertainty (in %) of trigger efficiency in B^+ p_{T} bins propagated from the efficiency in J/ψ p_{T} and y bins by the MC method.

p_{T} (GeV/c)	relative trigger uncertainty	p_{T} (GeV/c)	relative trigger uncertainty
(0.0, 0.5]	10.1	(7.0, 7.5]	1.1
(0.5, 1.0]	5.5	(7.5, 8.0]	0.7
(1.0, 1.5]	2.1	(8.0, 8.5]	0.7
(1.5, 2.0]	4.8	(8.5, 9.0]	1.0
(2.0, 2.5]	3.3	(9.0, 9.5]	1.5
(2.5, 3.0]	1.6	(9.5, 10.0]	1.1
(3.0, 3.5]	1.1	(10.0, 10.5]	2.3
(3.5, 4.0]	3.5	(10.5, 11.0]	1.8
(4.0, 4.5]	1.1	(11.0, 12.0]	1.0
(4.5, 5.0]	4.6	(12.0, 13.0]	1.3
(5.0, 5.5]	1.6	(13.0, 14.5]	1.9
(5.5, 6.0]	1.6	(14.5, 16.5]	2.5
(6.0, 6.5]	0.8	(16.5, 21.5]	1.5
(6.5, 7.0]	1.0	(21.5, 40.0]	2.0

the relative statistical uncertainty due to trigger efficiency is estimated to be 2.0%. The trigger efficiency in bins of B^+ p_{T} is calculated as the ratio of the signal yield in Table 4.6 and 4.7 to the yield weighted by the efficiency in Table 4.13 and 4.14. The results for the two TCK groups are listed in Table 4.16 and 4.17. The uncertainty is statistical and is calculated using the relative uncertainty in Table 4.15.

The second component of the trigger efficiency, which is not included in the efficiency discussed above, is the efficiency of the Global Event Cuts (GEC) applied at various stages of the trigger, as described in Section 3.2.5. Figure 4.17 shows the background

Table 4.16 Trigger efficiency in bins of B^+ p_T for the non-prescaled group of TCK (group 1).

p_T (GeV/c)	Trigger efficiency (%)	p_T (GeV/c)	Trigger efficiency (%)
(0.0, 0.5]	21.9 ± 2.2	(7.0, 7.5]	72.8 ± 0.8
(0.5, 1.0]	34.3 ± 1.9	(7.5, 8.0]	74.1 ± 0.5
(1.0, 1.5]	44.6 ± 0.9	(8.0, 8.5]	76.0 ± 0.5
(1.5, 2.0]	49.0 ± 2.3	(8.5, 9.0]	77.5 ± 0.8
(2.0, 2.5]	41.8 ± 1.4	(9.0, 9.5]	78.4 ± 1.1
(2.5, 3.0]	48.0 ± 0.8	(9.5, 10.0]	78.3 ± 0.9
(3.0, 3.5]	52.2 ± 0.6	(10.0, 10.5]	79.8 ± 2.6
(3.5, 4.0]	51.4 ± 1.8	(10.5, 11.0]	80.8 ± 1.4
(4.0, 4.5]	59.6 ± 0.7	(11.0, 12.0]	81.2 ± 0.8
(4.5, 5.0]	60.7 ± 2.8	(12.0, 13.0]	80.3 ± 1.1
(5.0, 5.5]	64.0 ± 1.0	(13.0, 14.5]	83.3 ± 1.6
(5.5, 6.0]	65.8 ± 1.0	(14.5, 16.5]	84.5 ± 2.2
(6.0, 6.5]	68.3 ± 0.5	(16.5, 21.5]	85.1 ± 1.3
(6.5, 7.0]	70.4 ± 0.7	(21.5, 40.0]	86.2 ± 1.7

Table 4.17 Trigger efficiency in bins of B^+ p_T for the prescaled group of TCK (group 2).

p_T (GeV/c)	Trigger efficiency (%)	p_T (GeV/c)	Trigger efficiency (%)
(0.0, 0.5]	28.4 ± 2.9	(7.0, 7.5]	34.2 ± 0.4
(0.5, 1.0]	38.4 ± 2.1	(7.5, 8.0]	39.6 ± 0.3
(1.0, 1.5]	28.3 ± 0.6	(8.0, 8.5]	41.3 ± 0.3
(1.5, 2.0]	20.5 ± 1.0	(8.5, 9.0]	44.0 ± 0.5
(2.0, 2.5]	26.2 ± 0.9	(9.0, 9.5]	45.5 ± 0.7
(2.5, 3.0]	29.3 ± 0.5	(9.5, 10.0]	43.2 ± 0.5
(3.0, 3.5]	32.7 ± 0.4	(10.0, 10.5]	42.8 ± 1.4
(3.5, 4.0]	29.5 ± 1.0	(10.5, 11.0]	47.1 ± 0.8
(4.0, 4.5]	31.0 ± 0.3	(11.0, 12.0]	47.4 ± 0.5
(4.5, 5.0]	25.3 ± 1.2	(12.0, 13.0]	44.2 ± 0.6
(5.0, 5.5]	32.7 ± 0.5	(13.0, 14.5]	46.3 ± 0.9
(5.5, 6.0]	33.7 ± 0.5	(14.5, 16.5]	50.6 ± 1.3
(6.0, 6.5]	37.6 ± 0.3	(16.5, 21.5]	52.7 ± 0.8
(6.5, 7.0]	33.5 ± 0.3	(21.5, 40.0]	54.1 ± 1.1

subtracted distributions of the quantities on which GEC are applied, for B^+ candidates, together with the same distributions seen in the MC simulation.

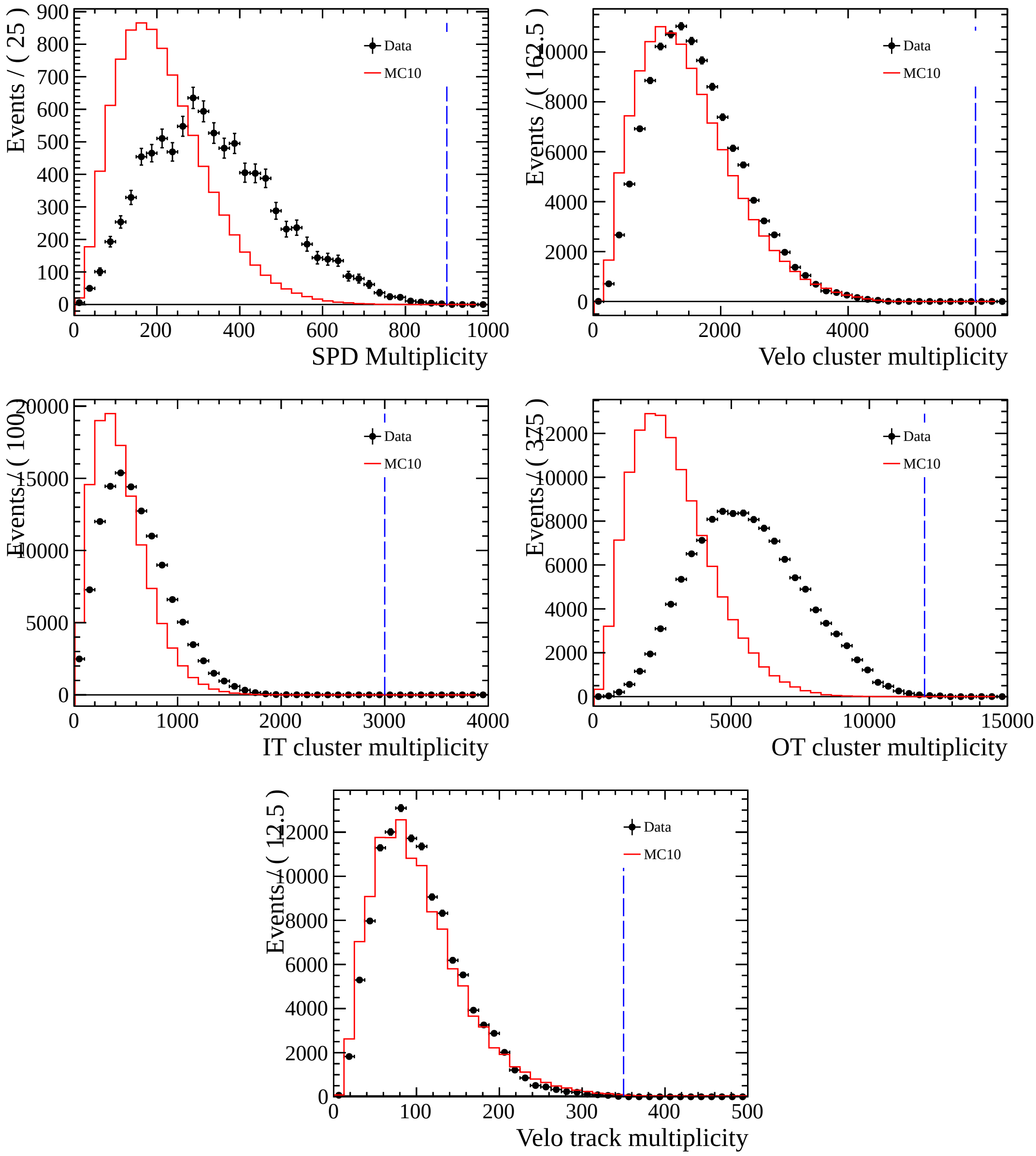

Figure 4.17 Distributions of GEC variables in data and MC simulation. On all plots, the black dots with error bars represent the background subtracted data distributions and the red histograms the MC distributions. The blue dashed lines show the cut values, as summarized in Table 4.2.

Due to the large amount of particles produced in the pp collision, the simulation can not describe the complicated collision process and detector response perfectly. The comparisons in Figure 4.17 show so large differences between data and MC simulation, that one can not trust the GEC efficiency extracted from simulation but have to estimate it from real data. Meanwhile, in all of the five GECs, only the cut of the VELO cluster multiplicity (VCM) rejects a significant fraction of signal events and only the VCM cut efficiency has to be considered.

The efficiency of the VCM cut is determined using the following method: from the minimum bias data sample① , the VCM distribution of minimum bias events with number of Primary Vertex (nPV) equal to 1, $P^1_{\rm mb}$, is extracted as shown in Figure 4.18. From the B^+ data sample, the VCM distribution of nPV=1 events $P^1_{B^+}$ is extracted by a background subtraction as shown in Figure 4.18. Both distributions are not biased by the VCM cut.

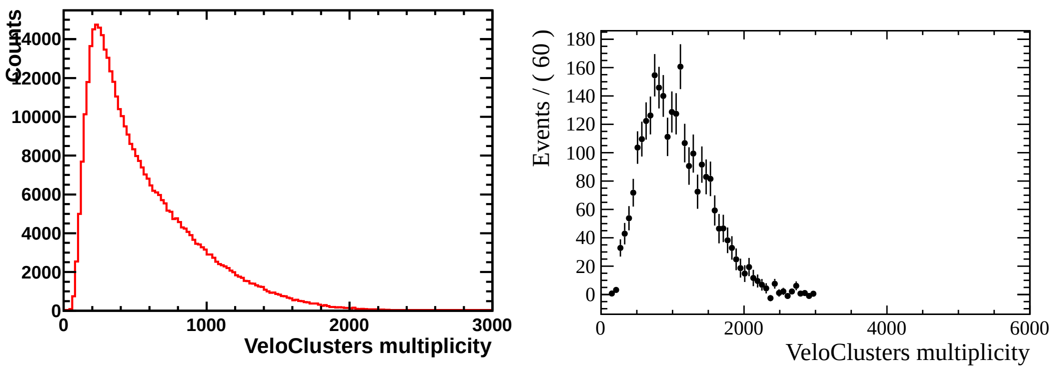

Figure 4.18 The VELO cluster multiplicity distributions of events with nPV=1 in *left*: minibias samples, $P^1_{\rm mb}$, and *right*: B^+ samples, $P^1_{B^+}$.

The VCM shape of B^+ data with nPV=i, $P^i_{B^+}$, can be estimated by overlaying the $P^1_{\rm mb}$ on the shape of B^+ data with nPV=1, $P^1_{B^+}$, for $i-1$ times. The $P^2_{B^+}$ and $P^3_{B^+}$ from this overlaying method are illustrated in Figure 4.19. The corresponding distributions of the background subtracted data are superimposed as a comparison. Good agreements are observed between the distributions from these two methods, and the overlaying method therefore provides a good estimation of the VCM shape. By the overlaying method, the VCM cut efficiency of events with nPV=1-10 are estimated as are listed in Table 4.18.

The VELO cluster multiplicity distributions of events with nPV=1 to 10 are weighted by the nPV fractions according to the background subtracted nPV distribution in the B^+ data sample, and then summed up to get the estimation of total distribution. The total distribution and comparison with the background subtracted distribution directly from data sample, together with a data fit result with a Gamma function as described in Section 4.4.2, are shown in Figure 4.20.

The VCM cut efficiency from data sample using the overlaying method is equal to $92.6 \pm 0.3\%$. This efficiency is assumed to be independent of the B^+ $p_{\rm T}$ and y. The trigger

① Sample collected by trigger with very loose requirements and minimally biased.

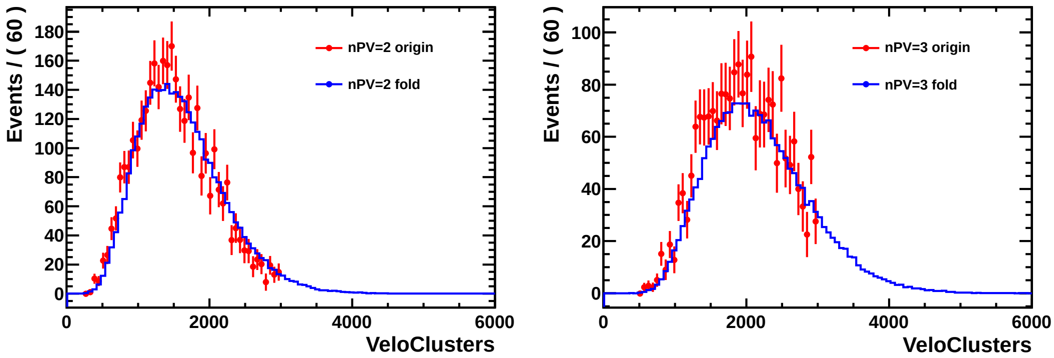

Figure 4.19 The comparison of VCM distributions with *left*: nPV=2 *right*: nPV=3 between background subtracted data (red) and the results from the overlaying method (blue).

Table 4.18 The VCM cut efficiencies of events with nPV=1-10 by the overlaying method.

nPV	Efficiency	Uncertainty
1	0.999	0.001
2	0.976	0.003
3	0.871	0.007
4	0.659	0.009
5	0.400	0.010
6	0.192	0.008
7	0.071	0.005
8	0.021	0.003
9	0.005	0.001
10	0.001	0.001

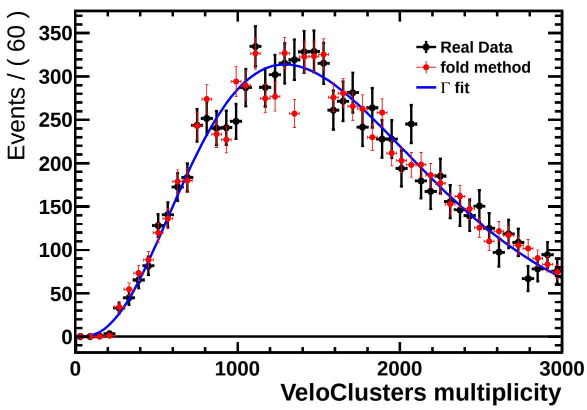

Figure 4.20 The VELO cluster multiplicity distributions from data and the overlaying method. The black points are the distributions of background subtracted data, the red points are the distributions from the overlaying method, while the blue line is the fit result to the data distribution with a Gamma function as described in Section 4.4.2.

efficiency is then the product of the J/ψ TOS efficiency by the efficiency of the VCM cut.

4.3.3 Luminosity determination

The luminosity is measured using Van der Meer scans and a beam-gas imaging method[105]. The knowledge of the absolute luminosity scale is used to calibrate the number of tracks in the vertex detector, which is found to be stable throughout the data-taking period and can therefore be used to monitor the instantaneous luminosity of the entire data sample. The integrated luminosity of the data sample used in this analysis is determined to be 34.6 pb^{-1}.

4.3.4 Uncertainty determination

The uncertainty of a measurement is composed of statistical and systematic components. The statistical uncertainty on the signal yield from the finite size of the data sample is determined by the fit and $_s\mathit{Plot}$ procedures in Section 4.3.1. As described in Section 4.3.2, the statistical uncertainties on the acceptance and reconstruction efficiencies are determined according to the signal yields in MC simulation samples. The uncertainty on the trigger efficiency is determined using the inclusive J/ψ real data sample by

$$\sigma(\epsilon)^2 = \frac{(1-\epsilon)^2\sigma(N_{\text{TOS\&TIS}})^2 + \epsilon^2\sigma N_{\overline{\text{TOS}}\text{\&TIS}}{}^2}{(N_{\text{TOS\&TIS}} + N_{\overline{\text{TOS}}\text{\&TIS}})^2} \tag{4-14}$$

where ϵ is the trigger efficiency, $N_{\text{TOS\&TIS}}$ the yield of TOS candidates in the TIS samples, $N_{\overline{\text{TOS}}\text{\&TIS}}$ the yield of not TOS candidates in the TIS samples, as discussed in Section 4.3.2[106]. Various systematic effects are discussed in the following Section 4.4.

4.4 Systematic uncertainty study

From Equation 4-1 and the discussions in Section 4.3, this measurement is affected by the systematic uncertainty on the determination of signal yields, efficiencies, branching fractions and luminosity.

4.4.1 Uncertainty from the determination of signal yields

We use a Crystal Ball function to describe the final state radiative tail of the signal peak in the mass fit. To estimate the systematic uncertainty, we merge a MC background sample whose shape is extracted from the data fit, and a MC signal sample. A fit to the mass distribution used in this analysis is performed. The difference (3.0%) between the true event number and the signal number from the fit is observed. The fitted signal yield is corrected by 3.0%, and an uncertainty of 1.5% is assigned as systematic uncertainty.

Considering the possible residue of the partially reconstructed physical background from another B meson decay in the mass region [5150,5200] MeV/c^2, we change the fit range to check the possible uncertainty. We also use two other regions to check the effects of changing the sideband range in the ${}_sPlot$ technique. The differences on the final results are shown in Table 4.19. The effects are negligible.

Table 4.19 Effects on the final results by changing the fit range.

Fit range	Differences on the final result
[5170, 5530]	0.3%
[5130, 5550]	0.4%
[5200, 5550]	0.5%

After all the selection cuts, there are collision events with more than one candidates selected. The correlation between the mass of the first candidate versus that of the second candidate for events with exactly two candidates is shown in Figure 4.21. There are

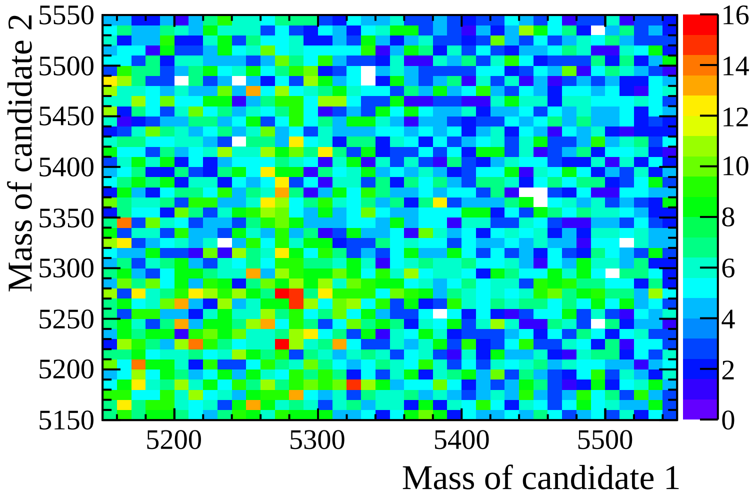

Figure 4.21 Correlation between the B^+ mass of the first candidate versus that of the second candidate in events with exactly two candidates.

less than fifty double-candidate events having two candidates with similar B^+ mass. The effects are less than 1% and negligible. We also make another test to keep only one candidate by the lowest B^+ vertex χ^2/ndf in each event. The signal yield from mass fit changes 0.8% percent.

Repeating the B^+ mass fit without considering the Cabibbo suppressed background affects the number of signal $B^+ \to J/\psi K^+$ events by 0.6%. The systematic uncertainty associated to the determination of Cabibbo suppressed background is therefore neglected.

In this analysis, the p_{T} bin size is determined in this way:

- The B^+ candidates in the data sample are binned in bins of 500 MeV/c.
- Some of these bins are combined to obtain enough entries.

The bin size 500 MeV/c are changed to other value in order to estimate the effects, as shown in Table 4.20. 2% is assigned as systematic uncertainty.

Table 4.20 Effects of changing bin sizes.

Bin size (MeV/c)	Difference(%)
400	1.7
800	0.6
1000	-1.9

Table 4.21 Effects of changing bin limits.

Bin size (MeV/c)	Difference(%)
500	0.1
1500	-0.2

When combining the p_{T} bins, the low limit of entries in each bin is set to 1000 to ensure there are enough statistics. Different limits are used to get different binning to estimate the uncertainty. The effects of changing limits are shown in Table 4.21. The effect is negligible.

4.4.2 Uncertainty from the determination of efficiencies

In addition to the statistical uncertainty of the trigger efficiency obtained with the method described in Section 4.3.2, another source of uncertainty associated to the trigger is the ability of the so-called TISTOS method to reproduce the trigger efficiency accurately. The bias of this method can be estimated by comparing in Monte Carlo simulated inclusive J/ψ samples, the efficiency obtained with the TISTOS method described in Section 4.3.2, with the true trigger efficiency. Since the pre-scale in trigger doesn't affect the TISTOS method, this comparison is done with the not pre-scale TCK MC sample.

In the HLT efficiency simulation, the HLT global lines don't take into account the effects of the random trigger so that the HLT global efficiency in MC is 100%. In the extraction of MC TISTOS efficiency, "Physics" trigger lines are used instead of the "Global" line. The Physics line is defined as a combination of several HLT determinations. In the calculation of MC true efficiency, the GEC cut efficiency is excluded as well as in the TISTOS method. The relative systematic uncertainties associated to the trigger, in bins of J/ψ p_{T} and y are listed in Table 4.22.

Table 4.22 Relative systematic uncertainties ($\frac{\epsilon_{\mathrm{TISTOS\,MC}}-\epsilon_{\mathrm{direct\,MC}}}{\epsilon_{\mathrm{direct\,MC}}}$ in %) associated to the trigger efficiency, in bins of J/ψ p_{T} and y.

p_{T} (GeV/c)	$2.0 < y < 2.5$	$2.5 < y < 3.0$	$3.0 < y < 3.5$	$3.5 < y < 4.0$	$4.0 < y < 4.5$
(0.0, 2.0]	-2.8	1.8	6.5	10.4	6.6
(2.0, 3.0]	-4.3	0.8	0.8	3.8	6.4
(3.0, 4.0]	-0.1	2.4	1.1	1.3	3.6
(4.0, 5.0]	5.4	1.7	3.4	3.5	2.3
(5.0, 6.0]	5.1	0.2	4.7	-0.1	0.2
(6.0, 7.0]	2.7	1.5	2.0	0.2	-4.1
(7.0, 8.0]	-1.4	4.5	0.1	-3.0	-2.8
(8.0, 9.0]	0.2	0.6	3.1	4.6	-0.1
(9.0, 11.0]	0.5	3.7	1.1	4.9	-0.5
(11.0, 15.0]	1.4	-1.5	-0.0	-2.2	-7.9

To reduce statistical fluctuations, we merge bins with small statistics. The selected MC B^+ candidates are weighted by the inverse of these efficiencies as done for data in Section 4.3.2. Considering the correlation amongst bins, the same MC method as that for the statistical uncertainty described above in Section 4.3.2 is used to estimate the systematic uncertainty due to the trigger efficiency. Table 4.23 shows the relative systematic uncertainties associated to the trigger, in bins of B^+ p_{T}. In total, by combining all bins, 0.7% is assigned as trigger efficiency systematic uncertainty.

The uncertainty on tracking efficiency includes two components: the first one is the differences in track reconstruction efficiency between data and simulation, estimated with a tag and probe method using $J/\psi \rightarrow \mu^+\mu^-$ events as described in Section 4.3.2; the second is due to the 2% uncertainty on the hadronic interaction length of the detector used in the simulation[107].

The bin dependent uncertainty propagated from the statistical uncertainty of the efficiency ratio is discussed in Section 4.3.2. The tracking efficiency correction does not cover all the differences between data and MC, *i.e.* the differences from MC reweighting in other parameters (*e.g.* ϕ, p_{T}, VELO cluster multiplicity). To account the systematic uncertainty from these, an additional 0.7% systematic uncertainty per track (2.1% in total) is

Table 4.23 Relative systematic uncertainties (in %) associated to the trigger efficiency, in bins of B^+ p_T .

p_T (GeV/c)	Systematic uncertainty	p_T (GeV/c)	Systematic uncertainty
$(0.0, 0.5]$	6.0	$(7.0, 7.5]$	0.8
$(0.5, 1.0]$	2.1	$(7.5, 8.0]$	0.7
$(1.0, 1.5]$	1.3	$(8.0, 8.5]$	0.7
$(1.5, 2.0]$	1.3	$(8.5, 9.0]$	0.8
$(2.0, 2.5]$	1.2	$(9.0, 9.5]$	0.5
$(2.5, 3.0]$	1.0	$(9.5, 10.0]$	0.6
$(3.0, 3.5]$	0.9	$(10.0, 10.5]$	0.5
$(3.5, 4.0]$	0.8	$(10.5, 11.0]$	0.6
$(4.0, 4.5]$	1.0	$(11.0, 12.0]$	0.6
$(4.5, 5.0]$	0.8	$(12.0, 13.0]$	0.6
$(5.0, 5.5]$	0.7	$(13.0, 14.5]$	0.5
$(5.5, 6.0]$	0.7	$(14.5, 16.5]$	0.6
$(6.0, 6.5]$	0.7	$(16.5, 21.5]$	0.6
$(6.5, 7.0]$	0.7	$(21.5, 40.0]$	0.7

assigned. Besides, the hadronic interactions already give a significant contribution to the systematic uncertainty. The material in the MC simulation in front of RICH2 amounts to about 20% of hadronic interaction length. Assuming an uncertainty on the material budget of 10% gives an uncertainty per long hadron track of 2.0%. This uncertainty can be reduced if the material budget is measured to a better precision. The relative systematic uncertainty due to the tracking efficiency is then calculated by

$$\sigma_{\text{track}} = \sqrt{\sigma_{\text{stat}}^2 + (0.7\% \times 3)^2 + (2\%)^2}. \tag{4-15}$$

The relative systematic uncertainties due to tracking are listed in Table 4.24. The overall systematic uncertainty of tracking efficiency is assigned to be 4.1%.

Figure 4.22 shows the comparison of track χ^2/ndf distribution in data and MC simulation for $\mu^\pm$ and K^+. There are some differences between data and MC, which contribute to the systematic uncertainty. The uncertainty on the efficiency of a $\chi^2/\text{ndf} < 5$ cut is already included in the tracking efficiency correction and tracking uncertainty. We need to estimate the uncertainty from the $\chi^2/\text{ndf} < 4$ cut on the candidates selected by the $\chi^2/\text{ndf} < 5$ cut. For muon tracks, the difference associated to cut requirement on the χ^2/ndf of the track fit has been estimated to be 0.3%. For kaon tracks, the difference has

Table 4.24 Relative systematic uncertainties (in %) including both bin dependent and independent part associated to the tracking efficiency, in bins of B^+ p_{T}.

p_{T} (GeV/c)	Systematic uncertainty (%)	p_{T} (GeV/c)	Systematic uncertainty (%)
0.0 – 0.5	4.4	7.0 – 7.5	4.1
0.5 – 1.0	4.4	7.5 – 8.0	4.1
1.0 – 1.5	4.3	8.0 – 8.5	4.1
1.5 – 2.0	4.4	8.5 – 9.0	4.0
2.0 – 2.5	4.3	9.0 – 9.5	4.0
2.5 – 3.0	4.4	9.5 – 10.0	4.0
3.0 – 3.5	4.4	10.0 – 10.5	4.0
3.5 – 4.0	4.3	10.5 – 11.0	4.0
4.0 – 4.5	4.3	11.0 – 12.0	3.9
4.5 – 5.0	4.3	12.0 – 13.0	3.9
5.0 – 5.5	4.4	13.0 – 14.5	4.0
5.5 – 6.0	4.3	14.5 – 16.5	3.9
6.0 – 6.5	4.3	16.5 – 21.5	4.0
6.5 – 7.0	4.2	21.5 – 40.0	4.2

been estimated to be 0.1%. The effects are negligible.

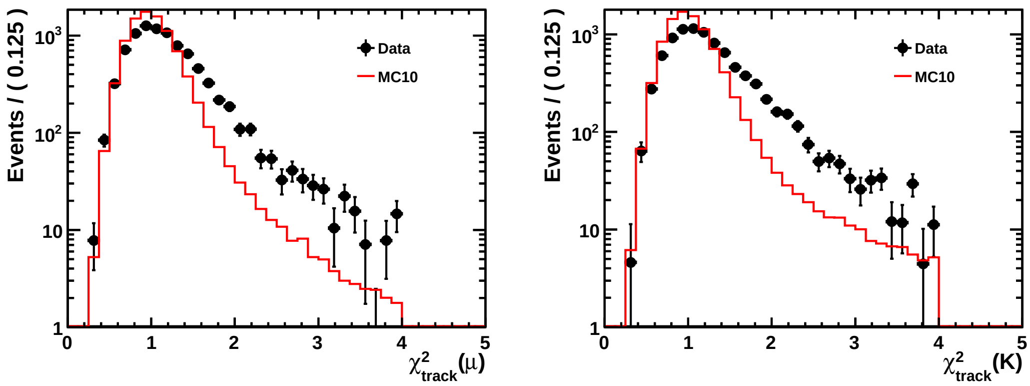

Figure 4.22 Comparison of track χ^2/ndf distributions in real data and MC simulation for *left*: μ and *right*:K. The data distributions are background subtracted.

Removing the clone rejection cut, the pseudo-efficiency of this cut is (98.4 ± 2.2)%, to be compared with (98.33 ± 0.02)% in MC simulation as shown in Table 4.10, no systematic uncertainty is assigned due to the clone rejection.

Figure 4.23 shows the comparison of vertex fit χ^2/ndf distribution in background subtracted data and MC for J/ψ and B^+. Obvious differences can be observed between these distributions in data and MC simulation samples. Since the stripping selection cuts have introduced a cut on the vertex fit quality using B^+ reconstructed from the inclusive J/ψ data, the vertex χ^2/ndf cuts of B^+ and J/ψ are relaxed from < 9 to < 50 at the same time, the fitted number of signal changed from (4291 ± 84) to (4456 ± 115). This ends with a conditional efficiency $\varepsilon(\chi^2/\mathrm{ndf} < 9 | \chi^2/\mathrm{ndf} < 50) = (96.3 \pm 0.3)\%$, while it is (97.26 ± 0.02) in MC. 1% is assigned as systematic uncertainty.

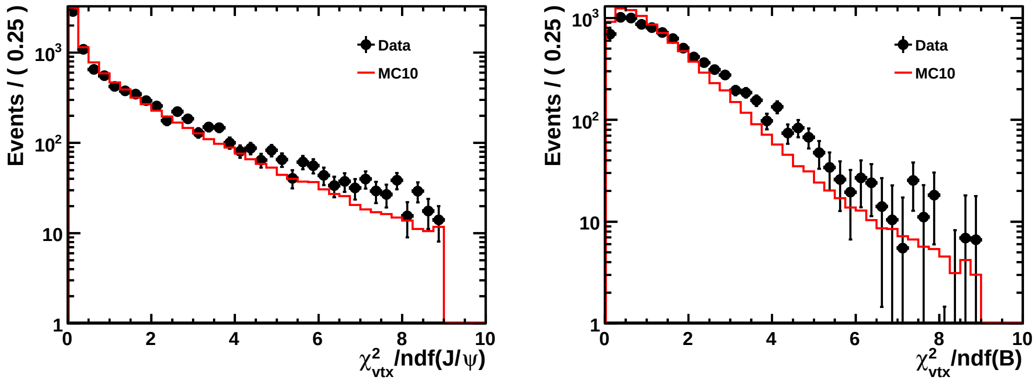

Figure 4.23 Comparison of vertex χ^2/ndf distributions in data and MC simulation for *left*: J/ψ and *right*: B^+. The data distributions are background subtracted.

As shown in Table 4.10, the efficiency of the J/ψ mass window cut $(3.04, 3.14]$ GeV/c^2 is only $(93.74 \pm 0.03)\%$, this inefficiency is mostly due to the final states radiation. A study is performed at the generator level using the $B^+ \to J/\psi K^+$ MC simulation sample, the true quantities of $J/\psi \to \mu^+\mu^-$ are smeared with the typical mass resolution of J/ψ, 10 MeV/c^2. When considering the final states radiation, *i.e.* using the invariant mass of $\mu^+\mu^-$ and smearing it with the resolution, the mass distributions in the full mass region, and in the J/ψ signal mass window are shown in Figure 4.24, one can easily get an efficiency of $(93.53 \pm 0.02)\%$. Changing the mass resolution to 15 MeV/c^2 ends with $(93.30 \pm 0.02)\%$, *i.e.* even the mass resolution of the data is worse by 50% than the MC simulation, the efficiency is only changed by 0.23%. Also, since the momentum scale may be different, say, by -5 MeV/c^2 in data, this is equivalent to change the mass window to $(3.045, 3.145]$ GeV/c^2, there is no visible effect with the current statistics. One can conclude that the differences of the mass resolution and momentum scale between data and MC have very small impact on the efficiency of the J/ψ mass window cut, so such effect will be neglected. As a further check that the inefficiency is mostly due to the final states radiation, the true J/ψ mass (with photons integrated) is smeared instead of the $\mu^+\mu^-$ mass, by 15 MeV/c^2, the efficiency of the mass window cut $(3.04, 3.14]$ GeV/c^2 is $(99.7952 \pm 0.0045)\%$.

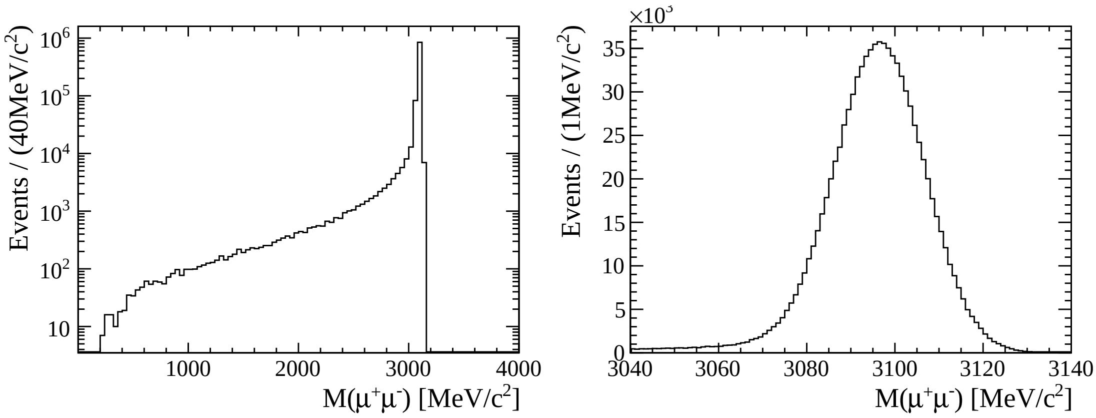

Figure 4.24 J/ψ mass distribution with final states radiation enabled for *left*: full mass range and *right*: J/ψ mass window, extracted from MC generator level simulation sample.

Systematic uncertainty associated with the GEC is estimated by comparing the GEC efficiency extracted by the overlaying method and true efficiency in MC10 simulation sample. The procedure described in Section 4.3.2 is repeated to extract the GEC efficiency. The total distribution of VCM using the overlaying method in MC sample and a comparison with VCM distribution directly extracted from the MC sample are shown in Figure 4.25. The VCM efficiency from MC using the overlaying method is 94.85±0.05%.

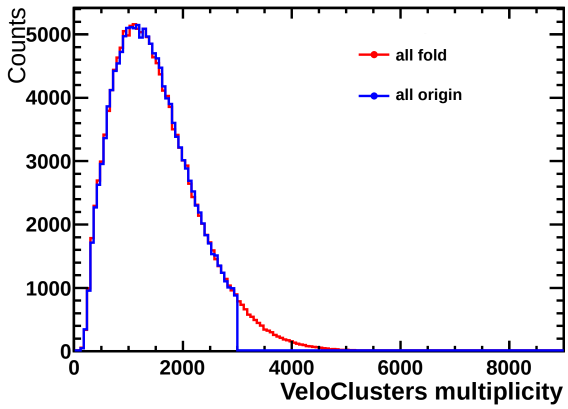

Figure 4.25 The MC VCM distribution from direct MC (blue) and the overlaying method (red).

Comparing with the efficiency directly from MC sample which is equal to $95.20 \pm 0.05\%$, the difference of the two efficiencies is 0.4%. It is assigned as systematic uncertainty due to the GEC efficiency.

To check the validity of the GEC efficiency estimation, the distribution of VCM is fitted with a Gamma function[108] and the number of events above the VCM threshold (3000) is estimated from the integral of the fit function between 3000 and $+\infty$. Figure 4.26 (left) shows the result of the fit on the background subtracted data distribution and Figure 4.26 (right) shows the result of the fit on the MC distribution for events on which GEC are not applied. From the Gamma function, the VCM cut efficiency for data

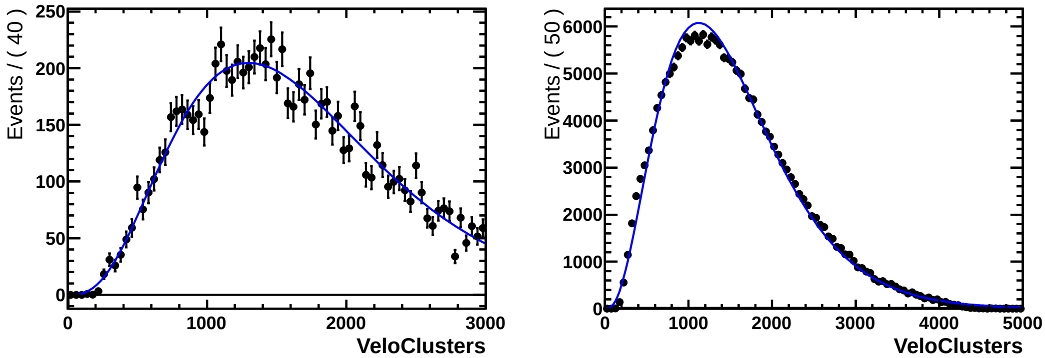

Figure 4.26 Gamma function fit to *left*: the background subtracted distribution of VCM in real data and *right*: the signal distribution in MC simulation.

is equal to 92.3 ± 0.4%, while the efficiency for the MC sample is equal to 95.0 ± 0.3%. These results are in good agreement with those from overlying method.

The uncertainty on the muon identification efficiency is extracted by a "tag and probe" method, as described in Ref.[12]. A value equal to 2.5% is taken as systematic uncertainty associated with the efficiency of the μ identification used in the J/ψ selection.

We smear the p_{T} distribution in the generator level sample and check the variation of acceptance efficiency. The effects are listed in Appendix B.3. The effects are found to be negligible.

4.4.3 Uncertainty from the determination of branching fractions

The values of $\mathcal{B}(B^{+} \to J/\psi K^{+}) = (1.013 \pm 0.034) \times 10^{-3}$ and $\mathcal{B}(J/\psi \to \mu^{+}\mu^{-}) = 5.93 \pm 0.06\%$ used for the measurement are extracted from the Particle Data Group review[28].

The correlations between the two branching ratios are estimated from the most precise measurement of $\mathcal{B}(B^{+} \to J/\psi K^{+}) = (1.061 \pm 0.015 \pm 0.048) \times 10^{-3}$ made by the BaBar Collaboration[109]. Using this branching ratio and $\mathcal{B}(J/\psi \to \mu^{+}\mu^{-}) = 5.88 \pm 0.1\%$ for the BaBar measurement, the uncertainty on the product of the two branching fractions directly is 4.6%. The systematic uncertainty $\Delta_{\mathcal{B}_{B^{+}} \times \mathcal{B}_{J/\psi}}$ on the product of the two branching fractions extracted from the uncertainty propagation formula

$$\Delta^{2}_{\mathcal{B}(B^{+} \to J/\psi K^{+})} = \left(\frac{\Delta_{\mathcal{B}_{B^{+}} \times \mathcal{B}_{J/\psi}}}{\mathcal{B}_{J/\psi}}\right)^{2} + \left(\frac{\Delta_{\mathcal{B}_{J/\psi}} \times \mathcal{B}_{B^{+}}\mathcal{B}_{J/\psi}}{\mathcal{B}^{2}_{J/\psi}}\right)^{2}$$

is 4.2%. Combining this systematic uncertainty with the statistical part 1.4%, The total uncertainty on the product of the two branching fractions from BaBar measurement is 4.4%. The product of the two branching fractions from PDG is 3.5%. Since the PDG average is dominated by BaBar measurement, the uncertainty on the product of the two branching fractions from PDG is scaled to be equal to $3.5\% \times \frac{4.4}{4.6} = 3.3\%$

4.4.4 Uncertainty from the determination of luminosity

As discussed in Section 4.3.3, the absolute luminosity scale is measured with a 3.5% uncertainty[105], dominated by the beam current uncertainty.

4.4.5 Other systematic check

The analysis procedures are repeated to check the effect of magnet polarity and kaon charge asymmetry. The results are shown in Table. 4.25. The results are nominal cross-sections and only used to make comparison. The uncertainties only contain statistic uncertainties. No obvious difference between two magnet polarities or kaon charges are found.

Table 4.25 Effects of magnet polarity and charge asymmetry.

Magnet polarity	Kaon charge	Results (μb)
Up	K^+	19.9 ± 1.0
Up	K^-	17.9 ± 0.9
Down	K^+	18.3 ± 1.0
Down	K^-	18.9 ± 1.0

The B^+ candidates are binned in rapidity using ${}_sWeight$ which depends on the mass of B^+. The efficiency dependence on the mass of B^+ candidate is checked. The average inverse efficiency $< \frac{1}{\epsilon} >$ distribution as a function of B^+ mass and the results of a linear fit to the distribution are illustrated in Figure 4.27. The distribution of average inverse efficiency in the sideband region is flat, thus there is no obvious efficiency dependence on the B^+ mass. In the signal region, since the signal has harder p_T spectrum, hence larger efficiency, the values should be lower than sidebands.

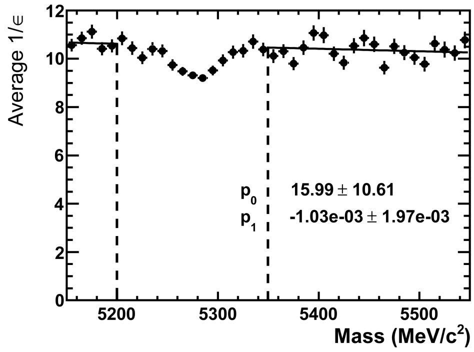

Figure 4.27 The $< \frac{1}{\epsilon} >$ distribution as a function of B^{+} mass. The results of a linear fit, with the constant p_0 and the slope p_1, are superimposed.

4.4.6 Systematic uncertainty summary

The systematic uncertainties that affect the cross-section measurement are summarized 2
in Table 4.26.

Table 4.26 Summary of systematic uncertainties.

Quantity	Systematic uncertainty (%)
Trigger efficiency	from 0.5 to 6.0
Muon identification	2.5
Vertex χ^2/ndf cut	1.0
Branching ratio	3.3
Signal fit model	1.5
Bin size	2.0
Luminosity	3.5
Tracking efficiency	from 3.9 to 4.4
Clone rejection	< 0.1
GEC	0.4
J/ψ mass window	0.2
Cabibbo suppressed background	0.6
Cross-feed	0.5
Fit range	0.5
Multi candidates	0.8
Track χ^2/ndf cut(the part from < 5 to < 4)	0.4
Total(Bin independent)	6.8

4.5 Results and discussion

The differential cross-section in bins of p_T is given in Table 4.27, for $2 < y < 4.5$. In this table, the first uncertainty is statistical and the second is systematic.

Table 4.27 Differential cross-section in bins of p_T.

p_T (GeV/c)	$d\sigma/dp_T$ (μb/(GeV/c))	p_T (GeV/c)	$d\sigma/dp_T$ (μb/(GeV/c))
0.0 – 0.5	1.37 ± 0.68 ± 0.13	7.0 – 7.5	2.42 ± 0.20 ± 0.18
0.5 – 1.0	3.12 ± 0.82 ± 0.24	7.5 – 8.0	2.09 ± 0.16 ± 0.15
1.0 – 1.5	3.90 ± 0.57 ± 0.29	8.0 – 8.5	1.44 ± 0.11 ± 0.11
1.5 – 2.0	5.67 ± 1.05 ± 0.43	8.5 – 9.0	1.33 ± 0.11 ± 0.10
2.0 – 2.5	8.44 ± 1.00 ± 0.64	9.0 – 9.5	1.22 ± 0.10 ± 0.09
2.5 – 3.0	6.33 ± 0.66 ± 0.48	9.5 – 10.0	0.83 ± 0.08 ± 0.06
3.0 – 3.5	5.04 ± 0.45 ± 0.38	10.0 – 10.5	0.80 ± 0.08 ± 0.06
3.5 – 4.0	6.99 ± 0.68 ± 0.52	10.5 – 11.0	0.65 ± 0.07 ± 0.05
4.0 – 4.5	5.48 ± 0.47 ± 0.41	11.0 – 12.0	0.54 ± 0.04 ± 0.04
4.5 – 5.0	6.54 ± 0.79 ± 0.49	12.0 – 13.0	0.41 ± 0.04 ± 0.03
5.0 – 5.5	4.42 ± 0.44 ± 0.33	13.0 – 14.5	0.28 ± 0.02 ± 0.02
5.5 – 6.0	4.16 ± 0.37 ± 0.31	14.5 – 16.5	0.17 ± 0.02 ± 0.01
6.0 – 6.5	3.40 ± 0.24 ± 0.25	16.5 – 21.5	0.062 ± 0.005 ± 0.005
6.5 – 7.0	2.82 ± 0.22 ± 0.21	21.5 – 40.0	0.011 ± 0.001 ± 0.001

The integrated cross-section of B^+ production over the fiducial region is equal to

$$\sigma(B^+, 2 < y < 4.5) = 41.4 \pm 1.4\,(\text{stat.}) \pm 3.2\,(\text{syst.})\ \mu\text{b}. \tag{4-16}$$

Figure 4.28 shows the measured differential cross-section and the cross-section in the LHCb simulation. As also observed in other measurements of the $b\bar{b}$ cross-section at LHCb, the cross-section in the LHCb simulation is a factor 2 higher than the one in data[11,12]. However, the p_T shapes are in good agreement.

The cross-section measurement obtained in this analysis is compared with a FONLL prediction[4,5,49] in Figure 4.29. The uncertainty of the FONLL computation includes the uncertainty of b-quark mass, renormalization/factorization scales, and the PDF uncertainty. Two different hadronisation fractions $f_{\bar{b}\to B^+}$ are assumed to fix the overall scale, one of which is 40.1 ± 1.3%[28], and the other is 33.7 ± 2.2% as discussed in Section 4.5. Good

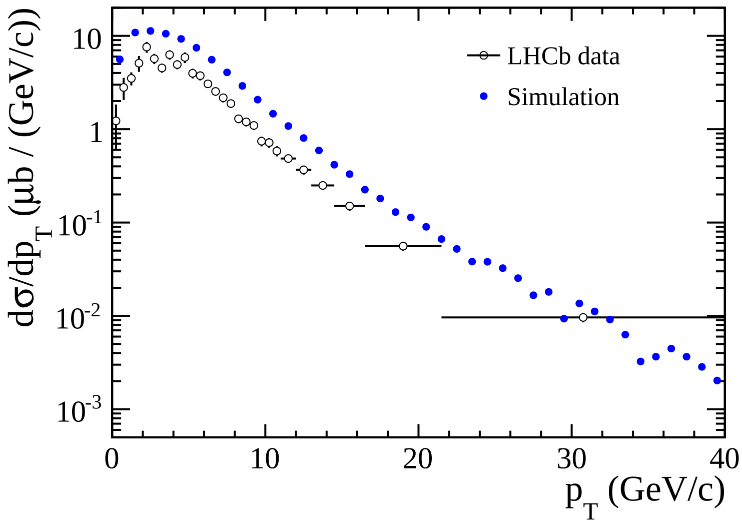

Figure 4.28 Differential production cross-section for B^+ as a function of the transverse momentum, in the LHCb simulation (blue) and in data (black).

agreement is observed between data and the FONLL prediction. Comparisons in other

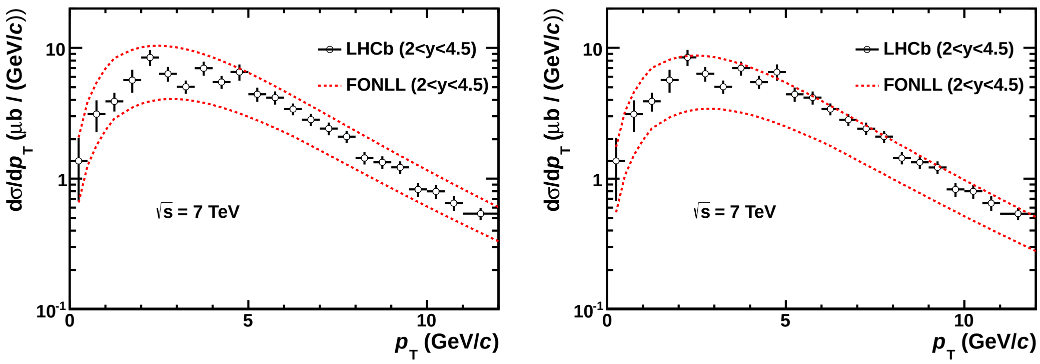

Figure 4.29 Differential production cross-section as a function of the B^+ transverse momentum [99]. The black dots with error bars are the LHCb measured values presented in this dissertation, the red dashed lines are the upper and lower uncertainty limits of the FONLL computation. The uncertainty of the FONLL computation includes the uncertainty of b-quark mass, renormalization/factorization scales, and the PDF uncertainty. The hadronisation fractions for left: $f_{\bar{b}\to B^+}$ of $40.1 \pm 1.3\%$ [28] and for right: $f_{\bar{b}\to B^+}$ of $33.7 \pm 2.2\%$ extracted in Section 4.5 are assumed to fix the overall scale.

two wider p_{T} ranges are demonstrated in Figure 4.30. The hadronisation fraction $f_{\bar{b}\to B^+}$ used is $40.1 \pm 1.3\%$ [28]. Except for the last p_{T} bin, $21.5 < p_{\mathrm{T}} < 40\,\mathrm{GeV}/c$, all the data points are located inside the theoretical uncertainty limits. Since the signal yield in the last p_{T} bin, $21.5 < p_{\mathrm{T}} < 40\,\mathrm{GeV}/c$, is very limited, it is difficult to determine the position of the data point. The discrepancy can be clarified with more statistics in 2011 data.

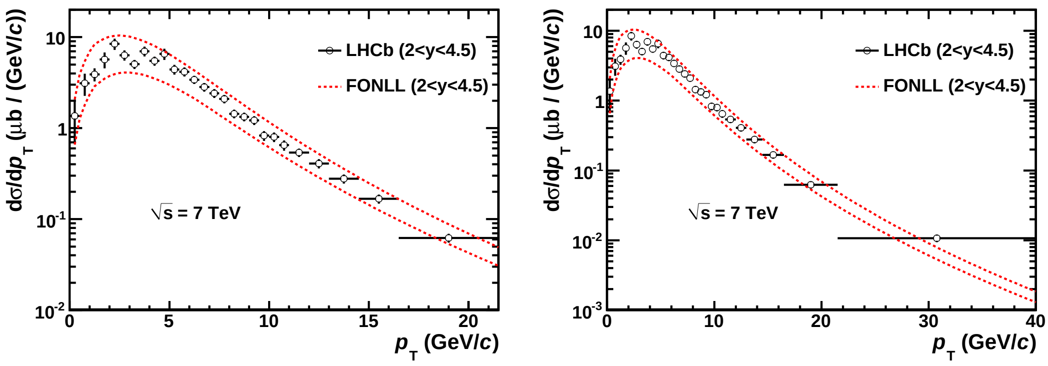

Figure 4.30 Differential production cross-section as a function of the B^+ transverse momentum. The black dots with error bars are the LHCb measured values presented in this dissertation, the red dashed lines are the upper and lower uncertainty limits of the FONLL computation. The uncertainty of the FONLL computation includes the uncertainty of b-quark mass, renormalization/factorization scales, and the PDF uncertainty. The hadronisation fractions $f_{\bar{b}\to B^+}$ of $40.1 \pm 1.3\%$[28] are assumed to fix the overall scale. The left plot shows the comparison in p_{T} range $[0, 21.5]$ GeV/c, while the right in p_{T} range $[0, 40]$ GeV/c

The result quoted in Equation 4-16 is extrapolated to 4π polar angle range by

$$\sigma(pp \to b\bar{b}X) = \frac{\alpha_{4\pi}\sigma(B^+, y \in [2, 4.5])}{2 \times f_{\bar{b}\to B^+}}, \tag{4-17}$$

where the $\alpha_{4\pi} = 5.14$ is the ratio of the number of B^+ in the full rapidity range to that in the $2.0 < y < 4.5$ region from FONLL computation and the $f_{\bar{b}\to B^+} = 40.1\%$ is the hadronisation fraction. The result is

$$\sigma(pp \to b\bar{b}X) = 266 \pm 9 \pm 20 \pm 9 \pm 12\,\mu\text{b}, \tag{4-18}$$

where the first uncertainty is statistical, the second is systematic from original $\sigma(B^+)$ measurement, the third is systematic from the uncertainty on $f_{\bar{b}\to B^+}$ and the fourth is systematic from the uncertainty on $\alpha_{4\pi}$. The uncertainty due to the extrapolation to 4π is estimated by comparing the result of the FONLL calculation (5.14) to the Pythia and EvtGen estimate (5.39). The extrapolated result is in good agreement with other two LHCb measurements: $255 \pm 4 \pm 43\mu$b[12] and $272 \pm 19 \pm 47\mu$b[11].

The b hadronization fractions have been measured recently by the LHCb collaboration[110] as

$$\begin{aligned} f_s/f_d &= 0.267^{+0.021}_{-0.020}, \\ \frac{f_{\Lambda_b}}{f_u + f_d} &= (0.404 \pm 0.017 \pm 0.027 \pm 0.105) \\ &\quad \times [1 - (0.031 \pm 0.004 \pm 0.003) \times p_{\mathrm{T}}(\mathrm{GeV/c})]. \end{aligned} \tag{4-19}$$

By this result, a estimation for hadronization fraction for B^+ can be given. The average p_T of Λ_b in the region $p_T \in (0, 14)$ GeV/c and $\eta \in (2, 5)$ is estimated by PYTHIA to be 4.2 GeV/c. Assuming $f_u = f_d$ and ignoring the B_c and other b hadrons, *i.e.* constraining $f_u + f_d + f_s + f_{\Lambda_b} = 1$, one can obtain $f_u = 0.337 \pm 0.022$. f_u is changed by only 1% if varying the average p_T of Λ_b by 20%. Then the extrapolated result using $\alpha_{4\pi}$ from PYTHIA is,

$$\sigma(pp \to b\bar{b}X) = 332 \pm 12 \pm 24 \pm 22 \pm 16 \mu\text{b}, \tag{4-20}$$

where the first uncertainty is statistical, the second is systematic from original $\sigma(B^+)$ measurement, the third is systematic from the uncertainty on $f_{\bar{b}\to B^+}$ and the fourth is systematic from the uncertainty on $\alpha_{4\pi}$. This is to be compared with the two LHCb measurements extrapolated with PYTHIA: $288 \pm 4 \pm 48\,\mu$b[12] and $284 \pm 20 \pm 49\,\mu$b[11]. And as discussed in Ref.[11], the latter would go up by 19% if using the b production fractions from TEVATRON, *i.e.* to $338 \pm 24 \pm 58\,\mu$b, and even higher if using the b hadronization fractions measured by LHCb①. The extrapolation results are summarized in Table 4.28.

Table 4.28 The extrapolation results with b hadronization fractions from PDG and LHCb, and extrapolation factor from FONLL and PYTHIA. The first uncertainty is statistical, the second is systematic from original $\sigma(B^+)$ measurement, the third is from the uncertainty on $f_{\bar{b}\to B^+}$ and the fourth is from the uncertainty on $\alpha_{4\pi}$.

	PDG b hadronization fraction	LHCb b hadronization fraction
FONLL α	$266 \pm 9 \pm 20 \pm 9 \pm 12\,\mu$b	$316 \pm 11 \pm 23 \pm 21 \pm 14\,\mu$b
PYTHIA α	$278 \pm 10 \pm 20 \pm 9 \pm 13\,\mu$b	$332 \pm 12 \pm 24 \pm 22 \pm 16\,\mu$b

① Compared to TEVATRON fractions on HFAG[111], the f_u is almost the same, while the f_s is smaller and f_{Λ_b} is larger.

Chapter 5 Measurements of B meson production cross-sections with 2011 data

Measurements of the total and differential production cross-sections for B^+, B^0 and B_s^0 using data collected by the LHCb detector in 2011 are given in this chapter. The total production cross-section is calculated by integrating the differential cross-section. The differential cross-sections are obtained from these formulas

$$\begin{aligned}
\frac{d^2\sigma(B^+)}{dp_T dy} &= \frac{N_B(p_T, y)}{\mathcal{L}_{int}\epsilon_{tot}(p_T, y)\mathcal{B}(B^+ \to J/\psi K^+)\mathcal{B}(J/\psi \to \mu^+\mu^-)\Delta p_T \Delta y}, \\
\frac{d^2\sigma(B^0)}{dp_T dy} &= \frac{N_B(p_T, y)}{\mathcal{L}_{int}\epsilon_{tot}(p_T, y)\mathcal{B}(B^0 \to J/\psi K^{*0})\mathcal{B}(J/\psi \to \mu^+\mu^-)\mathcal{B}(K^{*0} \to K^+\pi^-)\Delta p_T \Delta y}, \\
\frac{d\sigma(B_s^0)}{dp_T} &= \frac{N_B(p_T)}{\mathcal{L}_{int}\epsilon_{tot}(p_T)\mathcal{B}(B_s^0 \to J/\psi \phi)\mathcal{B}(J/\psi \to \mu^+\mu^-)\mathcal{B}(\phi \to K^+K^-)\Delta p_T}. \qquad (5\text{-}1)
\end{aligned}$$

$N_B(p_T)$ is the number of reconstructed signal in a given p_T bin, while $N_B(p_T, y)$ the number in a given (p_T,y) bin. $\mathcal{L}_{int}$ is the integrated luminosity. $\epsilon_{tot}(p_T)$ and $\epsilon_{tot}(p_T, y)$ are the total efficiencies, including acceptance, reconstruction, selection and trigger effects. $\mathcal{B}$ are the branching fractions. Δp_T and Δy are the p_T and y bin width. The determinations of all these quantities are discussed in this chapter.

We start with the data samples and corresponding triggers in Section 5.1. The event selection requirements are outlined in Section 5.2. The determinations of the quantities quoted in Equation 5-1 are presented in Section 5.3 and the systematic uncertainties on these parameters are discussed in Section 5.4. At last, Section 5.5 presents the results and some discussions.

5.1 Samples and trigger

These analyses use $370 \pm 13\,\text{pb}^{-1}$ of pp collision data taken at the LHC at a center-of-mass energy of 7 TeV between March and July 2011. The data were collected using 11 different TCKs, with different settings than the ones used in 2010. During these periods all sub-detectors were functional and operating in a stable condition.

The MC simulation samples used in this analysis were generated using the same configurations “MC10” as described in Section 4.1, taking the different trigger conditions into account.

The trigger settings used in 2011 are summarized in Table 5.1. The L0 trigger in this analysis still uses only information from the muon system. At this stage either a single muon candidate with p_{T} larger than $1.48\,\mathrm{GeV}/c$ or pair of candidates with the product of their p_{T} larger than $1.68(\mathrm{GeV}/c)^2$ is required. The HLT1 trigger confirms the single-muon or dimuon candidates from L0 and requires their combined mass to be greater than $2.7\,\mathrm{GeV}/c^2$, momentum higher than $6\,\mathrm{GeV}/c$ and transverse momentum higher than $0.5\,\mathrm{GeV}/c$. The HLT2 trigger selects events containing two oppositely charged muon candidates with an invariant mass in the mass range $2.977 - 3.217\ \mathrm{GeV}/c^2$.

Table 5.1 Summary of the trigger lines used for this analysis.

Trigger line	Main cuts
L0Muon	Spd(Mult)< 600 && $p_{\mathrm{T}}(\mu) > 1.48\,\mathrm{GeV}/c$
L0DiMuon	Spd(Mult)< 900 && $p_{\mathrm{T}}(\mu_1) \times p_{\mathrm{T}}(\mu_2) > 1.68(\mathrm{GeV}/c)^2$
Hlt1DiMuonHighMass	*L0Muon* or *L0DiMuon*
	$p_{\mathrm{T}}(\mu) > 0.5\,\mathrm{GeV}/c$ and $p(\mu) > 6\,\mathrm{GeV}/c$
	$M_{\mu\mu} > 2.7\,\mathrm{GeV}/c^2$
Hlt2DiMuonJPsi	$M_{\mu\mu} \in [M_{J/\psi} - 120\,\mathrm{MeV}/c^2; M_{J/\psi} + 120\,\mathrm{MeV}/c^2]$,

Some global event cuts were relaxed in 2011 data-taking to suit the higher multiplicities caused by the higher luminosity than 2010, *e.g.* the cut on the VELO cluster multiplicity (VCM) and the OT cluster multiplicity in 2010 had been too tight, thus they were relaxed in 2011. During the start of 2011 data-taking, the cut on VCM was over adjusted while the cut on OT cluster multiplicity was adjusted insufficiently. After May 3, the OT cluster multiplicity cut was relaxed and the VCM cut was tighten. The global event cuts used in 2011 data-taking are summarized in Table 5.2.

5.2 Event selection

The selection cuts on the J/ψ candidates are the same as described in Section 4.2, for all three channels. The stripping and final selection cuts on all the J/ψ candidates are listed in Table 5.3.

The $B^0 \to J/\psi\, K^{*0}$ and $B_s^0 \to J/\psi\, \phi$ decay channels have one more final state particle

Table 5.2 Summary of global event cuts (GEC) in 2011 data taking.

Trigger level	GEC	Cut value
L0	SPD hit multiplicity	< 900
HLT1	VELO cluster multiplicity	< 10000 before adjustment
		< 6000 after adjustment
	IT cluster multiplicity	< 3000
	OT cluster multiplicity	< 10000 before adjustment
		< 15000 after adjustment
HLT2	VELO track multiplicity	< 350

Table 5.3 The stripping and selection cuts on the J/ψ candidates.

Decay mode	Variable	Stripping cut	Selection cut
$J/\psi \to \mu^+\mu^-$	μ track	Long and isMuon	-
	$\mu\ p_{\mathrm{T}}$	-	$> 700\,\mathrm{MeV}/c$
	μ track χ^2/ndof	-	< 4
	$\mu\ \Delta\ln L_{\mu\pi}$	> 0	-
	Clone distance	-	< 0
	Mass window	$3017 < M_{\mu\mu} < 3177\,\mathrm{GeV}/c^2$	$3040 < M_{\mu\mu} < 3140\,\mathrm{GeV}/c^2$
	vertex fit χ^2/ndf	< 16	< 9

than the $B^+ \to J/\psi K^+$ channel, thus the combinatorial background levels of these two channels after stripping selections are much higher, as shown in Appendix A.3. In general, the combinatorial background candidates are composed of particles with lower p_{T}, and have worse vertex fit quality than signal candidates, due to the random combination by coincidence. Transverse momentum and vertex fit quality cuts on K^{*0} are applied to reduce these backgrounds. Another important handle to suppress the background uses the combined hadron identification variable $\mathrm{DLL}_{K\pi}$ defined in Section 3.2.4.

The J/ψ candidates are combined with a K^+, K^{*0} and ϕ to form a B^+, B^0 and B_s^0 meson, respectively. A vertex fit is performed that constrains the daughter J/ψ and to originate from a common point and the mass of the muon pair to match the nominal J/ψ mass. It is required that the χ^2/ndf of this fit is less than nine. To further reduce the combinatorial background due to particles produced in the primary pp interaction only candidates with a proper time larger than 0.3 ps are used. Finally, the fiducial requirement used in the analysis $2.0 < y < 4.5$ is applied.

The stripping and final selection cuts on K^+, K^{*0} and ϕ as well as their mother B mesons are listed in Table 5.4, 5.5 and 5.6. The selection cuts on $B^+ \to J/\psi K^+$

Table 5.4 The stripping and selection cuts of B^+ candidates.

Decay mode	Variable	Stripping cut	Selection cut
K^+	track χ^2/ndof	< 5	< 4
	K^+ p_{T}	-	$> 500\,\mathrm{MeV}/c$
	Clone distance	-	< 0
	$M(B^+)$	$[5100, 5550]\mathrm{MeV}/c^2$	$[5150, 5550]\mathrm{MeV}/c^2$
$B^+ \to J/\psi K^+$	vertex χ^2/ndof	< 10	< 9
	life time	> 0.15ps	> 0.3ps

candidates are the same as the 2010 analysis, so that it is easier to compare. A transverse momentum cut on the B^0 candidates is applied to reduce the background with low p_{T}.

5.3 Cross-section determination

The differential cross-sections are determined by Equation 5-1. The numbers of reconstructed signal B^+ and B^0 candidates are obtained from fits to their invariant mass distri-

Table 5.5 The stripping and selection cuts of B^0 candidates.

Decay mode	Variable	Stripping cut	Selection cut
$K^{*0} \to K^+\pi^-$	K, π track χ^2/ndof	< 5	< 4
	K, π clone distance	-	< 0
	K $\Delta \ln L_{K\pi}$	> -2	> 0
	K^{*0} p_{T}	$> 500\,\mathrm{MeV}/c$	$> 1\,\mathrm{GeV}/c$
	$M(K^+\pi^-)$	$[826, 966]\,\mathrm{MeV}/c^2$	$[826, 966]\,\mathrm{MeV}/c^2$
	K^{*0} vertex χ^2/ndof	< 16	-
	$M(B^0)$	$[5100, 5550]\,\mathrm{MeV}/c^2$	$[5150, 5400]\mathrm{MeV}/c^2$
$B^0 \to J/\psi\, K^{*0}$	vertex χ^2/ndof	< 10	< 9
	life time	> 0.15ps	> 0.3ps
	B^0 p_{T}	-	$> 2\,\mathrm{GeV}/c$

Table 5.6 The stripping and final selection cuts of B_s^0 candidates.

Decay mode	Variable	Stripping cut	Selection cut
$\phi \to K^+K^-$	K track χ^2/ndof	< 5	< 4
	K clone distance	-	< 0
	K $\Delta \ln L_{K\pi}$	> -2	> 0
	ϕ p_{T}	$> 500\,\mathrm{MeV}/c$	$> 1\,\mathrm{GeV}/c$
	$M(KK)$	$[980, 1050]\,\mathrm{MeV}/c^2$	$[1008, 1032]\,\mathrm{MeV}/c^2$
	ϕ vertex χ^2/ndof	< 16	-
	$M(B_s^0)$	$[5100, 5550]\mathrm{MeV}/c^2$	$[5150, 5550]\mathrm{MeV}/c^2$
$B_s^0 \to J/\psi\, \phi$	vertex χ^2/ndof	< 10	< 9
	life time	> 0.15ps	> 0.3ps

butions. Since there are enough candidates in 2011 data, the fits for B^+ and B^0 are made in bins of p_{T} and y. For B_s^0 the fit is still made in p_{T} bins and the $_s\mathcal{P}lot$ technique in Chapter 4 is used. The determinations of efficiency and luminosity follow similar methods as 2010 B^+ analysis.

5.3.1 Signal yield determination

Considering that the efficiencies depend on the y distribution, we estimate the signal yield in bins of p_{T} and y. The signal yield is extracted by a fit to the B meson mass distribution, and is corrected for the background which can't be separated from the signal by the mass fit.

In each p_{T} and y bin, we perform an extended unbinned maximum likelihood fit to the invariant mass distribution of the reconstructed B candidates in the interval $5.15 < M_B < 5.55\,\mathrm{GeV}/c^2$ for B^+ and $5.15 < M_B < 5.40\,\mathrm{GeV}/c^2$ for B^0. For B_s^0, since the event yield is not large enough to make a fit in bins of p_{T} and y, we perform the fit to the invariant mass distribution in each p_{T} bin in the interval $5.15 < M_{B_s^0} < 5.55\,\mathrm{GeV}/c^2$ and use $_s\mathcal{W}eights$ to extract the event yield in bins of p_{T} and y.

Two components are included in the fit procedure: the signal and background. Besides the FSR tails on the left side of the mass peak, tail shapes are also found on the right side, which are caused by the FSR and J/ψ mass constrain method in the reconstruction. The signal component of each decay channel is described by a Cruijff function, which is a modified Gaussian function with various resolutions and tail shapes on both sides. The Cruijff function is defined as

$$F_{\mathrm{Cruijff}}\left(x; M, \sigma_{\mathrm{left}}, \alpha_{\mathrm{left}}, \sigma_{\mathrm{right}}, \alpha_{\mathrm{right}}\right) = \begin{cases} \dfrac{1}{\sqrt{2\pi}\sigma_{\mathrm{left}}} e^{-\frac{(x-M)^2}{2\sigma^2_{\mathrm{left}}+\alpha_{\mathrm{left}}(x-M)^2}} & x < M \\ \dfrac{1}{\sqrt{2\pi}\sigma_{\mathrm{right}}} e^{-\frac{(x-M)^2}{2\sigma^2_{\mathrm{right}}+\alpha_{\mathrm{right}}(x-M)^2}} & x > M. \end{cases} \tag{5-2}$$

where M is the fitted mass, σ_{left} and σ_{right} the left and right resolutions of the mass peak, respectively. These two resolutions are set to be the same value σ. The α_{left} and α_{right} parameters define the tail shape of the function, which are correlated with the signal mass resolution σ. The relations between α and the resolution are obtained from fits to the mass distribution of a Gaussian smeared generator level MC simulation event sample. The parameterizations of α as a function of mass resolution are shown in Figure 5.1, 5.2

and 5.3.

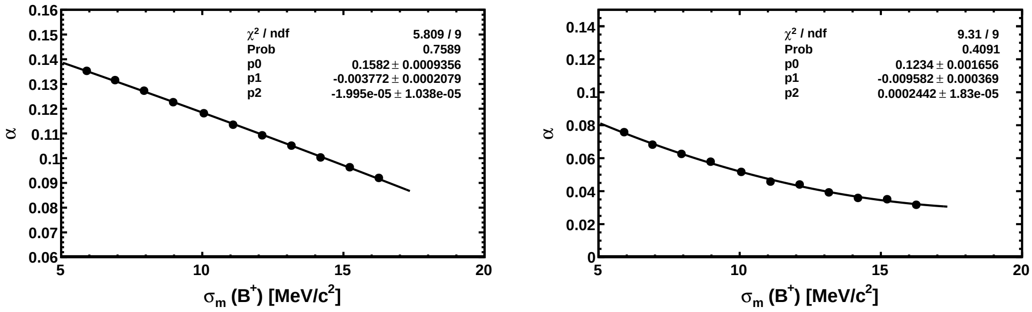

Figure 5.1 Parameterizations of Cruijff parameter *left*: α_{left}, *right*: α_{right} for B^+ as a function of mass resolution.

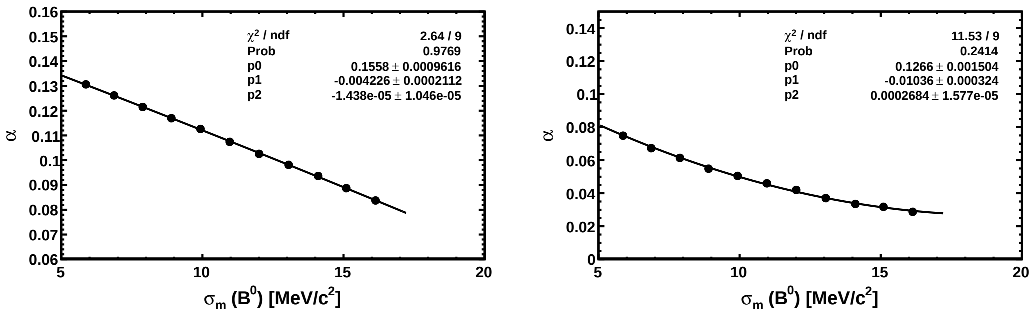

Figure 5.2 Parameterizations of Cruijff parameter *left*: α_{left}, *right*: α_{right} for B^0 as a function of mass resolution.

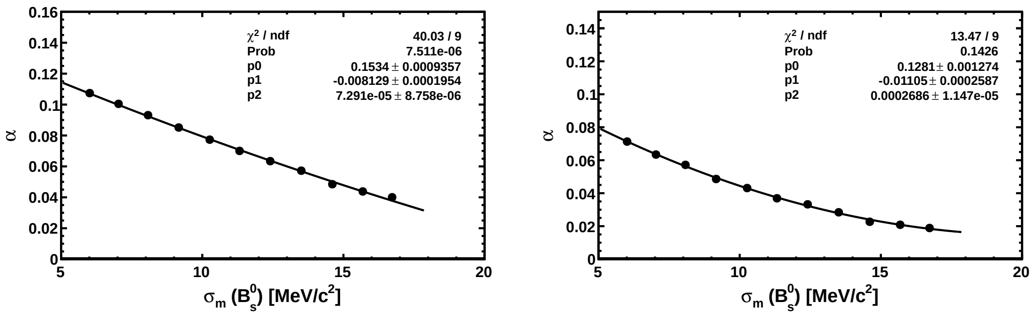

Figure 5.3 Parameterizations of Cruijff parameter *left*: α_{left}, *right*: α_{right} for B_s^0 as a function of mass resolution.

The background component of the fit function may include two different sources: the combinatorial and the partial reconstructed backgrounds. The combinatorial background for each channel is described by an exponential function as described in Section 4.3.1. For B^+, a double Crystal Ball function is used to describe the effects of the Cabibbo-suppressed decay $B^+ \to J/\psi\pi^+$ in the same way as in the 2010 analysis. The total fit function for B^+ is then defined by changing the Gaussian signal $F_{\mathrm{signal}}(x; M, \sigma)$ to the Cruijff signal $F_{\mathrm{signal}}(x; M, \sigma, \alpha_{\mathrm{left}}, \alpha_{\mathrm{right}})$ in Equation 4-7. The total fit function for B^0 and B_s^0 is

$$\begin{aligned} & F_{\mathrm{mass}}\left(x; M, \sigma, \alpha_{\mathrm{left}}, \alpha_{\mathrm{right}}, p, N_{\mathrm{signal}}, N_{\mathrm{background}}\right) \\ =& N_{\mathrm{signal}}\, F_{\mathrm{Cruijff}}(x; M, \sigma, \alpha_{\mathrm{left}}, \alpha_{\mathrm{right}}) + N_{\mathrm{background}}\, F_{\mathrm{background}}(x; p) \end{aligned} \tag{5-3}$$

The total invariant mass distributions of the inclusive $B^+ \to J/\psi K^+$, $B^0 \to J/\psi K^{*0}$ and $B_s^0 \to J/\psi \phi$ candidates are demonstrated in Figure 5.4 , 5.5 and 5.6. The total numbers of signal events are 124 031±541, 40 154±318 and 7 075±96, where the error is statistical only.

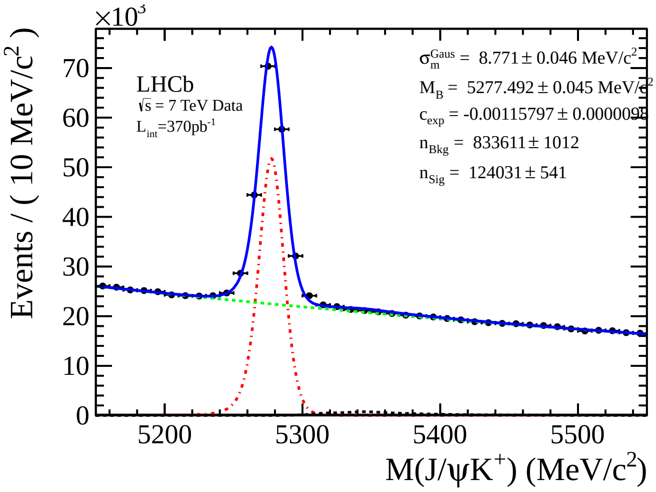

Figure 5.4 Invariant mass distribution of the selected $B^+ \to J/\psi K^+$ candidates. The results of the fit with the model described in the text are superimposed.

To extract the signal yield, the mass fits are made in bins of p_{T} and y for $B^+ \to J/\psi K^+$ and $B^0 \to J/\psi K^{*0}$, and in bins of p_{T} for $B_s^0 \to J/\psi \phi$. The binning for $B^+ \to J/\psi K^+$ is the same as the 2010 analysis. The binnings for $B^0 \to J/\psi K^{*0}$ and $B_s^0 \to J/\psi \phi$ are determined using the same method as the 2010 analysis, as described in Section 4.3.1.

Besides combinatorial background, final state particles can be combined to form a mass peak in the signal region by some physical reasons, and this kind of background can not be excluded by the mass fit. The S-wave decay background is considered in this analysis. For B^0, it comes from the direct $B^0 \to J/\psi K^+ \pi^-$ channel decay, which have the same four final state particles and peak the mass in the B^0 region. The S-wave decay can be distinguished by the background subtracted K^{*0} mass distribution, since the S-wave background K^{*0} candidates should not have mass peak. The background subtracted

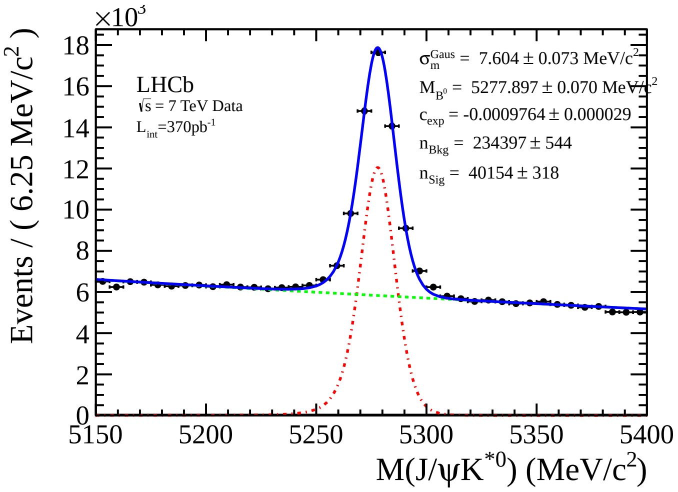

Figure 5.5 Invariant mass distribution of the selected $B^0 \to J/\psi K^{*0}$ candidates. The results of the fit with the model described in the text are superimposed.

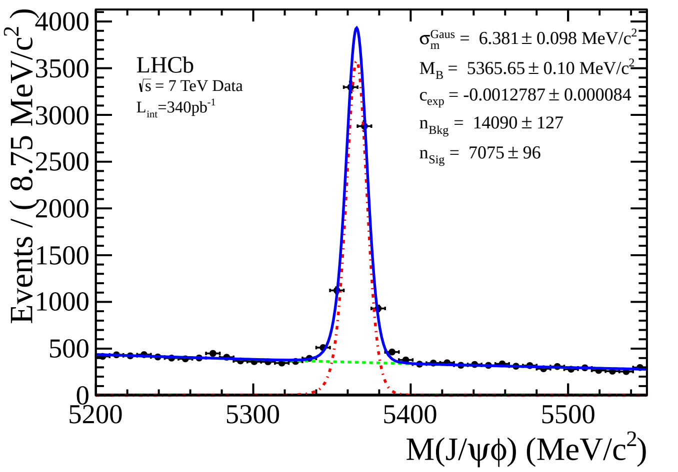

Figure 5.6 Invariant mass distribution of the selected $B_s^0 \to J/\psi\,\phi$ candidates. The results of the fit with the model described in the text are superimposed.

mass distributions of K^{*0} are shown in Figure 5.7. The fit function is composed of two

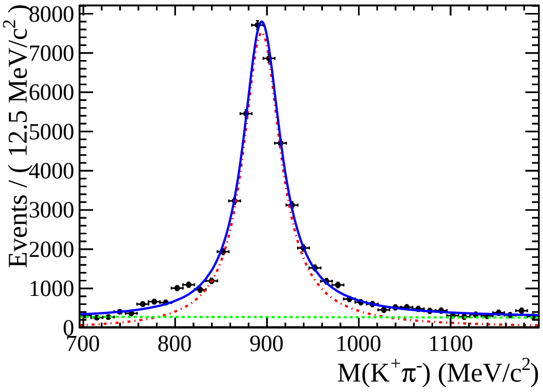

Figure 5.7 The background subtracted mass distributions of $K\pi$ and fit result. The signal function is a Gaussian⊗ Breit-Weigner function, and the background function is exponential.

components:

- The signal function can not be described by a Gaussian function, since the width of K^{*0} is much larger than the Gaussian resolution from detector effects. A convolution of a Gaussian and a Breit-Weigner function is used. The width of the K^{*0} is fixed to the value from Ref.[28];
- The flat component corresponding to the S-wave contribution is described by an exponential function.

The ratio of S-wave background yield with respect to the $B^0 \to J/\psi K^{*0}$ signal yield is determined from the fit result to be equal to 7.6% and used to correct the signal yield. The background subtracted mass distribution of ϕ candidates in $B_s^0 \to J/\psi \phi$ decay is shown in Figure 5.7. The ratio of the S-wave background yield with respect to the $B_s^0 \to J/\psi \phi$ signal yield is determined from the fit result to be equal to 2.5% and used to correct the signal yield.

5.3.2 Efficiency calculation

Simulated signal events are used to estimate the $\epsilon_{\rm acc}$ in bins of $p_{\rm T}$ and y, and a trigger unbiased inclusive J/ψ sample is used to determine the trigger efficiencies from data directly. The reconstruction efficiency for $B^0 \to J/\psi K^{*0}$ and $B_s^0 \to J/\psi \phi$ is determined with a different strategy than the 2010 B^+ analysis, since the PID information from RICH is used in the event selection. The total reconstruction efficiency $\epsilon_{\rm rec}$ is defined as

$$\epsilon_{\rm rec} = \epsilon_{\rm rec\&noPID} \times \epsilon_{\rm PID} \tag{5-4}$$

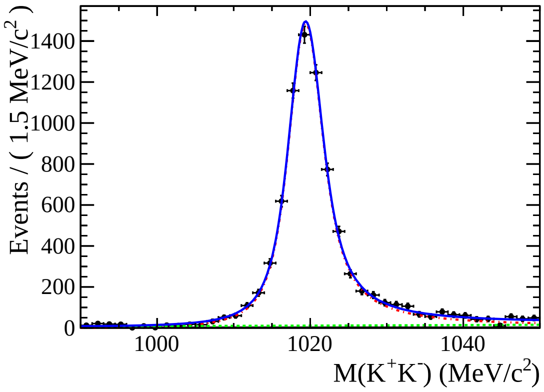

Figure 5.8 The background subtracted mass distributions of KK candidates in 2011 sample. The signal function is a Gaussian⊗ Breit-Weigner function, and the background function is exponential.

where $\epsilon_{\text{rec\&noPID}}$ consists of the efficiency for detection, reconstruction and selection without PID cuts, and ϵ_{PID} is the PID efficiency. $\epsilon_{\text{rec\&noPID}}$ is determined from MC10 simulation sample and ϵ_{PID} is determined from real data.

In the estimation of $\epsilon_{\text{rec\&noPID}}$, the tracking efficiency corrections are also included. The ratios of tracking efficiency from 2011 data with respect to that from MC are measured[102] to be different from 2010 due to different detector alignments and calibrations. The 2011 tracking efficiency ratio table is shown in Figure 5.9. The same approach as

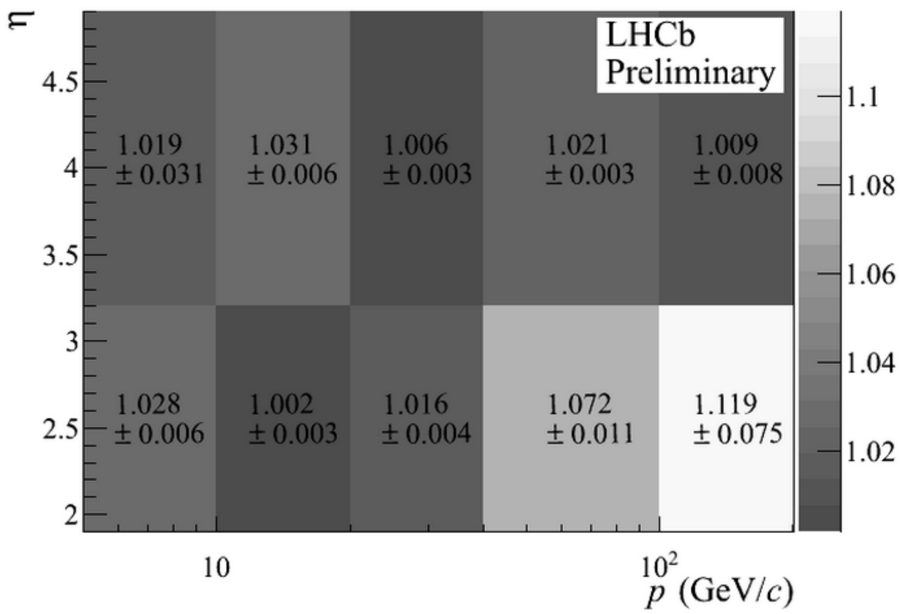

Figure 5.9 The ratio of tracking efficiency from 2011 data with respect to MC simulation[102].

described in Section 4.3.2 is used to correct the MC sample and estimate the statistical uncertainty due to the correction. The corrected reconstruction efficiency $\epsilon_{\text{rec\&noPID}}$ together with the acceptance efficiency for B^+, B^0 and B^0_s are listed in Appendix B.2.

The combined difference between logarithmic likelyhood for $K-\pi$ particle hypotheses, $\mathrm{DLL}_{K\pi}$, is used in the event selection to separate the kaon candidates from the pion background for the $B^0 \to J/\psi K^{*0}$ and $B^0_s \to J/\psi\phi$ decay channels. The distributions of $\mathrm{DLL}_{K\pi}$ in data and MC simulation are found to be very different as demonstrated in Figure 5.10. The PID efficiency couldn't be extracted from MC simulation directly, but

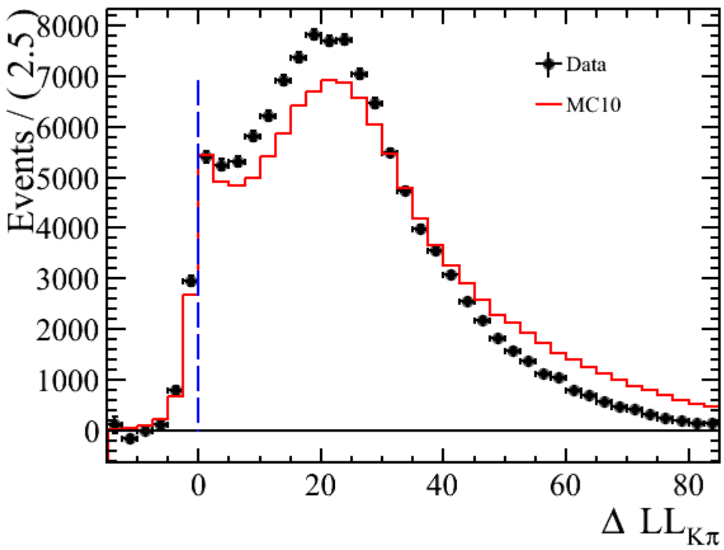

Figure 5.10 The background subtracted distribution of the kaon $\mathrm{DLL}_{K\pi}$ in real data (black) and the signal distribution in MC simulation (red).

is calculated using a PID calibration method[112].

The PID calibration method is based on a large set of calibration samples, in which the PID efficiency and misidentification (misID) rate for kaon are determined in the real data from the so-called "golden mode" decay channel, $D^* \to \pi D^0$. This decay channel can be reconstructed without using the information from RICH detectors. The calibration samples are used to calibrate the $\mathrm{DLL}_{K\pi}$ distribution of the signal modes and to extract the PID efficiency. The $\mathrm{DLL}_{K\pi}$ distributions of the kaon in the calibration samples correspond to the real response of RICH to kaons with the same kinematics. The $\mathrm{DLL}_{K\pi}$ distribution of a kaon is correlated with the kaon kinematic variables. Global event multiplicity variables affect the hit multiplicity in the detector thus also affect the RICH detector output.

The kaon momentum and pseudo rapidity as the kinematic variables, together with the best track multiplicity as the global event variable, are chosen to bin the signal and calibration samples. Assuming that the $\mathrm{DLL}_{K\pi}$ distribution only depends on these variables and the binning is properly set up, the $\mathrm{DLL}_{K\pi}$ distribution in the calibration sample can be treated as the real distribution for a specific kinematic bin. The momentum and pseudo rapidity distributions in the calibration samples are weighted to the background subtracted distributions in the signal samples. And then the $\mathrm{DLL}_{K\pi}$ distribution of the weighted calibration samples will describe the real distribution of the signal samples. The PID variable $\mathrm{DLL}_{K\pi}$ distributions before and after the weight are demonstrated in Figure 5.11. The calibration samples are reconstructed for two magnet polarities sep-

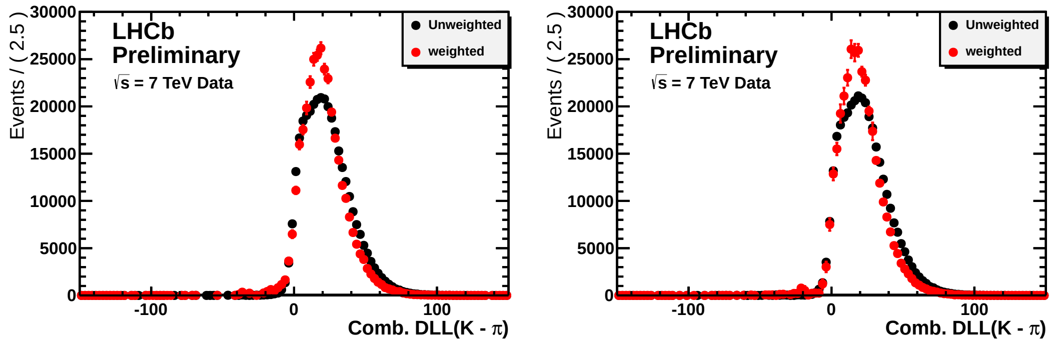

Figure 5.11 The PID variable $\mathrm{DLL}_{K\pi}$ distributions for kaon in $B^0 \to J/\psi K^{*0}$ channel in the data samples with magnet *left*: up and *right*: down polarity. The black and red points are the $\mathrm{DLL}_{K\pi}$ distributions of the unweighted and weighted calibration samples, respectively.

arately. The PID efficiencies can be determined for each $\mathrm{DLL}_{K\pi}$ cut value as shown in Figure 5.12. The PID efficiencies for both magnetic polarities and both channels are listed in Table 5.7.

Table 5.7 Kaon ID efficiencies (in %) for both magnetic polarities and both decay channels in 2011 analysis. The uncertainty is statistical.

	Magnet up	Magnet down
$B^0 \to J/\psi K^{*0}$	95.96 ± 0.04	95.92 ± 0.03
$B^0_s \to J/\psi \phi$	95.97 ± 0.04	95.92 ± 0.05

Since the trigger lines only depend on the J/ψ, the trigger efficiency is extracted from data using an inclusive J/ψ sample using TISTOS method. The TOS trigger uses the same requirements as the one presented in Table 5.1. The TIS trigger requirements are different and listed in Table 5.8. The Physics lines, described in Section 4.4.2 are used to keep as many candidates as possible. The original TOS efficiency of HLT muon line

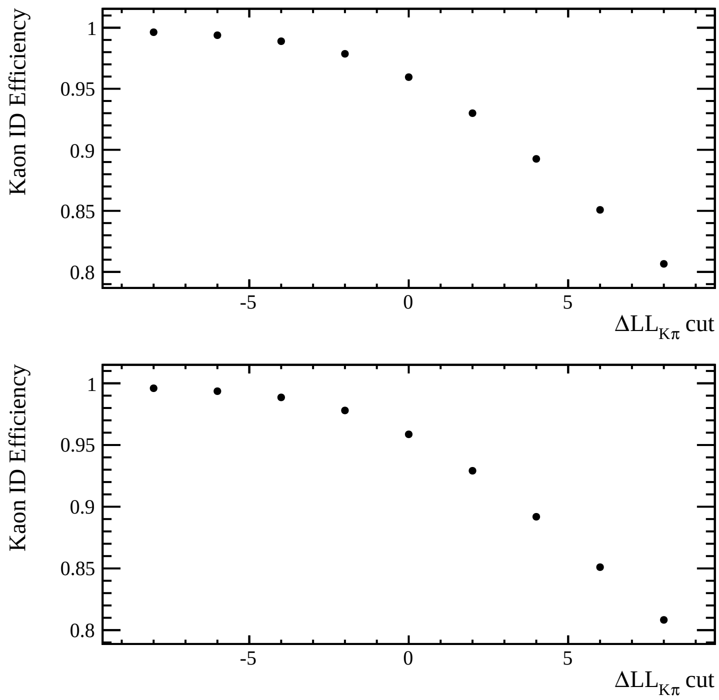

Figure 5.12 The PID efficiencies for each DLL$_{K\pi}$ cut value on the kaon of $B^0 \rightarrow J/\psi\, K^{*0}$ in the data samples with magnet *top*: up and *bottom* down polarity.

is extremely low; for this reason the information from muon stations is excluded for the TOS determination. The trigger efficiency weight procedure and uncertainty propagation

Table 5.8 Trigger lines for J/ψ TIS in 2011 analysis.

Trigger level	Trigger Lines
L0 TIS	L0Muon TIS or L0DiMuon TIS
HLT1 TIS	Hlt1Phys TIS
L0&HLT1 TIS	(L0Muon TIS or L0DiMuon TIS) and Hlt1Phys TIS
HLT2 TIS	Hlt2Phys TIS

are the same as in the 2010 analysis. The trigger efficiency of each *B* meson is listed in Appendix B.2.

The distributions of global event cut variables in real and simulated data are shown in Figure 5.13. As described in Section 5.1, the OT cluster multiplicity cut was 10 000 at first and then was changed to 15 000. The efficiency of OT cluster multiplicity cut for the data sample with 10 000 cut is extracted from the data sample with 15 000 cut to be 97.90 ± 0.05%. The VELO cluster multiplicity cut was 10 000 at first and then was changed to 6 000. However, from Figure 5.13, it is clear that the effect is negligible.

5.3.3 Integrated luminosity

The integrated luminosity was measured using the same methods as discussed in Section 4.3.3. The two integrated luminosity of the data samples with magnet up polarity from the two LHCb luminosity strategies: online (Van der meer) and offline (Beam-gas) differ by 20% due to the underestimation of "parasitic luminosity" entering the beam-gas correction[113,114]. The integrated luminosity is corrected according to the Stripping 17 correction[115] to be $370 \pm 13\,\mathrm{pb}^{-1}$.

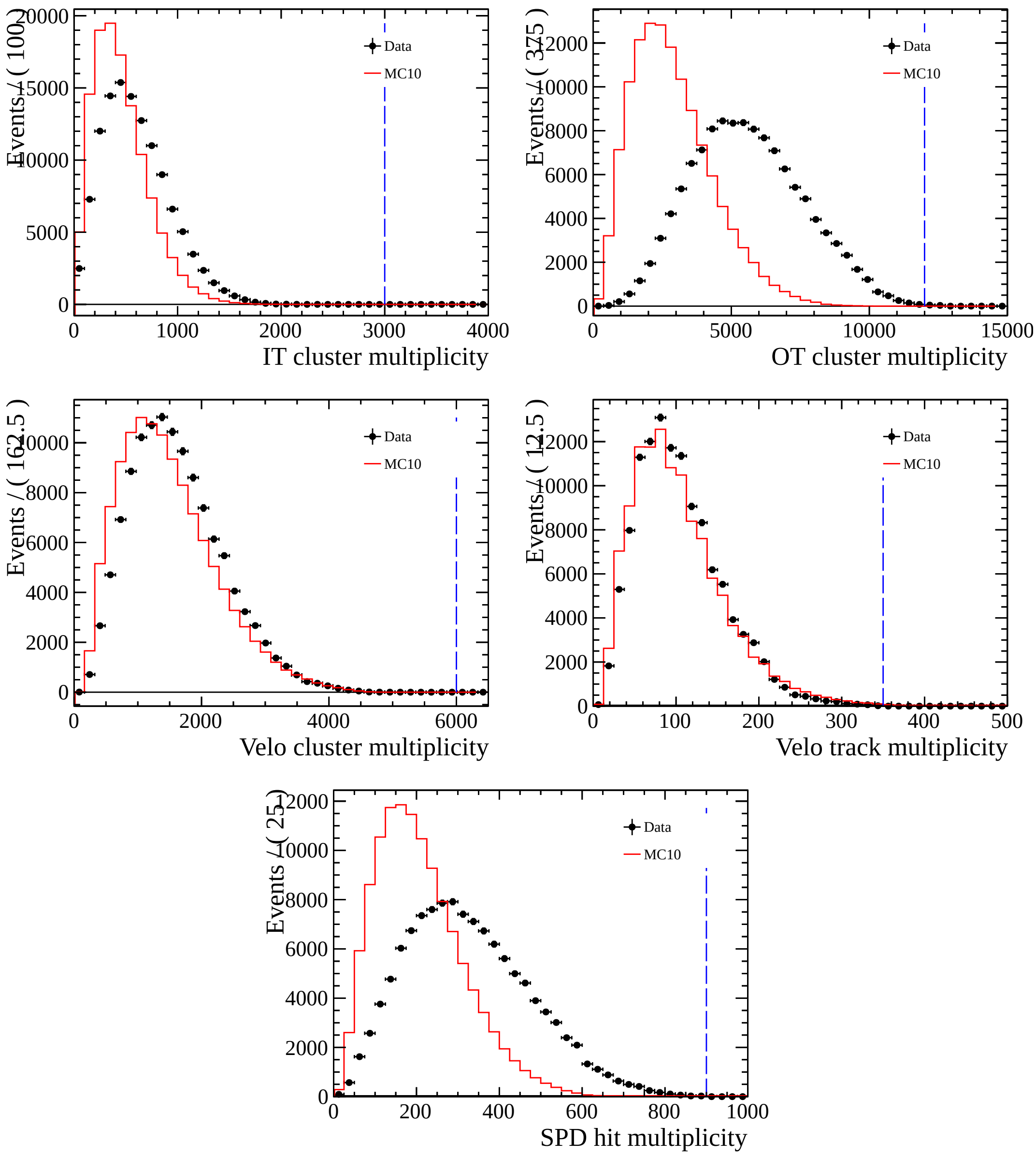

Figure 5.13 Distributions of GEC variables . On all plots, the black dots with error bars represent the background subtracted data distributions and the red histograms the MC distributions. The blue dashed lines show the cut values.

5.4 Systematic uncertainties

From Equation 5-1 and the discussions in the previous section, the production measurements are affected by the systematic uncertainties on the determination of signal yields, the efficiencies, the branching fractions and the luminosity.

The uncertainty on the determination of the signal yield mainly arises from the treatment of final state radiation in the signal fit. This is estimated by comparing the fitted and true signal yields in the MC simulation. The systematic uncertainties due to the FSR estimation are listed in Table 5.9. For B^+, we use the shape from MC simulation to estimate the Cabibbo-suppressed background effect. As discussed in Section 4.4.1, it is negligible. Different ranges are used to test the stability of the mass fit. For B^+, as discussed Section 4.4.1, it is negligible. The same procedure is repeated on B^0 and B_s^0 samples and the results are listed in Table 5.9. The ratios of non-resonant background are compared with other LHCb measurements[116,117] and the differences are assigned as systematic uncertainties, as summarized in Table 5.9.

Table 5.9 The systematic uncertainties due to the signal fit model and the mass fit range.

Channel	Signal model (%)	Mass fit range (%)	Non-resonant background (%)
$B^+ \to J/\psi K^+$	1.3	0.1	-
$B^0 \to J/\psi K^{*0}$	0.4	1.0	1.6
$B_s^0 \to J/\psi \phi$	0.2	0.4	0.5

The uncertainties on the efficiencies mainly arise from trigger, tracking, particle identification and vertex fit quality cut. Some other possible sources of systematic uncertainty are checked and most of them are found to be negligible.

The uncertainty on the trigger efficiency is estimated from the differences between the MC true efficiency and the efficiency measured using the TISTOS method with an inclusive J/ψ MC simulation sample. The systematic uncertainties are summarized in Table 5.10.

The uncertainty on the tracking efficiency is estimated in the same way as in the 2010 analysis with the 2011 efficiency ratio tables. The systematic uncertainties due to tracking efficiency, including all the three componets, are summarized in Table 5.11.

The angular distributions of the decay products of $B^0 \to J/\psi K^{*0}$ and $B_s^0 \to J/\psi \phi$ channels are measured by CDF[118,119] and LHCb[120]. Different angular distributions

Table 5.10 The systematic uncertainties due to the trigger efficiency.

Channel	Systematic uncertainties (%)		
	Total	In bins of p_{T}	In bins of p_{T} and y
$B^+ \to J/\psi K^+$	0.2	0.2-0.7	0.2-2.7
$B^0 \to J/\psi K^{*0}$	0.2	0.2-0.7	0.2-3.9
$B_s^0 \to J/\psi \phi$	0.2	0.2-0.7	0.2-3.2

Table 5.11 The systematic uncertainties due to the tracking efficiency.

Channel	Systematic uncertainties (%)		
	Total	In bins of p_{T}	In bins of p_{T} and y
$B^+ \to J/\psi K^+$	2.9	2.9-3.1	2.9-3.3
$B^0 \to J/\psi K^{*0}$	4.9	4.9-5.0	4.9-5.1
$B_s^0 \to J/\psi \phi$	4.9	4.9-5.0	4.9-5.1

may lead to various p_{T} and y spectra, and therefore change the efficiency. To estimate the effects of the uncertainties on these measurements, the procedures for acceptance efficiency estimation are repeated by varying the angular parameters in the generator level simulation by $\pm\sigma$, which is the uncertainty of the angular measurement. The fully simulated MC10 samples are weighted to vary the angular distributions. Using the new generater level simulation and weighted full simulation sample, the efficiencies are recalculated in bins of B p_{T} and y.

For the systematic uncertainties in bins of B p_{T}, and total systematic uncertainties, to account for the phase space distribution of the B mesons, the cross-section results are recalculated using the varied efficiencies. The differences between the varied results and the original ones are assigned as the systematic uncertainties and are summarized in Table 5.12.

Table 5.12 Systematic uncertainties (in %) due to angular distribution uncertainties.

Channel	in bins of p_{T} and y	in bins of p_{T}	total
$B^0 \to J/\psi K^{*0}$	0.1-6.2	0.0-0.3	0.1
$B_s^0 \to J/\psi \phi$	-	0.1-1.3	0.1

The systematic uncertainty due to muon identification efficiency is estimated to be no larger than 2% [12]. Hadron identification information based on the RICH is used for B^0 and B_s^0 decay to select kaon candidates. The systematic uncertainty on the PID efficiency is estimated using MC simulation samples by the same approach as used in Section 5.3.2. The originanl and weighted $\mathrm{DLL}_{K\pi}$ distributions in the MC calibration sample and the MC true distribution in the MC signal sample are illustrated in Figure 5.14. The PID

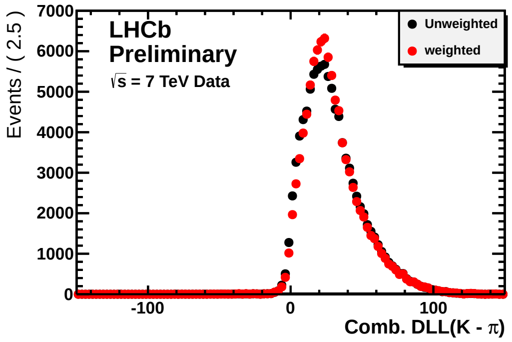

Figure 5.14 $\mathrm{DLL}_{K\pi}$ distributions for the kaon from *left*: $B^0 \to J/\psi\, K^{*0}$ and *right*: $B_s^0 \to J/\psi\, \phi$ in MC simulation samples. The black and red points are the $\mathrm{DLL}_{K\pi}$ distributions of the unweighted and weighted calibration samples, respectively.

efficiencies of the MC simulation sample for different $\mathrm{DLL}_{K\pi}$ cut value can be calculated and are shown in Figure 5.15. The differences between the efficiencies calculated from the

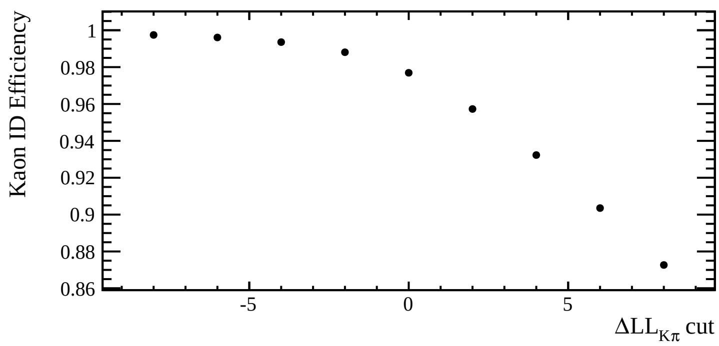

Figure 5.15 The PID efficiencies for each $\mathrm{DLL}_{K\pi}$ cut value on the kaon of $B^0 \to J/\psi\, K^{*0}$ in the MC simulation samples with magnet up polarity.

weighted $\mathrm{DLL}_{K\pi}$ distribution in the MC calibration sample, and the MC true distribution are assigned as the systematic uncertainties, as shown in Figure 5.16. The systematic uncertainties due to hadron identification are found to be 0.5% for $B^0 \to J/\psi\, K^{*0}$ and 0.8% for $B_s^0 \to J/\psi\, \phi$.

The GEC efficiency is extracted from data as discussed in Section 5.3.2. The background subtracted distributions of OT cluster multiplicity for samples with

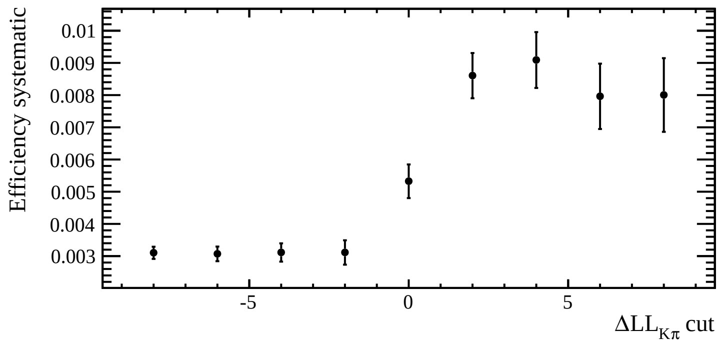

Figure 5.16 The PID efficiency systematic uncertainty for each DLL$_{K\pi}$ cut value on the kaon of $B^0 \to J/\psi K^{*0}$ in the MC simulation samples.

$N_{\mathrm{OTClusters}}$ <10 000 and $N_{\mathrm{OTClusters}}$ <15 000 cuts are shown in Figure 5.17. The differ-

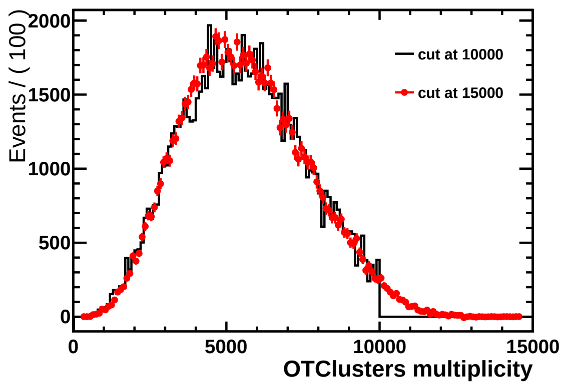

Figure 5.17 The background subtracted OT cluster multiplicity distributions for samples with $N_{\mathrm{OTClusters}} < 10\,000$ (black histogram) and $N_{\mathrm{OTClusters}} < 15\,000$ (red points) cuts.

ence between these two distributions is small and the systematic uncertainty due to this efficiency is negligible.

The systematic effects of the clone cut are estimated by removing the clone cut and repeating the mass fit in the real data sample. The differences between the efficiencies from data and MC are assigned as systematic uncertainties. The systematic uncertainties due to clone cut are listed in Table 5.13.

The uncertainties on vertex χ^2/ndf cut efficiency of B^0 and J/ψ due to the difference between real data and MC simulation are checked using the same method as described in Section 4.4.2. Since the decay topology of B_s^0 is similar to B^0, the same uncertainty is assigned to B_s^0. For B^+, the uncertainty from 2010 analysis is used. The results are summarized in Table 5.13. The uncertainties due to the choice of binning are checked using the same method as described in Section 4.4.2, and the results are listed in Table 5.14. The uncertainties are found to be negligible. For the 2010 data, these uncertainties could arise

Table 5.13 The systematic uncertainties due to the clone cut and vertex χ^2/ndf cut efficiencies.

Channel	Clone cut(%)	Vertex χ^2/ndf cut
$B^+ \to J/\psi K^+$	0.32	1.0
$B^0 \to J/\psi K^{*0}$	0.96	0.9
$B_s^0 \to J/\psi \phi$	1.46	0.9

Table 5.14 The differences due to the change of binning.

Channel	Change bin width(%)		Change bin entry(%)	
	400	800	-50	+50
$B^+ \to J/\psi K^+$	0.02	-0.02	< 0.01	< 0.01
$B^0 \to J/\psi K^{*0}$	0.30	-0.29	0.03	0.03
$B_s^0 \to J/\psi \phi$	0.06	< 0.01	< 0.01	< 0.01

from the large statistical uncertainties. Since the same MC10 sample is used to extract the efficiency, the systematic uncertainties on J/ψ mass window cut, Inter-bin cross-feed and Track χ^2/ndof cut are neglected as discussed in Section 4.4.

The systematic uncertainties due to the branching ratio are listed in Table 5.15. The correlation between the branching ratios of B and J/ψ decay is estimated using the same approach in Section 4.4.3. The most precise measurement of $\mathcal{B}(B^0 \to J/\psi K^{*0}) = (1.309 \pm 0.026 \pm 0.077) \times 10^{-3}$ made by the BaBar Collaboration[109] is used. Since the $\mathcal{B}(B_s^0 \to J/\psi \phi)$ has such a large uncertainty, the correlation is neglected. In the final result, the uncertainty from B_s^0 branching ratio is given separately.

Table 5.15 The systematic uncertainties due to the branching ratio.

Channel	Branching ratio			Systematic uncertainty	
	$J/\psi \to \mu^+\mu^-$	$K^{*0}(\phi)$ decay	B decay (10^{-3})	corr.	uncorr.
$B^+ \to J/\psi K^+$		-	1.013 ± 0.034	3.3%	3.5%
$B^0 \to J/\psi K^{*0}$	5.93 ± 0.06%	66.7%	1.33 ± 0.06	4.6%	4.6%
$B_s^0 \to J/\psi \phi$		48.9 ± 0.5%	1.3 ± 0.4	-	30.8%

As discussed in Section 4.4.4, 3.5% is assigned as the systematic uncertainty on the luminosity determination[105]. The systematic uncertainties that affect the cross-section measurements are summarized in Table 5.16.

Table 5.16 Summary of systematic uncertainties.

Quantity	Systematic uncertainty (%)		
	B^+	$B^0 \to J/\psi K^{*0}$	B_s^0
Signal fit model	1.3	0.4	0.2
Fit range	0.5	1.0	0.4
Non-resonant background	-	1.6	0.5
Bin size	< 0.1	0.3	< 0.1
Trigger efficiency	0.2 to 2.7	0.2 to 3.9	0.2 to 0.7
Tracking efficiency	2.9 to 3.3	4.9 to 5.1	4.9 to 5.0
Clone rejection	0.3	1.0	1.5
Vertex χ^2/ndf cut	1.0	0.9	0.9
Muon identification	2.5	2.5	2.5
Kaon identification	-	0.5	0.8
Angular distribution	-	0.1-6.2	0.1-1.3
Branching ratio	3.3	4.6	30.8
Luminosity	3.5	3.5	3.5
Total(Bin independent)	5.8	6.9	31.2

5.5 Results and discussions

The differential cross-sections of B^+ and B^0 in bins of p_{T} and y are shown in Figure 5.18 and listed in Appendix B.4. The differential cross-section of B_s^0 in bins of p_{T} is shown in

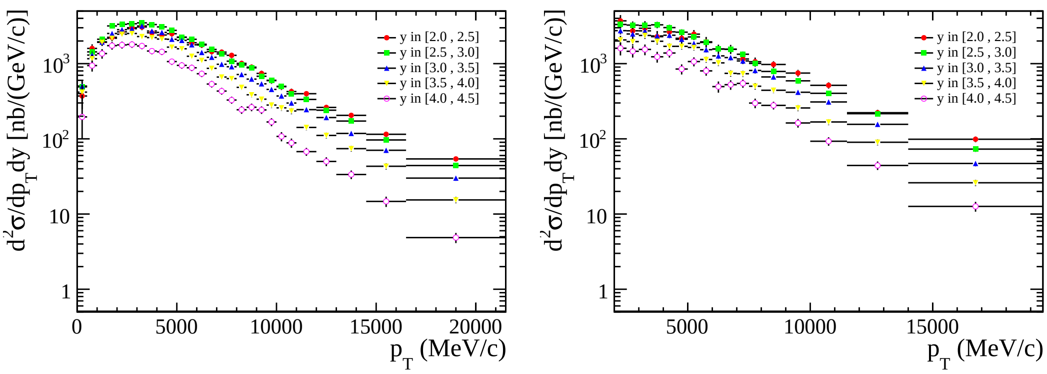

Figure 5.18 Differential production cross-sections for *left*: B^+ and *right*: B^0 as a function of the transverse momentum p_{T} and rapidity y.

Figure 5.20 and listed in Appendix B.4.

The integrated cross-sections of B^+ , B^0 and B_s^0 production over the fiducial region are calculated to be

$$\begin{aligned}
\sigma(B^+, 0 < p_{\mathrm{T}} < 40\,\mathrm{GeV}/c, 2.0 < y < 4.5) &= 41.6 \pm 0.3\,(\mathrm{stat.}) \pm 2.7\,(\mathrm{syst.})\ \mu\mathrm{b}\,, \\
\sigma(B^0, 2 < p_{\mathrm{T}} < 40\,\mathrm{GeV}/c, 2.0 < y < 4.5) &= 32.3 \pm 0.4\,(\mathrm{stat.}) \pm 2.4\,(\mathrm{syst.})\ \mu\mathrm{b}\,, \\
\sigma(B_s^0, 0 < p_{\mathrm{T}} < 40\,\mathrm{GeV}/c, 2.0 < y < 4.5) &= 7.9 \pm 0.2\,(\mathrm{stat.}) \pm 2.5\,(\mathrm{syst.})\ \mu\mathrm{b}\,,
\end{aligned}$$

The cross-section results obtained from this analysis are compared with the FONLL predictions[4,5,49] in Figure 5.19 and 5.20. The hadronisation fractions $f_{\bar{b}\to B^+}$ of 40.1 ± 1.3% ,$f_{\bar{b}\to B^0}$ of 40.1 ± 1.3% and $f_{\bar{b}\to B_s^0}$ of 11.3 ± 1.3% [28] are assumed to fix the overall scale of FONLL. Another fraction for B_s^0 extracted from LHCb measurement[110] is also used as a comparison. The uncertainty of the FONLL computation includes the uncertainty on the b-quark mass, renormalization/factorization scales, and the uncertainty on the CTEQ6.6[121] PDF. Good agreements are observed between the experimental and theoretical distributions.

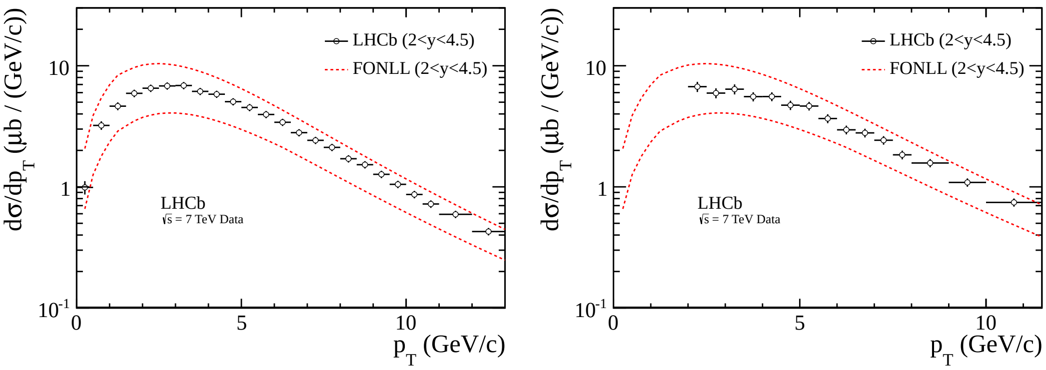

Figure 5.19 Differential production cross-sections for *left*: B^+ and *right*: B^0 as a function of the transverse momentum. The black dots with error bars are the measurements presented in this analysis, the red dashed lines are the upper and lower uncertainty limits of the FONLL computation[49]. The hadronisation fractions $f_{\bar{b}\to B^+}$ of $40.1 \pm 1.3\%$ and $f_{\bar{b}\to B^0}$ of $40.1 \pm 1.3\%$ [28] are assumed to fix the overall scale. The uncertainty of the FONLL computation includes the uncertainty of b-quark mass, renormalization/factorization scales, and the CTEQ6.6 PDF uncertainty.

To clarify the discrepancy between the experimental measurement and theory prediction of B^+ production cross-section in the last p_{T} bin in Section 4.5, the B^+ candidates with high p_{T} in 2011 data sample are divided into more bins and the results are demonstrated in Figure 5.21. Good agreement in the high p_{T} region is observed.

The integrated cross-sections in Equation 5-5 are extrapolated to 4π polar angle

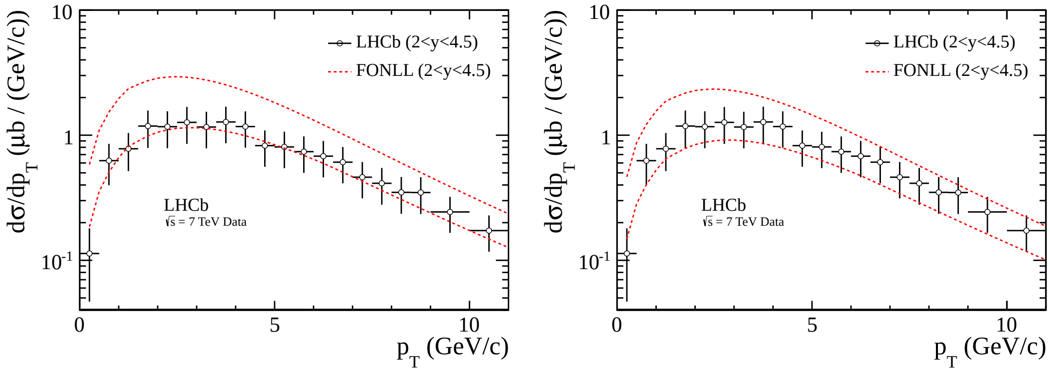

Figure 5.20 Differential production cross-section as a function of the B_s^0 transverse momentum. The black dots with error bars are the measurements presented in this analysis, the red dashed lines are the upper and lower uncertainty limits of the FONLL computation[49]. $\mathcal{B}(B_s^0 \to J/\psi\,\phi) = 0.13 \pm 0.04\%$ is used to calculate the The hadronisation fractions $f_{\bar{b}\to B_s^0}$ of *left*: $11.3 \pm 1.3\%$[28] and *right*: $9.0 \pm 0.9\%$[110] are assumed to fix the overall scale. The uncertainty of the FONLL computation includes the uncertainty of *b*-quark mass, renormalization/factorization scales, and the CTEQ6.6 PDF uncertainty.

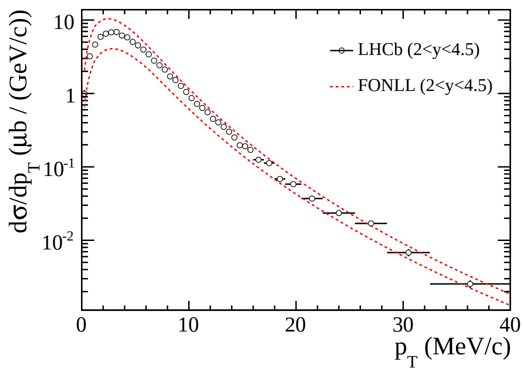

Figure 5.21 Differential production cross-section for B^+ as a function of the transverse momentum. The black dots with error bars are the measurements and the red dashed lines are the upper and lower uncertainty limits of the FONLL computation[49].

range

$$\sigma(pp \to b\bar{b}X) = \frac{\alpha_{4\pi}\sigma(B^+, 2.0 < y < 4.5)}{2 \times f_{\bar{b}\to B^+}}, \tag{5-6}$$

where the $\alpha_{4\pi}$ is the ratio of the number of B^+ in the full rapidity range to that in the $2.0 < y < 4.5$ region from the FONLL computation and the $f_{\bar{b}\to B^+}$ of 40.1 ± 1.3%, $f_{\bar{b}\to B^0}$ of 40.1 ± 1.3% and $f_{\bar{b}\to B^0_s}$ of 11.3 ± 1.3%[28] are the hadronisation fractions. The results are

$$\begin{aligned}
B^+ &: \quad \sigma(pp \to b\bar{b}X) = 267 \pm 2\,(\text{stat.}) \pm 23\,(\text{syst.})\ \mu\text{b},\\
B^0 &: \quad \sigma(pp \to b\bar{b}X) = 260 \pm 4\,(\text{stat.}) \pm 26\,(\text{syst.})\ \mu\text{b},\\
B^0_s &: \quad \sigma(pp \to b\bar{b}X) = 180 \pm 5\,(\text{stat.}) \pm 61\,(\text{syst.})\ \mu\text{b}
\end{aligned}$$

The uncertainties due to the extrapolation to 4π are estimated by comparing the results of the FONLL calculation to the Pythia and EvtGen estimate. The extrapolated results for B^+ and B^0 are in good agreement with two other LHCb measurements of the the b production cross-section: $255 \pm 4 \pm 43\mu$b[12] and $272 \pm 19 \pm 47\mu$b[11] and the result in Chapter 4. The result for B^0_s indicates that its hadronization fraction at LHC may differ from the one in Ref.[28]. This discrepancy can be clarified by a further measurement on the fraction.

Chapter 6 Measurement of B_c^+ production cross-section ratio with 2011 data

The measurement of the B_c^+ production cross-section ratio at a center-of-mass energy of $\sqrt{s} = 7\,\text{TeV}$ with the LHCb detector is given in this chapter. The nature of the B_c^+ is unique because it is the lightest state composed of a heavy quark and a heavy anti-quark of different flavors: $\overline{b}$ and c. The study of its production can then be used to constrain the QCD calculations[53]. The first observation of the B_c^+ was reported by the CDF collaboration[122]. But it is only recently that the B_c^+ has been observed with a significant number of candidates, in $p\overline{p}$ collisions at the TEVATRON[123,124], where reconstructed B_c^+ in the decay mode $B_c^+ \to J/\psi\,\pi^+$ were used to measure the mass. The only B_c^+ decay mode observed so far apart from the mode $B_c^+ \to J/\psi\,\pi^+$, is the semi-leptonic decay mode $B_c^+ \to J/\psi\,\ell\nu_\ell X$[125–127], which is used to measure the B_c^+ lifetime.

Experimentally, the only available measurements of B_c^+ production are indirect measurements of the production cross-section relative to B^+ production cross-section. The CDF collaboration measured the ratio

$$R_{c/u} = \frac{\sigma(B_c^+)\,\mathcal{B}\left(B_c^+ \to J/\psi\,\mu^+\nu_\mu\right)}{\sigma(B^+)\,\mathcal{B}(B^+ \to J/\psi\,K^+)}, \tag{6-1}$$

in $p\overline{p}$ collisions at the TEVATRON[128,129]. The measured values are

$$R_{c/u} = 0.295 \pm 0.040(\text{stat.})^{+0.033}_{-0.026}(\text{syst.}) \pm 0.036(p_\text{T}) \tag{6-2}$$

for $p_\text{T}(\text{B}) > 4\,\text{GeV}/c$, and

$$R_{c/u} = 0.227 \pm 0.040(\text{stat.})^{+0.024}_{-0.017}(\text{syst.}) \pm 0.014(p_\text{T}) \tag{6-3}$$

for $p_\text{T}(\text{B}) > 6\,\text{GeV}/c$.

Since no B_c^+ absolute branching fraction has been measured yet, the strategy of this analysis is to perform a measurement of the production cross-section times the branching fraction of a B_c^+ decay mode. The chosen mode is $B_c^+ \to J/\psi\,\pi^+$ which is the one expected to have the highest signal over background ratio. The B_c^+ production is measured relatively to the B^+ production. The chosen B^+ decay mode is $B^+ \to J/\psi\,K^+$, which has a well measured branching fraction and for which the main selection systematic uncertainties will cancel in the ratio of production cross-sections. The production ratio is determined by

$$R_{c/u} = \frac{\sigma\left(B_c^+\right) \times \mathcal{B}\left(B_c^+ \to J/\psi\,\pi^+\right)}{\sigma\left(B^+\right) \times \mathcal{B}\left(B^+ \to J/\psi\,K^+\right)}, \tag{6-4}$$

for $p_{\mathrm{T}}\left(B_c^+, B^+\right) > 4\,\mathrm{GeV}/c$ and $2.5 < \eta\left(B_c^+, B^+\right) < 4.5$. σ is the production cross-section and $\mathcal{B}$ is the branching fraction.

We start with the data samples and corresponding triggers in Section 6.1. The event selection requirements are outlined in Section 6.2. The determinations of the parameters quoted in Equation 6-4 are presented in Section 6.3 and their systematic uncertainties are discussed in Section 6.4. At last, Section 6.5 presents the result and some discussions.

6.1 The samples and triggers

This analysis uses $370 \pm 13\,\mathrm{pb}^{-1}$ of pp collision data as same as described in Section 5.1. The MC simulation samples with the same configuration "MC10" and TCK 0x00730035, as described in Section 4.1, are also used in this analysis. As described in Section 2.5, the BCVEGPY[59,61] generator is implemented as a Pythia external user process to generate B_c^+ quickly. The parton density function used is the CTEQ6LL PDF[130] and the BCVEGPY generator is configured to use the leading order running α_s and a characteristic energy scale $Q^2 = p_{\mathrm{T}}^2 + M_{B_c}^2$. The B_c^+ mass is taken equal to $M_{B_c} = 6\,276\,\mathrm{MeV}/c^2$ and the masses of the b and c quarks to $M_b = 4\,950\,\mathrm{MeV}/c^2$ and $M_c = 1\,326\,\mathrm{MeV}/c^2$, respectively. Meanwhile, the generator for B^+ production is described in Section 4.1.

In the MC simulation, the total cross-sections with this setup are, in the full polar angle range, 203 μb for the B^+ production and 269 nb for the B_c^+ production. The cross-sections in the pseudo rapidity range $2 < \eta < 5$ and with $p_{\mathrm{T}} > 4\,\mathrm{GeV}/c$ are 45.7 μb for the B^+ and 75 nb for the B_c^+. The B_c^+ and B^+ differential cross-sections as a function of the B meson p_{T} are shown in Figure 6.1.

This analysis is based on three L0 lines:

- the single muon, which requires one muon candidate with a p_{T} larger than $1.4\,\mathrm{GeV}/c$;
- the di-muon, which requires two muon candidates with the product of their p_{T} larger than $1.68(\mathrm{GeV}/c)^2$;
- the hadron, which requires one hadron candidate with a transverse energy larger than $3.5\,\mathrm{GeV}/c^2$.

They provide the input candidates for these three HLT1 lines:

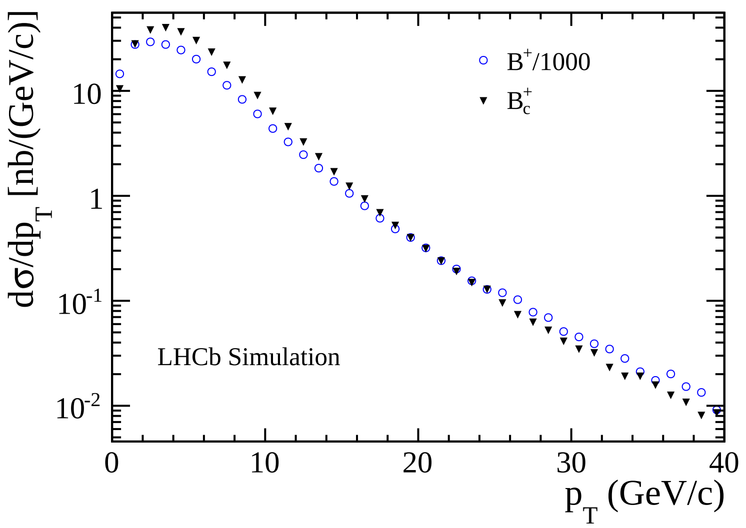

Figure 6.1 Differential production cross-section for B_c^+ (black triangles) and B^+ (blue squares, scaled by a factor 1000) as a function of the B transverse momentum in MC simulation.

- *Hlt1DiMuonHighMass* confirms the muon candidate found by the L0 single muon, applies a harder cut on the muon p_{T} at 1.8 GeV/c and requires their combined mass to be greater than 2.7 GeV/c^2;
- *Hlt1TrackAllL0* trigger L0-passed events with a well measured track, *e.g.* with p_{T} larger than 1.7 GeV/c, track IP χ^2/ndof > 2 *etc.*;
- *Hlt1TrackMuonDecision* confirms the muon or di-muon candidates, and requires the muon to be "isMuon" as defined in Table 3.1.

At the HLT2 level, three lines are used:

- *Hlt2DiMuonJPsi* selects events which have two muon candidates with an invariant mass in a ±120 MeV/c^2 mass window around the nominal J/ψ mass[28];
- *Hlt2TopoMu2BodyBBDT*;
- *Hlt2TopoMu3BodyBBDT*.

The topological trigger lines[131], specially introduced for typical B decays, are used to reduce the background retention rate and save data processing time. These lines look for 2,3 track combinations in a wide mass window with loose combinatorial cuts, *e.g.* on IP or vertex fit quality, and apply tighter cuts on the tracks, *e.g.* p_{T}, track χ^2/ndof and IP.

The GECs in this analysis are the same as described in Section 5.1.

6.2 Event selection

$B_c^+ \to J/\psi\,\pi^+$ and $B^+ \to J/\psi\,K^+$ are selected with as similar requirements as possible between the two hadron types. J/ψ candidates are formed from pairs of opposite sign particles that have p_{T} larger than 900 MeV/c, have a good quality of the track fit ($\chi^2/\mathrm{ndf} < 4$) and be identified as muons, requiring that the track has hits in the muon detector and that the $\Delta\mathrm{LL}_{\mu\pi}$s of the two muon tracks are larger than 0. The two muons are required to originate from a common vertex and only candidates with a χ^2/ndf of the vertex fit smaller than 9 are kept. To reduce the prompt J/ψ (J/ψ produced directly from the primary vertex) contribution, the impact parameter fit χ^2 of J/ψ is required to be larger than 4. The invariant mass of the J/ψ candidates is required to be between 3 040 MeV/c^2 and 3 140 MeV/c^2.

The selected J/ψ candidates are combined with a charged pion for the B_c^+ or a charged kaon for the B^+, with p_{T} above 1.5 GeV/c and a χ^2/ndf of the track fit smaller than 4. A vertex fit is performed that constrains the three daughter particles to originate from a common point and the mass of the muon pair to match the nominal J/ψ mass. The quality of this fit is required to have a χ^2/ndf smaller than 9. or clone tracks, by the reconstruction software. Clones are eliminated using the clone identification algorithm based on the Kullback-Liebler distance described in Ref.[93–95]. The impact parameter fit χ^2 of π^+ is required to be larger than 25 to get rid of the combination of J/ψ and prompt pion produced directly from the primary vertex.

The B candidates are selected with p_{T} larger than 4 GeV/c, a proper time larger than 0.25 ps and $2.5 < \eta < 4.5$. The fiducial region is chosen to be sufficiently far away from the detector acceptance ranges, in order to have a reasonably large efficiency over the acceptance. The impact parameter fit χ^2 of B_c^+ is required to be smaller than 25 since the B_c^+ is produced from the primary vertex. The final selection criteria are listed in Table 4.4. Figure 6.2 shows the invariant mass distributions of the $B_c^+ \to J/\psi\,\pi^+$ (left) and $B^+ \to J/\psi\,K^+$ (right) candidates obtained with the selection described above. Fit results with the shapes described in Section 6.3 are superimposed.

Table 6.1 $B_c^+ \to J/\psi\,\pi^+$ and $B^+ \to J/\psi\,K^+$ selection criteria.

Quantity	Requirement
μ	
Track	Long track with muon detector hits (IsMuon)
$\Delta\mathrm{LL}_{\mu\pi}$	> 0
p_T	$> 0.9\,\mathrm{GeV}/c$
Track fit quality χ^2/ndf	< 4
J/ψ	
Mass window	$3.04 < M_{\mu\mu} < 3.14\,\mathrm{GeV}/c^2$
Vertex fit χ^2/ndf	< 9
χ^2_IP	> 4 (only for B_c^+)
L0 Trigger On Signal	L0SingleMuon or L0DiMuon
HLT1 Trigger On Signal	Hlt1DiMuonHighMass
HLT2 Trigger On Signal	Hlt2DiMuonJPsi
Bachelor hadron (π^+ for B_c^+ and K^+ for B^+)	
p_T	$> 1.5\,\mathrm{GeV}/c$
Track fit quality χ^2/ndf	< 4
χ^2_IP	> 25 (only for B_c^+)
B_c^+ or B^+	
p_T	$> 4\,\mathrm{GeV}/c$
Vertex fit χ^2/ndf	< 9
χ^2_IP	< 5 (only for B_c^+)
τ	$> 0.25\,\mathrm{ps}$
Pseudo-rapidity	$2.5 < \eta < 4.5$
L0 Trigger On Signal	L0Hadron
HLT1 Trigger On Signal	Hlt1TrackAllL0 or Hlt1TrackMuon
HLT2 Trigger On Signal	Hlt2TopoMu2BodyBBDT or HltMu2Topo3BodyBBDT

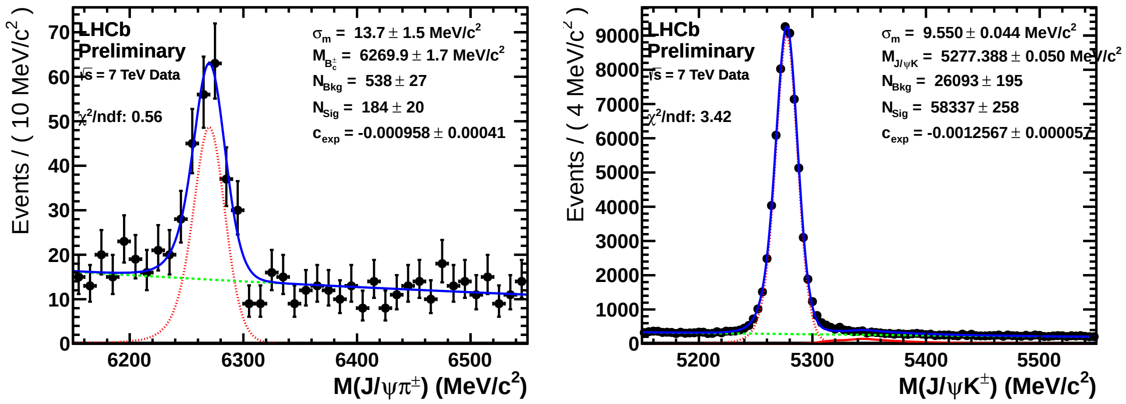

Figure 6.2 Invariant mass distributions of $B_c^+ \to J/\psi\pi^+$ candidates (left) and $B^+ \to J/\psi K^+$ candidates (right) obtained with the analysis selection. Fit results with the shapes described in Section 6.3 are superimposed. The solid blue line is the total fit function described in the text, the dashed red line shows the signal contribution, the green dashed line is the combinatorial background and the red solid line represents the feed-down from Cabbibo suppressed decays.

6.3 Cross-section ratio determination

The production cross-section ratio measured in the analysis is

$$R_{c/u} = \frac{\sigma(B_c^+) \times \mathcal{B}(B_c^+ \to J/\psi\pi^+)}{\sigma(B^+) \times \mathcal{B}(B^+ \to J/\psi K^+)} = \frac{N(B_c^+ \to J/\psi\pi^+)}{\epsilon_{\text{tot}}^c} \times \frac{\epsilon_{\text{tot}}^u}{N(B^+ \to J/\psi K^+)} \tag{6-5}$$

where $N(B_c^+ \to J/\psi\pi^+)$ and $N(B^+ \to J/\psi K^+)$ are the numbers of reconstructed $B_c^+ \to J/\psi\pi^+$ and $B^+ \to J/\psi K^+$signals, and ϵ_{tot}^c and ϵ_{tot}^u are the total efficiencies of $B_c^+ \to J/\psi\pi^+$ and $B^+ \to J/\psi K^+$, respectively, including the geometrical acceptance, and the efficiencies of the reconstruction, selection and trigger. The numbers of reconstructed signal candidates are obtained from a fit to invariant mass distribution of the B candidates. The efficiencies are determined from MC10 simulation sample.

6.3.1 Signal yield determination

The number of signal events are obtained from an extended unbinned maximum likelihood fit to the invariant mass distributions of the reconstructed B_c^+ and B^+, in the interval $M_{J/\psi\pi} \in [6.15; 6.55]\,\text{GeV}/c^2$ for B_c^+ and $M_{J/\psi K} \in [5.15; 5.55]\,\text{GeV}/c^2$ for B^+. The selected events entering the mass distributions can be divided into three components that are reflected in the choice of the fit function. The first component is the signal, which is described by a Cruijff function as described in Section 5.3.1. The Cruijff shapes are parameterized by the same approach in Section 5.3.1, and the parametrization results are demonstrated in Figure 6.3 for B_c^+ and Figure 6.4 for B^+.

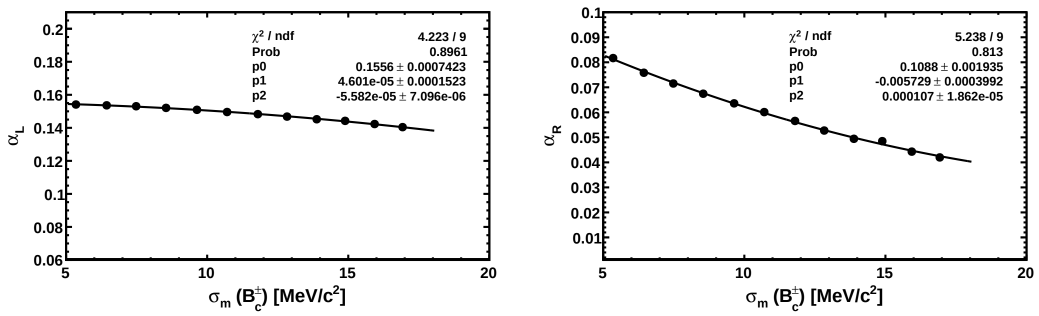

Figure 6.3 Parameterizations of Cruijff parameter for B_c^+ as a function of mass resolution: Left: α_{left}, Right: α_{right}.

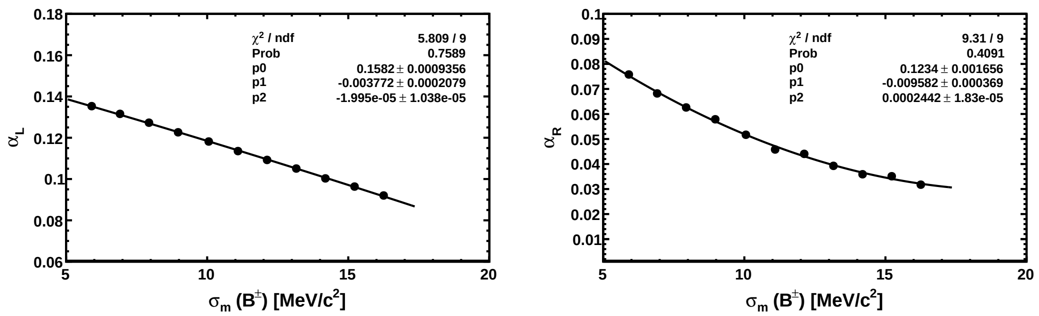

Figure 6.4 Parameterizations of Cruijff parameter for B^+ as a function of mass resolution: Left: α_{left}, Right: α_{right}.

The second component of the fit function is the combinatorial background which is described by the same exponential function used in Section 4.3.1. The last component of the fit function describes feed-down background from the Cabibbo suppressed decay mode $B^+ \to J/\psi\pi^+$. The shape of the Cabibbo suppressed feed-down $B_c^+ \to J/\psi K^+$ is not included in the fit function, since the B_c^+ yield is extremely low. The shape for B^+ is parameterized with a function which is the sum of two Crystal Ball functions as described in Section 4.3.1. And the ratio of the number of $B^+ \to J/\psi\pi^\pm$ candidates to that of the signal is fixed to $\mathcal{B}(B^+ \to J/\psi\pi^+)/\mathcal{B}(B^+ \to J/\psi K^+)$ from Ref.[28]. The total fit function is therefore

$$
\begin{aligned}
F_{\text{mass}}\left(x; M, \sigma, p, N_{\text{signal}}, N_{\text{background}}\right) =& N_{\text{signal}}\, F_{\text{Cruijff}}(x; M, \sigma) \\
&+ N_{\text{background}}\, F_{\text{background}}(x; p) \\
(\text{For B}^+\ ) &+ \frac{\mathcal{B}(B^+ \to J/\psi\pi^+)}{\mathcal{B}(B^+ \to J/\psi K^+)} N_{\text{Signal}} F_{\text{Cabibbo}}(x; M),
\end{aligned}
\tag{6-6}
$$

and has in total five free parameters. The result of the fit is shown in Figure 6.2. The fitted number of signal events is 184 ± 20 for B_c^+ and $58\,337 \pm 258$ for B^+. The mass of B_c^+ is blinded in the fit.

6.3.2 Efficiency calculation

Samples of fully simulated signal $B_c^+ \to J/\psi\pi^+$ and $B^+ \to J/\psi K^+$ events are used to estimate the total efficiencies $\epsilon_{\rm tot}^{c}$ and $\epsilon_{\rm tot}^{+}$. The total efficiencies include the geometrical acceptances $\epsilon_{\rm acc}^{c,+}$, the detection, reconstruction and selection efficiencies combined in an efficiency term $\epsilon_{\rm rec}^{c,+}$ and the trigger efficiencies $\epsilon_{\rm tri}^{c,+}$

$$\epsilon_{\rm tot}^{c,+} = \epsilon_{\rm acc}^{c,+} \times \epsilon_{\rm rec}^{c,+} \times \epsilon_{\rm tri}^{c,+}. \tag{6-7}$$

The first efficiency term is the generator-level acceptance, defined as

$$\epsilon_{\rm acc}^{c,+} = \frac{B_c^+ \text{ or } B^+ \text{ with } 2.5 < \eta < 4.5, p_{\rm T} > 4\,{\rm GeV}/c \text{ and all tracks in LHCb}}{B_c^+ \text{ or } B^+ \text{ with } 2.5 < \eta < 4.5 \text{ and } p_{\rm T} > 4\,{\rm GeV}/c}. \tag{6-8}$$

It is estimated with MC samples generated without any cut at generator level.

The second term of the efficiency $\epsilon_{\rm rec}^{c,+}$ combines the detection, reconstruction and selection efficiencies. It is defined as

$$\epsilon_{\rm rec}^{c,+} = \frac{B_c^+ \text{ or } B^+ \text{ detected, reconstructed and selected}}{B_c^+ \text{ or } B^+ \text{ with } 2.5 < \eta < 4.5, p_{\rm T} > 4\,{\rm GeV}/c \text{ and all tracks in LHCb}}. \tag{6-9}$$

Table 6.2 shows the break-down of the efficiencies of the successive selection requirements. The selection requirement $\tau > 0.3\,{\rm ps}$ is the one showing the highest difference between the B_c^+ and the B^+ selection efficiencies. This is explained by the fact that the two mesons have different lifetimes: $\tau(B_c^+) = 0.453 \pm 0.041\,{\rm ps}$ and $\tau(B^+) = 1.638 \pm 0.011\,{\rm ps}$[28].

The third term is the L0xHLT1xHLT2 trigger efficiency $\epsilon_{\rm tri}^{c,+}$. It is defined as

$$\epsilon_{\rm tri}^{c,+} = \frac{B_c^+ \text{ or } B^+ \text{ selected and with } J/\psi \text{ TOS of L0xHLT1xHLT2}}{B_c^+ \text{ or } B^+ \text{ selected}} \tag{6-10}$$

The total efficiencies calculated from the MC simulation in bins of $p_{\rm T}$ of η are shown in Figure 6.5.

6.3.3 Weighted signal yields

The efficiencies presented in Section 6.3.2 are obtained from the LHCb MC simulation where the B_c^+ and B^+ transverse momentum and pseudo-rapidity distributions are fixed

Table 6.2 Break-down of the selection efficiencies for $B_c^+ \to J/\psi\,\pi^+$ and $B^+ \to J/\psi\,K^+$.

Selection	$B_c^+ \to J/\psi\,\pi^+$	$B^+ \to J/\psi\,K^+$
All charged tracks reconstructed	$(58.27 \pm 0.05)\%$	$(59.00 \pm 0.05)\%$
χ^2/ndf of charged tracks <4	$(99.25 \pm 0.01)\%$	$(99.24 \pm 0.01)\%$
$p_{\mathrm{T}}(\mu) > 900\ \mathrm{MeV}/c$	$(78.96 \pm 0.05)\%$	$(76.13 \pm 0.06)\%$
$\Delta LL_{\mu\pi}(\mu) > 0$	$(83.87 \pm 0.06)\%$	$(83.94 \pm 0.06)\%$
J/ψ vertex χ^2/ndf<9	$(96.10 \pm 0.03)\%$	$(95.80 \pm 0.04)\%$
$M_{\mu\mu} \in [3040, 3140]\ \mathrm{MeV}/c^2$	$(93.91 \pm 0.04)\%$	$(93.86 \pm 0.04)\%$
$p_{\mathrm{T}}(\pi, K) > 1.5\ \mathrm{GeV}/c$	$(77.93 \pm 0.07)\%$	$(70.65 \pm 0.09)\%$
B vertex χ^2/ndf<9	$(98.58 \pm 0.02)\%$	$(98.61 \pm 0.03)\%$
B Mass window	$(98.82 \pm 0.02)\%$	$(99.42 \pm 0.02)\%$
$\tau(B) > 0.25$ ps	$(56.78 \pm 0.10)\%$	$(85.47 \pm 0.08)\%$
$\chi^2_{\mathrm{IP}}(J/\psi) > 4$	$(93.95 \pm 0.06)\%$	—
$\chi^2_{\mathrm{IP}}(\pi) > 25$	$(75.29 \pm 0.12)\%$	—
$\chi^2_{\mathrm{IP}}(B_c) < 25$	$(98.11 \pm 0.04)\%$	—
L0×Hlt1 TOS	$(89.17 \pm 0.10)\%$	$(89.88 \pm 0.07)\%$
Hlt2 TOS	$(96.78 \pm 0.06)\%$	$(97.15 \pm 0.04)\%$
$\epsilon_{\mathrm{sel/rec}}$	$(17.75 \pm 0.05)\%$	$(33.76 \pm 0.07)\%$

from the generator settings in BCVEGPY[59]. However, the B_c^+ spectra are subject to very large theoretical uncertainties and can vary a lot depending on the generator settings.

In order to deal with this problem, since there is not enough statistics to measure the B_c^+ spectra, each signal event is weighted by $(\epsilon_{\mathrm{tot}}^{c,+}(p_{\mathrm{T}}, \eta))^{-1}$, with a weight which is the inverse of the efficiency, as a function of p_{T} and η. The data signal p_{T} and η distributions for the B_c^+ and the B^+ are obtained subtracting the background contributions using the ${}_sPlot$ technique[96], where the signal and background functions are the ones described in Section 6.3.1. Figure 6.6 shows the resulting p_{T} and η distributions used for the signal efficiency corrected yield computations, together with the distributions extracted in the MC10 simulation.

The weighted signal yields are found to be equal to

$$\frac{N(B_c^+ \to J/\psi\,\pi^+)}{\epsilon_{\mathrm{tot}}^{c}} = 2719 \pm 373 \tag{6-11}$$

and

$$\frac{N(B^+ \to J/\psi\,K^+)}{\epsilon_{\mathrm{tot}}^{+}} = 379\,578 \pm 2316. \tag{6-12}$$

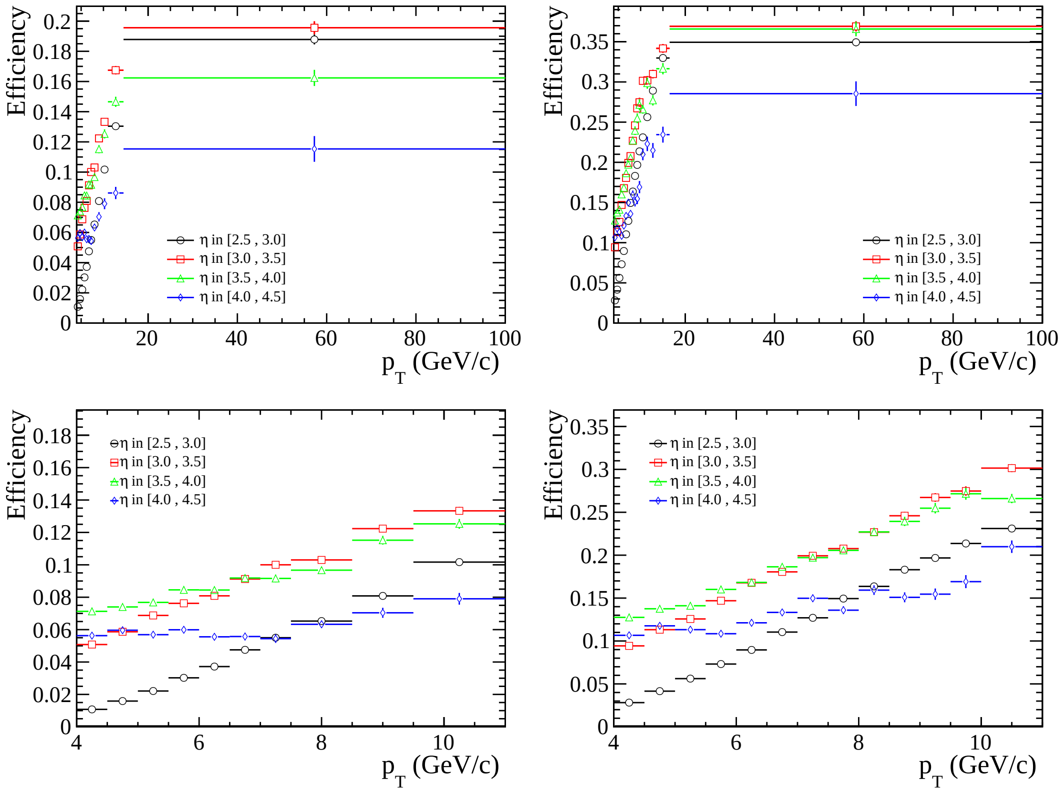

Figure 6.5 MC based total efficiency as a function of $p_{\rm T}$ in bins of η for *top, left*: B_c^+ and *top, right*: B^+ in the $p_{\rm T}$ range $4 < p_{\rm T} < 100\,{\rm GeV}/c$. Zoomed-in plots in the $p_{\rm T}$ range $4 < p_{\rm T} < 10\,{\rm GeV}/c$ are given for *bottom, left*: B_c^+ and *bottom, right*: B^+.

The uncertainties are statistical only. These lead to a ratio of

$$R_{c/u} = \frac{\sigma(B_c^+) \times \mathcal{B}(B_c^+ \to J/\psi\pi^+)}{\sigma(B^+) \times \mathcal{B}(B^+ \to J/\psi K^+)} = (0.72 \pm 0.10)\%. \tag{6-13}$$

6.4 Systematic studies

As discussed in Section 6.3.1, the tail parameters of the signal line shapes are parameterized as a function of the signal mass resolution. Using such parametrization, it is also studied by MC simulation to check how well the fitted number of signals agree with the generated one, as shown in Figure 6.7. The difference between the fitted number of signals and the generated ones is about 1.5% for $B_c^+ \to J/\psi\pi^+$ and 0.5% for $B^+ \to J/\psi K^+$. A systematic uncertainty of 1.5% is assigned.

Repeating the B^+ mass fit without considering the Cabbibo suppressed background affects the number of signal $B^+ \to J/\psi K^+$ events by less than 1%. The systematic uncertainty associated to the determination of Cabbibo suppressed background is therefore neglected.

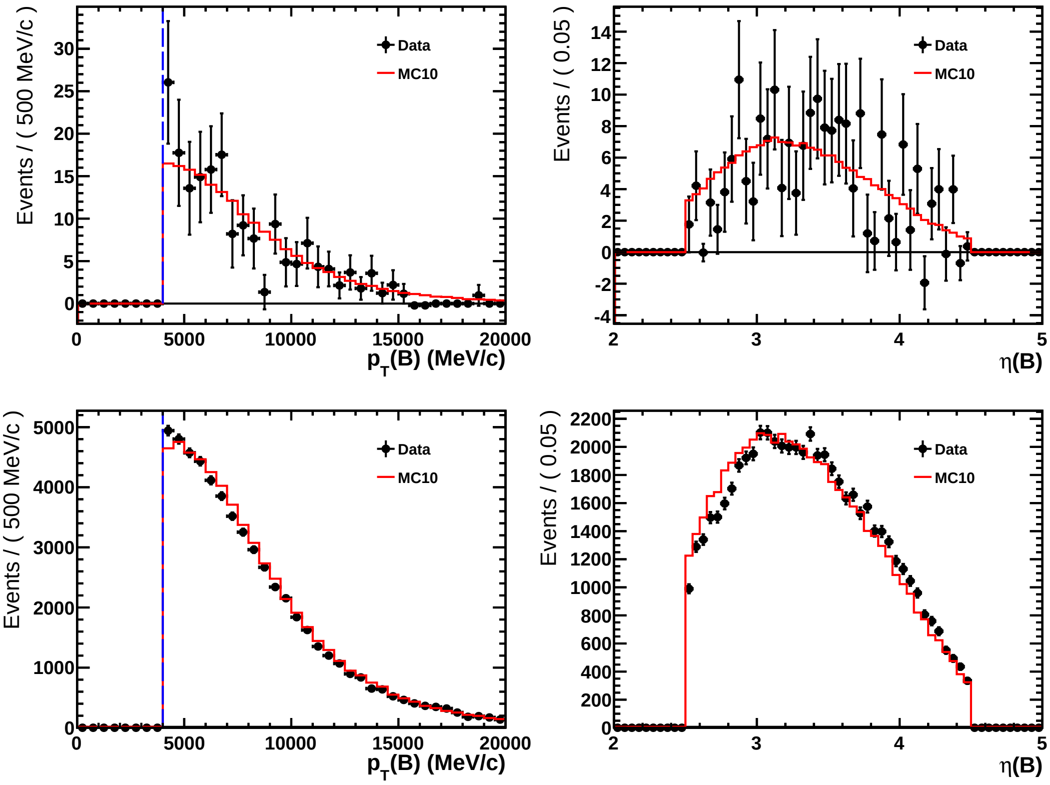

Figure 6.6 Background subtracted distributions for *top,left*: B_c^+ transverse momentum; *top,right*: B_c^+ pseudo-rapidity; *bottom, left*: B^+ transverse momentum; *bottom, right*: B^+ pseudo-rapidity. On all plots, the black dots with error bars represent the data distribution and the red histogram the MC distribution.

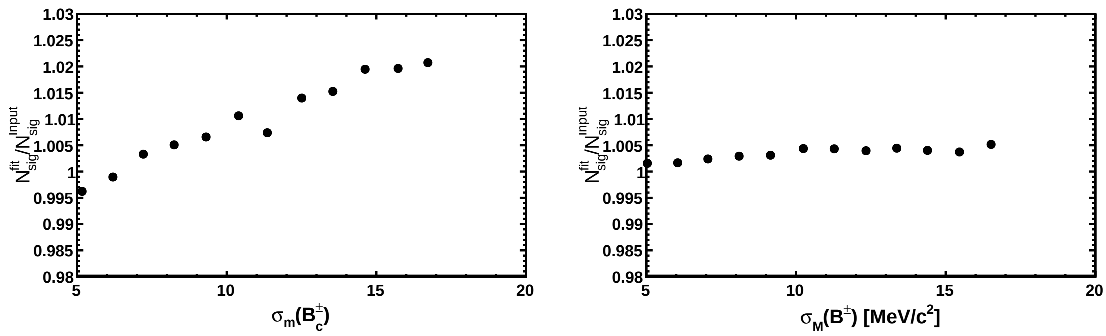

Figure 6.7 The difference between the fitted number of signals and the generated ones for *left*: $B_c^+ \to J/\psi\,\pi^+$ and *right*: $B^+ \to J/\psi\,K^+$.

The main systematic uncertainty comes from the knowledge of the B_c^+ lifetime. The B^+ lifetime is measured with a very small uncertainty[111]: $\tau(B^+) = 1.641 \pm 0.008$ ps and the value used in the simulation software is equal to $\tau(B^+)_{\mathrm{MC}} = 1.638$ ps. No uncertainty will be assigned to errors due to the value of the B^+ lifetime. On the other hand, the B_c^+ lifetime is measured with much less accuracy[111,122,125,127]: $\tau(B_c^+) = 0.461 \pm 0.036$ ps, and the value used in the simulation is $\tau(B_c^+)_{\mathrm{MC}} = 0.45$ ps. The effect from the B_c^+ lifetime uncertainty has been evaluated by changing it with $\pm\sigma$. The B_c^+ signal in the MC simulation sample has been reweighted accordingly to get the effects on the efficiencies, as shown in Table 6.3. Changing the B_c^+ lifetime by $+\sigma$ $(-\sigma)$ would change the relative efficiency

Table 6.3 Effects of varying the B_c^+ lifetime on the efficiencies of $B_c^+ \to J/\psi\pi^+$

Efficiency	$-\sigma$	Central	$+\sigma$
$\epsilon_{\mathrm{sel/rec}}$	(16.69 ± 0.05)%	(17.75 ± 0.05)%	(19.09 ± 0.05)%
$\epsilon_{\mathrm{trg/sel}}$	(86.12 ± 0.11)%	(86.30± 0.11)%	(86.48 ± 0.10)%

$\epsilon_{\mathrm{tot}}^{\mathrm{rel}}(= \frac{\epsilon_{\mathrm{tot}}^{u}}{\epsilon_{\mathrm{tot}}^{c}})$ by -7.3% (+6.5%), The variation 7.3% is assigned as systematic uncertainty.

Quantities used for the $B_c^+ \to J/\psi\pi^+$ and $B^+ \to J/\psi K^+$ selections are compared between the background subtracted distributions of the real data and those of the MC simulation. The comparisons are shown in Figure 6.8. No major deviation from simulation is observed. The vertex χ^2 selection on the B vertex is assumed to have equal efficiencies between B_c^+ and B^+ and thus no uncertainty is assigned. The muon PID related quantities show no large difference between data and simulation, and its uncertainty is negligible. The χ^2 vertex selection on the J/ψ vertex and the χ^2/ndf requirement on the muon tracks have been studied for the J/ψ production cross-section measurement[12]. Differences between the data and simulation have been observed. However, they should affect both $B_c^+ \to J/\psi\pi^+$ and $B^+ \to J/\psi K^+$ in the same way, no systematic uncertainty is assigned.

Discrepancy of MC and data distributions of impact parameter χ^2 is found as shown in Figure 6.9 (left). This discrepancy comes from the misalignments of VELO, and a smearing approach is introduced to smear the transverse position of the points near the beam pipe[132] and reduce the discrepancy. The distributions after smearing is shown in Figure 6.9 (right). The smearing approach affects the $B_c^+ \to J/\psi\pi^+$ and $B^+ \to J/\psi K^+$ at the same time. The production ratio is changed by only 0.2% after the IP smearing and

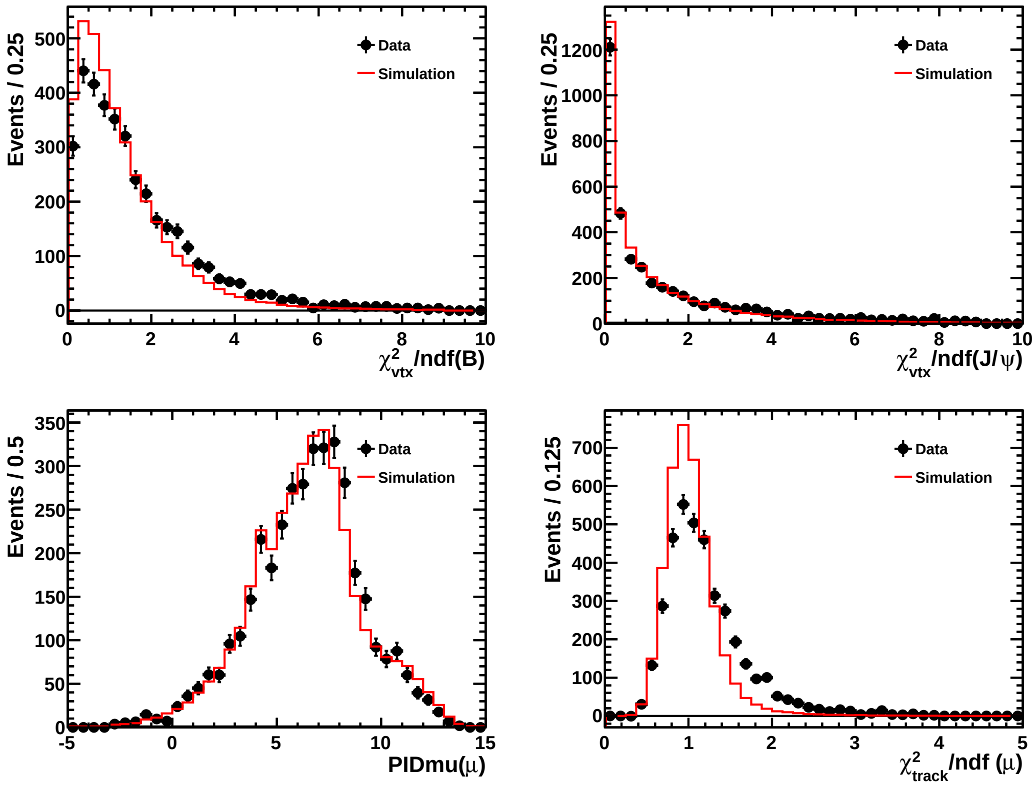

Figure 6.8 Comparison of selection quantities between data (black dots with error bars) and Monte Carlo simulation (red histogram) for $B^+ \to J/\psi\, K^+$: top,left: χ^2/ndf of the B vertex fit; top, right: χ^2/ndf of the J/ψ vertex fit; bottom, left: $\Delta \mathrm{LL}_{\mu\pi}$ of μ; bottom, right: μ track χ^2/ndf

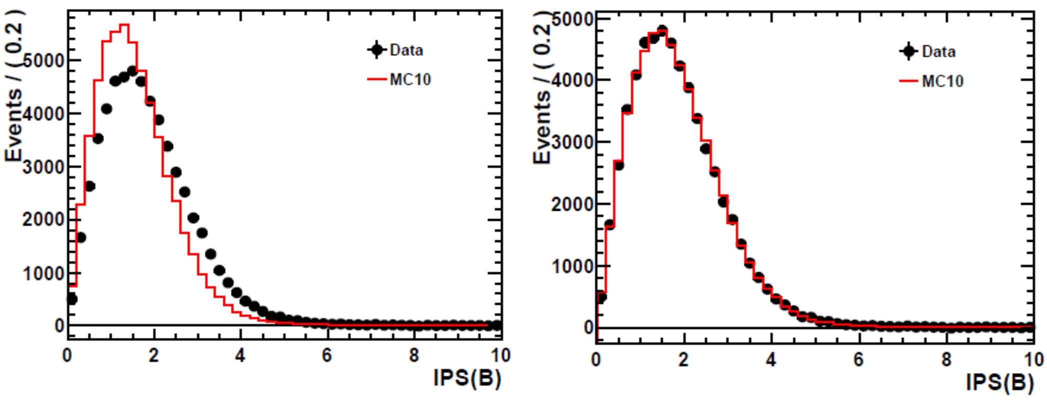

Figure 6.9 Comparison of IP χ^2 between data (black dots with error bars) and MC simulation (red histogram) for B^+ *left*: before and *right*: after IP smearing.

this effect is neglected.

Global event variable multiplicities are assumed to be equal between B_c^+ events and B^+ events, therefore global event cuts are assumed to have the same efficiency on $B^+ \to J/\psi K^+$ and $B_c^+ \to J/\psi \pi^+$ events, and their effect cancels in the ratio. No uncertainty is assigned to GEC.

The effect of the trigger requirement is estimated by repeating the analysis approach using a set of lifetime unbiased triggers. The lifetime unbiased triggers are listed in Table 6.4. The invariant mass distributions of the candidates obtained with the life time unbiased TOS trigger requirements together with the fit results are shown in Figure 6.10.

Table 6.4 The lifetime unbiased trigger lines used for the estimation of systematic uncertainty due to trigger efficiency.

Trigger line	Main cuts
L0Muon	Spd(Mult)< 600 && $p_{\mathrm{T}}(\mu) > 1.48\,\mathrm{GeV}/c$
L0DiMuon	Spd(Mult)< 900 && $p_{\mathrm{T}}(\mu_1) \times p_{\mathrm{T}}(\mu_2) > 1.68(\,\mathrm{GeV}/c)^2$
Hlt1DiMuonHighMass	*L0Muon* or *L0DiMuon*
	$p_{\mathrm{T}}(\mu) > 0.5\,\mathrm{GeV}/c$ and $p(\mu) > 6\,\mathrm{GeV}/c$
	$M_{\mu\mu} > 2.7\,\mathrm{GeV}/c^2$
Hlt2DiMuonJPsi	$M_{\mu\mu} \in [M_{J/\psi} - 120\,\mathrm{MeV}/c^2; M_{J/\psi} + 120\,\mathrm{MeV}/c^2]$,

The difference on the ratio caused by changing trigger set is found to be 8.0% and is assigned as the systematic uncertainty due to trigger efficiency.

In order to estimate the effect from the differences of the tracking efficiencies between data and MC simulation, the track reconstruction efficiency table in bins of p_{T} and η of charged tracks, as used in Section 5.3.2, is employed. Weighting this efficiency table to the simulated $B_c^+ \to J/\psi \pi^+$ and $B^+ \to J/\psi K^+$ MC samples affects the ratio of reconstruction efficiency between the two modes by 0.2%. An additional 2% systematic uncertainty is assigned due to hadronic interaction length of the detector in the MC simulation. This number is used as systematic uncertainty related to the tracking efficiency.

The determination of the ratio is repeated using different efficiency p_{T} bin sizes, and the effects of changing bin sizes are listed in Table 6.5. The effects due to bin size are negligible and no systematic uncertainty is assigned.

The systematic uncertainties that affect the cross-section ratio $R_{c/u}$ are summarized

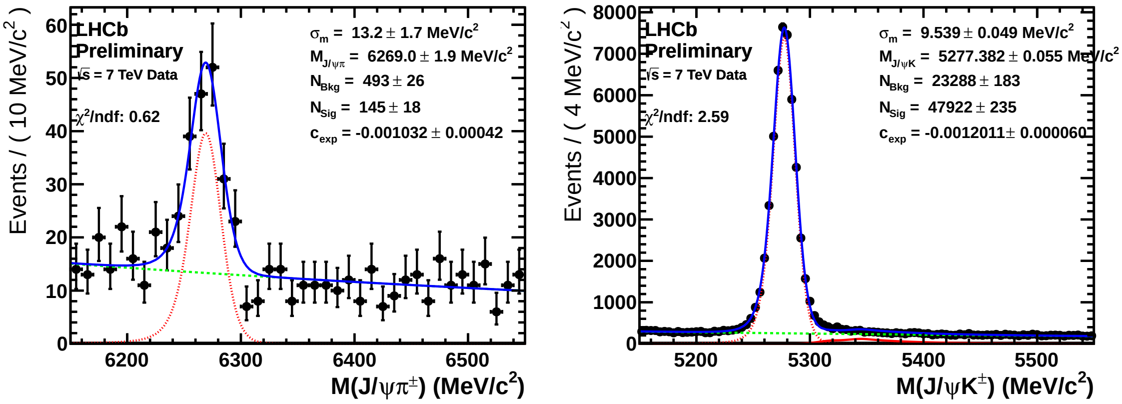

Figure 6.10 Invariant mass distributions of $B_c^+ \to J/\psi\,\pi^+$ candidates (left) and $B^+ \to J/\psi\,K^+$ candidates (right) obtained with the TOS of (di-)muon trigger requirements. The results of fits to the models described in the text are superimposed. On the mass distributions, the solid blue line is the total fit function, the dashed red line shows the signal contribution, the green dashed line is the combinatorial background and the red solid line is the feed-down from Cabbibo suppressed decays.

Table 6.5 Ratios measured using different efficiency p_{T} bin sizes.

Bin size (MeV/c)	B_c^+ yield	B^+ yield	Ratio (%)	Difference (%)
1000	2698	377435	0.715	0.7
250	2665	377115	0.707	0.5

in Table 6.6.

6.5 Result and discussions

The ratio of B_c^+ to B^+ production is measured to be

$$\begin{aligned} R_{c/u}(4 < p_{\mathrm{T}} < 100\,\mathrm{GeV}/c, 2.5 < \eta < 4.5) &= \frac{\sigma(B_c^+) \times \mathcal{B}(B_c^+ \to J/\psi\,\pi^+)}{\sigma(B^+) \times \mathcal{B}(B^+ \to J/\psi\,K^+)} \\ &= 0.72 \pm 0.10\,(\text{stat.}) \pm 0.08\,(\text{syst.})\%. \end{aligned}$$

This result may shed light on the production mechanism of doubly flavored hadrons.

The precision of this measurement is dominated by the limited statistics and can be improved with more data in 2012. Any absolute measurement of the B_c^+ production cross-section will be very difficult until an absolute branching fraction of a B_c^+ decay is established, or would rely on theoretical computations of these branching fractions.

Table 6.6 Summary of systematic uncertainties.

Quantity	Systematic uncertainty (%)
Fit model	1.5
B_c^+ lifetime	7.3
Selection	negligible
GEC	negligible
Cabibbo suppressed background	negligible
Trigger	8.0
Tracking	negligible
Nuclear interaction	2.0
Bin size	0.7
Total	11.0

Chapter 7 Summary

The first measurements of B^+ production cross-section in the forward region at $\sqrt{s} = 7$ TeV have been presented in this dissertation. The production cross-sections are measured individually using two data samples collected by the LHCb detector: $34.6 \pm 1.2\,\text{pb}^{-1}$ of data taken in 2010 and $370 \pm 13\,\text{pb}^{-1}$ in 2011. The B^+ mesons are reconstructed exclusively in the $B^+ \to J/\psi K^+$ mode, with $J/\psi \to \mu^+\mu^-$. The differential production cross-sections are measured as a function of the B^+ transverse momentum in the fiducial region $0 < p_T < 40$ GeV/c and with rapidity $2.0 < y < 4.5$. The total cross-sections are measured to be

$$\sigma(B^+, 0 < p_T < 40\,\text{GeV}/c, 2.0 < y < 4.5) = 41.4 \pm 1.4\,(\text{stat.}) \pm 3.2\,(\text{syst.})\ \mu\text{b}$$

using the 2010 data and

$$\sigma(B^+, 0 < p_T < 40\,\text{GeV}/c, 2.0 < y < 4.5) = 41.6 \pm 0.3\,(\text{stat.}) \pm 2.7\,(\text{syst.})\ \mu\text{b}$$

using the 2011 data. These two results are in good agreement.

The first measurements of B^0 and B_s^0 production cross-sections in the forward region at $\sqrt{s} = 7$ TeV have been reported in this dissertation. The production cross-sections are measured using $370 \pm 13\,\text{pb}^{-1}$ of data taken by the LHCb detector in 2011. The B^0 mesons are reconstructed exclusively in the $B^0 \to J/\psi K^{*0}$ mode, with $J/\psi \to \mu^+\mu^-$ and $K^{*0} \to K^+\pi^-$, while the B_s^0 mesons in the $B_s^0 \to J/\psi \phi$ mode, with $J/\psi \to \mu^+\mu^-$ and $\phi \to K^+K^-$. The differential production cross-section for B^0 is measured as a function of the transverse momentum and rapidity in the fiducial region $2 < p_T < 40$ GeV/c and with rapidity $2.0 < y < 4.5$, while for B_s^0 is measured as a function of the transverse momentum in the fiducial region $0 < p_T < 40$ GeV/c and with rapidity $2.0 < y < 4.5$. The differential cross-sections are given in this dissertation. The total cross-sections are measured to be

$$\begin{aligned}
\sigma(B^0, 2 < p_T < 40\,\text{GeV}/c, 2.0 < y < 4.5) &= 32.3 \pm 0.4\,(\text{stat.}) \pm 2.4\,(\text{syst.})\ \mu\text{b}, \\
\sigma(B_s^0, 0 < p_T < 40\,\text{GeV}/c, 2.0 < y < 4.5) &= 7.9 \pm 0.2\,(\text{stat.}) \pm 2.5\,(\text{syst.})\ \mu\text{b}.
\end{aligned}$$

Comparisons of the measured differential production cross-sections with the FONLL theoretical predictions using CTEQ6.6 PDF are given and good agreements for B^+

and B^0 are observed. In 2011 B^+ analysis, the larger statistics improve the capacity of this measurement in the high p_{T} region and give excellent agreement between the measurement and theory. The large systematic uncertainty from the $\mathcal{B}(B_s^0 \to J/\psi\,\phi)$ limits the precision of the B_s^0 cross-section. A better measurement of $\mathcal{B}(B_s^0 \to J/\psi\,\phi)$ will help to clarify the possible discrepancy between the measurement and theoretical predictions. A measurement of the Λ_b production cross-section could be a good continuation of these measurements. We can combine the absolute cross-section results to measure the b hadronization fractions.

The first measurement of the B_c^+ production ratio in the forward region at $\sqrt{s} = 7$ TeV has been given in this dissertation. Since no absolute B_c^+ branching fraction has been determined, the branching fractions of $B_c^+ \to J/\psi\,\pi^+$ and $B^+ \to J/\psi\,K^+$, through which modes the B_c^+ and B^+ mesons are reconstructed, respectively, are involved in the ratio measurement. The ratio of the B_c^+ with respect to B^+ production cross-sections is measured to be

$$\begin{aligned} R_{c/u} &= \frac{\sigma(B_c^+) \times \mathcal{B}(B_c^+ \to J/\psi\,\pi^+)}{\sigma(B^+) \times \mathcal{B}(B^+ \to J/\psi\,K^+)} \\ &= 0.72 \pm 0.10\,(\text{stat.}) \pm 0.08\,(\text{syst.})\% \end{aligned}$$

in the fiducial region $4 < p_{\mathrm{T}} < 100\,\text{GeV}/c$ and with pseudo rapidity $2.5 < \eta < 4.5$. This result can help to get further theoretical progress in understanding the production mechanisms of heavy quark bound states. The precision of this measurement is dominated by the low statistics and can be improved using more data collected in 2012. A precise measurement of the B_c^+ lifetime will also be an important step forward.

Reference

[1] L. Evans and P. Bryant, *LHC Machine*, JINST **3** (2008) S08001.

[2] The LHCb Collaboration, A. A. Alves Jr. *et al.*, *The LHCb detector at the LHC*, JINST **3** (2008) S08005.

[3] P. Nason, S. Dawson, and R. K. Ellis, *The total cross-section for the production of heavy quarks in hadronic collisions*, Nucl. Phys. **B303** (1988) 607.

[4] M. Cacciari, M. Greco, and P. Nason, *The p_T spectrum in heavy flavor hadroproduction*, JHEP **9805** (1998) 007, `arXiv:hep-ph/9803400`.

[5] M. Cacciari, S. Frixione, and P. Nason, *The p_T spectrum in heavy flavor photoproduction*, JHEP **0103** (2001) 006, `arXiv:hep-ph/0102134`.

[6] M. Cacciari *et al.*, *QCD analysis of first b cross-section data at 1.96 TeV*, JHEP **0407** (2004) 033, `arXiv:hep-ph/0312132`.

[7] The CDF Collaboration, A. Abulencia *et al.*, *Measurement of the B^+ production cross-section in $p\bar{p}$ collisions at $\sqrt{s}$ = 1960 GeV*, Phys. Rev. **D75** (2007) 012010, `arXiv:hep-ex/0612015`.

[8] The CMS Collaboration, V. Khachatryan *et al.*, *Measurement of the B^+ production cross section in pp collisions at $\sqrt{s}$ = 7 TeV*, Phys. Rev. Lett. **106** (2011) 112001, `arXiv:1101.0131`.

[9] The CMS Collaboration, S. Chatrchyan *et al.*, *Measurement of the B^0 production cross section in pp collisions at $\sqrt{s}$ = 7 TeV*, Phys. Rev. Lett. **106** (2011) 252001, `arXiv:1104.2892`.

[10] The CMS Collaboration, S. Chatrchyan *et al.*, *Measurement of the strange B meson production cross section with J/ψ ϕ decays in pp collisions at $\sqrt{s}$ = 7 TeV*, Phys. Rev. **D84** (2011) 052008, `arXiv:1106.4048`.

[11] The LHCb Collaboration, R. Aaij *et al.*, *Measurement of $\sigma(pp \to b\bar{b}X)$ at $\sqrt{s}$ = 7 TeV in the forward region*, Phys. Lett. **B694** (2010) 209, `arXiv:1009.2731`.

[12] The LHCb Collaboration, R. Aaij *et al.*, *Measurement of J/ψ production in pp collisions at $\sqrt{s}$=7 TeV*, Eur. Phys. J. **C71** (2011) 1645, `arXiv:1103.0423`.

[13] C. Gao and J. Zeng, *Lectures on particle physics and nuclear physics*. Higher Education Press, Beijing, China, 1990.

[14] S. Weinberg, *Quantum Field Theory, Vols. I to III*. Cambridge University Press, Cambridge, UK., 2000.

[15] Z. Ma, *Applications of group theory in Particle Physics*. Science Press, Beijing, China, 1998.

[16] D. H. Perkins, *Introduction to high energy physics*. Cambridge University Press, Cambridge, UK., 1999.

[17] P. A. M. Dirac, *On the theory of quantum mechanics*, Proceedings of the Royal Society of London. Series A **112** (1926), no. 762 661.

[18] S. L. Glashow, J. Iliopoulos, and L. Maiani, *Weak Interactions with Lepton-Hadron Symmetry*, Phys. Rev. **D2** (1970) 1285.

[19] T. D. Lee and C. N. Yang, *Question of parity conservation in weak interactions*, Phys. Rev. **104** (1956) 254.

[20] M. Kobayashi and T. Maskawa, *Cp-violation in the renormalizable theory of weak interaction*, Progress of Theoretical Physics **49** (1973), no. 2 652.

[21] I. Bigi and A. Sanda, *CP Violation*. Cambridge University Press, 1999.

[22] CKMfitter Group, J. Charles *et al.*, *CP violation and the CKM matrix: Assessing the impact of the asymmetric B factories*, Eur. Phys. J. **C41** (2005) 1, arXiv:hep-ph/0406184.

[23] P. Higgs, *Broken symmetries, massless particles and gauge fields*, Physics Letters **12** (1964), no. 2 132 .

[24] The ATLAS Collaboration, *Combined search for the Standard Model Higgs boson using up to 4.9 fb^{-1} of pp collision data at $\sqrt{s}$ = 7 TeV with the ATLAS detector at the LHC*, arXiv:1202.1408.

[25] The CMS Collaboration, S. Chatrchyan *et al.*, *Combined results of searches for the standard model Higgs boson in pp collisions at $\sqrt{s}$ = 7 TeV*, arXiv:1202.1488.

[26] The Super-Kamiokande Collaboration, Y. Fukuda *et al.*, *Measurements of the solar neutrino flux from Super-Kamiokande's first 300 days*, Phys. Rev. Lett. **81** (1998) 1158, arXiv:hep-ex/9805021.

[27] V. Trimble, *Existence and nature of dark matter in the universe*, Annual Review of Astronomy and Astrophysics **25** (1987) 425.

[28] Particle Data Group, K. Nakamura *et al.*, *Review of particle physics*, J. Phys. G **37** (2010) 075021.

[29] R. Ellis, W. Stirling, and B. Webber, *QCD and collider physics*. Higher Education Press, Beijing, China, 1996.

[30] C. Becchi, A. Rouet, and R. Stora, *Renormalization of gauge theories*, Annals of Physics **98** (1976), no. 2 287 .

[31] C. Cao, *Non-Abelien guage field theory*. Science Press, Beijing, China, 2008.

[32] Y. Dai, *Gauge theory of interactions*. Science Press, Beijing, China, 2005.

[33] S. Weinberg, *New approach to the renormalization group*, Phys. Rev. D **8** (1973) 3497.

[34] I. I. Bigi *et al.*, *The pole mass of the heavy quark. Perturbation theory and beyond*, Phys. Rev. **D50** (1994) 2234, arXiv:hep-ph/9402360.

[35] M. Beneke, *Renormalons*, Phys. Rept. **317** (1999) 1, arXiv:hep-ph/9807443.

[36] H. Harari, *A new quark model for hadrons*, Physics Letters B **57** (1975), no. 3 265 .

[37] S. W. Herb *et al.*, *Observation of a dimuon resonance at 9.5* GeV *in 400-* GeV *proton-nucleus collisions*, Phys. Rev. Lett. **39** (1977) 252.

[38] J. D. Bjorken and E. A. Paschos, *Inelastic electron-proton and γ-proton scattering and the structure of the nucleon*, Phys. Rev. **185** (1969) 1975.

[39] J. C. Collins, D. E. Soper, and G. F. Sterman, *Factorization for Short Distance Hadron - Hadron Scattering*, Nucl. Phys. **B261** (1985) 104.

[40] V. N. Gribov and L. N. Lipatov, *Deep inelastic e p scattering in perturbation theory*, Sov. J. Nucl. Phys. **15** (1972) 438.

[41] G. Altarelli and G. Parisi, *Asymptotic Freedom in Parton Language*, Nucl. Phys. **B126** (1977) 298.

[42] Y. L. Dokshitzer, *Calculation of the Structure Functions for Deep Inelastic Scattering and e+ e- Annihilation by Perturbation Theory in Quantum Chromodynamics*, Sov. Phys. JETP **46** (1977) 641.

[43] P. Nason *et al.*, *Bottom production*, `arXiv:hep-ph/0003142`.

[44] E. A. Kuraev, L. N. Lipatov, and V. S. Fadin, *The Pomeranchuk Singularity in Nonabelian Gauge Theories*, Sov. Phys. JETP **45** (1977) 199.

[45] I. I. Balitsky and L. N. Lipatov, *The Pomeranchuk Singularity in Quantum Chromodynamics*, Sov. J. Nucl. Phys. **28** (1978) 822.

[46] J. Collins, F. Wilczek, and A. Zee, *Low-energy manifestations of heavy particles: Application to the neutral current*, Phys. Rev. D **18** (1978) 242.

[47] M. Cacciari and M. Greco, *Large p_T hadroproduction of heavy quarks*, Nucl. Phys. **B421** (1994) 530, `arXiv:hep-ph/9311260`.

[48] C. Peterson *et al.*, *Scaling Violations in Inclusive e+ e- Annihilation Spectra*, Phys. Rev. **D27** (1983) 105.

[49] M. Cacciari, *FONLL Heavy Quark Production*. http://www.lpthe.jussieu.fr/~cacciari/fonll/fonllform-5.html.

[50] E. Braaten, K.-m. Cheung, and T. C. Yuan, *Perturbative QCD fragmentation functions for B_c and B_c^* production*, Phys. Rev. **D48** (1993) 5049, `arXiv:hep-ph/9305206`.

[51] K.-m. Cheung, *B_c meson production at the Tevatron revisited*, Phys. Lett. **B472** (2000) 408, `arXiv:hep-ph/9908405`.

[52] P. Artoisenet, J. Lansberg, and F. Maltoni, *Hadroproduction of J/ψ and Υ in association with a heavy-quark pair*, Phys. Lett. **B653** (2007) 60, `arXiv:hep-ph/0703129`.

[53] N. Brambilla *et al.*, *Heavy quarkonium: progress, puzzles, and opportunities*, Eur. Phys. J. **C71** (2011) 1534, `arXiv:1010.5827`.

[54] C.-H. Chang *et al.*, *Hadronic production of $B_c(B_c^*)$ meson induced by the heavy quarks inside the collision hadrons*, Phys. Rev. **D72** (2005) 114009, `arXiv:hep-ph/0509040`.

[55] F. I. Olness, R. Scalise, and W.-K. Tung, *Heavy quark hadroproduction in perturbative QCD*, Phys. Rev. **D59** (1999) 014506, `arXiv:hep-ph/9712494`.

[56] C.-H. Chang, Y.-Q. Chen, G.-P. Han, and H.-T. Jiang, *On hadronic production of the B_c meson*, Phys. Lett. **B364** (1995) 78, `arXiv:hep-ph/9408242`.

[57] K. Kolodziej, A. Leike, and R. Ruckl, *Production of B_c mesons in hadronic collisions*, Phys. Lett. **B355** (1995) 337, `arXiv:hep-ph/9505298`.

[58] T. Sjostrand, S. Mrenna, and P. Z. Skands, *PYTHIA 6.4 Physics and Manual*, JHEP **0605** (2006) 026, `arXiv:hep-ph/0603175`.

[59] C.-H. Chang *et al.*, *BCVEGPY: An event generator for hadronic production of the B_c meson*, Comput. Phys. Commun. **159** (2004) 192, `arXiv:hep-ph/0309120`.

[60] C.-H. Chang, J.-X. Wang, and X.-G. Wu, *BCVEGPY2.0: A upgrade version of the generator BCVEGPY with an addendum about hadroproduction of the P-wave B/c states*, Comput. Phys. Commun. **174** (2006) 241, `arXiv:hep-ph/0504017`.

[61] C.-H. Chang, J.-X. Wang, and X.-G. Wu, *An upgraded version of the generator BCVEGPY2.0 for hadronic production of B_c^+ meson and its excited states*, Comput. Phys. Commun. **175** (2006) 624, `arXiv:hep-ph/0604238`.

[62] A. Einstein, *Ist die trägheit eines körpers von seinem energieinhalt abhängig?*, Annalen der Physik **323** (1905), no. 13 639.

[63] L. D. Broglie, *Researches on the quantum theory*. PhD thesis, Paris, 1924.

[64] L. D. BroglieAnn. Phys. **3** (1925) 22.

[65] B. Gorini and E. Meschi, *LHC Programme Coordination web pages*. http://lpc.web.cern.ch/lpc/.

[66] LHC Experiments Committee, *LHCb : Technical Proposal*. Tech. Proposal. CERN, Geneva, 1998.

[67] R. Antunes-Nobrega *et al.*, *LHCb reoptimized detector design and performance: Technical Design Report*. Technical Design Report LHCb. CERN, Geneva, 2003.

[68] S. Amato *et al.*, *LHCb magnet: Technical Design Report*. Technical Design Report LHCb. CERN, Geneva, 2000.

[69] M. Patel, M. Losasso, and T. Gys, *Magnetic shielding studies of the lhcb rich photon detectors*, Nuclear Instruments and Methods in Physics Research Section A: Accelerators, Spectrometers, Detectors and Associated Equipment **553** (2005), no. 1-2 114 , Proceedings of the fifth International Workshop on Ring Imaging Detectors.

[70] The LHCb VELO Group, *Performance of the LHCb Vertex Locator*. LHCb detector paper to be published.

[71] M. van Beuzekom, *Performance of the lhcb detector during 2010-2011 data taking*, Tech. Rep. LHCb-PROC-2012-012;LHCb-TALK-2011-147; CERN-LHCb-PROC-2012-012, CERN, Geneva, Feb, 2012.

[72] The LHCb OT Group, *Performance of the LHCb Outer Tracker*. LHCb detector paper to be published.

[73] The LHCb Collaboration, R. Aaij *et al.*, *Measurement of b-hadron masses*, Phys. Lett. **B708** (2012) 241, `arXiv:1112.4896`.

[74] Nobelprize.org, *The Nobel Prize in physics 1958 C P. A. Cherenkov*. http://www.nobelprize.org/nobel_prizes/physics/laureates/1958/.

[75] R. W. Forty and O. Schneider, *Rich pattern recognition*, Tech. Rep. LHCb-98-040, CERN, Geneva, Apr, 1998.

[76] The LHCb RICH group, *PID performance plots*. https://lbtwiki.cern.ch/bin/view/RICH/RichPIDPerformancePlots.

[77] J. Badier *et al.*, *Shashlik calorimeter beam-test results*, Nuclear Instruments and Methods in Physics Research Section A: Accelerators, Spectrometers, Detectors and Associated Equipment **348** (1994), no. 1 74 .

[78] The LHCb Muon Group, E. Helder, B. Matteo, and J. Xabier, *Status of the muonID performance paper*. https://indico.cern.ch/contributionDisplay.py?contribId=25&confId=181368.

[79] R. Antunes-Nobrega *et al.*, *LHCb trigger system: Technical Design Report*. Technical Design Report LHCb. CERN, Geneva, 2003.

[80] The LHCb Collaboration, *The BRUNEL Project*. http://lhcb-release-area.web.cern.ch/LHCb-release-area/DOC/brunel/.

[81] The LHCb Collaboration, *The GAUSS Project*. http://lhcb-release-area.web.cern.ch/LHCb-release-area/DOC/gauss/.

[82] The LHCb Collaboration, *The BOOLE Project*. http://lhcb-release-area.web.cern.ch/LHCb-release-area/DOC/boole/.

[83] The LHCb Collaboration, *The MOORE Project*. http://lhcb-release-area.web.cern.ch/LHCb-release-area/DOC/moore/.

[84] I. Belyaev *et al.*, *Handling of the generation of primary events in Gauss, the LHCb simulation framework*, Nuclear Science Symposium Conference Record (NSS/MIC) **IEEE** (2010) 1155.

[85] D. J. Lange, *The EVTGEN particle decay simulation package*, Nucl. Instrum. Methods A **462** (2001) 152.

[86] P. Golonka and Z. Was, *PHOTOS Monte Carlo: A Precision tool for QED corrections in Z and W decays*, Eur. Phys. J. **C45** (2006) 97, `arXiv:hep-ph/0506026`.

[87] The GEANT4 Collaboration, S. Agostinelli *et al.*, *GEANT4: a simulation toolkit*, Nucl. Instrum. Methods A **506** (2003) 250.

[88] The LHCb Collaboration, *The DIRAC Project*. http://lhcb-release-area.web.cern.ch/LHCb-release-area/DOC/lhcbdirac/.

[89] J. T. Mościcki *et al.*, *GANGA: A tool for computational-task management and easy access to Grid resources*, Computer Physics Communications **180** (2009) 2303, `arXiv:0902.2685`.

[90] The LHCb Collaboration, *The DAVINCI Project*. http://lhcb-release-area.web.cern.ch/LHCb-release-area/DOC/davinci/.

[91] The ROOT development team, *The ROOT Project*. http://root.cern.ch/drupal/.

[92] V. E. Herwijnen, *The lhcb trigger*, Tech. Rep. LHCb-PROC-2010-055 ; CERN-LHCb-PROC-2010-055, CERN, Geneva, Jul, 2010.

[93] S. Kullback and R. Leibler, *On information and sufficiency*, Annals of Mathematical Statistics **22** (1951) 79.

[94] S. Kullback, *Letter to editor: the Kullback-Leibler distance*, The American Statistician **41** (1987) 340.

[95] M. Needham, *Clone track identification using the kullback-liebler distance*, Tech. Rep. LHCb-2008-002. CERN-LHCb-2008-002. LPHE-2008-002, CERN, Geneva, Jan, 2008.

[96] M. Pivk and F. R. Le Diberder, *sPlots: A statistical tool to unfold data distributions*, Nuclear Instruments and Methods in Physics Research A **555** (2005) 356, `physics/0`.

[97] J. E. Gaiser, *Charmonium spectroscopy from radiative decays of the J/ψ and ψ'*, Ph.D. Thesis, SLAC-R-255 (1982).

[98] T. Skwarnicki, *A study of the radiative cascade transitions between the Υ' and Υ resonances*, Ph.D. Thesis, DESY-F31-86-02 (1986).

[99] The LHCb Collaboration, R. Aaij *et al.*, *Measurement of the B^+ production cross-section in pp collisions at $\sqrt{s} = 7$ TeV*, arXiv:1202.4812.

[100] The LHCb Collaboration, R. Aaij *et al.*, *Prompt K_s^0 production in pp collisions at $\sqrt{s} = 0.9$ TeV*, Phys. Lett. **B693** (2010) 69, arXiv:1008.3105.

[101] A. Jaeger, P. Seyfert, M. De Cian, J. van Tilburg, and S. Hansmann-Menzemer, *Measurement of the track finding efficiency*, Tech. Rep. LHCb-PUB-2011-025. CERN-LHCb-PUB-2011-025, CERN, Geneva, Nov, 2011.

[102] The LHCb tracking group, *LHCb tracking performance web page*. https://twiki.cern.ch/twiki/bin/view/LHCb/TrackingEffStatusUpdated.

[103] The LHCb tracking group, *Correcting for the tracking efficiency in your MC*. https://twiki.cern.ch/twiki/bin/view/LHCb/TrackingEffRatio.

[104] The LHCb tracking group, *Tracking strategies used in LHCb*. https://twiki.cern.ch/twiki/bin/view/LHCb/LHCbTrackingStrategies.

[105] The LHCb Collaboration, R. Aaij *et al.*, *Absolute luminosity measurements with the LHCb detector at the LHC*, arXiv:1110.2866.

[106] T. C. Collaboration, *Questions submitted to the cdf statistics committee*, http://www-cdf.fnal.gov/physics/statistics/statistics_faq.html#ssel4.

[107] The LHCb tracking group, *Information on the absorption of hadrons*. https://twiki.cern.ch/twiki/bin/view/LHCb/TrackingEffAbsLength.

[108] *Engineering statistics handbook*, http://www.itl.nist.gov/div898/handbook/eda/section3/eda366b.htm.

[109] The BaBar Collaboration, B. Aubert *et al.*, *Measurement of branching fractions and charge asymmetries for exclusive B decays to charmonium*, Phys. Rev. Lett. **94** (2005) 141801, arXiv:hep-ex/0412062.

[110] The LHCb Collaboration, R. Aaij *et al.*, *Measurement of b hadron production fractions in 7 TeV pp collisions*, arXiv:1111.2357.

[111] Heavy Flavor Averaging Group, D. Asner *et al.*, *Averages of b-hadron, c-hadron, and τ-lepton properties*, arXiv:1010.1589.

[112] The LHCb RICH group, *PIDCalib packages*. https://twiki.cern.ch/twiki/bin/view/LHCb/PIDCalibPackage.

[113] The LHCb Online Group, J. Panman, *Online luminosity*. http://indico.cern.ch/getFile.py/access?subContId=3&contribId=1&resId=1&materialId=slides&confId=134896.

[114] The LHCb Online Group, J. Panman, *On-line aspects of "off-line" luminosity: relative luminosity tracking for 2011 data*. http://indico.cern.ch/getFile.py/access?contribId=20&resId=0&materialId=slides&confId=159865.

[115] The LHCb Online Group, J. Panman, *Online versus offline luminosity for 2011 data*. https://indico.cern.ch/contributionDisplay.py?contribId=1&confId=134905.

[116] B. Pal, S. Stone, and L. Zhang, *Absolute b of* $b_s \rightarrow J/\psi\pi^+\pi^- \& B_s^0 \rightarrow J/\psi\phi$, http://indico.cern.ch/getFile.py/access?contribId=2&resId=0&materialId=slides&confId=168717

[117] B. A. *et al.*, $B^0 \rightarrow J/\psi K^{*0}$ *angular analysis with 1* fb^{-1}, https://indico.cern.ch/getFile.py/access?contribId=5&resId=0&materialId=slides&confId=181432.

[118] The CDF collaboration, *Angular analysis of* $B_s^0 \rightarrow J/\psi\phi$ *and* $B^0 \rightarrow J/\psi K^{*0}$ *decays and measurement of* $\Delta\Gamma_s$ *and* ϕ_s, Tech. Rep. CDF public note (8950). http://www-cdf.fnal.gov/physics/new/bottom/070809.blessed-DG-BsPsiPhi/.

[119] The CDF Collaboration, D. Acosta *et al.*, *Measurement of the lifetime difference between B(s) mass eigenstates*, Phys. Rev. Lett. **94** (2005) 101803, `arXiv:hep-ex/0412057`.

[120] The LHCb Collaboration, R. Aaij *et al.*, *Measurement of the CP-violating phase* ϕ_s *in the decay* $B_s^0 \rightarrow J/\psi\phi$, `arXiv:1112.3183`.

[121] P. M. Nadolsky *et al.*, *Implications of CTEQ global analysis for collider observables*, Phys. Rev. **D78** (2008) 013004, `arXiv:0802.0007`.

[122] The CDF Collaboration, F. Abe *et al.*, *Observation of the* B_c *meson in* $p\bar{p}$ *collisions at* $\sqrt{s} = 1.8$ *TeV*, Phys. Rev. Lett. **81** (1998) 2432, `arXiv:hep-ex/9805034`.

[123] The CDF Collaboration, T. Aaltonen *et al.*, *Observation of the decay* $B_c^\pm \rightarrow J/\psi\pi^\pm$ *and measurement of the* $B_c^\pm$ *mass*, Phys. Rev. Lett. **100** (2008) 182002, `arXiv:0712.1506`.

[124] The D0 Collaboration, V. Abazov *et al.*, *Observation of the* B_c *meson in the exclusive decay* $B_c \rightarrow J/\psi\pi$, Phys. Rev. Lett. **101** (2008) 012001, `arXiv:0802.4258`.

[125] The CDF Collaboration, A. Abulencia *et al.*, *Measurement of the* B_c^+ *meson lifetime using* $B_c^+ \rightarrow J/\psi e^+\nu_e$, Phys. Rev. Lett. **97** (2006) 012002, `arXiv:hep-ex/0603027`.

[126] The CDF Collaboration, T. Nigmanov *et al.*, *Measurement of* B_c^+ *properties at CDF*, `arXiv:0910.3013`.

[127] The D0 Collaboration, V. Abazov *et al.*, *Measurement of the lifetime of the* $B_c^\pm$ *meson in the semileptonic decay channel*, Phys. Rev. Lett. **102** (2009) 092001, `arXiv:0805.2614`.

[128] The CDF collaboration, *Study of* $B_c \rightarrow J/\psi\mu X$ *in Run II data*, Tech. Rep. CDF public note (7649). http://www-cdf.fnal.gov/physics/new/bottom/050330.blessed-bc-jpsimu/blessed-bc-jpsimu/blessed-bc-jpsimu.html.

[129] The CDF collaboration, *An updated measurement of the ratio* $[\sigma(B_c^+) \times \mathcal{B}(B_c^+ \rightarrow J/\psi\mu^+\nu)]/[\sigma(B^+) \times \mathcal{B}(B^+ \rightarrow J/\psi K^+)]$ *using* $1\,\mathrm{fb}^{-1}$ *of integrated luminosity*, Tech. Rep. CDF public note (9740). http://www-cdf.fnal.gov/physics/new/bottom/090305.blessed-bc-slXsec/.

[130] J. Pumplin *et al.*, *New generation of parton distributions with uncertainties from global QCD analysis*, JHEP **0207** (2002) 012, `arXiv:hep-ph/0201195`.

[131] M. Williams *et al.*, *The hlt2 topological lines*, Tech. Rep. LHCb-PUB-2011-002. CERN-LHCb-PUB-2011-002, CERN, Geneva, Jan, 2011.

[132] K. Akiba *et al.*, *Measurement of* Δm_s *in the decay* $B_s \rightarrow D_s(K^+K^-\pi^-)\pi^+$ *and* $B_s \rightarrow D_s(K^+K^-\pi^-)\pi^+\pi^+\pi^-$, , LHCb-CONF-2011-005.

Acknowledgement

The research work presented in this dissertation is partly supported by the National Natural Science Foundation of China (NSFC). The China Scholarship Council (CSC) provided the travel and living expenses for my stay at LAL, France.

It is my pleasure to thank the people who made this dissertation possible.

I wish to thank my supervisor Professor GAO Yuanning. He taught me a lot on not only scientific research but also self-actualization. His erudition, diligence and optimism will allow me a lifetime.

I wish to thank Drs. Patrick ROBBE and He, Jibo, for the close collaboration on carrying out the research work presented in this dissertation, and for their kindness and helps I received during my stay at LAL, France.

I wish to thank the fellows in the LHC and LHCb collaborations, and the countries and organizations who fund the research at CERN. Without their efforts and supports, none of the analysis in this dissertation would have been possible.

I wish to thank my girlfriend JIA Juanjuan. She helped a lot during my research and the dissertation writing. She encouraged me when I was stuck. She tracked my dissertation writing and prevented my laziness.

I wish to thank my parents, LIU Jingxiang and LI Baowen. They gave me birth, raised me up and offered my education. They support my probable money-less dream on physics. Although I always feel tired of their chatter and old fashion, at this time I can't help crying to say my love. I wish this dissertation to be a nice gift for my parents and Juanjuan.

声　明

本人郑重声明：所呈交的学位论文，是本人在导师指导下，独立进行研究工作所取得的成果。尽我所知，除文中已经注明引用的内容外，本学位论文的研究成果不包含任何他人享有著作权的内容。对本论文所涉及的研究工作做出贡献的其他个人和集体，均已在文中以明确方式标明。

签　名：____________ 日　期：____________

Appendix A Appendicular plots

A.1 Comparisons of selection variable distributions between data and MC

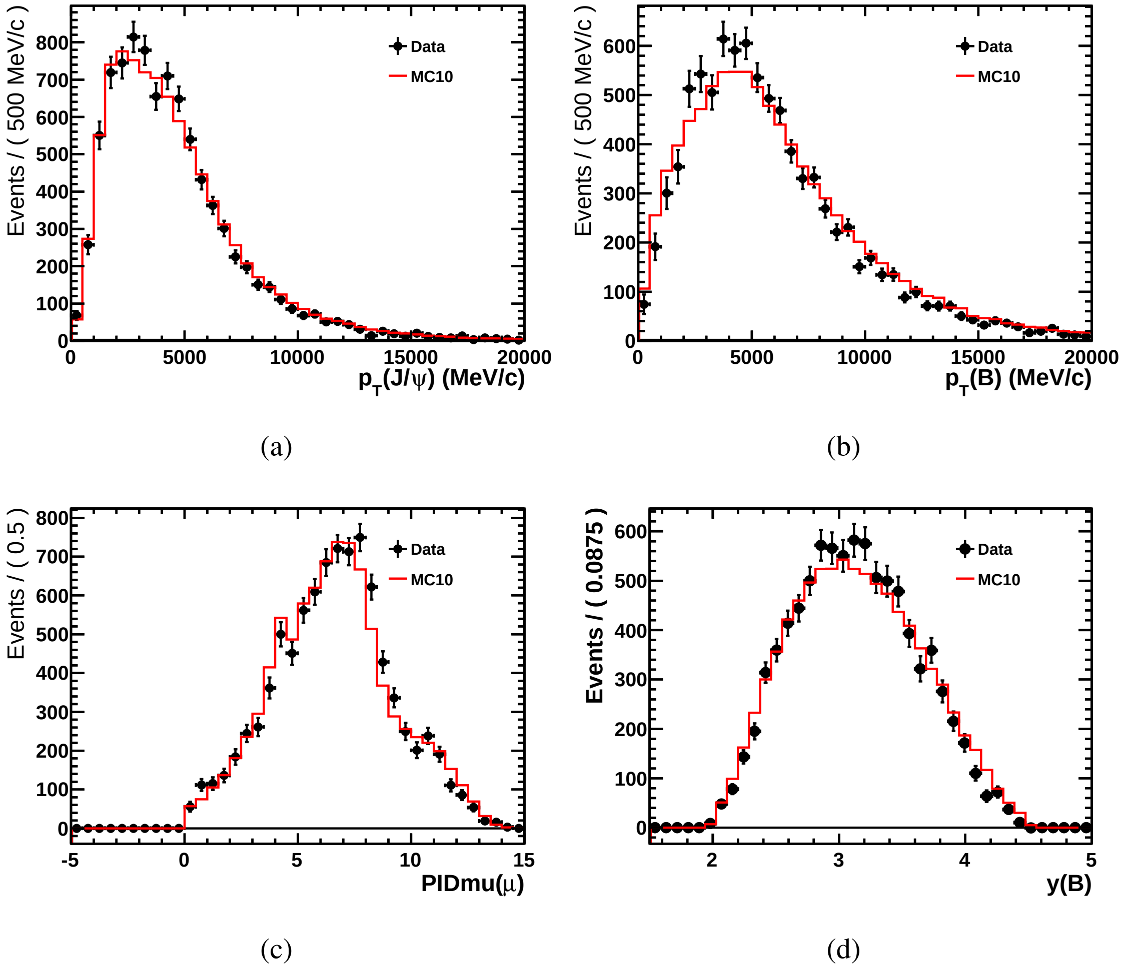

Figure A.1 The comparisons of distributions of *left top*: $p_{\mathrm{T}}(J/\psi)$, *right top*: $p_{\mathrm{T}}(B)$, *left bottom*: $\mathrm{PID}_{\mu}(\mu)$, *right bottom*: $y(B)$ between background subtracted data and MC. The black points are the distributions of background subtracted data, while the red lines are the distributions of MC.

A.2 Mass fit results in bins

The mass distributions and corresponding fit results of B^{+} as described in Section 4.3.1 are demonstrated in Figure A.3.

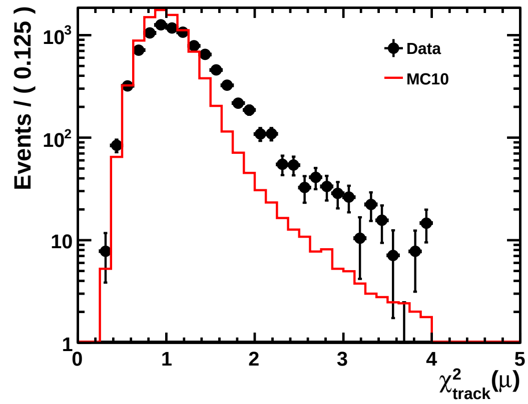

(a)

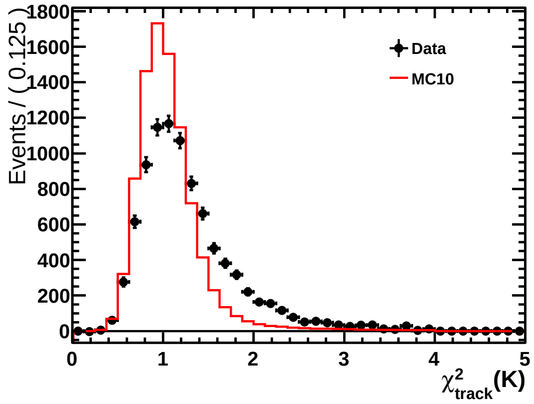

(b)

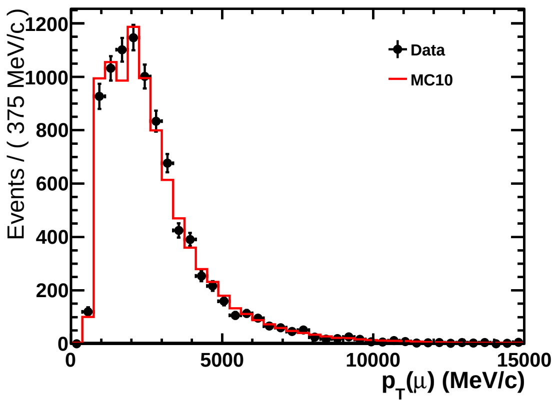

(c)

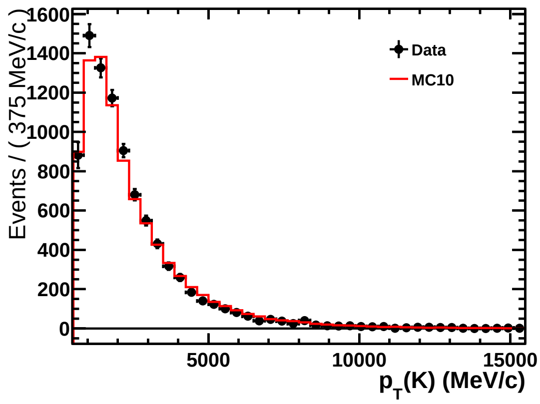

(d)

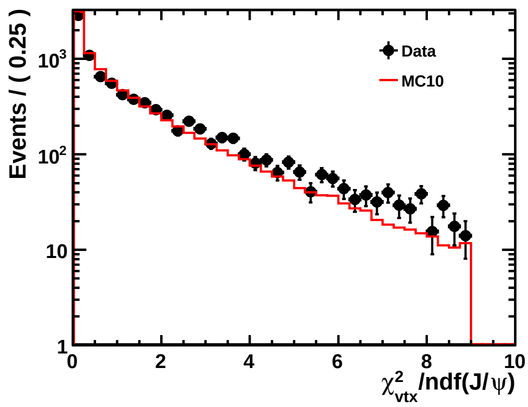

(e)

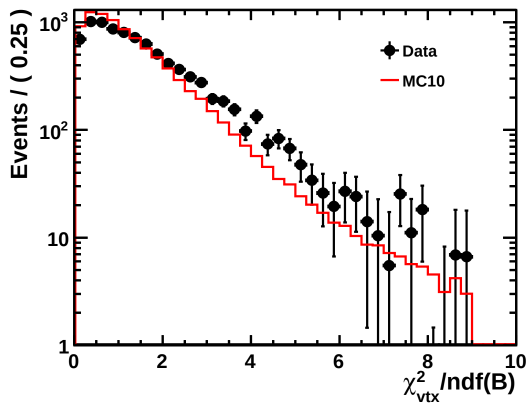

(f)

Figure A.2 The comparison of distributions of *left top*: $\chi^2_{\text{vtx}}/ndf(J/\psi)$, *tight top*: $\chi^2_{\text{vtx}}/ndf(B)$, *left middle*: $\chi^2_{\text{track}}(\mu)$, *right middle*: $\chi^2_{\text{track}}(K)$, *left bottom*: $p_T(\mu)$, *right bottom*: $p_T(K)$ between background subtracted data and MC. The black points are the distributions of background subtracted data, while the red lines are the distributions of MC.

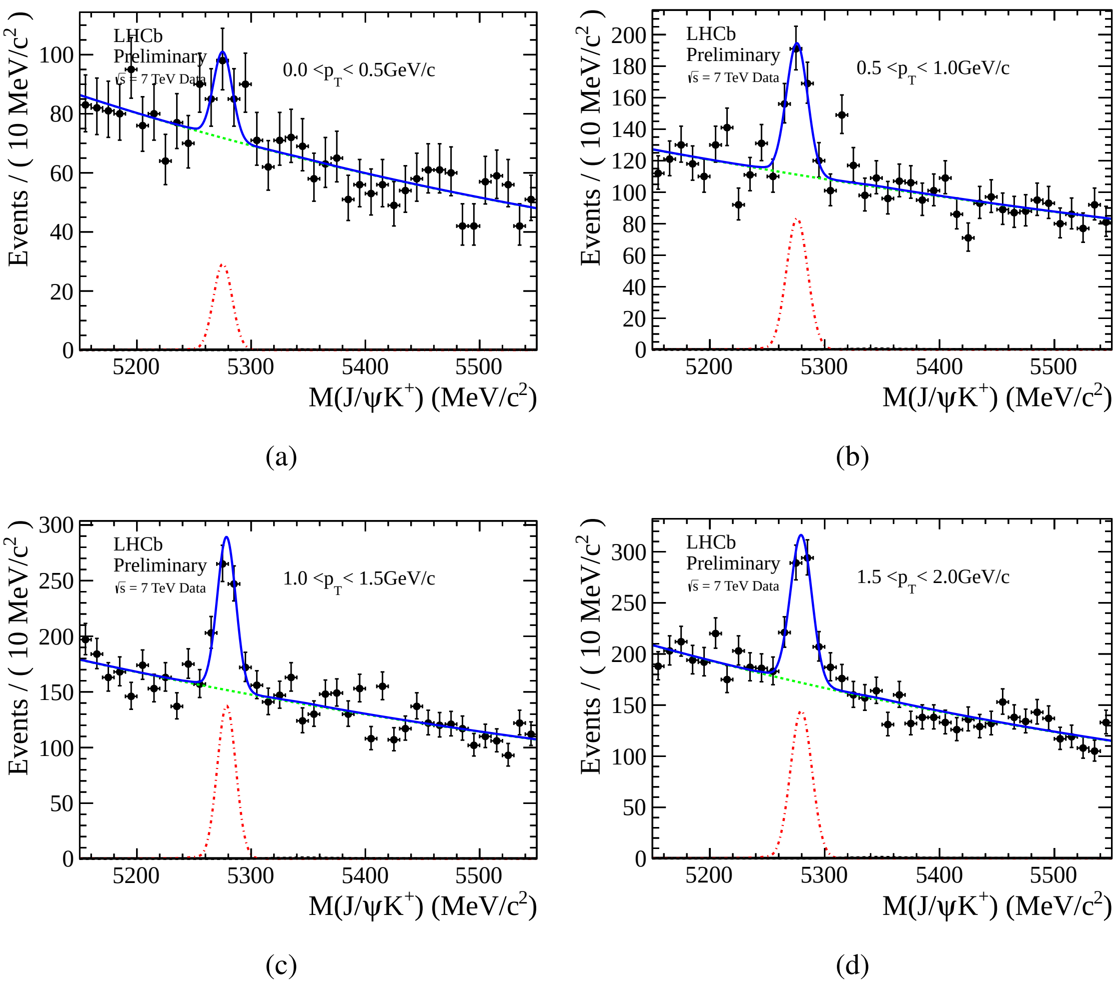

(a) (b)

(c) (d)

Figure A.3 Mass distribution fits for B^{+} in bins of p_{T} in 2011 data (to be continued).

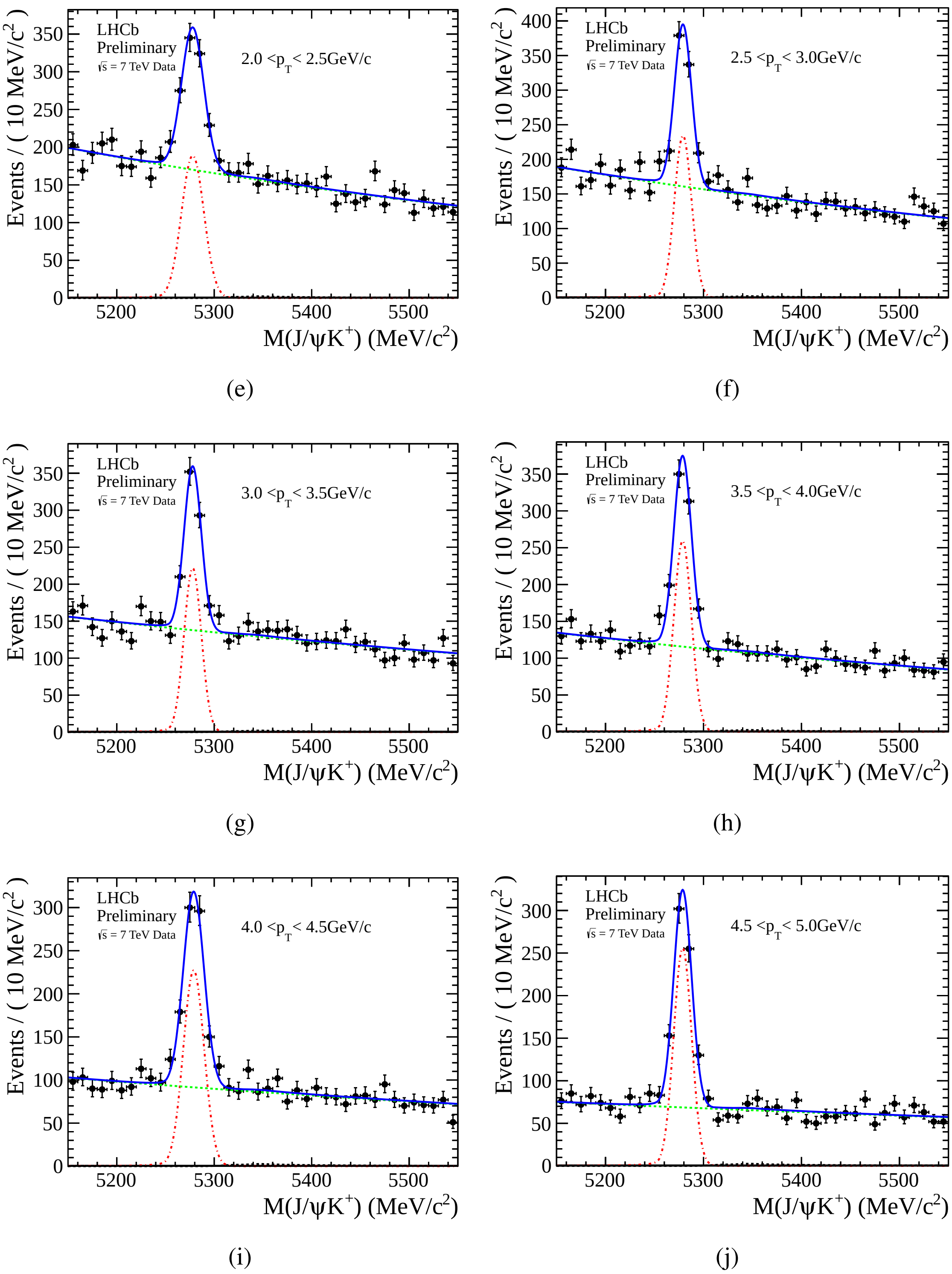

Figure A.3　Mass distribution fits for B^{+} in bins of p_{T} in 2011 data (to be continued).

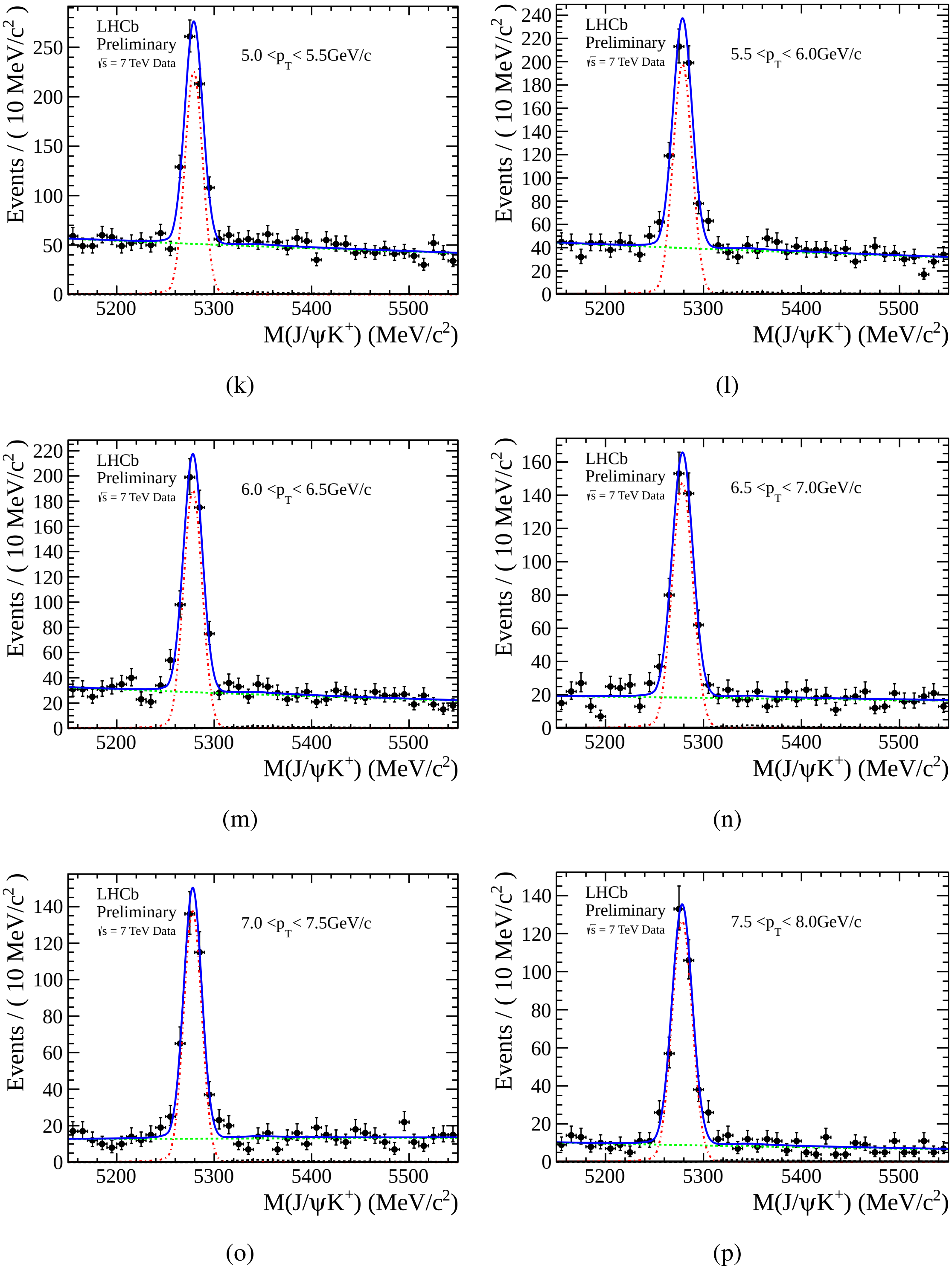

Figure A.3 Mass distribution fits for B^{+} in bins of p_{T} in 2011 data (to be continued).

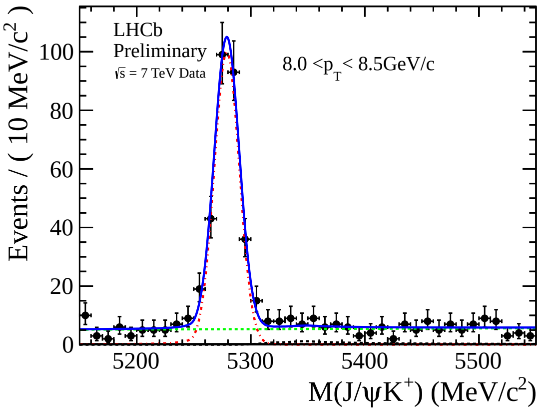

(q)

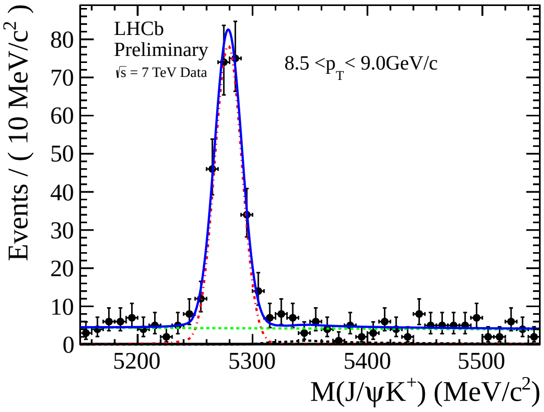

(r)

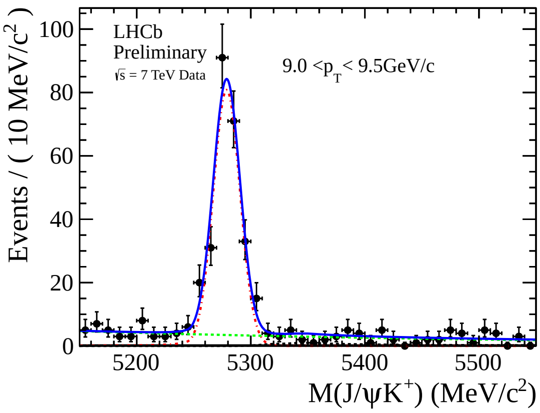

(s)

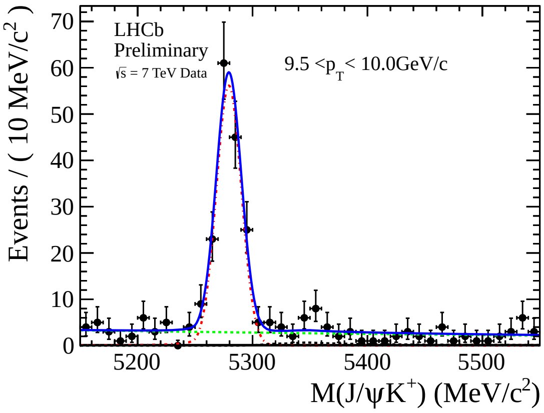

(t)

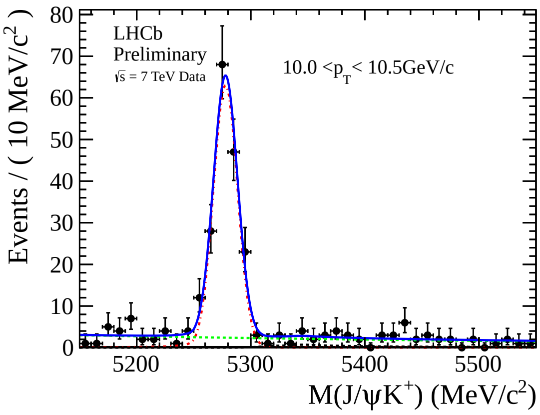

(u)

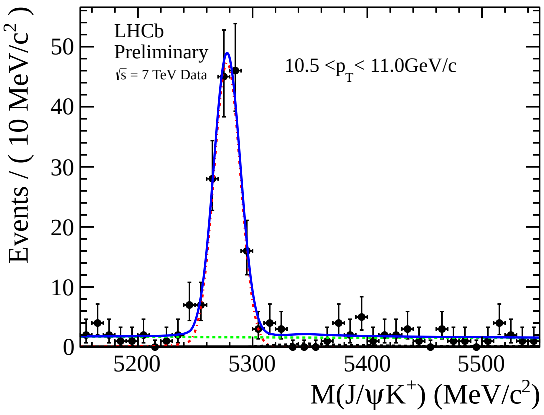

(v)

Figure A.3 Mass distribution fits for B^+ in bins of p_T in 2010 data (to be continued).

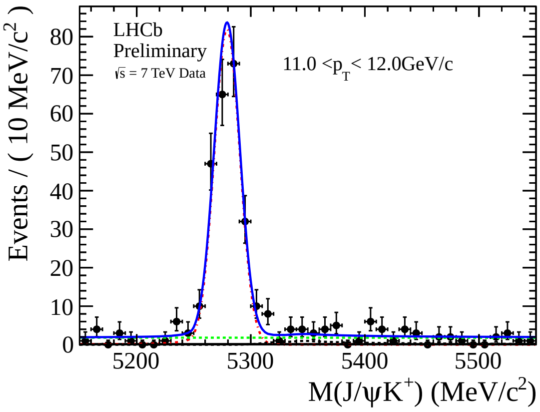

(k)

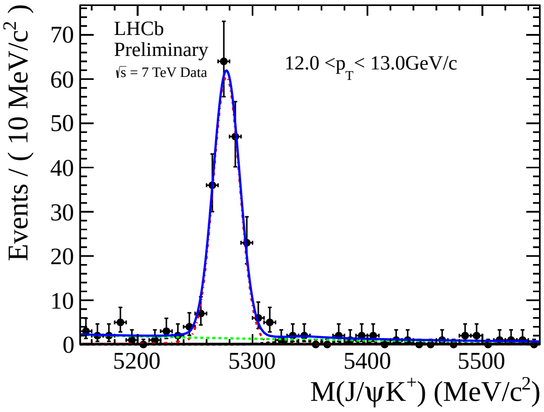

(l)

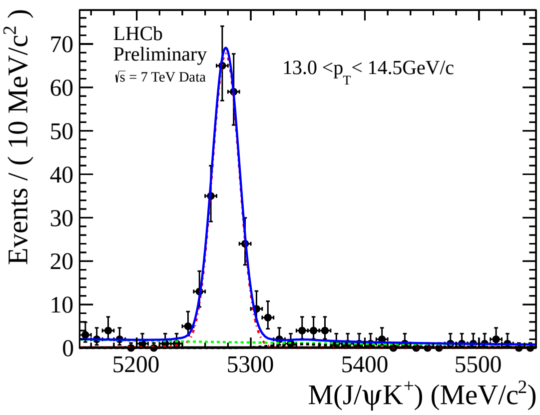

(m)

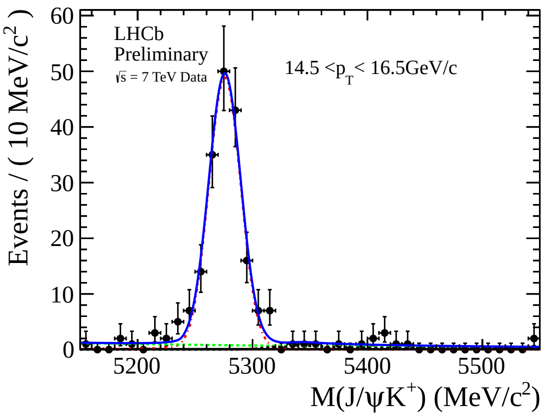

(n)

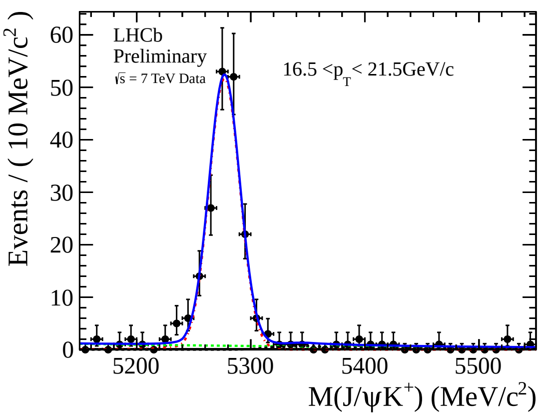

(o)

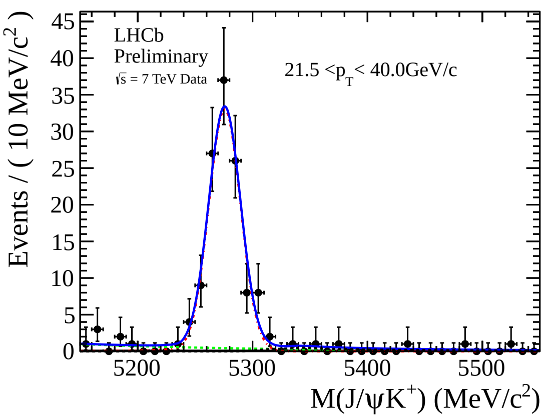

(p)

Figure A.3 Mass distribution fits for B^+ in bins of p_{T} in 2010 data .

A.3 Mass distributions of K^{*0} and ϕ

The mass distributions for K^{*0} and ϕ of the selected B candidates are shown in Figure A.4.

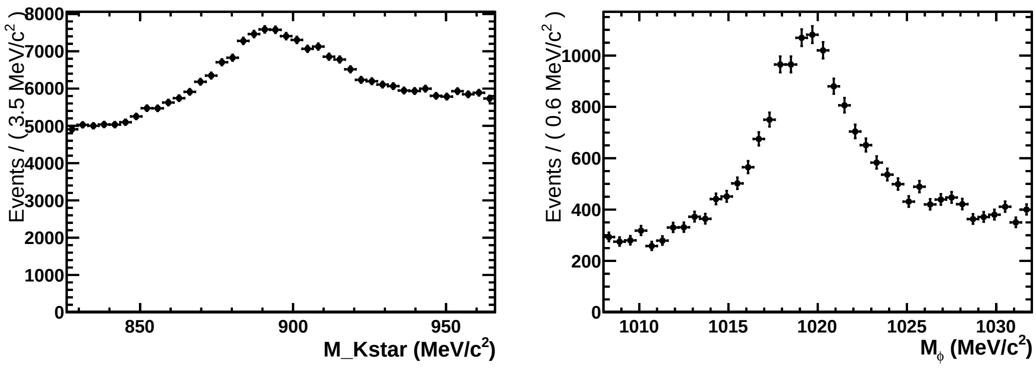

Figure A.4 Invariant mass distributions of the selected *left*: K^{*0} and *right*: ϕ candidates.

A.4 Partial reconstructed background

The possible partial reconstructed background is studied with inclusive J/ψ MC sample, and $B_d^0 \to J/\psi K^{*0}$, $B_s^0 \to J/\psi\phi$ decays in real data sample.

Figure A.5 shows the mass distribution of $J/\psi K$ candidates selected using the selection as in this analysis from the inclusive J/ψ MC sample. One can see that the partial backgrounds remaining in the mass window $[5150, 5550]$ MeV/c^2 are small.

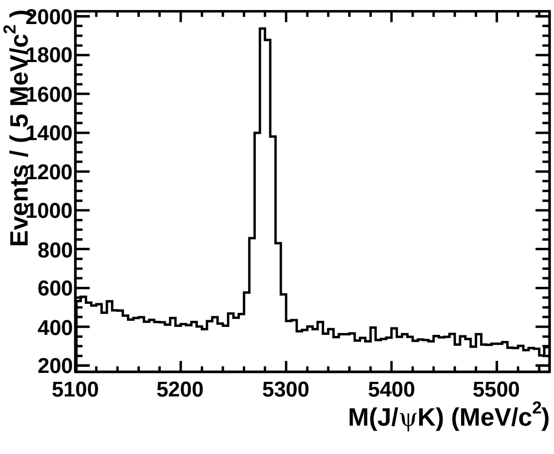

Figure A.5 Mass distribution of $J/\psi K$ candidates from the inclusive J/ψ MC sample.

This is validated further using the high yield channels, like $B_d^0 \to J/\psi K^{*0}$ and $B_s^0 \to J/\psi\phi$ in data. Figure A.6 shows the $J/\psi K$ mass distribution from the decay $B_d^0 \to J/\psi K^{*0}$

in data while the π is missing. Figure A.7 shows the $J/\psi K$ mass distribution from the decay $B_d^0 \rightarrow J/\psi K^{*0}$ in data while the K is missing, but the π is mis-identified as K. Figure A.8 shows the mass distribution of $J/\psi K$ candidates from the $B_s^0 \rightarrow J/\psi\phi$ decay in data while one of the kaons is missing.

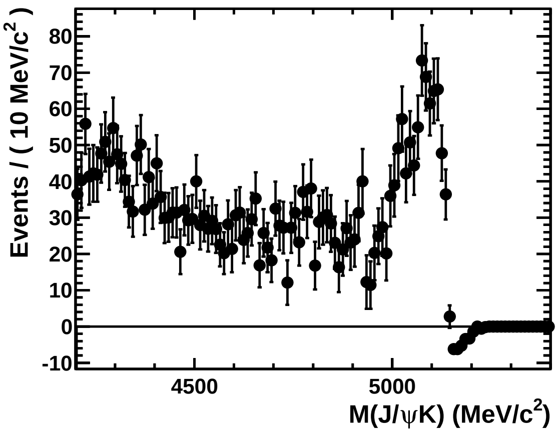

Figure A.6 Mass distribution of $J/\psi K$ candidates from $B_d^0 \rightarrow J/\psi K^{*0}$ while the π is missing.

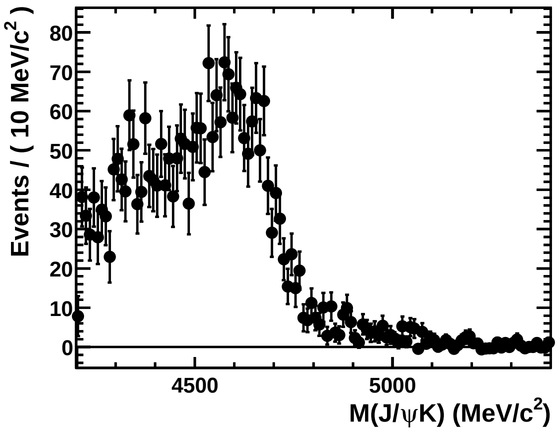

Figure A.7 Mass distribution of $J/\psi K$ candidates from the $B_d^0 \rightarrow J/\psi K^{*0}$ decay in data while the K is missing, but the π is mis-identified as K.

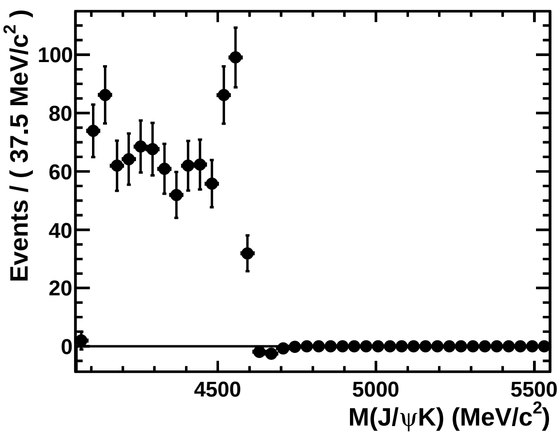

Figure A.8 Mass distribution of $J/\psi K$ candidates from the $B_s^0 \rightarrow J/\psi\phi$ decay in data while one of the kaons is missing.

Appendix B Appendicular tables

B.1 Signal yield tables

The signal yields in bins of p_T and y for $B^0 \to J/\psi K^{*0}$ and $B^+ \to J/\psi K^+$ in 2011 data samples are listed in Table B.2 and B.1. The signal yields in bins of p_T and y for $B_s^0 \to J/\psi \phi$ in 2011 data samples are extracted from ${}_s$*Weight* and listed in Table B.3.

Table B.1 Number of signal candidates for the $B^0 \to J/\psi K^{*0}$ in 2011 data.

p_T (GeV/c)	$2.0 < y < 2.5$	$2.5 < y < 3.0$	$3.0 < y < 3.5$	$3.5 < y < 4.0$	$4.0 < y < 4.5$	Total
(2.0, 2.5]	81.5 ± 14.3	567.1 ± 47.1	948.0 ± 71.4	686.3 ± 73.6	198.6 ± 35.7	2481.5 ± 119.2
(2.5, 3.0]	66.8 ± 13.3	567.2 ± 50.5	927.7 ± 64.4	680.0 ± 57.8	198.4 ± 30.4	2440.0 ± 105.5
(3.0, 3.5]	78.8 ± 17.9	677.9 ± 43.9	1023.4 ± 58.4	831.0 ± 54.3	223.8 ± 31.7	2834.9 ± 98.1
(3.5, 4.0]	72.9 ± 12.5	703.3 ± 45.1	951.4 ± 56.1	751.9 ± 47.2	194.5 ± 27.8	2674.1 ± 91.3
(4.0, 4.5]	92.8 ± 13.1	690.3 ± 39.2	1025.4 ± 50.2	705.6 ± 42.5	211.3 ± 21.9	2725.5 ± 80.7
(4.5, 5.0]	88.6 ± 16.6	677.5 ± 36.4	1039.1 ± 45.8	745.8 ± 40.6	158.1 ± 20.7	2709.1 ± 76.0
(5.0, 5.5]	117.8 ± 13.0	650.9 ± 34.0	949.4 ± 40.9	778.6 ± 38.7	196.1 ± 21.9	2692.9 ± 70.5
(5.5, 6.0]	103.7 ± 14.6	596.4 ± 31.6	855.2 ± 37.6	559.8 ± 32.2	162.0 ± 18.3	2277.1 ± 63.2
(6.0, 6.5]	106.9 ± 12.9	551.8 ± 28.7	778.8 ± 35.1	534.5 ± 29.6	107.3 ± 16.0	2079.4 ± 57.9
(6.5, 7.0]	112.4 ± 12.9	587.2 ± 29.4	717.7 ± 32.8	416.6 ± 26.2	117.6 ± 14.3	1951.5 ± 54.8
(7.0, 7.5]	104.4 ± 12.6	563.8 ± 27.5	742.6 ± 31.7	427.5 ± 23.9	132.9 ± 12.9	1971.3 ± 51.6
(7.5, 8.0]	105.5 ± 11.9	469.9 ± 24.7	555.1 ± 27.2	327.6 ± 21.0	95.9 ± 11.6	1554.0 ± 45.4
(8.0, 9.0]	225.9 ± 17.1	824.5 ± 32.1	1016.1 ± 35.7	647.7 ± 28.6	174.2 ± 15.3	2888.5 ± 60.4
(9.0, 10.0]	215.8 ± 15.6	684.0 ± 29.0	701.4 ± 29.0	402.8 ± 22.7	110.7 ± 11.8	2114.7 ± 50.8
(10.0, 11.5]	303.6 ± 18.4	809.4 ± 30.2	822.1 ± 30.8	476.4 ± 24.5	120.6 ± 12.4	2532.1 ± 54.4
(11.5, 14.0]	327.4 ± 19.3	863.1 ± 30.8	755.2 ± 29.3	406.8 ± 21.4	117.7 ± 12.0	2470.2 ± 52.8
(14.0, 19.5]	431.3 ± 21.5	742.1 ± 28.5	561.3 ± 25.0	313.0 ± 18.5	79.8 ± 9.7	2127.5 ± 48.3
(19.5, 40.0]	240.0 ± 15.9	310.2 ± 18.2	200.2 ± 14.9	74.5 ± 9.5	12.6 ± 3.7	837.5 ± 30.2

B.2 Efficiency tables

The ϵ_{acc} for $B^+ \to J/\psi K^+$ is the same as the 2010 analysis as listed in Table 4.8. The ϵ_{rec} for $B^+ \to J/\psi K^+$ after tracking efficiency correction are listed in Table B.5. The ϵ_{acc} and $\epsilon_{\text{rec\&noPID}}$ for $B^0 \to J/\psi K^{*0}$ and $B_s^0 \to J/\psi \phi$ are listed in Table B.4, B.6, B.7 and B.8, respectively.

Table B.2 Number of signal candidates for the $B^+ \to J/\psi K^+$ in 2011 data.

p_T (GeV/c)	$2.0 < y < 2.5$	$2.5 < y < 3.0$	$3.0 < y < 3.5$	$3.5 < y < 4.0$	$4.0 < y < 4.5$	Total
(0.0, 0.5]	28.5 ± 9.1	261.8 ± 36.3	453.1 ± 76.5	314.1 ± 71.7	62.9 ± 29.8	1120.4 ± 115.2
(0.5, 1.0]	149.3 ± 16.3	752.4 ± 57.7	1165.5 ± 97.3	904.6 ± 87.5	306.6 ± 45.2	3278.4 ± 150.9
(1.0, 1.5]	185.9 ± 17.6	1140.7 ± 63.4	1776.3 ± 100.0	1549.2 ± 92.1	471.0 ± 58.2	5123.1 ± 161.8
(1.5, 2.0]	235.0 ± 20.4	1690.9 ± 72.8	2385.0 ± 102.3	1840.8 ± 89.1	628.1 ± 56.3	6779.9 ± 165.2
(2.0, 2.5]	287.1 ± 21.9	1884.7 ± 73.9	2806.4 ± 102.0	2134.8 ± 87.3	666.2 ± 50.2	7779.2 ± 162.7
(2.5, 3.0]	383.6 ± 25.5	2049.1 ± 73.6	2945.6 ± 97.6	2298.4 ± 84.9	731.2 ± 48.8	8407.9 ± 158.7
(3.0, 3.5]	410.9 ± 26.0	2249.9 ± 73.1	3209.5 ± 94.6	2246.7 ± 74.8	700.2 ± 43.9	8817.3 ± 150.0
(3.5, 4.0]	394.6 ± 24.9	2245.6 ± 68.3	2986.4 ± 85.1	2227.2 ± 72.2	645.6 ± 39.6	8499.4 ± 139.0
(4.0, 4.5]	388.8 ± 25.5	2219.1 ± 66.3	2938.7 ± 77.9	2132.9 ± 66.6	655.4 ± 38.5	8334.9 ± 130.5
(4.5, 5.0]	465.5 ± 27.0	2104.6 ± 61.0	2548.4 ± 69.4	1782.6 ± 57.8	506.7 ± 32.4	7407.8 ± 116.9
(5.0, 5.5]	434.2 ± 25.7	1865.0 ± 55.3	2394.4 ± 64.8	1698.7 ± 53.3	464.6 ± 30.3	6857.0 ± 108.0
(5.5, 6.0]	417.7 ± 24.8	1810.1 ± 53.1	2193.0 ± 59.2	1417.6 ± 48.3	423.2 ± 27.4	6261.7 ± 100.1
(6.0, 6.5]	437.7 ± 24.5	1655.2 ± 48.4	1834.3 ± 52.2	1291.4 ± 44.2	397.3 ± 25.1	5615.9 ± 90.8
(6.5, 7.0]	385.7 ± 22.5	1498.6 ± 44.6	1614.7 ± 47.8	1081.1 ± 39.0	313.4 ± 21.4	4893.6 ± 82.2
(7.0, 7.5]	416.2 ± 22.8	1332.6 ± 41.4	1346.0 ± 42.6	886.2 ± 34.2	263.3 ± 18.8	4244.4 ± 74.7
(7.5, 8.0]	407.7 ± 22.0	1171.4 ± 37.7	1224.8 ± 39.3	789.3 ± 31.7	223.8 ± 17.0	3817.0 ± 69.0
(8.0, 8.5]	353.6 ± 20.5	1110.9 ± 36.2	1032.3 ± 35.4	703.5 ± 29.4	168.1 ± 14.8	3368.5 ± 63.8
(8.5, 9.0]	351.4 ± 20.3	1013.1 ± 34.1	965.7 ± 33.4	558.2 ± 25.9	169.9 ± 14.4	3058.3 ± 59.8
(9.0, 9.5]	294.1 ± 18.3	855.3 ± 30.9	842.8 ± 31.1	511.1 ± 24.6	173.7 ± 14.1	2677.0 ± 55.3
(9.5, 10.0]	283.5 ± 17.9	776.1 ± 29.1	761.2 ± 29.4	424.9 ± 22.4	143.4 ± 12.9	2389.1 ± 52.0
(10.0, 10.5]	252.9 ± 16.7	648.8 ± 26.8	617.0 ± 26.5	415.7 ± 21.6	95.1 ± 10.7	2029.5 ± 47.7
(10.5, 11.0]	238.8 ± 16.0	583.7 ± 25.2	553.3 ± 24.8	318.7 ± 19.0	91.7 ± 10.2	1786.1 ± 44.4
(11.0, 12.0]	442.3 ± 21.7	966.0 ± 32.2	835.6 ± 30.5	474.8 ± 23.2	139.5 ± 12.6	2858.2 ± 56.0
(12.0, 13.0]	333.9 ± 18.8	730.8 ± 27.8	626.3 ± 25.9	362.5 ± 20.1	102.4 ± 10.6	2155.9 ± 48.1
(13.0, 14.5]	456.6 ± 22.1	863.2 ± 30.1	638.0 ± 26.2	350.8 ± 19.5	112.3 ± 11.0	2420.9 ± 50.8
(14.5, 16.5]	385.9 ± 19.9	708.2 ± 26.9	506.1 ± 23.3	283.4 ± 17.4	71.7 ± 9.0	1955.2 ± 45.2
(16.5, 21.5]	548.5 ± 23.7	834.3 ± 29.5	568.2 ± 24.3	281.9 ± 17.4	73.7 ± 8.7	2306.6 ± 49.0
(21.5, 40.0]	407.1 ± 20.3	432.9 ± 21.3	262.8 ± 16.6	85.1 ± 9.6	16.4 ± 4.5	1204.3 ± 35.4

Table B.3 Number of signal candidates for the $B_s^0 \to J/\psi\,\phi$ in 2011 data.

p_{T} (GeV/c)	$2.0 < y < 2.5$	$2.5 < y < 3.0$	$3.0 < y < 3.5$	$3.5 < y < 4.0$	$4.0 < y < 4.5$	Total
(0.0, 0.5]	-0.0 ± 0.6	9.4 ± 5.7	14.6 ± 7.0	19.2 ± 6.8	2.9 ± 3.2	46.1 ± 11.8
(0.5, 1.0]	8.2 ± 3.5	42.6 ± 9.0	77.4 ± 11.7	40.8 ± 9.2	2.8 ± 3.4	171.8 ± 18.1
(1.0, 1.5]	6.1 ± 3.2	63.2 ± 10.4	127.5 ± 14.2	69.7 ± 10.9	8.6 ± 4.8	275.1 ± 21.5
(1.5, 2.0]	10.2 ± 4.0	77.8 ± 11.6	140.2 ± 15.3	108.1 ± 13.1	28.0 ± 6.7	364.3 ± 24.5
(2.0, 2.5]	12.3 ± 3.9	71.8 ± 10.8	148.5 ± 14.4	114.4 ± 12.4	15.0 ± 4.7	361.9 ± 22.7
(2.5, 3.0]	12.7 ± 4.1	97.1 ± 11.4	157.9 ± 14.7	104.6 ± 11.8	21.9 ± 5.5	394.2 ± 23.1
(3.0, 3.5]	8.5 ± 3.4	110.5 ± 11.8	162.9 ± 14.2	106.5 ± 11.4	20.4 ± 5.1	408.9 ± 22.6
(3.5, 4.0]	20.6 ± 4.8	122.6 ± 12.2	151.1 ± 13.5	106.6 ± 11.2	21.0 ± 5.0	421.7 ± 22.4
(4.0, 4.5]	17.8 ± 4.6	103.6 ± 11.3	189.7 ± 14.7	135.1 ± 12.3	19.9 ± 5.0	466.2 ± 23.2
(4.5, 5.0]	8.8 ± 3.4	116.4 ± 11.4	134.5 ± 12.5	97.3 ± 10.4	11.6 ± 3.7	368.5 ± 20.5
(5.0, 5.5]	12.9 ± 3.9	112.8 ± 11.3	134.4 ± 12.2	82.9 ± 9.7	16.4 ± 4.1	359.4 ± 20.1
(5.5, 6.0]	14.1 ± 4.0	100.1 ± 10.4	116.3 ± 11.3	96.4 ± 10.1	21.7 ± 4.7	348.6 ± 19.4
(6.0, 6.5]	17.6 ± 4.4	89.0 ± 9.9	145.4 ± 12.5	71.2 ± 8.9	19.6 ± 4.4	342.9 ± 19.3
(6.5, 7.0]	19.9 ± 4.7	100.0 ± 10.4	106.1 ± 10.7	72.6 ± 8.7	18.9 ± 4.5	317.6 ± 18.4
(7.0, 7.5]	12.1 ± 3.7	83.3 ± 9.5	107.5 ± 10.7	56.2 ± 7.7	21.6 ± 4.7	280.8 ± 17.3
(7.5, 8.0]	22.9 ± 4.9	72.0 ± 8.8	79.1 ± 9.1	52.6 ± 7.4	12.6 ± 3.6	239.3 ± 15.9
(8.0, 8.5]	15.1 ± 4.0	76.8 ± 8.9	76.3 ± 9.0	49.9 ± 7.3	13.6 ± 3.7	231.7 ± 15.6
(8.5, 9.0]	27.2 ± 5.3	55.3 ± 7.7	89.3 ± 9.7	45.9 ± 6.9	3.7 ± 2.0	221.5 ± 15.2
(9.0, 10.0]	29.5 ± 5.5	132.6 ± 11.7	130.5 ± 11.5	63.7 ± 8.1	14.8 ± 3.9	371.0 ± 19.6
(10.0, 11.0]	31.5 ± 5.7	93.4 ± 9.8	86.1 ± 9.4	49.3 ± 7.2	8.6 ± 2.9	269.0 ± 16.7
(11.0, 12.5]	36.5 ± 6.2	103.3 ± 10.3	71.3 ± 8.5	30.6 ± 5.8	4.8 ± 2.5	246.5 ± 16.0
(12.5, 14.5]	33.5 ± 6.0	86.7 ± 9.5	70.0 ± 8.4	37.4 ± 6.2	7.2 ± 2.7	234.8 ± 15.6
(14.5, 18.5]	58.1 ± 7.7	77.4 ± 9.0	67.8 ± 8.4	19.2 ± 4.5	7.4 ± 2.8	230.1 ± 15.4
(18.5, 40.0]	42.3 ± 6.6	50.9 ± 7.3	32.2 ± 5.8	13.5 ± 3.7	2.7 ± 1.7	141.5 ± 12.1

Table B.4 Acceptance efficiencies (in %) for $B^0 \to J/\psi K^{*0}$ in bins of p_T and y.

p_T (GeV/c)	$2.0 < y < 2.5$	$2.5 < y < 3.0$	$3.0 < y < 3.5$	$3.5 < y < 4.0$	$4.0 < y < 4.5$
(2.0, 2.5]	42.6 ± 0.9	76.3 ± 0.8	88.2 ± 0.7	83.3 ± 1.0	61.9 ± 1.5
(2.5, 3.0]	45.5 ± 0.9	79.3 ± 0.8	88.5 ± 0.7	84.0 ± 1.0	63.5 ± 1.5
(3.0, 3.5]	45.7 ± 0.9	79.5 ± 0.8	89.4 ± 0.7	85.1 ± 0.9	66.2 ± 1.5
(3.5, 4.0]	49.5 ± 0.9	82.9 ± 0.8	90.2 ± 0.7	84.3 ± 1.0	70.0 ± 1.5
(4.0, 4.5]	52.3 ± 1.0	83.2 ± 0.8	89.6 ± 0.7	88.9 ± 0.9	68.9 ± 1.6
(4.5, 5.0]	55.7 ± 1.0	84.0 ± 0.8	91.5 ± 0.7	88.6 ± 0.9	72.1 ± 1.7
(5.0, 5.5]	57.5 ± 1.0	86.4 ± 0.8	93.8 ± 0.6	90.1 ± 0.9	75.6 ± 1.7
(5.5, 6.0]	56.8 ± 1.1	84.5 ± 0.9	92.4 ± 0.8	90.8 ± 1.0	78.2 ± 1.8
(6.0, 6.5]	61.3 ± 1.2	88.6 ± 0.8	94.4 ± 0.7	91.9 ± 1.0	80.9 ± 1.8
(6.5, 7.0]	62.7 ± 1.2	88.4 ± 0.9	94.1 ± 0.8	91.4 ± 1.1	78.2 ± 2.1
(7.0, 7.5]	66.3 ± 1.3	89.5 ± 0.9	95.3 ± 0.8	93.3 ± 1.1	83.7 ± 2.0
(7.5, 8.0]	67.1 ± 1.4	90.9 ± 1.0	96.3 ± 0.7	94.5 ± 1.1	82.4 ± 2.5
(8.0, 9.0]	69.7 ± 1.1	90.5 ± 0.8	95.5 ± 0.6	93.9 ± 0.9	88.2 ± 1.7
(9.0, 10.0]	73.6 ± 1.2	94.5 ± 0.7	96.5 ± 0.7	96.0 ± 0.9	90.5 ± 1.8
(10.0, 11.5]	74.5 ± 1.2	94.7 ± 0.7	97.3 ± 0.6	95.5 ± 1.0	89.4 ± 2.0
(11.5, 14.0]	82.5 ± 1.1	96.0 ± 0.6	97.9 ± 0.6	98.2 ± 0.7	93.5 ± 1.9
(14.0, 19.5]	86.4 ± 1.1	97.6 ± 0.6	99.6 ± 0.3	99.1 ± 0.6	95.9 ± 2.0
(19.5, 40.0]	92.8 ± 1.3	98.5 ± 0.7	99.3 ± 0.7	98.5 ± 1.5	100.0 ± 0.0

The ϵ_{tri} for $B^+ \to J/\psi K^+$ and $B^0 \to J/\psi K^{*0}$ in bins of p_T and y are listed in Table B.10 and B.9. The ϵ_{tri} for $B_s^0 \to J/\psi \phi$ in bins of p_T are listed in Table B.11.

The total MC efficiency $\epsilon_{\text{acc}} \times \epsilon_{\text{rec}} \times \epsilon_{\text{tri}}$ for $B_c^+ \to J/\psi \pi^+$ and $B^+ \to J/\psi K^+$ are listed in Table B.13 and B.12, respectively.

B.3 Inter-bin cross-feed effects

The acceptance efficiency variations (in %) of smearing the generator level p_T distribution in bins of p_T and y are listed in Table B.14.

B.4 Differential cross-sections tables for B mesons in 2011 data

The differential cross-section of B_s^0 in bins of p_T is given in Table B.15, in which the first uncertainty is statistical and the second is systematic. The differential cross-sections of B^+ and B^0 in bins of p_T and y are given in Table B.16 and B.17, in which the first

Table B.5 Reconstruction efficiencies (in %) for $B^+ \to J/\psi K^+$ in bins of p_T and y. The effects of tracking efficiency corrections are included.

p_T (GeV/c)	$2.0 < y < 2.5$	$2.5 < y < 3.0$	$3.0 < y < 3.5$	$3.5 < y < 4.0$	$4.0 < y < 4.5$
(0.0, 0.5]	11.8 ± 0.4	25.4 ± 0.5	30.7 ± 0.5	25.7 ± 0.5	12.6 ± 0.4
(0.5, 1.0]	13.0 ± 0.3	25.2 ± 0.3	30.5 ± 0.3	26.4 ± 0.3	12.9 ± 0.3
(1.0, 1.5]	12.3 ± 0.2	25.7 ± 0.2	31.1 ± 0.3	26.6 ± 0.3	13.5 ± 0.3
(1.5, 2.0]	13.1 ± 0.2	25.3 ± 0.2	31.9 ± 0.3	27.6 ± 0.3	14.1 ± 0.3
(2.0, 2.5]	12.4 ± 0.2	25.6 ± 0.2	32.9 ± 0.3	27.6 ± 0.3	13.9 ± 0.3
(2.5, 3.0]	13.2 ± 0.2	26.0 ± 0.2	32.8 ± 0.3	28.2 ± 0.3	14.4 ± 0.3
(3.0, 3.5]	13.0 ± 0.2	26.6 ± 0.2	32.2 ± 0.3	29.7 ± 0.3	14.2 ± 0.3
(3.5, 4.0]	13.3 ± 0.2	27.4 ± 0.2	33.9 ± 0.3	29.6 ± 0.3	14.8 ± 0.3
(4.0, 4.5]	12.9 ± 0.2	27.1 ± 0.2	33.9 ± 0.3	28.7 ± 0.3	14.7 ± 0.3
(4.5, 5.0]	13.7 ± 0.2	27.5 ± 0.2	35.1 ± 0.3	30.1 ± 0.3	15.2 ± 0.4
(5.0, 5.5]	13.1 ± 0.2	28.6 ± 0.3	33.2 ± 0.3	29.5 ± 0.4	14.9 ± 0.4
(5.5, 6.0]	13.7 ± 0.2	28.9 ± 0.3	34.3 ± 0.3	30.1 ± 0.4	14.2 ± 0.4
(6.0, 6.5]	14.2 ± 0.3	29.6 ± 0.3	35.0 ± 0.4	30.8 ± 0.4	15.7 ± 0.4
(6.5, 7.0]	14.4 ± 0.3	30.3 ± 0.3	35.4 ± 0.4	32.4 ± 0.5	16.6 ± 0.5
(7.0, 7.5]	14.9 ± 0.3	30.0 ± 0.3	35.6 ± 0.4	33.8 ± 0.5	17.1 ± 0.6
(7.5, 8.0]	14.7 ± 0.3	32.0 ± 0.4	34.9 ± 0.4	31.1 ± 0.5	18.7 ± 0.6
(8.0, 8.5]	15.9 ± 0.3	33.0 ± 0.4	36.8 ± 0.5	35.4 ± 0.6	18.6 ± 0.7
(8.5, 9.0]	17.3 ± 0.4	32.4 ± 0.4	39.2 ± 0.5	35.6 ± 0.7	16.9 ± 0.7
(9.0, 9.5]	16.6 ± 0.4	34.9 ± 0.5	38.7 ± 0.6	36.6 ± 0.7	19.2 ± 0.9
(9.5, 10.0]	19.3 ± 0.4	35.2 ± 0.5	41.1 ± 0.7	36.1 ± 0.8	21.5 ± 1.0
(10.0, 10.5]	19.9 ± 0.5	34.8 ± 0.6	40.8 ± 0.7	39.0 ± 0.9	22.1 ± 1.1
(10.5, 11.0]	20.6 ± 0.5	39.4 ± 0.6	44.7 ± 0.8	32.6 ± 0.9	24.7 ± 1.3
(11.0, 12.0]	20.7 ± 0.4	38.0 ± 0.5	41.2 ± 0.6	39.3 ± 0.8	24.7 ± 1.0
(12.0, 13.0]	21.3 ± 0.5	39.2 ± 0.6	39.1 ± 0.7	38.0 ± 0.9	24.1 ± 1.2
(13.0, 14.5]	24.5 ± 0.5	42.6 ± 0.6	42.7 ± 0.7	36.8 ± 0.8	25.8 ± 1.3
(14.5, 16.5]	26.8 ± 0.5	45.7 ± 0.7	42.2 ± 0.8	37.9 ± 1.0	29.0 ± 1.6
(16.5, 21.5]	30.0 ± 0.5	45.8 ± 0.6	44.5 ± 0.8	42.5 ± 1.1	37.3 ± 2.0
(21.5, 40.0]	31.9 ± 0.7	38.9 ± 0.8	50.0 ± 1.3	47.2 ± 1.9	30.4 ± 3.5

Table B.6 Acceptance efficiencies (in %) for $B_s^0 \to J/\psi\,\phi$ in bins of p_T and y.

p_T (GeV/c)	$2.0 < y < 2.5$	$2.5 < y < 3.0$	$3.0 < y < 3.5$	$3.5 < y < 4.0$	$4.0 < y < 4.5$
(0.0, 0.5]	51.0 ± 1.5	78.4 ± 1.2	87.4 ± 1.1	83.8 ± 1.3	64.7 ± 1.7
(0.5, 1.0]	51.7 ± 0.9	79.1 ± 0.8	88.1 ± 0.6	83.0 ± 0.8	63.3 ± 1.1
(1.0, 1.5]	52.6 ± 0.7	80.1 ± 0.6	87.7 ± 0.6	83.0 ± 0.7	63.2 ± 1.1
(1.5, 2.0]	53.0 ± 0.7	81.3 ± 0.6	88.6 ± 0.5	83.8 ± 0.7	63.4 ± 1.1
(2.0, 2.5]	54.2 ± 0.7	81.6 ± 0.6	89.2 ± 0.5	84.5 ± 0.7	64.7 ± 1.1
(2.5, 3.0]	55.1 ± 0.7	82.6 ± 0.6	89.8 ± 0.5	85.7 ± 0.7	67.9 ± 1.1
(3.0, 3.5]	56.7 ± 0.7	83.1 ± 0.6	90.5 ± 0.5	85.3 ± 0.7	69.4 ± 1.1
(3.5, 4.0]	58.1 ± 0.7	83.9 ± 0.6	90.8 ± 0.5	88.0 ± 0.7	72.9 ± 1.1
(4.0, 4.5]	61.1 ± 0.7	85.5 ± 0.6	91.5 ± 0.5	87.6 ± 0.7	72.3 ± 1.2
(4.5, 5.0]	61.9 ± 0.7	87.9 ± 0.5	91.6 ± 0.5	88.1 ± 0.7	74.0 ± 1.2
(5.0, 5.5]	64.2 ± 0.8	87.6 ± 0.6	91.2 ± 0.5	88.1 ± 0.7	75.1 ± 1.3
(5.5, 6.0]	66.7 ± 0.8	88.9 ± 0.6	93.2 ± 0.5	89.9 ± 0.8	76.3 ± 1.3
(6.0, 6.5]	67.8 ± 0.8	89.8 ± 0.6	93.1 ± 0.6	90.8 ± 0.8	79.7 ± 1.4
(6.5, 7.0]	70.7 ± 0.9	90.4 ± 0.6	93.6 ± 0.6	92.2 ± 0.8	79.9 ± 1.5
(7.0, 7.5]	74.6 ± 0.9	90.9 ± 0.6	94.7 ± 0.6	92.2 ± 0.9	80.8 ± 1.7
(7.5, 8.0]	74.1 ± 1.0	93.2 ± 0.6	95.5 ± 0.6	93.1 ± 0.9	80.9 ± 1.8
(8.0, 8.5]	77.6 ± 1.0	94.0 ± 0.6	96.3 ± 0.6	94.2 ± 0.9	86.8 ± 1.8
(8.5, 9.0]	75.2 ± 1.1	91.3 ± 0.8	96.7 ± 0.6	92.7 ± 1.1	85.1 ± 2.0
(9.0, 10.0]	78.8 ± 0.8	93.6 ± 0.6	96.8 ± 0.5	94.9 ± 0.7	89.1 ± 1.4
(10.0, 11.0]	80.0 ± 0.9	94.5 ± 0.6	98.6 ± 0.4	96.1 ± 0.8	91.2 ± 1.6
(11.0, 12.5]	83.2 ± 0.9	96.4 ± 0.5	98.7 ± 0.4	98.0 ± 0.6	90.2 ± 1.7
(12.5, 14.5]	87.6 ± 0.9	96.9 ± 0.5	98.8 ± 0.4	98.5 ± 0.6	96.1 ± 1.4
(14.5, 18.5]	91.4 ± 0.8	97.5 ± 0.5	99.0 ± 0.4	99.4 ± 0.4	95.9 ± 1.8
(18.5, 40.0]	93.7 ± 0.8	99.2 ± 0.4	100.0 ± 0.0	100.0 ± 0.0	96.0 ± 2.8

Table B.7 Reconstruction efficiencies (in %) for $B^0 \to J/\psi K^{*0}$ in bins of p_{T} and y. The effects of tracking efficiency corrections are included while the PID efficiencies are not included.

p_{T} (GeV/c)	$2.0 < y < 2.5$	$2.5 < y < 3.0$	$3.0 < y < 3.5$	$3.5 < y < 4.0$	$4.0 < y < 4.5$
(2.0, 2.5]	3.2 ± 0.1	9.2 ± 0.1	12.8 ± 0.1	11.7 ± 0.1	5.4 ± 0.1
(2.5, 3.0]	3.0 ± 0.1	8.9 ± 0.1	13.3 ± 0.1	12.0 ± 0.1	5.8 ± 0.1
(3.0, 3.5]	3.2 ± 0.1	10.1 ± 0.1	13.1 ± 0.1	11.8 ± 0.1	5.9 ± 0.1
(3.5, 4.0]	3.3 ± 0.1	9.8 ± 0.1	13.8 ± 0.1	12.6 ± 0.1	6.0 ± 0.1
(4.0, 4.5]	3.4 ± 0.1	10.1 ± 0.1	14.4 ± 0.1	13.1 ± 0.1	5.9 ± 0.1
(4.5, 5.0]	3.5 ± 0.1	10.4 ± 0.1	15.7 ± 0.1	13.4 ± 0.1	6.8 ± 0.2
(5.0, 5.5]	3.9 ± 0.1	11.4 ± 0.1	15.5 ± 0.1	14.1 ± 0.2	6.2 ± 0.1
(5.5, 6.0]	4.2 ± 0.1	12.0 ± 0.1	17.0 ± 0.2	14.2 ± 0.2	6.5 ± 0.2
(6.0, 6.5]	4.6 ± 0.1	12.4 ± 0.1	17.8 ± 0.2	14.7 ± 0.2	6.7 ± 0.2
(6.5, 7.0]	4.8 ± 0.1	13.0 ± 0.1	17.0 ± 0.2	15.6 ± 0.2	7.0 ± 0.2
(7.0, 7.5]	5.1 ± 0.1	14.2 ± 0.2	18.8 ± 0.2	15.7 ± 0.2	7.1 ± 0.2
(7.5, 8.0]	5.3 ± 0.1	14.9 ± 0.2	18.6 ± 0.2	17.1 ± 0.2	9.5 ± 0.3
(8.0, 9.0]	6.0 ± 0.1	16.6 ± 0.1	20.4 ± 0.2	19.1 ± 0.2	8.5 ± 0.2
(9.0, 10.0]	6.6 ± 0.1	16.8 ± 0.2	21.8 ± 0.2	19.7 ± 0.3	9.0 ± 0.2
(10.0, 11.5]	8.3 ± 0.1	18.7 ± 0.2	22.4 ± 0.2	23.7 ± 0.3	11.4 ± 0.3
(11.5, 14.0]	10.6 ± 0.1	21.4 ± 0.2	24.0 ± 0.2	21.7 ± 0.3	13.1 ± 0.4
(14.0, 19.5]	13.1 ± 0.2	23.6 ± 0.2	26.2 ± 0.3	26.1 ± 0.4	14.1 ± 0.5
(19.5, 40.0]	17.0 ± 0.3	25.4 ± 0.4	28.5 ± 0.5	21.3 ± 0.7	20.7 ± 1.4

uncertainty is statistical and the second systematic.

Table B.8 Reconstruction efficiencies (in %) for $B_s^0 \to J/\psi\,\phi$ in bins of p_T and y. The effects of tracking efficiency corrections are included while the PID efficiencies are not included.

p_T (GeV/c)	$2.0 < y < 2.5$	$2.5 < y < 3.0$	$3.0 < y < 3.5$	$3.5 < y < 4.0$	$4.0 < y < 4.5$
(0.0, 0.5]	3.9 ± 0.3	12.2 ± 0.4	16.0 ± 0.4	12.7 ± 0.4	5.2 ± 0.3
(0.5, 1.0]	3.3 ± 0.1	11.7 ± 0.2	16.2 ± 0.3	13.7 ± 0.3	5.8 ± 0.2
(1.0, 1.5]	3.7 ± 0.1	11.9 ± 0.2	16.0 ± 0.2	13.7 ± 0.2	5.7 ± 0.2
(1.5, 2.0]	3.5 ± 0.1	11.4 ± 0.2	15.6 ± 0.2	14.1 ± 0.2	5.5 ± 0.2
(2.0, 2.5]	3.8 ± 0.1	11.1 ± 0.2	15.1 ± 0.2	13.0 ± 0.2	6.1 ± 0.2
(2.5, 3.0]	3.6 ± 0.1	11.3 ± 0.2	15.9 ± 0.2	13.4 ± 0.2	6.5 ± 0.2
(3.0, 3.5]	3.9 ± 0.1	11.6 ± 0.2	15.9 ± 0.2	14.5 ± 0.2	6.2 ± 0.2
(3.5, 4.0]	4.0 ± 0.1	12.2 ± 0.2	16.2 ± 0.2	14.0 ± 0.2	6.2 ± 0.2
(4.0, 4.5]	4.0 ± 0.1	12.2 ± 0.2	17.2 ± 0.2	14.7 ± 0.3	6.4 ± 0.2
(4.5, 5.0]	4.9 ± 0.1	12.8 ± 0.2	17.0 ± 0.2	15.1 ± 0.3	6.8 ± 0.3
(5.0, 5.5]	4.8 ± 0.1	13.5 ± 0.2	17.6 ± 0.2	15.5 ± 0.3	7.8 ± 0.3
(5.5, 6.0]	5.0 ± 0.1	14.4 ± 0.2	19.1 ± 0.3	16.5 ± 0.3	7.7 ± 0.3
(6.0, 6.5]	5.3 ± 0.2	14.8 ± 0.2	19.2 ± 0.3	17.0 ± 0.3	8.0 ± 0.3
(6.5, 7.0]	6.0 ± 0.2	15.5 ± 0.3	20.0 ± 0.3	16.5 ± 0.4	7.3 ± 0.4
(7.0, 7.5]	6.4 ± 0.2	16.0 ± 0.3	20.4 ± 0.4	19.0 ± 0.4	9.8 ± 0.5
(7.5, 8.0]	6.8 ± 0.2	17.7 ± 0.3	21.3 ± 0.4	19.2 ± 0.5	9.8 ± 0.5
(8.0, 8.5]	6.6 ± 0.2	18.6 ± 0.3	23.7 ± 0.4	20.6 ± 0.5	8.9 ± 0.5
(8.5, 9.0]	7.3 ± 0.3	19.4 ± 0.4	21.6 ± 0.4	22.4 ± 0.6	11.4 ± 0.6
(9.0, 10.0]	8.2 ± 0.2	19.8 ± 0.3	22.9 ± 0.4	20.8 ± 0.4	10.8 ± 0.5
(10.0, 11.0]	9.2 ± 0.2	20.8 ± 0.4	24.2 ± 0.4	24.5 ± 0.6	11.0 ± 0.6
(11.0, 12.5]	10.7 ± 0.3	22.9 ± 0.4	25.8 ± 0.5	22.3 ± 0.5	13.2 ± 0.7
(12.5, 14.5]	12.3 ± 0.3	24.0 ± 0.4	27.5 ± 0.5	24.8 ± 0.7	13.5 ± 0.8
(14.5, 18.5]	14.0 ± 0.3	25.5 ± 0.4	32.3 ± 0.6	28.3 ± 0.8	18.2 ± 1.2
(18.5, 40.0]	17.4 ± 0.4	28.0 ± 0.6	28.3 ± 0.8	28.1 ± 1.2	14.8 ± 1.7

Table B.9 Trigger efficiencies (in %) for $B^0 \to J/\psi\, K^{*0}$ in bins of p_T and y.

p_T (GeV/c)	$2.0 < y < 2.5$	$2.5 < y < 3.0$	$3.0 < y < 3.5$	$3.5 < y < 4.0$	$4.0 < y < 4.5$
(2.0, 2.5]	30.8 ± 0.1	45.9 ± 0.2	57.5 ± 0.3	64.0 ± 0.3	69.2 ± 0.3
(2.5, 3.0]	33.2 ± 0.1	47.2 ± 0.2	60.1 ± 0.3	64.8 ± 0.3	69.8 ± 0.3
(3.0, 3.5]	34.2 ± 0.1	50.1 ± 0.2	60.3 ± 0.2	65.8 ± 0.2	69.4 ± 0.2
(3.5, 4.0]	37.1 ± 0.1	50.2 ± 0.1	61.7 ± 0.2	67.0 ± 0.2	71.1 ± 0.2
(4.0, 4.5]	37.5 ± 0.1	51.9 ± 0.1	62.8 ± 0.2	67.7 ± 0.2	70.9 ± 0.2
(4.5, 5.0]	39.1 ± 0.1	55.7 ± 0.1	64.8 ± 0.2	69.7 ± 0.2	71.4 ± 0.2
(5.0, 5.5]	40.1 ± 0.1	55.2 ± 0.1	66.4 ± 0.2	70.5 ± 0.2	73.9 ± 0.2
(5.5, 6.0]	41.8 ± 0.1	57.9 ± 0.1	67.0 ± 0.2	72.2 ± 0.2	74.4 ± 0.2
(6.0, 6.5]	45.9 ± 0.1	60.3 ± 0.1	69.1 ± 0.1	72.9 ± 0.2	75.9 ± 0.2
(6.5, 7.0]	45.5 ± 0.1	62.2 ± 0.1	70.1 ± 0.2	74.2 ± 0.2	77.2 ± 0.2
(7.0, 7.5]	50.2 ± 0.1	62.9 ± 0.1	71.9 ± 0.1	75.1 ± 0.1	77.7 ± 0.2
(7.5, 8.0]	52.6 ± 0.1	64.9 ± 0.1	72.1 ± 0.1	76.1 ± 0.2	77.3 ± 0.2
(8.0, 9.0]	52.2 ± 0.1	66.0 ± 0.1	74.1 ± 0.1	77.0 ± 0.2	78.3 ± 0.2
(9.0, 10.0]	56.2 ± 0.1	68.8 ± 0.1	75.5 ± 0.2	78.1 ± 0.2	79.0 ± 0.2
(10.0, 11.5]	59.8 ± 0.1	71.2 ± 0.1	76.5 ± 0.2	78.9 ± 0.2	80.3 ± 0.2
(11.5, 14.0]	63.3 ± 0.1	73.4 ± 0.2	77.9 ± 0.2	79.8 ± 0.2	81.5 ± 0.2
(14.0, 19.5]	66.4 ± 0.3	75.6 ± 0.3	78.3 ± 0.3	79.7 ± 0.3	80.3 ± 0.3
(19.5, 40.0]	68.0 ± 0.5	76.8 ± 0.6	78.1 ± 0.6	78.7 ± 0.6	73.9 ± 0.5

Table B.10 Trigger efficiencies (in %) for $B^+ \to J/\psi K^+$ in bins of p_T and y.

p_T (GeV/c)	$2.0 < y < 2.5$	$2.5 < y < 3.0$	$3.0 < y < 3.5$	$3.5 < y < 4.0$	$4.0 < y < 4.5$
(0.0, 0.5]	28.3 ± 0.2	50.4 ± 0.3	60.4 ± 0.4	62.9 ± 0.4	68.4 ± 0.4
(0.5, 1.0]	33.0 ± 0.1	49.8 ± 0.2	60.6 ± 0.3	63.5 ± 0.3	68.6 ± 0.3
(1.0, 1.5]	33.8 ± 0.1	50.0 ± 0.2	60.4 ± 0.2	65.0 ± 0.2	69.0 ± 0.2
(1.5, 2.0]	35.1 ± 0.1	49.6 ± 0.2	60.3 ± 0.2	64.9 ± 0.2	69.3 ± 0.2
(2.0, 2.5]	35.8 ± 0.1	50.5 ± 0.2	61.1 ± 0.2	65.8 ± 0.2	70.2 ± 0.2
(2.5, 3.0]	39.1 ± 0.1	52.5 ± 0.2	62.0 ± 0.2	67.4 ± 0.2	70.0 ± 0.2
(3.0, 3.5]	39.1 ± 0.1	53.6 ± 0.1	62.7 ± 0.2	68.2 ± 0.2	70.8 ± 0.2
(3.5, 4.0]	42.2 ± 0.1	54.6 ± 0.1	64.3 ± 0.2	69.3 ± 0.2	72.1 ± 0.2
(4.0, 4.5]	43.3 ± 0.1	56.9 ± 0.1	65.7 ± 0.1	70.7 ± 0.2	73.0 ± 0.2
(4.5, 5.0]	45.1 ± 0.1	58.4 ± 0.1	67.5 ± 0.1	71.5 ± 0.2	73.7 ± 0.2
(5.0, 5.5]	46.4 ± 0.1	60.4 ± 0.1	68.6 ± 0.1	72.4 ± 0.2	75.3 ± 0.2
(5.5, 6.0]	48.3 ± 0.1	61.3 ± 0.1	69.9 ± 0.1	73.8 ± 0.1	75.7 ± 0.1
(6.0, 6.5]	50.9 ± 0.1	63.0 ± 0.1	71.0 ± 0.1	74.7 ± 0.1	76.3 ± 0.1
(6.5, 7.0]	52.0 ± 0.1	64.5 ± 0.1	71.9 ± 0.1	75.4 ± 0.2	77.0 ± 0.2
(7.0, 7.5]	53.9 ± 0.1	66.0 ± 0.1	72.9 ± 0.1	76.1 ± 0.2	77.5 ± 0.2
(7.5, 8.0]	55.0 ± 0.1	67.0 ± 0.1	73.2 ± 0.1	76.9 ± 0.2	78.4 ± 0.2
(8.0, 8.5]	57.2 ± 0.1	68.6 ± 0.1	74.3 ± 0.1	77.5 ± 0.1	78.3 ± 0.2
(8.5, 9.0]	56.8 ± 0.1	69.7 ± 0.1	75.0 ± 0.2	77.6 ± 0.2	78.7 ± 0.2
(9.0, 9.5]	58.0 ± 0.1	70.3 ± 0.1	75.7 ± 0.1	78.4 ± 0.1	79.1 ± 0.1
(9.5, 10.0]	59.5 ± 0.1	70.8 ± 0.1	76.4 ± 0.1	78.8 ± 0.2	80.2 ± 0.2
(10.0, 10.5]	61.1 ± 0.1	71.5 ± 0.1	76.5 ± 0.2	78.9 ± 0.2	79.9 ± 0.2
(10.5, 11.0]	62.1 ± 0.1	72.5 ± 0.2	77.2 ± 0.2	79.3 ± 0.2	80.4 ± 0.2
(11.0, 12.0]	62.3 ± 0.2	72.9 ± 0.2	77.2 ± 0.2	79.5 ± 0.2	81.0 ± 0.2
(12.0, 13.0]	63.8 ± 0.2	73.5 ± 0.2	77.6 ± 0.2	79.8 ± 0.2	81.5 ± 0.2
(13.0, 14.5]	64.9 ± 0.2	74.3 ± 0.2	78.0 ± 0.2	79.8 ± 0.2	81.4 ± 0.2
(14.5, 16.5]	66.0 ± 0.3	75.2 ± 0.3	78.3 ± 0.3	79.6 ± 0.3	80.8 ± 0.3
(16.5, 21.5]	67.4 ± 0.3	76.2 ± 0.4	78.3 ± 0.4	79.3 ± 0.4	76.7 ± 0.4
(21.5, 40.0]	68.6 ± 0.5	77.1 ± 0.6	78.1 ± 0.6	78.9 ± 0.6	74.5 ± 0.6

Table B.11 Trigger efficiency for $B_s^0 \to J/\psi\,\phi$ in bins of p_T.

p_T (GeV/c)	Trigger efficiency (%)	p_T (GeV/c)	Trigger efficiency (%)
(0.0, 0.5]	61.2 ± 0.3	(6.0, 6.5]	65.3 ± 0.1
(0.5, 1.0]	55.0 ± 0.3	(6.5, 7.0]	66.5 ± 0.1
(1.0, 1.5]	56.2 ± 0.2	(7.0, 7.5]	67.3 ± 0.1
(1.5, 2.0]	55.8 ± 0.2	(7.5, 8.0]	67.9 ± 0.1
(2.0, 2.5]	55.9 ± 0.3	(8.0, 8.5]	69.1 ± 0.1
(2.5, 3.0]	55.1 ± 0.3	(8.5, 9.0]	70.1 ± 0.2
(3.0, 3.5]	55.9 ± 0.2	(9.0, 10.0]	71.8 ± 0.1
(3.5, 4.0]	57.7 ± 0.2	(10.0, 11.0]	71.8 ± 0.1
(4.0, 4.5]	60.4 ± 0.1	(11.0, 12.5]	73.0 ± 0.2
(4.5, 5.0]	60.4 ± 0.2	(12.5, 14.5]	74.2 ± 0.2
(5.0, 5.5]	61.9 ± 0.1	(14.5, 18.5]	73.9 ± 0.2
(5.5, 6.0]	63.5 ± 0.2	(18.5, 40.0]	74.1 ± 0.3

Table B.12 Total efficiencies (in %) for $B^+ \to J/\psi\,K^+$ in bins of p_T and y in the B_c^+ production ratio measurement.

p_T (GeV/c)	$2.5 < y < 3.0$	$3.0 < y < 3.5$	$3.5 < y < 4.0$	$4.0 < y < 4.5$
(4.0, 4.5]	2.8 ± 0.1	9.4 ± 0.1	12.8 ± 0.2	10.7 ± 0.2
(4.5, 5.0]	4.2 ± 0.1	11.3 ± 0.2	13.8 ± 0.2	11.8 ± 0.2
(5.0, 5.5]	5.6 ± 0.1	12.6 ± 0.2	14.1 ± 0.2	11.3 ± 0.3
(5.5, 6.0]	7.3 ± 0.1	14.7 ± 0.2	16.0 ± 0.3	10.8 ± 0.3
(6.0, 6.5]	9.0 ± 0.2	16.8 ± 0.2	16.8 ± 0.3	12.1 ± 0.3
(6.5, 7.0]	11.0 ± 0.2	18.1 ± 0.3	18.6 ± 0.3	13.3 ± 0.4
(7.0, 7.5]	12.7 ± 0.2	19.9 ± 0.3	19.7 ± 0.4	15.0 ± 0.4
(7.5, 8.0]	14.9 ± 0.3	20.8 ± 0.3	20.6 ± 0.4	13.6 ± 0.5
(8.0, 8.5]	16.4 ± 0.3	22.7 ± 0.4	22.7 ± 0.5	15.9 ± 0.6
(8.5, 9.0]	18.3 ± 0.3	24.6 ± 0.4	23.9 ± 0.5	15.1 ± 0.6
(9.0, 9.5]	19.7 ± 0.4	26.7 ± 0.5	25.5 ± 0.6	15.5 ± 0.7
(9.5, 10.0]	21.4 ± 0.4	27.5 ± 0.6	27.2 ± 0.7	16.9 ± 0.8
(10.0, 11.0]	23.1 ± 0.3	30.1 ± 0.5	26.6 ± 0.5	21.0 ± 0.7
(11.0, 12.0]	25.6 ± 0.4	30.2 ± 0.5	29.9 ± 0.7	22.3 ± 0.9
(12.0, 13.5]	28.9 ± 0.4	31.0 ± 0.5	27.7 ± 0.6	21.5 ± 0.9
(13.5, 16.5]	33.0 ± 0.5	34.2 ± 0.5	31.6 ± 0.7	23.4 ± 1.0
(16.5, 100.0]	34.9 ± 0.5	36.9 ± 0.6	36.6 ± 0.9	28.5 ± 1.5

Table B.13 Total efficiencies (in %) for $B_c^+ \to J/\psi\pi^+$ in bins of p_T and y in the B_c^+ production ratio measurement.

p_T (GeV/c)	$2.5 < y < 3.0$	$3.0 < y < 3.5$	$3.5 < y < 4.0$	$4.0 < y < 4.5$
(4.0, 4.5]	1.1 ± 0.0	5.1 ± 0.1	7.1 ± 0.1	5.6 ± 0.1
(4.5, 5.0]	1.6 ± 0.1	5.9 ± 0.1	7.4 ± 0.1	6.0 ± 0.2
(5.0, 5.5]	2.2 ± 0.1	6.9 ± 0.1	7.7 ± 0.2	5.7 ± 0.2
(5.5, 6.0]	3.0 ± 0.1	7.6 ± 0.1	8.5 ± 0.2	6.0 ± 0.2
(6.0, 6.5]	3.7 ± 0.1	8.1 ± 0.2	8.4 ± 0.2	5.6 ± 0.2
(6.5, 7.0]	4.8 ± 0.1	9.1 ± 0.2	9.2 ± 0.2	5.6 ± 0.2
(7.0, 7.5]	5.5 ± 0.1	10.0 ± 0.2	9.2 ± 0.2	5.4 ± 0.3
(7.5, 8.5]	6.5 ± 0.1	10.3 ± 0.2	9.7 ± 0.2	6.3 ± 0.2
(8.5, 9.5]	8.1 ± 0.2	12.2 ± 0.2	11.5 ± 0.3	7.0 ± 0.3
(9.5, 11.0]	10.2 ± 0.2	13.3 ± 0.2	12.5 ± 0.3	7.9 ± 0.4
(11.0, 14.5]	13.0 ± 0.2	16.7 ± 0.3	14.7 ± 0.3	8.6 ± 0.4
(14.5, 100.0]	18.8 ± 0.3	19.6 ± 0.4	16.2 ± 0.5	11.5 ± 0.9

Table B.14 Acceptance efficiency variation (in %) of smearing the generator level p_T distribution in bins of p_T and y.

p_T (GeV/c)	$2.0 < y < 2.5$	$2.5 < y < 3.0$	$3.0 < y < 3.5$	$3.5 < y < 4.0$	$4.0 < y < 4.5$
(0.0, 0.5]	0.31	-0.29	0.00	0.99	1.22
(0.5, 1.0]	-0.60	-0.59	-0.03	-0.41	-0.63
(1.0, 1.5]	0.13	0.47	0.75	0.29	-0.03
(1.5, 2.0]	0.21	0.07	-0.52	-0.43	0.00
(2.0, 2.5]	0.29	0.53	-0.62	0.28	0.27
(2.5, 3.0]	-0.60	-0.53	0.37	0.20	0.40
(3.0, 3.5]	0.27	-0.10	-0.09	-0.18	-0.19
(3.5, 4.0]	-0.32	-0.02	0.38	-0.33	-0.30
(4.0, 4.5]	0.26	0.45	-0.23	0.12	0.73
(4.5, 5.0]	0.36	-0.21	0.07	-0.42	-1.33
(5.0, 5.5]	-0.11	0.14	-0.10	-0.04	0.82
(5.5, 6.0]	-0.32	-0.47	-0.09	1.33	-0.67
(6.0, 6.5]	0.41	0.08	0.10	-1.12	0.00
(6.5, 7.0]	-0.39	-0.15	0.64	0.18	0.30
(7.0, 8.0]	0.08	0.08	-0.20	-0.15	-0.33
(8.0, 9.5]	-0.10	0.26	-0.08	-0.04	0.29
(9.5, 12.0]	0.03	-0.42	0.06	0.49	0.00
(12.0, 30.0]	0.05	0.16	-0.03	-0.06	0.16
(30.0, 40.0]	0.68	0.00	0.00	0.00	0.00

Table B.15 Differential cross-section ($\frac{\div\sigma}{\div p_{\mathrm{T}}}$ [μb/(GeV/c)]) of B_s^0 in bins of p_{T} for $y \in [2, 4.5]$. The uncertainties in the cross-sections are statistical and systematic, respectively.

p_{T} (GeV/c)	$\mathrm{d}\sigma/\mathrm{d}p_{\mathrm{T}}$ (μb)	p_{T} (GeV/c)	$\mathrm{d}\sigma/\mathrm{d}p_{\mathrm{T}}$ (μb)
0.0 – 0.5	0.11 ± 0.04 ± 0.05	6.0 – 6.5	0.68 ± 0.05 ± 0.21
0.5 – 1.0	0.63 ± 0.12 ± 0.20	6.5 – 7.0	0.61 ± 0.05 ± 0.19
1.0 – 1.5	0.78 ± 0.10 ± 0.24	7.0 – 7.5	0.46 ± 0.04 ± 0.14
1.5 – 2.0	1.18 ± 0.13 ± 0.37	7.5 – 8.0	0.41 ± 0.04 ± 0.13
2.0 – 2.5	1.17 ± 0.11 ± 0.37	8.0 – 8.5	0.35 ± 0.03 ± 0.11
2.5 – 3.0	1.27 ± 0.12 ± 0.40	8.5 – 9.0	0.35 ± 0.03 ± 0.11
3.0 – 3.5	1.16 ± 0.10 ± 0.36	9.0 – 10.0	0.24 ± 0.02 ± 0.08
3.5 – 4.0	1.28 ± 0.11 ± 0.40	10.0 – 11.0	0.17 ± 0.01 ± 0.05
4.0 – 4.5	1.17 ± 0.09 ± 0.37	11.0 – 12.5	0.096 ± 0.007 ± 0.030
4.5 – 5.0	0.83 ± 0.06 ± 0.26	12.5 – 14.5	0.061 ± 0.005 ± 0.019
5.0 – 5.5	0.81 ± 0.06 ± 0.25	14.5 – 18.5	0.029 ± 0.002 ± 0.009
5.5 – 6.0	0.74 ± 0.06 ± 0.23	18.5 – 40.0	0.0030 ± 0.0003 ± 0.0009

p_T (GeV/c)	$2.0 < y < 2.5$	$2.5 < y < 3.0$	$3.0 < y < 3.5$	$3.5 < y < 4.0$	$4.0 < y < 4.5$
0.0 – 0.5	0.37 ± 0.12 ± 0.03	0.49 ± 0.07 ± 0.03	0.50 ± 0.09 ± 0.03	0.42 ± 0.10 ± 0.03	0.20 ± 0.09 ± 0.02
0.5 – 1.0	1.59 ± 0.18 ± 0.12	1.43 ± 0.11 ± 0.09	1.30 ± 0.11 ± 0.09	1.16 ± 0.11 ± 0.08	0.94 ± 0.14 ± 0.07
1.0 – 1.5	1.95 ± 0.19 ± 0.13	2.11 ± 0.12 ± 0.14	1.93 ± 0.11 ± 0.13	1.92 ± 0.12 ± 0.13	1.36 ± 0.17 ± 0.10
1.5 – 2.0	2.24 ± 0.20 ± 0.15	3.17 ± 0.14 ± 0.21	2.52 ± 0.11 ± 0.17	2.18 ± 0.11 ± 0.15	1.74 ± 0.16 ± 0.12
2.0 – 2.5	2.65 ± 0.21 ± 0.18	3.34 ± 0.13 ± 0.22	2.83 ± 0.11 ± 0.19	2.46 ± 0.10 ± 0.17	1.77 ± 0.14 ± 0.12
2.5 – 3.0	3.00 ± 0.21 ± 0.20	3.39 ± 0.13 ± 0.22	2.92 ± 0.10 ± 0.19	2.52 ± 0.10 ± 0.17	1.80 ± 0.13 ± 0.12
3.0 – 3.5	3.07 ± 0.20 ± 0.20	3.48 ± 0.12 ± 0.23	3.17 ± 0.10 ± 0.21	2.29 ± 0.08 ± 0.15	1.72 ± 0.11 ± 0.12
3.5 – 4.0	2.57 ± 0.17 ± 0.17	3.31 ± 0.11 ± 0.22	2.71 ± 0.08 ± 0.18	2.22 ± 0.08 ± 0.15	1.47 ± 0.10 ± 0.10
4.0 – 4.5	2.40 ± 0.16 ± 0.16	3.08 ± 0.10 ± 0.20	2.60 ± 0.07 ± 0.17	2.12 ± 0.07 ± 0.14	1.44 ± 0.09 ± 0.10
4.5 – 5.0	2.50 ± 0.15 ± 0.17	2.77 ± 0.08 ± 0.18	2.11 ± 0.06 ± 0.14	1.66 ± 0.06 ± 0.11	1.07 ± 0.07 ± 0.07
5.0 – 5.5	2.23 ± 0.14 ± 0.15	2.25 ± 0.07 ± 0.15	2.04 ± 0.06 ± 0.13	1.58 ± 0.05 ± 0.10	0.95 ± 0.07 ± 0.06
5.5 – 6.0	1.90 ± 0.12 ± 0.13	2.11 ± 0.07 ± 0.14	1.78 ± 0.05 ± 0.12	1.25 ± 0.05 ± 0.08	0.88 ± 0.06 ± 0.06
6.0 – 6.5	1.77 ± 0.10 ± 0.12	1.81 ± 0.06 ± 0.12	1.41 ± 0.04 ± 0.09	1.11 ± 0.04 ± 0.07	0.73 ± 0.05 ± 0.05
6.5 – 7.0	1.45 ± 0.09 ± 0.10	1.54 ± 0.05 ± 0.10	1.21 ± 0.04 ± 0.08	0.87 ± 0.03 ± 0.06	0.54 ± 0.04 ± 0.04
7.0 – 7.5	1.42 ± 0.08 ± 0.09	1.35 ± 0.04 ± 0.09	0.98 ± 0.03 ± 0.06	0.66 ± 0.03 ± 0.04	0.43 ± 0.03 ± 0.03
7.5 – 8.0	1.29 ± 0.07 ± 0.08	1.08 ± 0.04 ± 0.07	0.91 ± 0.03 ± 0.06	0.63 ± 0.03 ± 0.04	0.33 ± 0.03 ± 0.02
8.0 – 8.5	1.01 ± 0.06 ± 0.07	0.96 ± 0.03 ± 0.06	0.72 ± 0.03 ± 0.05	0.48 ± 0.02 ± 0.03	0.24 ± 0.02 ± 0.02
8.5 – 9.0	0.90 ± 0.06 ± 0.06	0.88 ± 0.03 ± 0.06	0.62 ± 0.02 ± 0.04	0.39 ± 0.02 ± 0.03	0.26 ± 0.02 ± 0.02
9.0 – 9.5	0.74 ± 0.05 ± 0.05	0.68 ± 0.03 ± 0.04	0.54 ± 0.02 ± 0.04	0.34 ± 0.02 ± 0.02	0.24 ± 0.02 ± 0.02
9.5 – 10.0	0.59 ± 0.04 ± 0.04	0.60 ± 0.02 ± 0.04	0.45 ± 0.02 ± 0.03	0.28 ± 0.02 ± 0.02	0.17 ± 0.02 ± 0.01
10.0 – 10.5	0.49 ± 0.03 ± 0.03	0.50 ± 0.02 ± 0.03	0.37 ± 0.02 ± 0.02	0.26 ± 0.01 ± 0.02	0.11 ± 0.01 ± 0.01
10.5 – 11.0	0.43 ± 0.03 ± 0.03	0.40 ± 0.02 ± 0.03	0.30 ± 0.01 ± 0.02	0.23 ± 0.02 ± 0.02	0.09 ± 0.01 ± 0.01
11.0 – 12.0	0.40 ± 0.02 ± 0.03	0.33 ± 0.01 ± 0.02	0.245 ± 0.010 ± 0.016	0.142 ± 0.008 ± 0.009	0.068 ± 0.007 ± 0.005
12.0 – 13.0	0.26 ± 0.02 ± 0.02	0.240 ± 0.010 ± 0.016	0.192 ± 0.009 ± 0.013	0.111 ± 0.007 ± 0.007	0.050 ± 0.006 ± 0.003
13.0 – 14.5	0.21 ± 0.01 ± 0.01	0.172 ± 0.007 ± 0.011	0.118 ± 0.005 ± 0.008	0.074 ± 0.004 ± 0.005	0.034 ± 0.004 ± 0.002
14.5 – 16.5	0.115 ± 0.006 ± 0.008	0.097 ± 0.004 ± 0.006	0.070 ± 0.004 ± 0.005	0.043 ± 0.003 ± 0.003	0.015 ± 0.002 ± 0.001
16.5 – 21.5	0.054 ± 0.003 ± 0.004	0.044 ± 0.002 ± 0.003	0.030 ± 0.001 ± 0.002	0.015 ± 0.001 ± 0.001	0.0049 ± 0.0006 ± 0.0004
21.5 – 40.0	0.0096 ± 0.0005 ± 0.0006	0.0071 ± 0.0004 ± 0.0005	0.0033 ± 0.0002 ± 0.0002	0.00113 ± 0.00014 ± 0.00008	0.00036 ± 0.00011 ± 0.00003

Table B.16 Differential cross-section ($\frac{d^2\sigma}{\div p_T \div y}$ [μb/(GeV/c)]) of B^+ in bins of p_T and y. The first uncertainty is statistical and the second systematic.

p_T (GeV/c)	$2.0 < y < 2.5$	$2.5 < y < 3.0$	$3.0 < y < 3.5$	$3.5 < y < 4.0$	$4.0 < y < 4.5$
2.0 – 2.5	3.71 ± 0.66 ± 0.29	3.31 ± 0.28 ± 0.24	2.75 ± 0.21 ± 0.20	2.06 ± 0.22 ± 0.16	1.60 ± 0.29 ± 0.13
2.5 – 3.0	2.73 ± 0.55 ± 0.21	3.26 ± 0.29 ± 0.24	2.48 ± 0.17 ± 0.18	1.96 ± 0.17 ± 0.15	1.46 ± 0.23 ± 0.11
3.0 – 3.5	2.96 ± 0.67 ± 0.23	3.21 ± 0.21 ± 0.23	2.73 ± 0.16 ± 0.20	2.37 ± 0.16 ± 0.18	1.54 ± 0.22 ± 0.12
3.5 – 4.0	2.28 ± 0.39 ± 0.17	3.28 ± 0.21 ± 0.24	2.33 ± 0.14 ± 0.17	1.98 ± 0.13 ± 0.15	1.23 ± 0.18 ± 0.10
4.0 – 4.5	2.65 ± 0.38 ± 0.20	3.01 ± 0.17 ± 0.22	2.39 ± 0.12 ± 0.17	1.70 ± 0.10 ± 0.13	1.38 ± 0.15 ± 0.11
4.5 – 5.0	2.17 ± 0.41 ± 0.16	2.62 ± 0.14 ± 0.19	2.11 ± 0.09 ± 0.15	1.70 ± 0.09 ± 0.13	0.85 ± 0.11 ± 0.07
5.0 – 5.5	2.47 ± 0.28 ± 0.18	2.26 ± 0.12 ± 0.16	1.86 ± 0.08 ± 0.14	1.64 ± 0.08 ± 0.12	1.07 ± 0.12 ± 0.08
5.5 – 6.0	1.95 ± 0.28 ± 0.14	1.91 ± 0.10 ± 0.14	1.53 ± 0.07 ± 0.11	1.13 ± 0.07 ± 0.08	0.80 ± 0.09 ± 0.06
6.0 – 6.5	1.56 ± 0.19 ± 0.12	1.57 ± 0.08 ± 0.11	1.27 ± 0.06 ± 0.09	1.02 ± 0.06 ± 0.07	0.49 ± 0.08 ± 0.04
6.5 – 7.0	1.56 ± 0.18 ± 0.11	1.55 ± 0.08 ± 0.11	1.20 ± 0.06 ± 0.09	0.74 ± 0.05 ± 0.05	0.52 ± 0.07 ± 0.04
7.0 – 7.5	1.15 ± 0.14 ± 0.08	1.33 ± 0.07 ± 0.10	1.09 ± 0.05 ± 0.08	0.73 ± 0.04 ± 0.05	0.55 ± 0.06 ± 0.04
7.5 – 8.0	1.06 ± 0.12 ± 0.08	1.01 ± 0.05 ± 0.07	0.81 ± 0.04 ± 0.06	0.50 ± 0.03 ± 0.04	0.30 ± 0.04 ± 0.02
8.0 – 9.0	0.97 ± 0.08 ± 0.07	0.79 ± 0.03 ± 0.06	0.67 ± 0.02 ± 0.05	0.44 ± 0.02 ± 0.03	0.28 ± 0.03 ± 0.02
9.0 – 10.0	0.75 ± 0.06 ± 0.05	0.59 ± 0.03 ± 0.04	0.42 ± 0.02 ± 0.03	0.26 ± 0.01 ± 0.02	0.16 ± 0.02 ± 0.01
10.0 – 11.5	0.51 ± 0.03 ± 0.04	0.40 ± 0.02 ± 0.03	0.31 ± 0.01 ± 0.02	0.168 ± 0.009 ± 0.012	0.093 ± 0.010 ± 0.007
11.5 – 14.0	0.22 ± 0.01 ± 0.02	0.216 ± 0.008 ± 0.016	0.156 ± 0.006 ± 0.011	0.090 ± 0.005 ± 0.007	0.044 ± 0.005 ± 0.003
14.0 – 19.5	0.099 ± 0.005 ± 0.007	0.073 ± 0.003 ± 0.005	0.047 ± 0.002 ± 0.003	0.026 ± 0.002 ± 0.002	0.013 ± 0.002 ± 0.001
19.5 – 40.0	0.0103 ± 0.0007 ± 0.0008	0.0074 ± 0.0005 ± 0.0005	0.0042 ± 0.0003 ± 0.0003	0.0021 ± 0.0003 ± 0.0002	0.00039 ± 0.00012 ± 0.00004

Table B.17 Differential cross-section ($\frac{d^2\sigma}{\div p_T \div y}$ [μb/(GeV/c)]) of B^0 in bins of p_T and y. The first uncertainty is statistical and the second systematic.

Resume and publications

Personal

- Date of birth: Oct. 29, 1984
- Place of birth: Liaoning Province, China

Education

- Jan. 2012 - present Ph.D. candidate in Physics.
  Department of Engineering Physics, Tsinghua University, Beijing, China
- Jan. 2011 - Jan. 2012 Joint Ph.D. candidate in Physics.
  LAL, IN2P3/CNRS, Orsay, France
- Sep. 2007 - Jan. 2011 Ph.D. candidate in Physics.
  Department of Engineering Physics, Tsinghua University, Beijing, China
- Sep. 2003 - Jul. 2007 B.S. in Engineering Physics.
  Department of Engineering Physics, Tsinghua University, Beijing, China

Publications

[1] The LHCb Collaboration, R. Aaij and others (contact author Bo Liu), Measurement of the $B^{\pm}$ production cross-section in pp collisions at $\sqrt{s}$=7 TeV, arXiv:1202.4812 [hep-ex], accepted by JHEP.

[2] Bo Liu (on behalf of the LHCb Collaboration), Exotic spectroscopy and quarkonia at LHCb, Proceeding of the XIV International Conference on Hadron Spectroscopy, 13-17 June 2011, Munich, Germany. arXiv:1108.5877v1 [hep-ex]